UNDERWATER LUMINESCENCE OF $SrAl_2O_4:Eu^{2+}, Dy^{3+}$ PERSISTENT PHOSPHOR

M. Nazarov [1,2], *A.* Nor Nazida[1], M. N. Ahmad-Fauzi[1], A. Badri Ismail[1], and P. Ivannikov[3]

[1]*School of Materials and Mineral Resources Engineering, Universiti Sains Malaysia,*
Engineering Campus, 14300 Nibong Tebal, Pulau Pinang, Malaysia
[2]*Institute of Applied Physics, Academiei Str. 5, Chisinau, MD-2028 Republic of Moldova*
[3]*Moscow State University, Moscow, Russia*

(Received 13 July 2012)

Abstract

An artificial block from concrete and sand covered by $SrAl_2O_4:Eu^{2+}$, Dy^{3+} based phosphor was prepared, and a new direction in the study and application of persistent phosphors was proposed. For the first time, underwater luminescence was experimentally studied in real sea conditions. The bright blue-green long-lasting afterglow was demonstrated and registered from a depth of 5 m. The fishes were attracted by the light of the artificial reef.

1. Introduction

Persistent phosphors can emit light for a long time from a few seconds to many hours after the excitation has ended. The irradiation used may be UV, visible light, X-ray, gamma radiation, as well as usual sun light.

Persistent luminescence has intrigued people for hundreds of years. The situation drastically changed about 16 years ago when Matsuzawa *et al.* discovered bright and long-lasting luminescence in $SrAl_2O_4$:Eu,Dy [1]. By codoping the green-emitting phosphor $SrAl_2O_4:Eu^{2+}$ (already showing a relatively strong and long-lasting afterglow by itself [2]) with the rare earth element dysprosium (Dy^{3+}), they were able to create a material that emitted bright light for hours after ending the excitation (simultaneously and independently, Takasaki *et al*. reported similar results [3]). They found an afterglow with both a far higher initial intensity and a much longer lifetime compared to traditional ZnS:Cu,Co. These investigations have led to a renewed research interest, and it promoted the use of these green-emitting persistent phosphors in signalization, glow-in-the-dark toys, emergency signs, dials and displays, textile printing, medical diagnostics, and many other applications. Applications of persistent luminescence phosphors are rapidly expanding.

In this article, we propose a new direction in study and application these materials, namely underwater investigations of persistent luminescence. A new multiphase blue-green phosphor based on $SrAl_2O_4$ was synthesized and applied in real sea conditions.

2. Experimental procedures

2.1. Sample preparation

An artificial rock and block made of a steel slag hybrid matrix have been recently developed in Japan [4, 5]. We propose to prepare an experimental artificial glow reef from concrete and sand to provide a hard surface. Another decision is to cover the real corals by persistent phosphors. The main goal of these experiments is to cultivate the algae in the future and to attract the fish. For this purpose, the artificial block must be luminescent and preferably excite the green light. The $SrAl_2O_4:Eu^{2+}$, Dy^{3+} persistent phosphor as a phosphorescence material and polymer epoxy as a coating layer are proposed. Strontium aluminate phosphor doped with Eu^{2+} and co-doped with Dy^{3+} $SrAl_2O_4:Eu^{2+}$, Dy^{3+} were prepared by a solid state reaction approach using strontium carbonate ($SrCO_3$; Aldrich, 99.9 %), aluminum oxide (Al_2O_3), europium oxide (Eu_2O_3; Aldrich, 99.99 %), and dysprosium oxide (Dy_2O_3; Aldrich, 99.99 %) as starting materials. A small amount (0.2 mol %) of H_3BO_3 was used as a flux. Prior to heating at 1250ºC, the reagents were ground using a ball mill to form a homogeneous mixture. First, the dry milling was used for 30 min and then continued using a wet-mixing machine for 30 min. The resulting slurry was dried at 150°C for 3 h to remove the water content. After fully dried, the mixed white powder was placed in a small alumina crucible and then fired at 1250°C for 2 h under a mild reducing atmosphere. A graphite crucible was used to create the reducing atmosphere and to ensure complete reduction of Eu^{3+} to Eu^{2+} and to crystallize and form the luminescence centers. The mixing–milling process to get a smaller particle size and a homogenous mixture was used after calcination. This phosphor excited by UV or sun light shows bright blue-green luminescence (Fig. 1).

Fig. 1. Bright luminescence of $SrAl_2O_4:Eu^{2+}$, Dy^{3+} based phosphor in the open air under sun light excitation.

In this study, an epoxy layer of the $SrAl_2O_4:Eu^{2+}$, Dy^{3+} phosphor was deposited on the reef surface by a brushing technique. A certain amount of mixed polymers Epoxy DEN 431 and polyetheramine D230 hardener was prepared, and 30–40 wt% of the $SrAl_2O_4:Eu^{2+}$, Dy^{3+} phosphor pigment were added to produce a high glowing intensity. After precise weighing of all materials, the slip mixture was manually mixed to a homogeneous composition of the epoxy solution and phosphor pigments. This solution was applied on the reef surface by a brushing technique with controlled thickness of the coating layer. The surface interactions between the epoxy layer of $SrAl_2O_4:Eu^{2+}$, Dy^{3+} and reef took place during the curing process at 100ºC for 1 h. The final artificial block and coral are shown in Fig. 2.

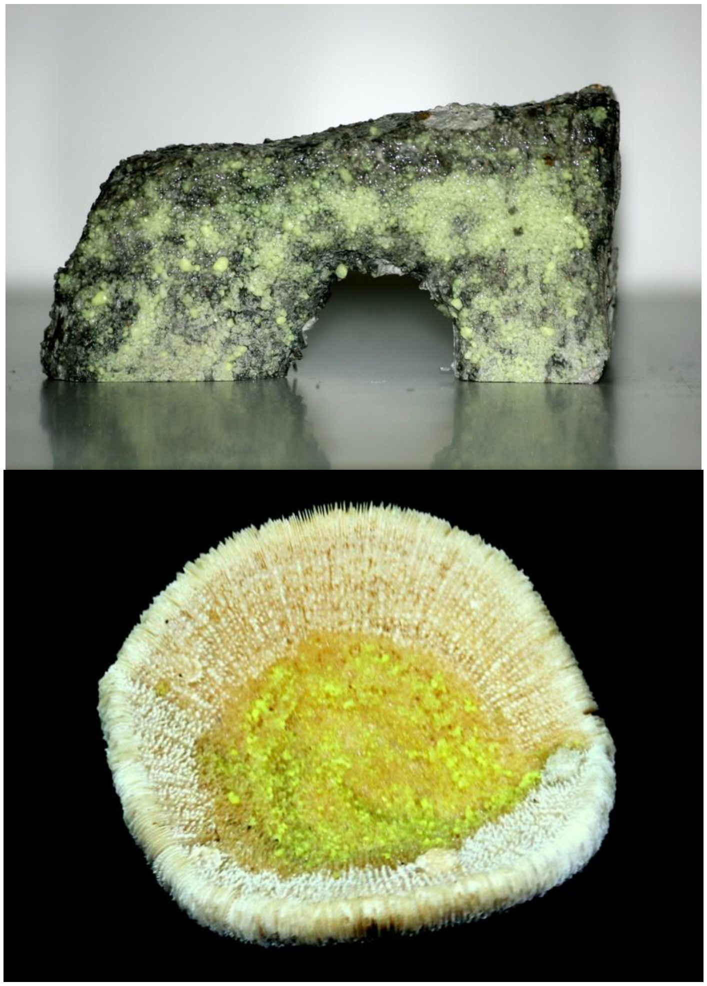

Fig. 2. Artificial block from concrete and sand covered by $SrAl_2O_4:Eu^{2+}, Dy^{3+}$ (top) and real coral with phosphor inside (bottom)

The persistent effect or long-lasting afterglow luminescence is seen in Fig. 3. The phosphor inside the coral was excited by the sun light in the daytime and shows very bright green luminescence in the night.

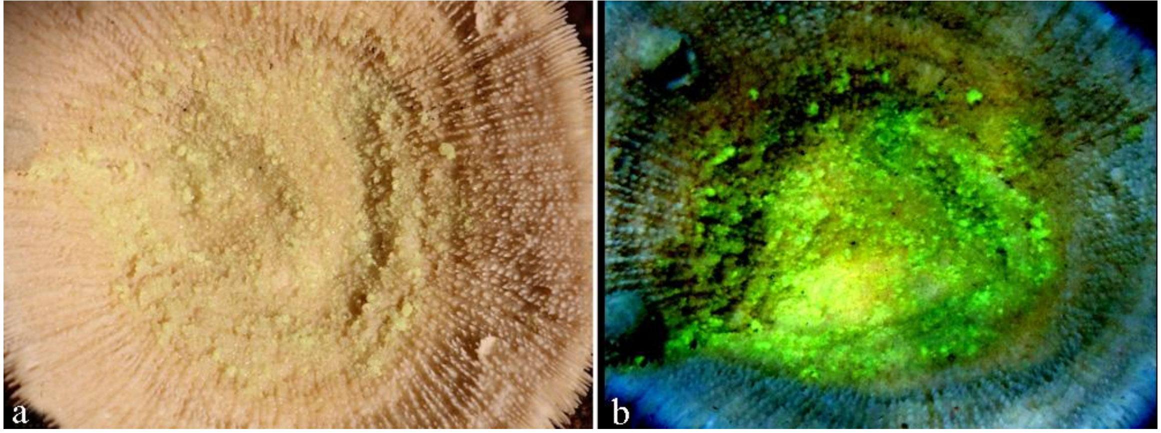

Fig. 3. Day (a) and night (b) luminescence of $SrAl_2O_4:Eu^{2+}, Dy^{3+}$.

2.2. Sample characterization

The morphology and structure of the as heated products were studied by an XRD Bruker, D8 Advance X-ray Diffractometer with Cu-Kα radiation at a wavelength of 1.54 Å. Data have been collected by step-scanning 2θ from 10 to 90° and 0.034 s counting time at each step at room temperature.

The photoluminescence excitation and emission spectra were recorded using a Horiba Jobin Yvon IHR 550 UV Fluorescence Spectrometer. All the samples were excited by 325-nm radiation from a 450 W pulsed Xenon lamp.

No single method (XRD or PL) can supply the necessary information, which is now required for detailed analysis. The microscopic properties of synthesized materials are often caused by inhomogeneities on a microscopic scale. We have also chosen some of the traditional and some original modes and image processing to illustrate these possibilities. The luminescence properties were investigated with a modified Stereoscan SEM with an additional attachment for the color cathodoluminescence (CCL) mode [6]. CCL techniques used in conjunction with SEM can give both spectral and spatial information with high resolution. We used a recording system consisting of three multipliers with different light filters (R, G, B) and of a multichannel device connected with photomultipliers. It allows simultaneous transmission of video signals on all channels in any pre-determined range of the spectrum. Images of the surface under study and the corresponding CL emission from the surface were displayed on video monitors. The CL images can be recorded with the total emitted integral (panchromatic) CL as well as with light of fixed spectral wavelength by using a suitable photodetector. The combination with the secondary electron image with the backscattered electrons allows the analytical CL image to be compared with the surface topography of the sample. To avoid charging effects, all the samples were coated with a thin conductive aluminum layer (about 100 Å) before the SEM examinations.

3. Results and discussion

3.1. Structure, morphology, and luminescence

Figure 4 shows the XRD patterns of $SrAl_2O_4:Eu^{2+}$, Dy^{3+} annealed at 1250°C for 2 h in an active carbon atmosphere.

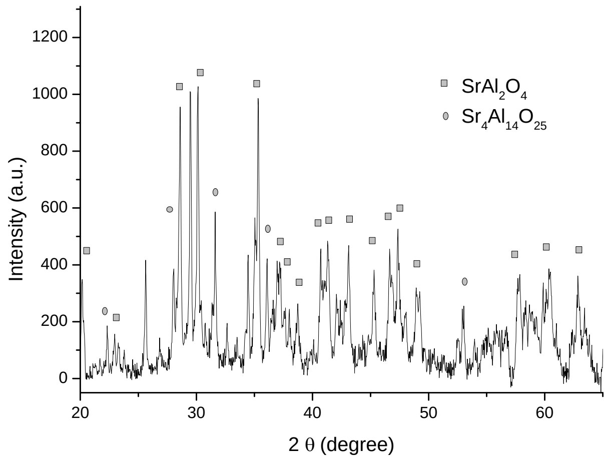

Fig. 4. XRD patterns of the synthesized phosphor.

From Fig. 4, it is seen that the XRD patterns include two phases $SrAl_2O_4$ and $Sr_4Al_{14}O_{25,}$ indicating the formation of mixed oxide phases. As the firing temperature is raised to 1250°C, the XRD peaks become sharper and stable phases of $SrAl_2O_4$ and $Sr_4Al_{14}O_{25}$ with higher crystallinity can be obtained.

PL spectroscopy indirectly confirms the presence of two phases. The detailed results of these experiments are given in our previous articles [7-9]. Here in Fig. 5 we show the emission spectra of synthesized phosphor.

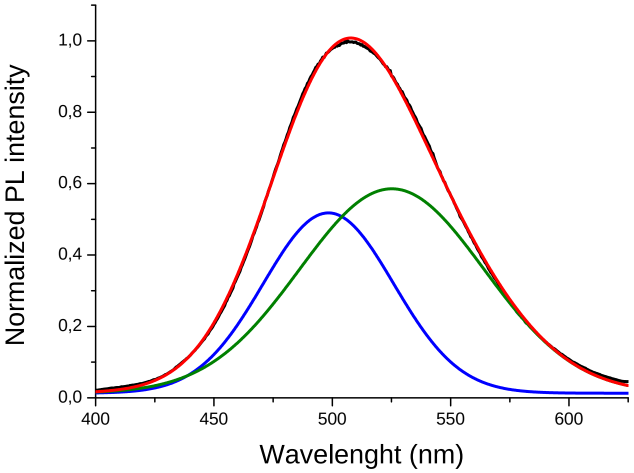

Fig. 5. Decomposition of total PL intensity on blue and green bands.

The asymmetry of PL emission intensity allows us to decompose this spectrum into blue and green bands peaked around 490 and 520 nm. These bands correspond to $Sr_4Al_{14}O_{25}$ (490 nm) and $SrAl_2O_4$ (520 nm) phases doped with Eu^{2+}.

A direct confirmation of this hypothesis follows from cathodoluminescence measurements. The results of experimental investigations of the prepared phosphors by secondary electrons and color cathodoluminescence, as well as combined signal, are presented in Fig. 6. In all experiments, the accelerating voltage in SEM was 20 kV and the beam current 100 nA. The diameter of the electron beam did not exceed 0.1 μm. We used a recording system consisting of three multipliers with different light filters (R, G, B) and a multichannel device connected with photomultipliers. It allows simultaneous transmission of video signals on all channels in any pre-determined range of the spectrum. Images of the surface under study and the corresponding CL emission from the surface were displayed on video monitors.

In secondary electrons (Fig. 6a) we can see only the topography of agglomerated powder. CCL (Fig. 6b) shows the spatial distributions of different CL spectral bands (green 520 nm and blue 490 nm) belonging to $SrAl_2O_4:Eu^{2+}$, Dy^{3+} and $Sr_4Al_{14}O_{25}:Eu^{2+}$, Dy^{3+}, respectively. This direct experiment really confirms the existence of two different phases with different colors. Moreover, the absence of red color centers proves that all Eu^{3+} was reduced to Eu^{2+} in synthesis process. The combination of CCL with the secondary electron image (Fig. 6c) allows the analytical CL image to be compared with the surface topography of the sample.

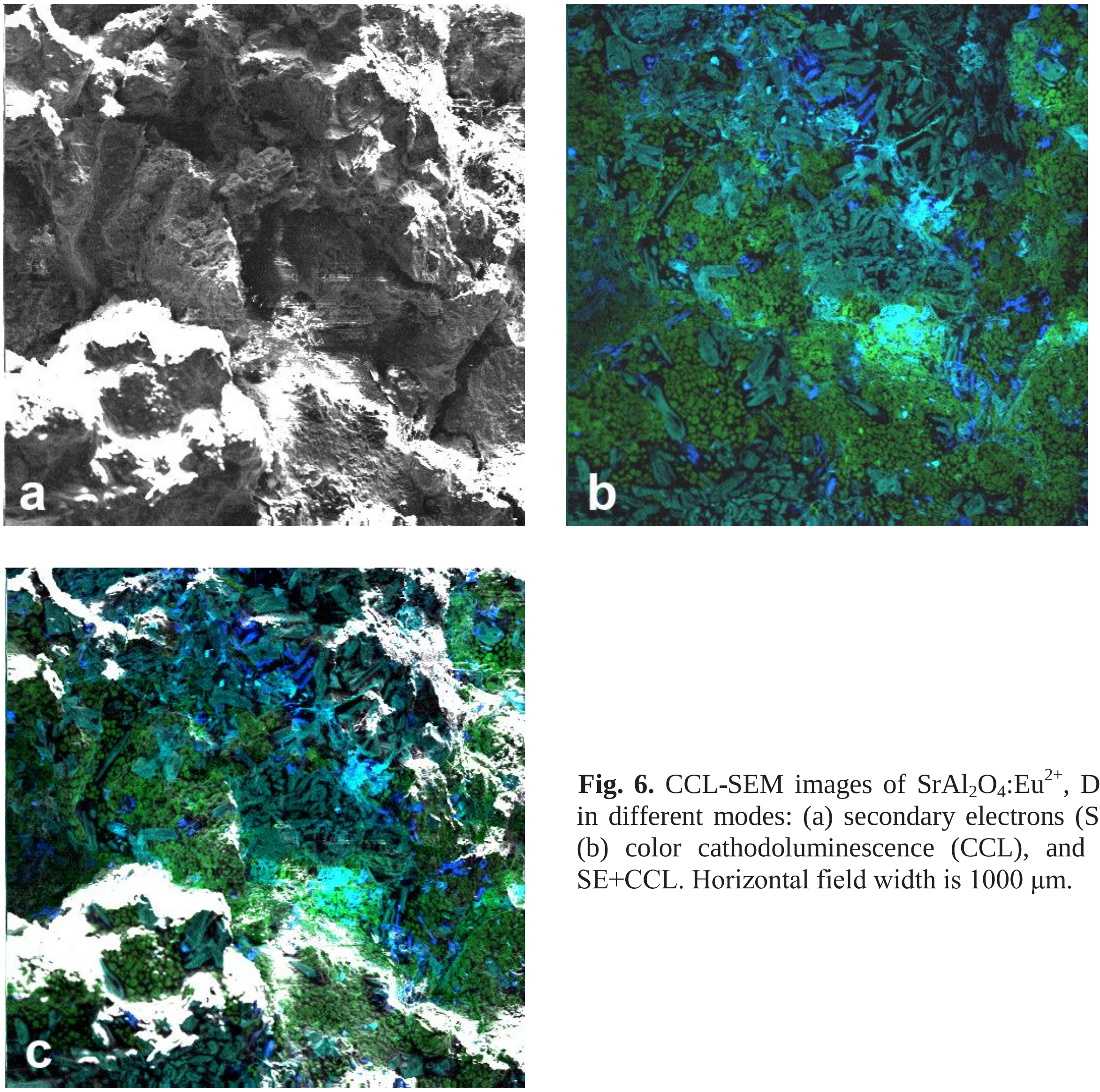

Fig. 6. CCL-SEM images of $SrAl_2O_4$:Eu^{2+}, Dy^{3+} in different modes: (a) secondary electrons (SE), (b) color cathodoluminescence (CCL), and (c) SE+CCL. Horizontal field width is 1000 μm.

3.2. Underwater phosphor application

The first experiments with underwater luminescence were carried out in a room aquarium. Two glass cans with the $SrAl_2O_4$:Eu^{2+}, Dy^{3+} phosphor were installed near the surface and on the bottom of the aquarium. The left can was illuminated by the visible light, and the phosphor was excited in comparison with the right one (Fig. 7).

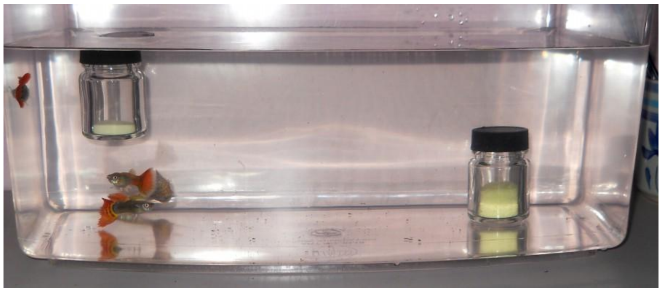

Fig. 7. Aquarium with excited (left) and nonexcited (right) phosphors.

The experiments show that the aquarium fishes mostly prefer to stay in the left part of the aquarium near the luminescent phosphor.

The real underwater experiments in sea conditions were carried out in Pulau Payar and Pulau Kapas, Malaysia. First, the artificial blocks covered by $SrAl_2O_4:Eu^{2+}$, Dy^{3+} and excited by the sun light were installed on the ocean floor with different relief (agropora corals, rocks, sand) and at different depth of 2 to 6 m. Figure 8 shows the process of installation of the artificial luminescent block on a real stone and corals in the sea at a depth of about 5 m.

Fig. 8. Installation of a concrete matrix covered by $SrAl_2O_4:Eu^{2+}$, Dy^{3+} on the stone (top) and on the real corals (bottom).

The next step was underwater luminescence investigations. All blocks showed the bright blue-green luminescence from all the places regardless of relief and depth. One of the examples is demonstrated in Fig. 9.

Fig. 9. Blue-Green color luminescence of an artificial concrete rock and a real coral covered by $SrAl_2O_4:Eu^{2+},Dy^{3+}$ from a depth of 5 m in real sea conditions

After some minutes, the fishes were interested in a new luminescent object and gathered around it (Fig. 10).

Fig. 10. The fishes are attracted by bright and long-lasting luminescence of $SrAl_2O_4$:Eu^{2+}, Dy^{3+}.

Fig. 11. Concrete matrix inside of Tridacna.

Finally, the black-tip shark was also interested in luminescence and came near our artificial sample (Fig. 12).

Fig. 12. The black-tip shark is also interested in luminescence

4. Conclusions

A multiphase blue-green persistent phosphor with turquoise luminescence was synthesized and applied for sea investigations. For the first time, the experiments with an artificial stone and coral covered by the $SrAl_2O_4:Eu^{2+}$, Dy^{3+} based phosphor were carried out in real sea conditions in Pulau Payar Marine Park and Pulau Kapas Malaysia. Strong and bright turquoise luminescence was observed and registered under the water. The fishes were attracted by the light of the artificial reef.

References

[1] T. Matsuzawa, Y. Aoki, N. Takeuchi, and Y. Murayama, J. Electrochem. Soc., 143, 2670 (1996).
[2] V. Abbruscato, J. Electrochem. Soc., 118, 930 (1971).
[3] H. Takasaki, S. Tanabe, and T. Hanada, J. Ceram. Soc. Jpn., 104, 322 (1996).
[4] T. Takahashi and K. Yabuta, NKK Technical review, 87 (2002).
[5] N. Isoo et al., J. Japan. Soc. Fish. Sci., 66, 647 (2000).
[6] S.K. Obyden, P.V. Ivannikov, and G.V. Saparin, Scanning 19, 533 (1997).
[7] A. Nor Nazida, M.N. Ahmad-Fauzi, M. Nazarov, A. Azizan, and K. Shah Rizal, J. Mold. Phys Sci., 11, 1-2, 78 (2012).
[8] S. C. M. Calyn, M. Nazarov, A. Nor Nazida, M.N. Ahmad-Fauzi, J. Mold. Phys Sci., 11, 1-2, 112 (2012).
[9] M. Nazarov, A. Nor Nazida, A. Azizan, K. Shah Rizal1, S. C. M. Calyn, and M.N. Ahmad-Fauzi, J. Mold. Phys Sci., 11, 1-2, 67 (2012).

STRUCTURAL FEATURES AND ELECTRICAL CONDUCTIVITY OF THE GaSb-FeGa$_{1.3}$ AND GaSb-CoGa$_{1.3}$ EUTECTIC COMPOSITES

M. I. Aliyev, I. Kh. Mammadov*, A. A. Khalilova, R. N. Rahimov, and D. H. Arasly

Institute of Physics of the Azerbaijan National Academy of Sciences;
**Azerbaijan National Academy of Aviation*
E-mail: rashad@physics.ab.az

(Received 11 September 2012)

Abstract

The thermography, XRD, and microstructural study of the electrical properties of the GaSb-FeGa$_{1.3}$ and GaSb-CoGa$_{1.3}$ eutectic composites at the temperature range of 80-450K have been performed. The thermodynamic parameters have been determined by thermography. The analysis of the XRD spectra showed that no structural change occurs with temperature. The microstructure and elemental compositions of the matrix, metallic inclusions, and interphase zone have been determined by scanning electron microscope and EDX, respectively. It has been shown that the presence of metal inclusions leads to the anisotropy of electrical conductivity and Hall effect. The calculation of the total electrical conductivity of composites, which was carried out in the framework of the effective media theory, reveals that the role of the interphase zone is an essential factor in the short-circuiting action by inclusions leading to the anisotropy of electrical parameters.

1. Introduction

Eutectic composites based on III-V compound semiconductors and 3d-transition elements, in which the metallic phase exists in the form of needles, are best materials for heterogeneous semiconductors. Despite the fact that they are widely applied for designing galvanomagnetic, thermomagnetic, photothermomagnetic, and strain sensitive translators [1-4], a satisfactory explanation of some features of their physical properties has not been found to the moment. A study of the crystal structure and microstructure of the systems can explain these features. In this work, the diffraction patterns at various temperatures, the microstructure, elemental composition, and electrical properties of GaSb-FeGa$_{1,3}$ and GaSb-CoGa$_{1,3}$ composites have been studied.

2. Experimental

GaSb-FeGa$_{1,3}$ and GaSb-CoGa$_{1,3}$ composites are synthesized by alloying GaSb with 4.0 wt % Fe and 3.1 wt % Co and the quantity of Ga corresponding to the formula of FeGa$_{1.3}$ and CoGa$_{1.3}$, respectively. The synthesis was conducted at a temperature of 900 K and under vibration for 3 h. After that, the alloys were heated to a temperature of 1300 K and after full homogenization they were taken from the furnace and rapidly hardened. Immediately after this, the ingot was subjected to oriented re-crystallization by the vertical Bridgman method. To avoid ampoule vibration that can disturb the solid-melt interface, the prepared sample was kept motionless with the movement of the freezing interface accomplished by lifting the furnace at a rate of 1 mm/min. After the oriented re-crystallization, 85-90% of the ingot length consisted of GaSb-FeGa$_{1,3}$ and GaSb-CoGa$_{1,3}$ eutectic composite. The obtained composite was characterized by the uniform distribution of the metal inclusions in the GaSb matrix. GaSb-FeGa$_{1,3}$ and GaSb-CoGa$_{1,3}$ composites have p-type conductivity with charge carrier concentration of about 1.2 x 10^{18} cm^{-3} and 1.8 x 10^{18} cm^{-3}, respectively, at the room temperature.

The thermographic analysis was realized on a Derivatograph instrument, where the samples were heated to 1300 K at a rate of 10 K/min. The thermography data for GaSb-FeGa$_{1,3}$ and GaSb-CoGa$_{1,3}$ composites are presented Fig. 1.

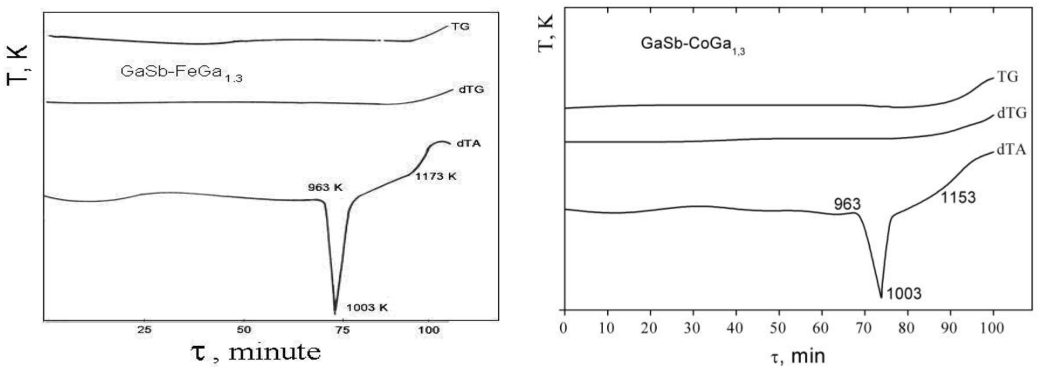

Fig. 1 Thermography of (a) the GaSb-FeGa$_{1.3}$ and (b) GaSb-CoGa$_{1.3}$ eutectic composites.

An Advanse D8 diffractometer for XRD study was used. The diffraction patterns for GaSb-FeGa$_{1.3}$ eutectic composite at temperatures of 210, 350, and 420 K and for GaSb-CoGa$_{1.3}$ eutectic composite at room temperature are shown in Fig. 2.

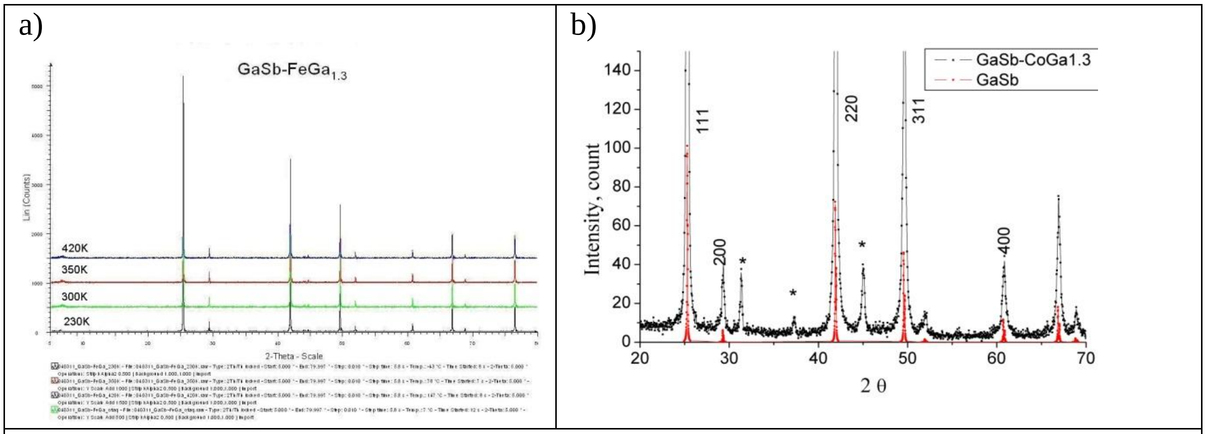

Fig. 2. Diffraction patterns for (a) GaSb-FeGa$_{1.3}$ and (b) GaSb-CoGa$_{1.3}$.

The microstructure and morphology of the GaSb-FeGa$_{1.3}$ and GaSb-CoGa$_{1,3}$ eutectic composites were investigated using a Philips^{TM} scanning electron microscope, model with the prefix of X-ray spectroscope (EDX) model EDAX^{TM}. The accelerating voltage during EDX analysis was 15 kV. The SEM images and EDX spectra for GaSb-FeGa$_{1.3}$ and GaSb-CoGa$_{1.3}$ eutectic composites are given in Fig. 3.

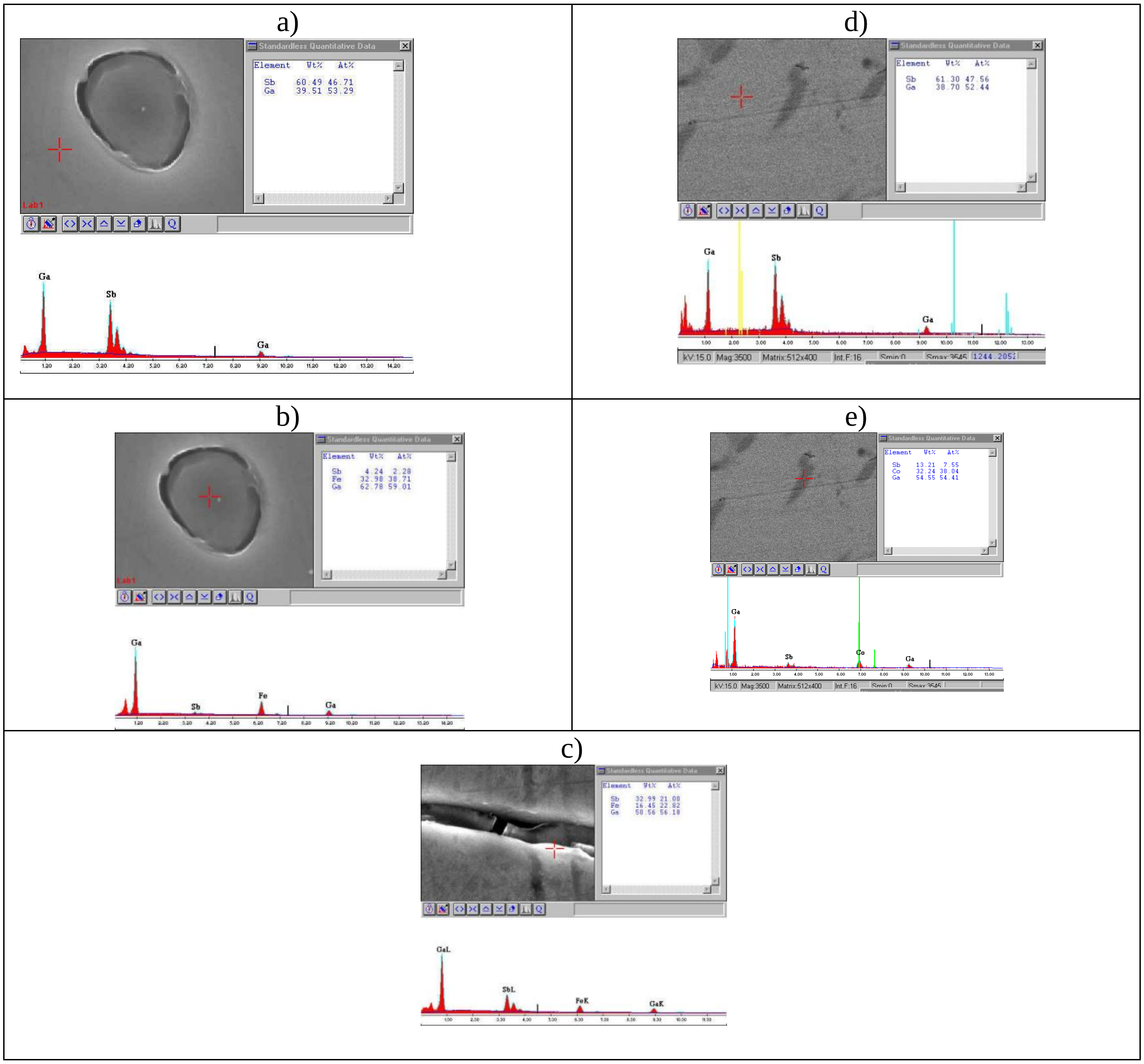

a)

```
Element   Wt%   At%

  Sb    60.49 46.71
  Ga    39.51 53.29
```

d)

```
Element   Wt%   At%

  Sb    61.30 47.56
  Ga    38.70 52.44
```

```
kV:15.0  Mag:3500  Matrix:512x400  Int.F:16  Smin:0  Smax:3545  1244.2052
```

b)

```
Element   Wt%   At%

  Sb     4.24  2.28
  Fe    32.98 38.71
  Ga    62.78 59.01
```

e)

```
Element   Wt%   At%

  Sb    13.21  7.55
  Co    32.24 38.04
  Ga    54.55 54.41
```

```
kV:15.0  Mag:3500  Matrix:512x400  Int.F:16  Smin:0  Smax:3545
```

c)

```
Element   Wt%   At%

  Sb    32.99 21.00
  Fe    16.45 22.82
  Ga    50.56 56.18
```

Fig. 3. SEM micrographs and X-ray spectra of (a, b, c) the GaSb-$FeGa_{1.3}$ and (d, e) GaSb-$CoGa_{1.3}$ composites obtained by SEM-EDX.

The temperature dependence of the electrical conductivity and Hall coefficient measured with the compensation method with 2% and 5% accuracy, respectively, is plotted in Figs. 4 and 5.

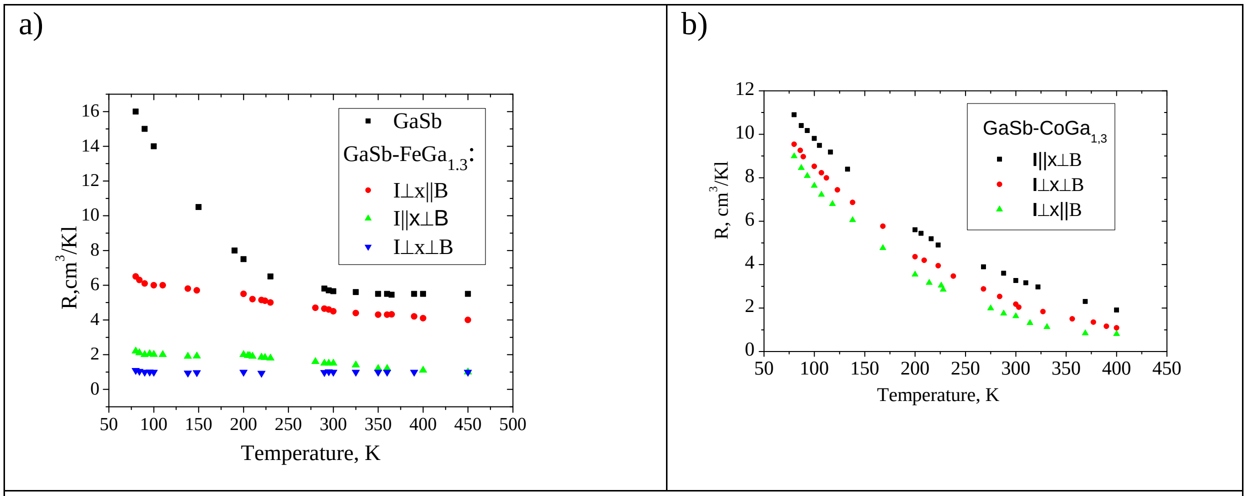

Fig. 4. Temperature dependence of Hall coefficient of (a) GaSb-FeGa$_{1.3}$ and (b) GaSb-CoGa$_{1.3}$.

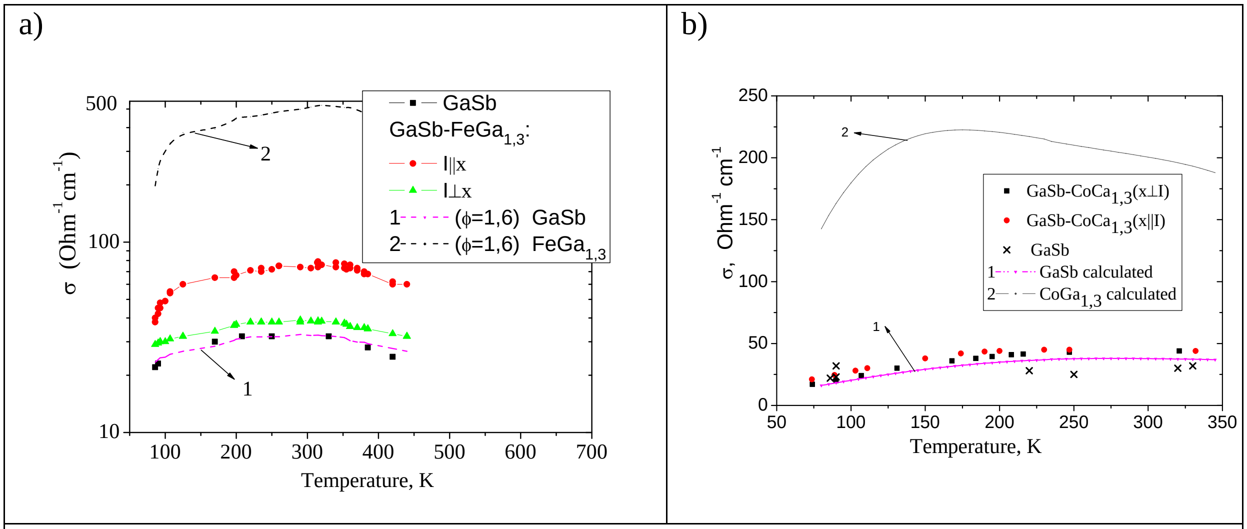

Fig. 5. Temperature dependence of electric conductivity of (a) GaSb-FeGa$_{1.3}$ and (b) GaSb-CoGa$_{1.3}$.

3. Discussion

The initial and final temperatures of melting with respect to heat and entropy for eutectic composites were determined with 2-3% accuracy by thermography. The calculated values are listed in Table 1.

Analyses of the diffraction patterns by the TOPAZ and EVA programs revealed that GaSb-FeGa$_{1,3}$ and GaSb-CoGa$_{1,3}$ composites consist of 97% matrix and 3% metal inclusions. The intensive peaks in the diffraction patterns correspond to the GaSb matrix. The weak peaks in the GaSb-FeGa$_{1.3}$ diffraction patterns mainly correspond to peaks of the Fe$_3$Ga$_4$ compound; however, in the GaSb-CoGa$_{1.3}$ diffraction patterns they do not correspond to the peaks of the CoGa or CoGa$_3$ compounds (in Fig. 1b these peaks are marked with the symbol *). It is evident that no structural change with temperature is observed for GaSb-CoGa$_{1.3}$ eutectic composite.

The SEM image (Fig.3) shows that the needle-shaped metallic phase is oriented in a solidification direction and is uniformly distributed within the matrix for these composites. The diameter, length, and density of the metallic inclusions found from SEM images are listed in Table 1. It should be noted that the metallic phase in the GaSb-FeGa$_{1,3}$ composite is longer, strictly parallel, and surrounded by the cover. However, in the GaSb-CoGa$_{1,3}$ composite, the metallic phase is shorter, less uniformly distributed, and the cover was not observed.

Table 1. Characteristic parameters of the GaSb-FeGa$_{1.3}$ vә GaSb-CoGa$_{1.3}$ eutectic composites

	GaSb-FeGa$_{1,3}$	GaSb-CoGa$_{1,3}$
Charge carrier concentration, (cm^{-3})	p=1,2x10^{18}	p=1.8x10^{18}
Length of metallic inclusion, (μm)	20-150	5-20
Diameter of metallic inclusion, (μm)	1÷2	0.5÷2
Density of metallic inclusion, (mm^{-2})	3 x10^{4}	20 x10^{4}
Initial temperature of melting, (K)	963	963
Final temperature of melting, (K)	1003	1003
Heat of melting, (J/g)	32.4	31.768
Entropy of melting, (J/K.mol)	6174	6019

The temperature dependence of Hall coefficient (R) at different mutual directions of current (I), magnetic field (B) and needle orientation axis (x) are given in Fig. 4. The decrease in the Hall coefficient along the sample in the case of $I \parallel x \perp B$ is due to short-circuit, and the Hall voltage has a minimum value in the case of $I \perp x \perp B$. The charge carrier concentration was calculated from Hall coefficient, and it achieves a maximum in the case of $I \perp x \parallel B$.

The temperature dependence of the electrical conductivity for GaSb-FeGa$_{1.3}$ and GaSb-CoGa$_{1.3}$ measured in a temperature range of 80-450 K at different mutual directions of current (I) and needle orientation axis (x) are given in Fig. 5. It is evident from this figure that the electrical conductivity depending on mutual directions of current and metallic inclusions has the anisotropy in the temperature range. In the case of $I \perp x$, the $\sigma_\perp$ (T) for the eutectic alloys is similar to that of the matrix material with the respective concentration. In the case of $I \parallel x$ the electrical conductivity was far above the conductivity for the case of $I \perp x$.

At present, the calculation of effective conductivity for composite materials Maxwell-Garnett approximation and Bruggeman effective medium theory are frequently used due to their physical obviousness [5-8].

The effective electric conductivity at parallel ($\sigma_\parallel$) and perpendicular directions of current to the metal inclusions ($\sigma_\perp$) is determined by the following formulas [8]:

$$\sigma_\parallel = \sigma_1 \frac{1}{1+c} + \sigma_2 \frac{c}{1+c}, \qquad \sigma_\perp = \frac{(\sigma_1 - \sigma_2)\left(1 - \sqrt{\frac{c}{1+c}}\right) + \sigma_1 \sqrt{\frac{1+c}{c}}}{1 + \frac{\sigma_2}{\sigma_1}\left(\sqrt{\frac{1+c}{c}} - 1\right)}, \tag{1}$$

where σ_1 and σ_2 are the electric conductivity of the matrix and inclusions, respectively, c is the volume fraction of metal inclusions, which is determined as follows:

$$c = \frac{V_i N}{V_m} = \frac{V_i N}{1 - V_i N}, \tag{2}$$

where N is density of the needles and V_m and V_i are the volume of the matrix and the metallic needle, respectively.

It should be noted that the interface interaction is not taken into account in the presented models. We assume that the interface interactions can be accounted by introducing the interphase zone fraction into calculations of effective conductivity. Therefore, the volume V_i in formula (2) is substituted by V_{ef} effective volume equal to

$$V_{ef} = \pi b^2 NL \quad , \tag{3}$$

where L is the length of metallic inclusions. If the ratio of the effective volume and inclusion radii are designated by ϕ, then

$$b = a\phi \ ; \quad V_{ef} = V_i N\phi \quad , \tag{4}$$

where *a* and *b* are the real and effective radii of inclusions, respectively. Then

$$c_{ef} = \frac{V_{ef} N}{V_m} = \frac{V_i N\phi^2}{1 - V_i N\phi^2} \tag{5}$$

The curves calculated by formulas (1)-(5) are plotted in Fig. 5. It is evident from this figure that the interphase zone together with metallic inclusions plays an especially role in short-circuiting leading to the anisotropy of the electrical conductivity.

4. Conclusion

It is established that, in the GaSb-FeGa$_{1.3}$ and GaSb-CoGa$_{1.3}$ eutectic composites, no structural change with temperature is observed.

It is shown that the role of interphase zone is an essential factor in the short-circuiting action by inclusions leading to the anisotropy on the electrical conductivity.

Acknowledgements

This work was supported by the Science Development Foundation under the President of the Republic of Azerbaijan, grant no. EİF-2011-1(3)/82/05/1.

References

[1] M.A. Sopovskaya, and Y.S. Smetannikova, Fiz. Tekh. Poluprovod. 21, 7, 1242 (1987).
[2] M.I. Aliyev, A.A. Khalilova, D.H. Arasly, R.N. Rahimov, M. Tanoglu, and L. Ozyuzer, Appl.Phys.:A 79, 8, 2075 (2004).
[3] R.N.Rahimov, I.Kh.Mamedov, D.H.Arasly, A.A.Khalilova, and R.M.Jabbarov, Prikl. Fiz., 5, 86 (2006).
[4] R.N. Rahimov, A.A. Khalilova, D.H. Arasly, M.I. Aliyev,M. Tanoglu, and L. Ozyuzer, Sensors and Actuators A: Physical, 147, 436 (2008).
[5] J.R. Kalnin and E. Kotomin, J.Phys.A: Math. Gem. 31, 7227 (1998).
[6] D.A.G. Bruggeman, Ann. Phys. (Leipzig) 24, 636 (1935).
[7] Qingzhong Xue, Physica B, 325, 195 (2003).
[8] B.I. Odelevskiy, J. Tech Phys. (in Russian) 21, 667 (1951).

SOME FEATURES OF ABSORPTION AND PHOTOLUMINESCENCE OF WULFENITE ($PbMoO_4$) CRYSTALS

V. Musinschi[1] and C. Musinschi[2]

[1] *State University of Moldova, A. Mateevici str. 60, Chisinau, Republic of Moldova*
[2] *Technical University of Moldova, Stefan cel Mare pr. 168, Chisinau,*
Republic of Moldova
E-mail: v_musinschi@yahoo.com

(Received 11 September 2012)

Abstract

A description of experimental results of studying the optical absorption and photoluminescence (PL) of tetragonal (class 4/m) $PbMoO_4$ crystals is given. The light transmitted and reflected in the polarized radiation for both orientation ($E \parallel C_4$ and $E \perp C_4$,) at 300 and 77 K is measured. The spectral dependence of the absorption coefficient at the edge absorption ($\lambda \approx 0.3-0.5$ μm) shows that the edge absorption is determined by phonon-assisted indirect transitions.

Spectral characteristics of the absorption coefficient of crystals with two radiation polarizations in the temperature range from 77 to 300 K are investigated. The measured spectral dependence of the absorption coefficient at two orientation of polarization of light and the known theoretical dependence were combined and compared for determination the types of optical transitions in fundamental absorption of $PbMoO_4$ crystals. Limited energies E_g^{ind} and E_g^{dir} for $E \parallel C_4$ and $E \perp C_4$ were found. A detailed investigation of the fundamental absorption of $PbMoO_4$ crystals is given. The direct optical edge E_g at T = 300 K is 3.28 eV and 3.36 eV for $E \parallel C_4$ and $E \perp C_4$, respectively. Pure lead molybdate single crystals grown by the Czochralski method were investigated by optical absorption and PL methods. The radiative recombination mainly for interbands transitions in $PbMoO_4$ crystals excited with a 365-nm wavelength was observed and analyzed. All PL spectra undergo a Stokes shift and can be characterized by a large half-width.

The absorption spectra were compared with both PL and calculated emission intensity for a degenerate electron gas of the conduction band and nondegenerate hole gas in the valence band for direct transitions [1] .

1. Introduction

Lead molybdate (PbMoO4 or PM) crystals, class 4/m, are extensively employed in acousto-optic device applications because of a high acousto-optic figure of merit ($M_2 = 37.10^{-8}$ s^3/g), low acoustic and optical loss below 1 GHz, and favorable mechanical impedance for acoustic matching. Recently, this material has been found to be useful as a scintillator for the double β decay experiment below 100 K.

The physical and optical properties of $PbMoO_4$ are shown below: density at 293 K ρ =6.95 g/cm^3, melting temperature of 1330°C, effective birefringence (λ = 1.55 μm) $\Delta n_{eff} = 0.103$, transmittance range of 0.4-5.5 μm , refractive index at 633 nm $n_o = 2.38$, $n_e = 2.25$ [2].

Crystals of lead molybdate with a diameter of up to 16 mm and a length of 60–80 mm are grown by the Czochralsky-Kyropulos method. Lead molybdate AO elements possess low optical losses, high optical homogeneity, and stability to laser radiation. High crystal homogeneity also allows vacuum thermopressure bonding for large aperture devices.

Lead molybdate crystal features low optical losses [3], high optical homogeneity, and stability to laser radiation. The dark conductivity of $PbMoO_4$ crystals depends on change composition and varies from 10^{-7} to 10^{-14} s/cm [4].

The interest in the study of the optical properties of PbMoO4 crystals is determined not only by the fundamental physical mechanism present in this material, but also by a wide range of possible applications in high speed acousto-optic devices : intensity modulators, acousto-optic deflectors and tunable filters, power spectra analyzer, ion conductors, etc.

In this work, we used $PbMoO_4$ crystals that belong to the space-symmetric group 4/m obtained through extraction from melt according to the Czochralski method mainly to the [100] direction having the lattice parameters a = 5.4312 Å and c = 12.1 Å, light yellow color, tetragonal crystal type group, negative uniaxial.

The optical properties were analyzed by ultraviolet-visible (UV-Vis) absorption and photoluminescence (PL) measurement. A description of experimental results of studying the optical absorption and photoluminescence (PL) of tetragonal (class 4/m) $PbMoO_4$ crystals is given. The measurements of light transmitted and reflected in the polarized radiation for both orientation ($E \parallel C_4$ and $E \perp C_4$), where C_4 is the optical axis of crystal corresponding to the crystallographic [001] direction at 300 and 77 K, were performed.

In this paper, we report the results of studying the fundamental absorption and PL on PbMoO4 crystals grown from melts of controlled stoichiometric (1 : 1) molar mixture of the constituent oxides, PbO, and MoO_3 and employing the Czochralski technique) [5]. Pure lead molybdate single crystals were investigated by optical absorption and PL methods.

2. Fundamental optical absorption

Optical measurements have many unique and attractive features for studying and characterizing crystal properties. They are contactless, nondestructive, and compatible with any transparent ambient and are useful for in-situ analysis on processing system.

In this work, we used $PbMoO_4$ crystals (F. 1) that belong to the space-symmetric group 4/m obtained through extraction from melt according to the Czochralsky method mainly to the [100] direction having the lattice parameters a = 5.4312 Å and c = 12.1 Å, light white-yellow color, tetragonal crystal type group, negative uniaxial. In our study, two types of plate were used:
(1) plates in which the developed faces contained the C_4-axis and (2) plates in which the developed faces were perpendicular to the C_4-axis. Transmission T(hv) and reflection R(hv) were recorded in polarized light using a spectrophotometric setup based on an M-40 spectrophotometer and a Glan-Thompson prism in a wavelength range of 200 to 900 nm.

Measurements of optical transmission and reflection were analyzed in the standard way to yield the optical absorption coefficient α as a function of photon energy hv.

Transmission T of a thin slab of known thickness ($d \approx 10 - 40$ μm) and absolute reflectivity R at nearly normal incidence in two radiation polarizations ($E \parallel C_4$ and $E \perp C_4$, where C_4 is the optical axis of crystals) were measured. The optical measurements were carried out in a range of the liquid nitrogen (77 K) to room temperature (300 K).

Figure 1b shows a probe for optical absorption studies.

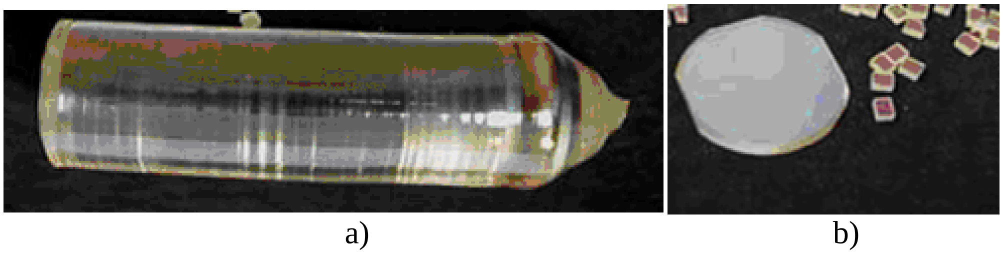
a) b)

Fig. 1. Photograph[5] of (a) a typical $PbMoO_4$ crystal grown by the Czochralski method and (b) the probe used for optical absorption and PL studies.

Absorption coefficient α was calculated by the following relationship [5]

$$\alpha(\nu) = \frac{(1-R)^2 e^{-\alpha d}}{1-R^2 e^{-2\alpha d}} \tag{1}$$

where ν is the light frequency and d is the thickness of the plates.

In the high-absorption range, the optical gap was evaluated from Tauc's equation

$$\alpha h\nu = B\,(h\nu - E_g)^{1/2} \tag{2}$$

where E_g is the energy distance between the valence and conduction band mobility edges.

In this spectral region, the extremely sharp absorption edge is best fit by (2) near the edge. The parameter B given by the slope of the plots is an interesting parameter, since it can be taken as a measure of the disorder.

Figure 2 shows plots of $(\alpha h\nu)^{1/2}$(curve 2) versus photon energy hν for $PbMoO_4$ crystals at 300 K for $E \parallel C_4$. The characteristic optical parameters $E_g^{dir.}$(eV) present the edge of direct optical transitions of electrons from the valence to conduction band in crystals.

Fundamental optical absorption characterized by an exponential spectral dependence was observed in a variety of crystals.

The direct optical edges $E_g^{dir.}$ at T = 300 K are 3.28 and 3.36 eV for $E \parallel C_4$ and $E \perp C_4$, respectively. Possibilities of interpretation of the particularity of absorption spectra on the basis of the proposed band structure were examined in [6].

The calculation of the electronic structure of $PbMoO_4$ showed [1] that the valence and conduction bands are mainly composed of the O 2p and Mo 4d states, respectively, and the Pb state appreciably contributes to the valence band top and the conduction band bottom. In this work, the importance of the exciton transition was explained in terms of the cationic Pb 6s ⟶ 6p excitation model taking into account the crystal-field splitting and the spin-orbit interaction of Pb 6p state in $PbMoO_4$ crystals . The authors of this work found that the doublet exciton band absorption at 3.6 eV shows a doublet structure with distinct dichroism.

Figure 2 (curve *1*) shows that, at hν <3.2 eV for $E \parallel C_4$, absorption coefficient α increases with photon energy loss hν indicated by expression (2).

This behavior of absorption in $PbMoO_4$ crystal (curve*1*) indicated that absorption in this energy range is determined by optical transitions, where the maximum valence-band energy and the minimum conduction-band energy do not occur at the same k –vector (an indirect transition appears, see [6] for details).

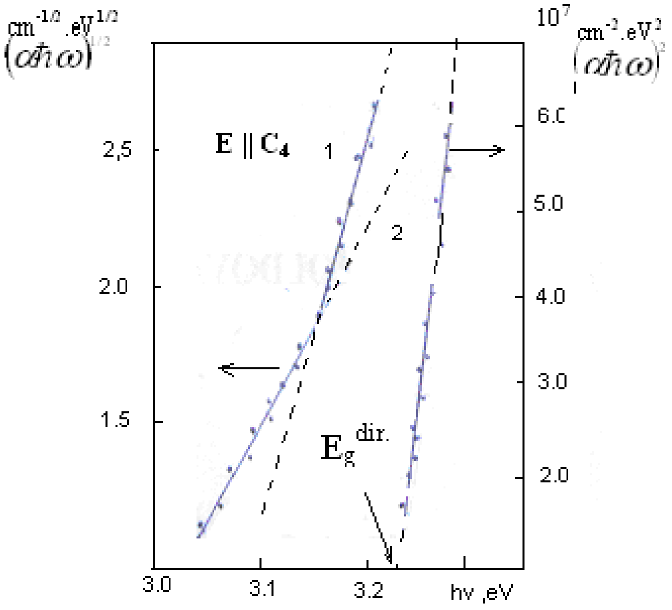

Fig. 2. Theoretical fit to the experimental absorption edge of $PbMoO_4$ at 300 K for **E || C$_4$**.

In this case, the indirect-gap absorption coefficient that corresponds to the allowed indirect transition is defined by

$$\alpha h\nu = C^{(ab)}\frac{\left(h\nu - E_g^{ind} + h\nu_{ph}\right)^2}{\exp\left(\frac{h\nu_{ph}}{kT}\right)-1} + C^{(em)}\frac{\left(h\nu - E_g^{ind} - h\nu_{ph}\right)^2}{1-\exp\left(-\frac{h\nu_{ph}}{kT}\right)} \quad (3)$$

where $h\nu_{ph}$ is the energy of the phonon-assisted transition, the superscripts (ab) and (em) refer to phonon absorption and emission, respectively.

This expression is nonzero if the quantities in parentheses are positive, i.e.,

$$h\nu \pm h\nu_{ph} > E_g^{ind} \quad (4)$$

where E_g^{ind} is the indirect edge-energy interval between the valence band and the absolute minimum of the conduction band of the crystal (see the bend structure from [6]).

By extrapolating the linear region of curve *1* ($(\alpha h\nu)^{1/2} \sim h\nu$) to value by $\alpha = 0$ in two types of polarization of radiation, the minimum energy gap E_g^{ind} was determined.

The indirect gaps E_g^{ind} are 3.08 eV and 3.16 eV for E || C_4 and E ⊥ C_4, respectively. The interband (direct and indirect) transitions are temperature functions and decrease with its increase. The minima of interband transition were determined and the temperature dependence of the absorption edge shift was studied. The temperature coefficient of shift of E_g^{ind} is $1.8.10^{-4}$ eV/deg. Possibilities of the interpretation of the particularity of absorption spectra on the basis of the proposed band structure were examined.

3. Photoluminescence

The luminescence study was used to obtain additional information of interband optical transitions in the $PbMoO_4$ crystal**.** To study luminescence, it is necessary to optically pump into the absorption spectrum using high-intensity sources .

Typical sources used in luminescence spectroscopy, which have broad bands in near ultraviolet and blue regions , include usually hydrogen, xenon, or mercury (Hg) arc lamps .

High-pressure mercury (Hg) arc lamps have higher intensities than Xe arc lamps and its intensity is concentrated in sharp lines. Consequently, these lamps are mainly utilized with broadband absorbers that are crystals.

In this work, the radiative recombination was mainly studied for interband transitions in $PbMoO_4$ crystals.

PL measurements of wulfenite ($PbMoO_4$) were performed at room temperature for crystals with different size. PL was excited by 365-nm (E_{ex} =3.39 eV, Hg triplet 6^3P_2-6^3D_3) photons of an focused super-high-pressure Hg lamp beam and detected by a FEU-38 photomultiplier with associated high-voltage power supplies through a grating monochromator using the look-in technique. Luminescence spectra were recorded at a constant excitation wavelength, which resulted in the most intense emission, followed by scanning the wavelength of the monochromator emission.

These ideal light sources, monochromators, and phototubes are not available, and it is necessary to make a settlement with the selection of components and to correct the nonideal response of the luminescence spectrometer.

Generally, luminescence spectra are recorded by selecting the excitation wavelength, which results in the most intense emission, followed by scanning the wavelength of the emission monochromator. In consequence, techniques must be developed to allow for the wavelength-dependent efficiency of the emission monochromator and photomultiplier tube. In general terms, the light signal is detected using a photomultiplier tube in which the photon flux produces an electrical current proportional to the light intensity. The device is based on the photoelectric effect.

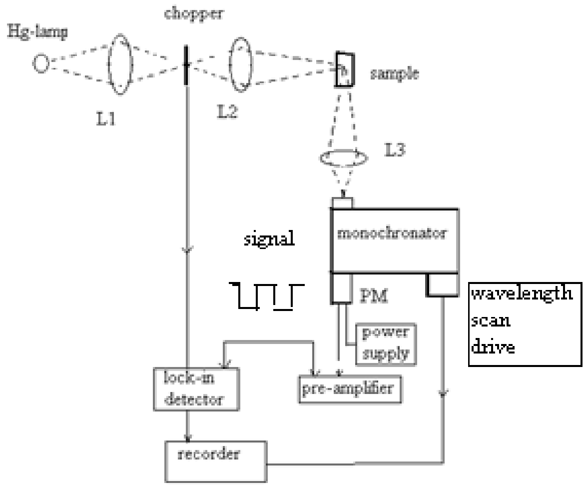

Fig. 3. Schematic of a spectrometer for measuring luminescence spectra.

The phenomena usually studied to obtain information on the optical properties of crystals are absorption and PL in a large wavelength range.

The radiative recombination mainly for interband transitions in $PbMoO_4$ crystals was observed and analyzed at excitation by a 365-nm wavelength.

PL measurements of wulfenite ($PbMoO_4$) were performed at room temperature for crystals with different size. An intense blue-green PL band emission was observed.

Figure 4 shows the relative positions of the absorption spectra at two polarizations (for E $\parallel$ C_4 and E $\perp$ C_4, respectively) and the PL band at 300 K. An intense blue-green PL broadened band emission was observed.

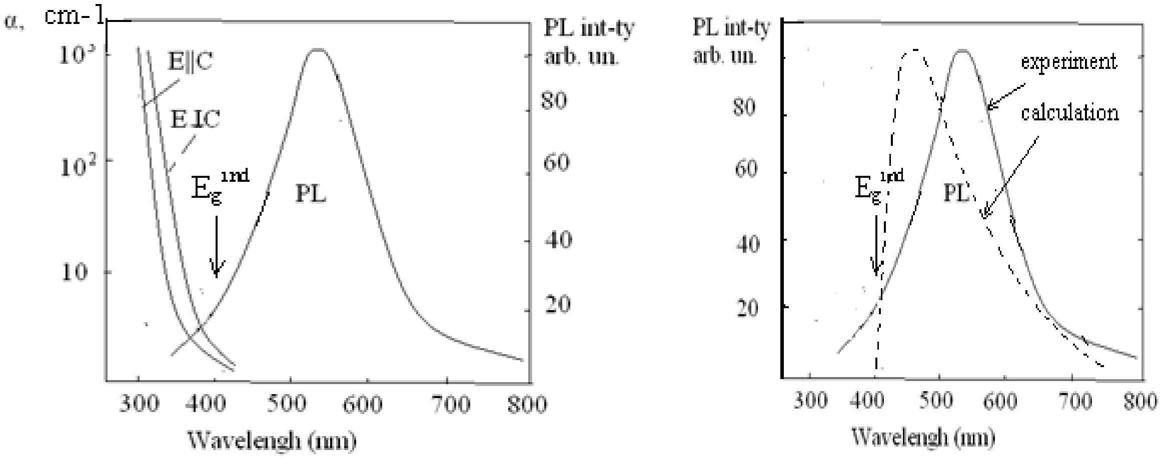

a) b)

Fig. 4. (a) Relative positions of the absorption spectra at two polarizations and PL band of $PbMoO_4$ at 300 K excited by 365 nm (E_{ex} =3.39 eV) and (b) emission (solid curve) and calculated (dashed curve) spectra for a direct transition.

PL relative intensity versus wavelength shows that the illumination of crystal samples results in not only a change in the concentration of nonequilibrium free carriers by their interband transitions but also capturing in localized states.

It is evident from Fig. 4a that there are red shifts of the PL peak relatively optical band gaps. All the observed spectra in these crystals undergo a Stokes shift and can be characterized by a large band half-width and solely by Eg gap.

If spontaneous emission intensity of PL appears from recombination of nondegenerate electrons of the conduction band and nondegenerate holes of the valence band, a spectral dependence may be presented, as shown in [7], by

$$I(\nu) \sim \nu^2(h\nu - E_g)^{1/2}\exp[-a\frac{h\nu - Eg}{kT}] \times \{1+[b\frac{h\nu - Eg}{kT} - c] \qquad (5)$$

where $a = m_c/m_c-|m_v|$, $b = |m_c|/m_c+|m_v|$, and $c = 30$ meV.

Figure 4b depicts the results of calculated PL emission intensity of PbMoO4 according to (5).

4. Conclusions

The results of experimental studies of the spectral characteristics of the absorption coefficient of tetragonal (class 4/m) $PbMoO_4$ crystals are given. The light transmitted and reflected in the polarized radiation for both orientations in a temperature range of 77 to 300 K was measured. A detailed investigation of the fundamental absorption of PbMoO4 crystals is presented.

Direct and indirect optical transitions in $PbMoO_4$ crystals were observed.

1. The spectral dependence of the absorption coefficient at the edge absorption $\lambda \approx 0.3–0.5$ μm) showed that the edge absorption is determined by phonon-assisted

indirect transitions. Values of E_g^{dir} and E_g^{indir} and their temperature dependences for both ($E \parallel C_4$ and $E \perp C_4$) at 300 to 77 K were studied.

2. Limited energies E_g^{ind} and E_g^{dir} for $E \parallel C_4$ and $E \perp C_4$ were found.
3. Joint optical properties were analyzed by ultraviolet-visible (UV-Vis) absorption and PL measurements. A description of experimental results of studying the optical absorption and PL of $PbMoO_4$ crystals is given. The PL measurements of wulfenite ($PbMoO_4$) excited by 365 nm (E_{ex} =3.39 eV, Hg triplet 6^3P_2-6^3D_3) were performed at room temperature.
4. All PL spectra undergo a Stokes shift and can be characterized by a large band half-width and solely by Eg gap.

References

[1] Masami Fujita, Minoru Itoh, Hiroyuki Mitami, Sangeeta, and Mohist Tyagi, Phys.Stat. Sol.(RRL)-Rapid Research Letters 247, 2, 405 (2010).

[2] Hand book of Optics by the Optical Society of America; Michael Bass editor in chief, 2nd edition, vol. II, (1995), part 4, Optical and Physical Properties of Materials.

[3] V. Musinschi, M.Caraman, C.Musinschi, and N.Syrbu,, Mold. J. Phys. Sci. 2, 2, 185 (2009).

[4] N.R. Agamalyan , E. S., Vartanyan, L. M .Kazaryan, and R-K. Ovsepyan, Inorg. Mater. 34, 11, 1164 (2000).

[5] D.Piwowarska, S.M.Kaczmarek, and M.Berci, Non-Cryst. Solids, DOI:10.1016,2008.

[6] V.Musinschi, M Caraman, and C. Musinschi, Mold. J. Phys. Sci. 10, 1, 65 (2011).

[7] P.T.Landsberg , Recombination in semiconductors,Cambridge Univ.Press, 1991.

THE POLYTYPISM OF Cu(D-Ser)(L-Ser) CRYSTALS

I. Diacon[1], S. Donu[2], and L. Chapurina[3]

[1]Institute of Applied Physics, Academy of Sciences of Moldova,
[2]Institute of Electronic Engineering and Nanotechnologies "D.Ghitu",
Academy of Sciences of Moldova,
[3]Institute of Chemistry, Academy of Sciences of Moldova

(Received 13 July 2012)

Abstract

Based on the theory of polytypism, 16 polytypic modifications of crystals of the Cu(D-Ser)(L-Ser) active coordination compound were deduced and described. They belong to the monoclinic and orthorhombic syngony, and their structures are pairwise identical.

1. Introduction

Earlier [1], using the electron diffraction method, we have determined the atomic structure of crystals of the biologically active coordination compound of copper(II) with racemic serine Cu(DL-Ser), the crystallographic characteristics of the compound are as follows: a= 9.56 (1) Å, b=4.97 (1) Å, c=20.15 (3) Å, Z=4, the space group of symmetry – $Pna2_1$. The structure of this compound is composed of individual centrosymmetrical Cu(D-Ser)(L-Ser) complexes, the centers of symmetry of which are occupied by copper ions. These centers are local elements of symmetry. In the structure, the complexes are connected to each other in identical layers by hydrogen bonds N1– H··· O9, N1– H··· O10, N2– H··· O11, N2– H··· O12 and by the interaction forces Cu --- O7, Cu--- O8 of copper ions with oxygen atoms of the carboxyl groups of serine residues of the adjacent complexes (Fig. 1).

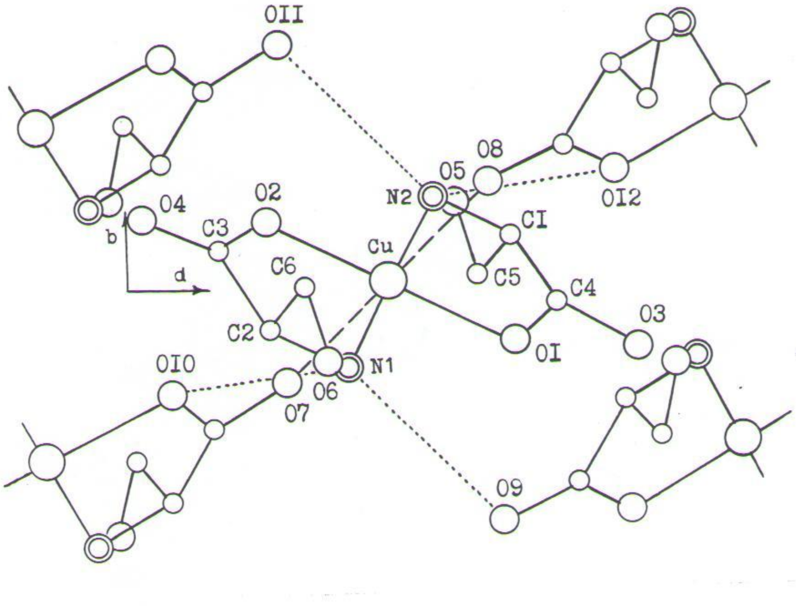

Fig. 1. Composition of a separate layer of the structure of Cu(D-Ser)(L-Ser).

Layers in the structure are situated parallel to the coordinate *ab* plane in a such a way that adjacent layers are symmetrically bound by a twofold screw axis parallel to the *c* axis. Within the layer, the complexes are crystallographically bound to each other by glide reflection plane *a*. The O6H, O7H, O8H, O9H, O10H, O11H… hydroxyl groups of serine residues of the complexes are concentrated in the interlayer space (Fig. 2) and form hydrogen bonds between them; moreover, each hydroxyl group of one layer interacts with two hydroxyl groups of the adjacent layer, thus forming an infinite chain of cooperative hydrogen bonds.

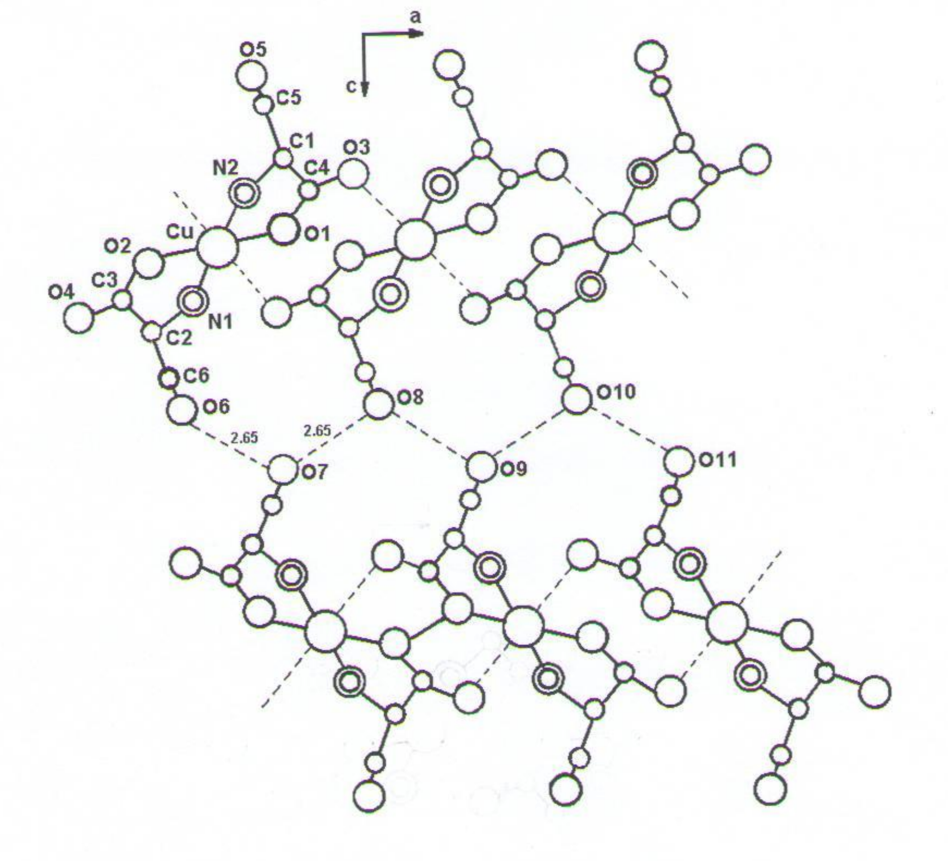

Fig. 2. Structure of the Cu(D-Ser)(L-Ser) crystals.

2. Polytypism of crystalline substance

Polytypism is a crystal-chemical phenomenon which is defined as the ability of a substance to crystallize in different modifications, the structure of which is composed of the same one-dimensional or two-dimensional periodic structure units (layers, chains, tapes, rods) of one or more varieties [2]. Each modification of the structural units has different rules of mutual arrangement. Thus, the possibility of a polytypism of a crystalline substance is established by identifying one-dimensional or two-dimensional structural units in its structure that can adjoin each other in different versions so that one version of the mutual arrangement of the structural units does not exclude the other.

3. Deduction and description of polytypic modifications of Cu(D-Ser)(L-Ser) crystals

As noted above, the crystal structure of Cu(D-Ser)(L-Ser) has a layered pattern and in this regard is more convenient to describe it using structural units in the form of layers of the same kind. For deduction of the polytypic modifications of the crystal structure of the Cu(D-Ser)(L-Ser) compound using the layers, it necessary to specify the rules of structure formation from the examined layers and find those versions of their mutual arrangement under which these rules are satisfied.

In the structure of Cu(D-Ser)(L-Ser) crystals, the individual rods of the oxygen atoms of the hydroxyl groups of serine O6 – O8 – O10 · · · , O7 – O9 – O11 · · · (Fig. 2) are formed on the surfaces of the layers directed along the *a* axis. The rods alternate in the [010] direction with a period equal to *b*. However, the alternating layers of rods on both sides of the layer are displaced relative to each other on *b/*2 along the *b* axis. The layers forming a three-dimensional structure contact through their rods. This is schematically illustrated in Fig. 3 in the normal projection onto the *bc* plane of the Cu(D-Ser)(L-Ser) structure, where the strokes denote the layers and the circles stand for the cross-sections of the rods. The mutual arrangement of the rods in the interlayer space characterizes the form of layer sequence in the structure of Cu(D-Ser)(L-Ser).

The layers in the structure could adjoin each other in several ways, rather than in a unique manner, without violating the condition of neighborhood of the rods of the adjacent layers, as can be seen from the layer arrangement illustrated in Fig. 3. If the origin is placed in the position of the copper atom of the layer and taking into account the symmetry of the arrangement of the rods on the layer surface, it is clear that the adjacent layers run into one another by the following symmetric procedures (Fig. 3):

1. Translation [0 ½ ½],
2. Translation [0 ½ ½] and rotation by 180º around the *a* axis,
3. Translation [0 0 ½] and rotation by 180º around the *b* axis,
4. Translation [0 0 ½] and rotation by 180º around the *c* axis,
5. Translation [0 ½ ½] and reflection in a plane perpendicular to the *a* axis,
6. Translation [0 0 ½] and reflection in a plane perpendicular to the *b* axis,
7. Translation [0 0 ½] and reflection in a plane perpendicular to the *c* axis,
8. Translation [0 ½ ½] and inversion at the point (the origin).

However, these procedures not take into account the conditions of neighborhood of oxygen atoms of the carboxyl groups of the rods that come into contact in the interlayer space. The oxygen atoms of the hydroxyl groups are distributed along the rods periodically with a period *a/*2, and the adjacent rods are displaced relative to each other by *a/*4 (Fig. 2). The last fact represents the rules of combining for adjacent rods. Thus, in using operations 1–8, the displacement of the layers *t* in their sequence along the *a* axis should be taken into account. In using operations 1–8, the displacement *t* along the *a* axis of the next layer relative to the previous: *t*=0, *t*=*a*/2 in the case of operations 1, 3, 6, and 8 and the displacements *t*=*a*/4, *t*= 3/4*a* in the case of operations 2, 4, 5, and 7 are possible (Figs. 2, 3).

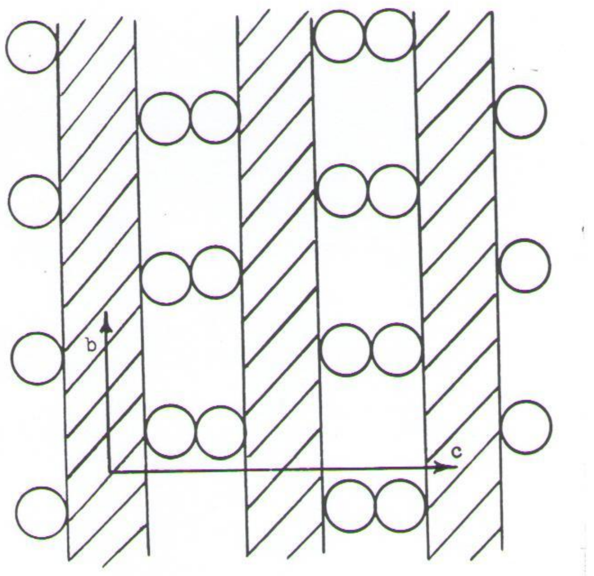

Fig. 3. Scheme of the mutual arrangement of layers in the structure of Cu(D-Ser)(L-Ser).

4. Conclusion

Based on the above, 16 polytypic modifications are possible for the determined structure of Cu(D-Ser)(L-Ser) crystals with layers of a fixed structure. Using the rules of combination of layers and rods, the crystal structures of these modifications were theoretically deduced and described. It was found that the crystals of the 16 possible polytypes belong to monoclinic and orthorhombic syngony and their structures are pairwise identical.

References

[1] D'yakon I.A., Donu S.V., Chapurina L.F., and Kairyak L.N., Kristallografiya, 37, 6, 1391 (1992).
[2] Zvyagin B.B., Vrublevskaya Z.V., Zhukhlistov A.P., et al., Vysokovoltnaya electronografiya v issledovanii sloistykh mineralov, M., Nauka, 224, (1979).

LANDAU QUANTIZATION OF TWO-DIMENSIONAL HEAVY HOLES, ENERGY SPECTRUM OF MAGNETOEXCITONS, AND OPTICAL QUANTUM TRANSITIONS

I. V. Podlesny[1], S. A. Moskalenko[1], A. A. Kiselyov[2], and L. Gherciu[1]

[1]*Institute of Applied Physics, Academy of Sciences of Moldova, Academiei str. 5, Chisinau, MD–2028 Republic of Moldova*

[2]*State University of Civil Aviation, Pilotov str. 38, St. Petersburg, 196210 Russia*

(Received 7 June 2012)

Abstract

The Landau quantization of the two-dimensional (2D) heavy holes, its influence on the energy spectrum of 2D magnetoexcitons, and their optical orientation are studied. The Hamiltonian of the heavy holes is written in a two-band model taking into account the Rashba spin-orbit coupling (RSOC) with two spin projections, but with nonparabolic dispersion law and third order chirality terms. The most Landau levels, except three with $m = 0, 1, 2,$ are characterized by two quantum numbers $m - 3$ and m for $m \geq 3$ for two spin projections, respectively. The difference between them is determined by the third order chirality. Four lowest Landau levels (LLLs) for heavy holes were combined with two LLLs for conduction electron, which were taken the same as they were deduced by Rashba in his theory of spin-orbit coupling (SOC) based on the initial parabolic dispersion law and first order chirality terms. As a result of these combinations, eight 2D magnetoexciton states were formed. Their energy spectrum and the selection rules for the quantum transitions from the ground state of the crystal to exciton states were determined. On this base, optical orientation effects, such as spin polarization and magnetoexciton alignment, are discussed.

1. Introduction

The quantum states of a free spinless electron with a parabolic dispersion law under the influence of a magnetic field were investigated by Landau [1]. This procedure is known as Landau quantization.

The Landau quantization of an electron with the spin taking into account the spin-orbit coupling (SOC) was firstly studied by Rashba [2] in terms of a two-band model. Its Hamiltonian has diagonal elements expressed through the initial parabolic dispersion law $\hbar^2 k^2 \big/ 2m$ and the nondiagonal elements containing the first order chirality terms $k_{\pm} = k_x \pm i k_y,$ where $\vec{k}$ is the wave vector of the conduction electron in a bulk crystal. The SOC and chirality terms in [2] are induced by the external electric field E_z applied parallel to the magnetic field. The electron wave functions were written in a spinor form with two components corresponding to spin orientation along the z axis. The energy levels except one with $n = 0$ are characterized by two quantum numbers n and n' different for two spin projections. They differ by 1 in the case of first order chirality terms. The method proposed by Rashba [2] was applied in [3, 4] to describe the Landau quantization of two-dimensional (2D) heavy holes with nonparabolic initial dispersion law, two spin projections and third order chirality terms proportional to $(k_{\pm})^3$, as well as to the electron in the biased bilayer graphene with nonparabolic initial dispersion law, two pseudospin components and second order chirality terms proportional to $(k_{\pm})^2$. In both cases, the two-band models were applied and the differences between the numbers m and m' were equal to 3 and 2, respectively.

The aim of our paper is to obtain new information, in comparison with [3], concerning the 2D heavy holes and their Landau quantization levels in dependence on the magnetic field strength at different parameters of the initial nonparabolic dispersion law. These details influence the electron structure of the 2D magnetoexcitons and determine the selection rules of the quantum transitions from the ground state of the crystal to exciton states.

2. Landau quantization energy levels of 2D heavy holes

The full Landau-Rashba Hamiltonian for 2D heavy holes was discussed in [3] following formulas (13)-(20). It can be expressed through the Bose-type creation and annihilation operators $a^{\dagger}$, a acting on the Fock quantum states $\left|n\right\rangle = (a^{\dagger})^n \big/ \sqrt{n!}\left|0\right\rangle$, where $\left|0\right\rangle$ is the vacuum state of a harmonic oscillator. The Hamiltonian has the form

$$\hat{H}_h = \hbar\omega_{ch}\left(\left[\left(a^{\dagger}a+\frac{1}{2}\right)+\delta\left(a^{\dagger}a+\frac{1}{2}\right)^2\right]\hat{I}+i\beta 2\sqrt{2}\begin{vmatrix} 0 & (a^{\dagger})^3 \\ -a^3 & 0\end{vmatrix}\right);\ \hat{I}=\begin{vmatrix}1 & 0\\ 0 & 1\end{vmatrix} \quad (1)$$

with the denotations

$$\omega_{ch}=\frac{|e|H}{m_h c};\ \delta=\frac{\left|\delta_h E_z\right|\hbar^4}{l^4\hbar\omega_{ch}};\ \beta=\frac{\beta_h E_z}{l^3\hbar\omega_{ch}};\ l=\sqrt{\frac{\hbar c}{|e|H}}. \quad (2)$$

The parameter δ_h is not well known, what permits to consider different variants mentioned below.

The exact solution of the Pauli-type Hamiltonian is described by formulas (21)-(31) of [3] and has the spinor form:

$$\hat{H}_h\begin{vmatrix} f_1 \\ f_2\end{vmatrix}=E_h\begin{vmatrix} f_1\\ f_2\end{vmatrix};\ f_1=\sum_{n=0}^{\infty}c_n\left|n\right\rangle;\ f_2=\sum_{n=0}^{\infty}d_n\left|n\right\rangle;\sum_{n=0}^{\infty}|c_n|^2+\sum_{n=0}^{\infty}|d_n|^2=1. \quad (3)$$

First three solutions depend only on one quantum number m with the values $0, 1, 2$ as follows

$$\begin{aligned}
E_h(m=0) &= \hbar\omega_{ch}\left(\frac{1}{2}+\delta\right);\ \Psi(m=0)=\left|\begin{matrix}\left|0\right\rangle\\ 0\end{matrix}\right|,\\
E_h(m=1) &= \hbar\omega_{ch}\left(\frac{3}{2}+9\delta\right);\ \Psi(m=1)=\left|\begin{matrix}\left|1\right\rangle\\ 0\end{matrix}\right|,\\
E_h(m=2) &= \hbar\omega_{ch}\left(\frac{5}{2}+25\delta\right);\ \Psi(m=2)=\left|\begin{matrix}\left|2\right\rangle\\ 0\end{matrix}\right|.
\end{aligned} \tag{4}$$

All another solutions with $m \geq 3$ depend on two quantum numbers $(m-5/2)$ and $(m+1/2)$ and have the general expression

$$\begin{aligned}
\varepsilon_h^{\pm}(m-\frac{5}{2};m+\frac{1}{2}) &= \frac{E_h^{\pm}(m-5/2;m+1/2)}{\hbar\omega_{ch}} = (m-1)+\frac{\delta}{2}\left[(2m+1)^2+(2m-5)^2\right]\\
&\pm\left(\left(\frac{3}{2}+\frac{\delta}{2}\left[(2m+1)^2-(2m-5)^2\right]\right)^2+8\beta^2 m(m-1)(m-2)\right)^{1/2},\ m\geq 3.
\end{aligned} \tag{5}$$

The corresponding wave functions for $m=3$ and $m=4$ are

$$\Psi_h^{\pm}(m=3)=\left|\begin{matrix}c_3\left|3\right\rangle\\ d_0\left|0\right\rangle\end{matrix}\right| \text{ and } \Psi_h^{\pm}(m=4)=\left|\begin{matrix}c_4\left|4\right\rangle\\ d_1\left|1\right\rangle\end{matrix}\right|. \tag{6}$$

They depend on the coefficients c_m and d_{m-3}, which obey to the equations

$$\begin{aligned}
c_m\left(m+\frac{1}{2}+\delta(2m+1)^2-\varepsilon_h\right) &= -i\beta 2\sqrt{2}\sqrt{m(m-1)(m-2)}\,d_{m-3};\\
d_{m-3}\left(m-\frac{5}{2}+\delta(2m-5)^2-\varepsilon_h\right) &= i\beta 2\sqrt{2}\sqrt{m(m-1)(m-2)}\,c_m;\\
|\,c_m\,|^2+|\,d_{m-3}\,|^2 &= 1.
\end{aligned} \tag{7}$$

There are two different solutions $\varepsilon_h^{\pm}(m)$ at a given value of $m \geq 3$ and two different pairs of the coefficients $(c_m^{\pm}, d_{m-3}^{\pm})$.

The dependences of the parameters ω_{ch}, β and δ on the electric and magnetic fields strengths may be represented for the GaAs-type quantum wells as follows $H = y\ \mathrm{T}$; $E_z = x\ \mathrm{kV/cm}$; $m_h = 0.25m_0$; $\hbar\omega_{ch} = 0.4y\ \mathrm{meV}$; $\beta = 1.062\cdot 10^{-2}x\sqrt{y}$; $\delta = 10^{-4}Cxy$ with unknown parameter C, which will be varied in more large interval of values. We cannot neglect the parameter C putting it equal to zero, because in this case, as was argued in [3] formula (10), the lower spinor branch of the heavy hole dispersion law

$$E_h^{-}(k_{\|}) = \frac{\hbar^2\vec{k}_{\|}^2}{2m_h} - \left|\frac{\beta_h E_z}{2}\right|\left|\vec{k}_{\|}\right|^3$$

has an unlimited decreasing, deeply penetrating inside the semiconductor energy gap at great values of $\left|\vec{k}_{||}\right|$. To avoid this unphysical situation the positive quartic term $\left|\delta_h E_z\right| \vec{k}_{||}^4$ was added in the starting Hamiltonian. The new dependences will be compared with the drawings calculated in Fig. 2 of [3] in the case $E_z = 10\ \mathrm{kV/cm}$ and $C = 10$. Four lowest Landau levels (LLLs) for heavy holes are selected as in [3]. In addition to them we will study else three levels as follows

$$\begin{gathered}
E_h(R_1) = E_h^-\left(\frac{1}{2},\frac{7}{2}\right);\ E_h(R_2) = E_h(m=0);\\
E_h(R_3) = E_h^-\left(\frac{3}{2},\frac{9}{2}\right);\ E_h(R_4) = E_h(m=1);\\
E_h(R_5) = E_h^-\left(\frac{5}{2},\frac{11}{2}\right);\ E_h(R_6) = E_h(m=2);\\
E_h(R_7) = E_h^-\left(\frac{7}{2},\frac{13}{2}\right).
\end{gathered} \tag{8}$$

Their dependences on the magnetic field strength are represented in Figs. 1 and 2 at different parameters x and C.

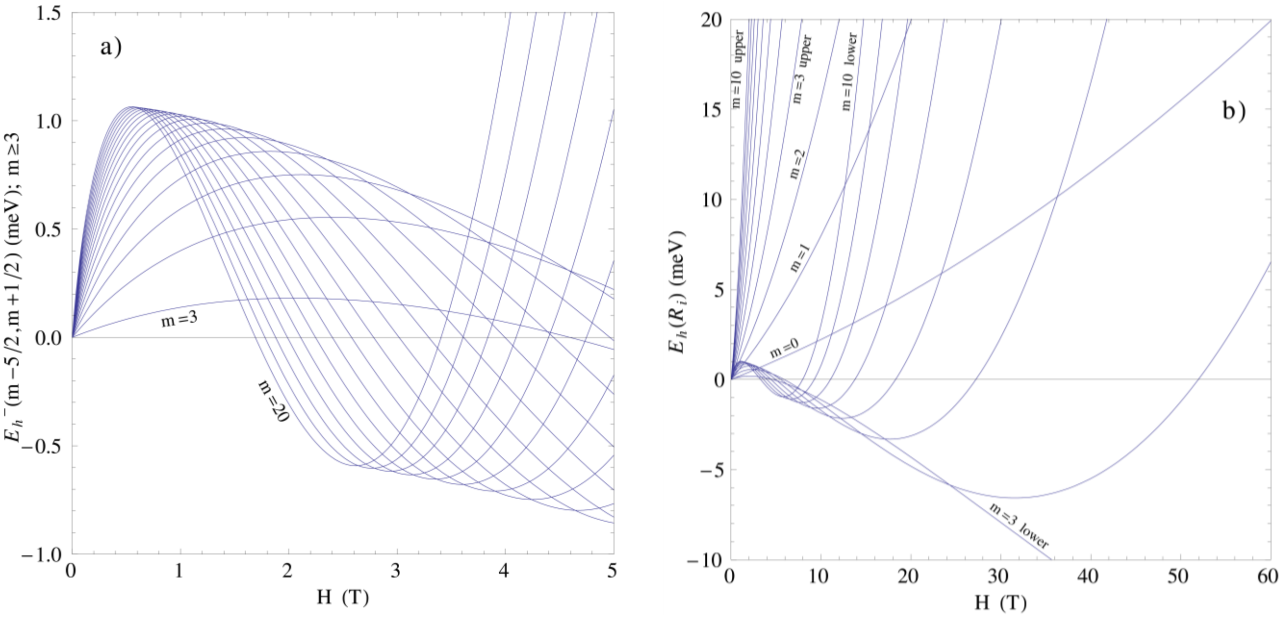

Fig. 1. a) Lower branches of the heavy hole Landau quantization levels E_h^- $\mathrm{m}-5/2;\ \mathrm{m}+1/2$ for $m \geq 3$ at the parameters $E_z = 10\ \mathrm{kV/cm}$ and $\mathrm{C} = 5.5$; b) General view of the all heavy hole Landau quantization levels with $m = 0, 1, \ldots, 10$ at the same parameters E_z and C.

The general view of the lower branches $E_h^-(m - 5/2, m + 1/2)$ of the heavy hole Landau quantization levels with $m \geq 3$ as a functions of the magnetic field strength are represented in Fig. 1a following formula (5). The upper branches have more simple monotonous behavior and are drawn in Fig. 1b together with some curves of the lower branches. All the lower branches in their initial parts have a linear increasing behavior up till they achieve the maximal values succeeded by the minimal values in the middle parts of their evolutions being transformed in the final quadratic increasing dependences. The values of the magnetic field strength corresponding to the minima and to the maxima decrease with the increasing of the number m. These peculiarities can be compared with the case of Landau quantization of the 2D electron in the biased bilayer graphene described in [4]. The last case is characterized by the initial dispersion law without parabolic part and by second order chirality terms. They both lead to dependences on the magnetic field strength for the lower dispersion branches with sharp initial decreasing parts and minimal values succeeded by the quadratic increasing behavior. The differences between the initial dispersion laws and chirality terms in two cases of bilayer graphene and heavy holes lead to different intersections and degeneracies of the Landau levels. Figure 2 shows that the change of the parameter C at a given parameter E_z (or vice versa) shifts significantly on the energy scale the lower branches of the heavy hole Landau levels. It can be observed in all four sections of Fig. 2. But there is a special case in the section 2b, where the degeneracy of the levels R_1, R_3, R_5, and R_7 take places in the range of magnetic field strength $(5-10)\ \mathrm{T}$. More so, the degeneracy of the levels R_1 and R_3 persists to exist even in a larger interval as $(5-20)\ \mathrm{T}$.

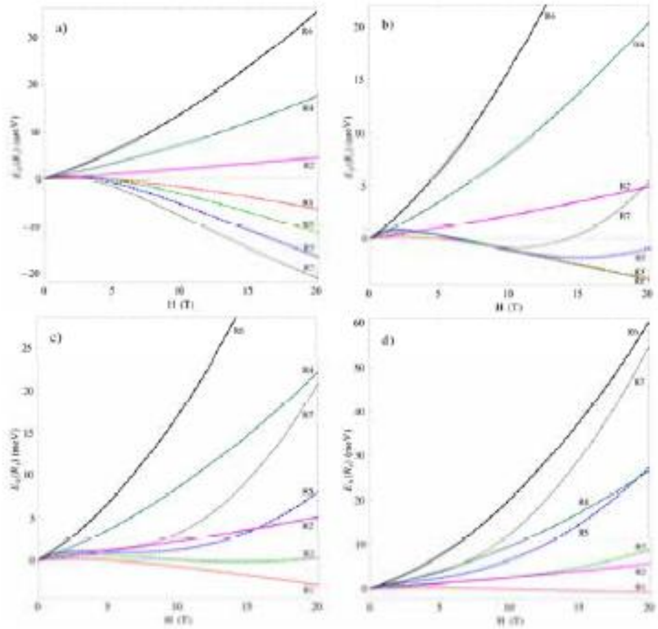

Fig. 2. Seven branches of the heavy hole Landau quantization levels with $m = 0, 1, \ldots, 6$ at the parameter $E_z = 10\ \mathrm{kV/cm}$ and different values of the parameter C: 3.8 (a), 5.8 (b), 7.05 (c), and 10 (d).

The degeneracy of two lowest Landau levels (LLLs) in biased bilayer graphene was suggested to explain the experimental results related with the fractional quantum Hall effects [5, 6]. Meanwhile the degeneracy of two LLLs in biased bilayer graphene in [4] was revealed only near the intersection point at a given value of the magnetic field strength. To obtain a more complete and wide degeneracy in the calculations concerning the biased bilayer graphene one could employ a mixed model using the results reflected in Fig. 2.

The Landau quantization of the electrons and holes determine the energies of the optical band-to-band quantum transitions as well as of the magnetoexcitons creation. The band-to-band quantum transitions can be discussed in a larger range of parameters because they do not need the knowledge about the ionization potentials of the magnetoexcitons. By this reason, the quantum transitions from the ground state of the crystal to the exciton states will be confined by the quantum numbers $m \leq 4$. The heavy hole LLLs denoted as (hR_j) with $j = 1, 2, 3, 4$ were combined with two LLLs of the conduction electron (eR_i) with $i = 1, 2$. These combinations have the energies of the band-to-band transitions $E_{cv}(F_n)$ accounted from the semiconductor energy gap E_g equal to

$$E_{cv}(F_n) - E_g = E_e(R_i) + E_h(R_j). \quad (9)$$

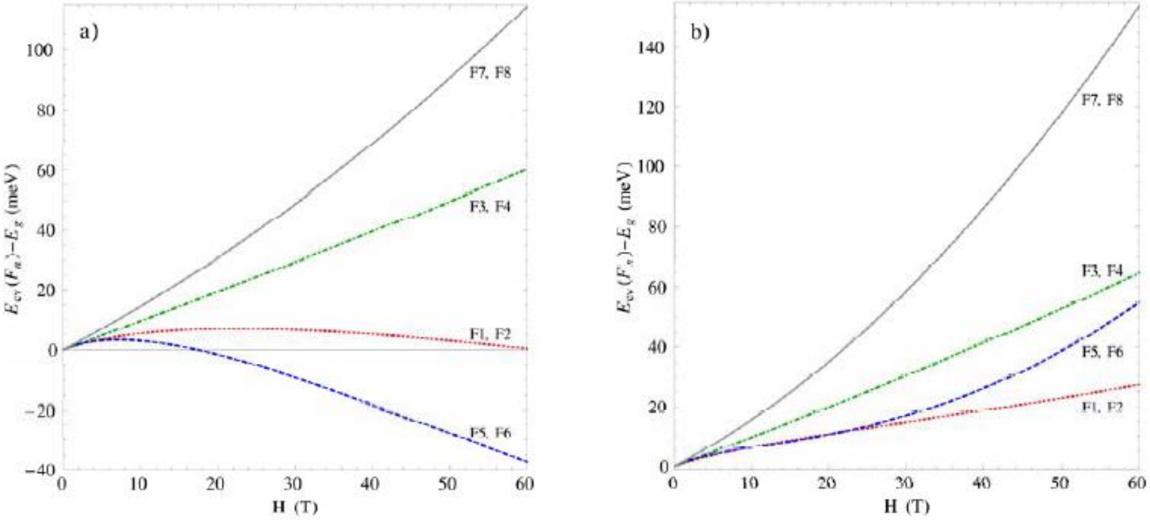

Fig. 3. The energies $E_{cv}(F_n)$ of the band-to-band quantum transitions starting from the LLLs of the heavy holes with the creation of the conduction electrons on the nearly degenerate two LLLs at the parameter $E_z = 10\ \mathrm{kV/cm}$ and two values of the constant $C = 2.6$ (a) and 5.65 (b).

They are represented in Fig. 3 in dependence on the magnetic field strength for the parameter $E_z = 10\ \mathrm{kV/cm}$ and two values of the coefficient C : 2.6 (a) and 5.65 (b). The lines on the drawings are doubled because the differences between the electron LLs (eR_1) and (eR_2) are too small and the positions of the curves are mainly determined by the structure of the heavy hole LLs.

Energy spectrum and selection rules for 2D magnetoexcitons

The four LLLs for 2D heavy holes were combined with two LLLs for 2D conduction electrons giving rise to eight 2D magnetoexciton states F_n with $n = 1, 2, \ldots, 8.$ They were determined by formulas (37)-(42) of [3]. The creation energies of the eight magnetoexciton states are

$$E_{ex}(F_n, k) = E_{cv}(F_n) - I_{ex}(F_n, k), \quad (10)$$

where

$$\begin{aligned} &E_{cv}(F_1) - E_g = E_e(R_1) + E_h(R_1), \\ &I_{ex}(F_1, \vec{k}) = I_{ex}(e, R_1; h, R_1; \vec{k}) \\ &= |a_0|^2 |d_0|^2 I_{ex}^{(0,0)}(\vec{k}) + |a_0|^2 |c_3|^2 I_{ex}^{(0,3)}(\vec{k}) \\ &+ |d_0|^2 |b_1|^2 I_{ex}^{(0,1)}(\vec{k}) + |b_1|^2 |c_3|^2 I_{ex}^{(1,3)}(\vec{k}); \end{aligned}$$

$$\begin{aligned} &E_{cv}(F_2) - E_g = E_e(R_2) + E_h(R_1), \\ &I_{ex}(F_2, \vec{k}) = I_{ex}(e, R_2; h, R_1; \vec{k}) \\ &= |d_0|^2 I_{ex}^{(0,0)}(\vec{k}) + |c_3|^2 I_{ex}^{(0,3)}(\vec{k}); \end{aligned}$$

$$\begin{aligned} &E_{cv}(F_3) - E_g = E_e(R_1) + E_h(R_2), \\ &I_{ex}(F_3, \vec{k}) = I_{ex}(e, R_1; h, R_2; \vec{k}) \\ &= |a_0|^2 I_{ex}^{(0,0)}(\vec{k}) + |b_1|^2 I_{ex}^{(0,1)}(\vec{k}); \end{aligned}$$

$$\begin{aligned} &E_{cv}(F_4) - E_g = E_e(R_2) + E_h(R_2), \\ &I_{ex}(F_4, \vec{k}) = I_{ex}(e, R_2; h, R_2; \vec{k}) = I_{ex}^{(0,0)}(\vec{k}); \end{aligned}$$

$$\begin{aligned} &E_{cv}(F_5) - E_g = E_e(R_1) + E_h(R_3), \\ &I_{ex}(F_5, \vec{k}) = I_{ex}(e, R_1; h, R_3; \vec{k}) \\ &= |a_0|^2 |c_4|^2 I_{ex}^{(0,4)}(\vec{k}) + |a_0|^2 |d_1|^2 I_{ex}^{(0,1)}(\vec{k}) \\ &+ |b_1|^2 |c_4|^2 I_{ex}^{(1,4)}(\vec{k}) + |b_1|^2 |d_1|^2 I_{ex}^{(1,1)}(\vec{k}); \end{aligned}$$

$$\begin{aligned} &E_{cv}(F_6) - E_g = E_e(R_2) + E_h(R_3), \\ &I_{ex}(F_6, \vec{k}) = I_{ex}(e, R_2; h, R_3; \vec{k}) \\ &= |c_4|^2 I_{ex}^{(0,4)}(\vec{k}) + |d_1|^2 I_{ex}^{(0,1)}(\vec{k}); \end{aligned}$$

$$\begin{aligned} &E_{cv}(F_7) - E_g = E_e(R_1) + E_h(R_4), \\ &I_{ex}(F_7, \vec{k}) = I_{ex}(e, R_1; h, R_4; \vec{k}) \\ &= |a_0|^2 I_{ex}^{(0,1)}(\vec{k}) + |b_1|^2 I_{ex}^{(1,1)}(\vec{k}); \end{aligned}$$

$$
\begin{aligned}
&E_{cv}(F_8) - E_g = E_e(R_2) + E_h(R_4), \\
&I_{ex}(F_8, \vec{k}) = I_{ex}(e, R_2; h, R_4; \vec{k}) = I_{ex}^{(0,1)}(\vec{k}).
\end{aligned} \tag{11}
$$

The ionization potentials $I_{ex}(e, R_i; h, R_j; \vec{k})$ are determined by the Coulomb electron-hole interaction integrals

$$
I_{ex}(e, R_i; h, R_j; \vec{k}) = \frac{1}{N}\sum_{p,s} e^{ik_y sl^2} F_{e-h}(e, R_i, p; h, R_j, k_x - p; e, R_i, p - s; h, R_j, k_x + s - p). \tag{12}
$$

The most of them were calculated in [3, 7], whereas the values $I_{ex}^{(0,4)}(\vec{k})$ and $I_{ex}^{(1,4)}(\vec{k})$ are determined below. Their dependences on the magnetic field strength H can be demonstrated only in the range of $H \geq 7\ \mathrm{T}$, because the magnetoexcitons do exist only when the cyclotron energy is greater than the Coulomb interaction between electrons and holes. The criterion $I_l < \hbar\omega_c$ is used.

Eight lowest exciton energy levels in the point $k = 0$, where the optical quantum transitions take place, are of greatest interest. Four of them, namely $E_{ex}(F_1, 0)$, $E_{ex}(F_2, 0)$, $E_{ex}(F_3, 0)$, $E_{ex}(F_4, 0)$, were discussed in [3]. Other four exciton levels, i.e., F_5, F_6, F_7, and F_8, we calculated below and are represented in Figs. 4 and 5.

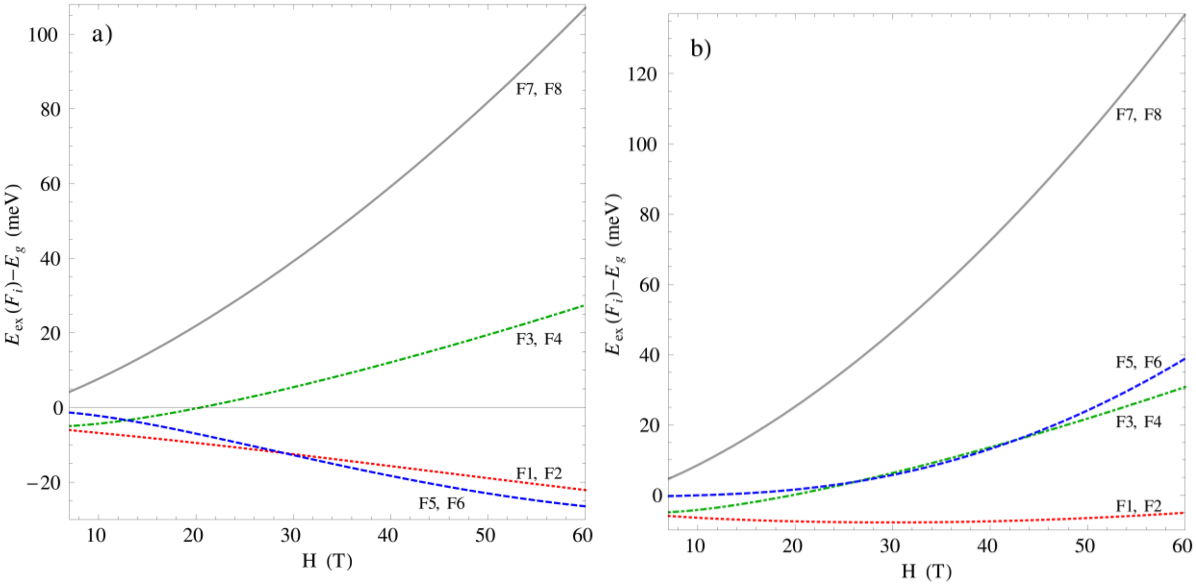

Fig. 4. The exciton energy levels in dependence on magnetic field strength H at the parameter $E_z = 10\ \mathrm{kV/cm}$ and two values of the coefficient C: 3.35 (a) and 5.65 (b).

In Figs. 4a and 4b the exciton energy levels are drawn in dependence on magnetic field strength H at the same parameter $E_z = 10\ \mathrm{kV/cm}$ but at different values of coefficient C

equal to 3.35 and 5.65, respectively. The arrangement of the exciton energy levels on the energy scale in the order from the lower to upper values depends on the range of magnetic field strength. In Fig. 4a, in the range of $(7-13)\ \mathrm{T}$, their disposition is as follows: the dipole active state $F_1(d.a.)$, the forbidden state $F_2(f.)$, the quadrupole-active state $F_3(q.a.)$, the dipole active state $F_4(d.a.)$, the quadrupole-active state $F_5(q.a.)$, the forbidden state $F_6(f.)$, the dipole active state $F_7(d.a.)$ and the quadrupole-active state $F_8(q.a.)$. There are three dipole-active states (F_1, F_4, F_7), three quadrupole-active states (F_2, F_3, F_8) and two forbidden states (F_2, F_6). In the middle range of $H=(13-27)\ \mathrm{T}$ their distribution is another as follows $F_1(d.a.)$, $F_2(f.)$, $F_5(q.a.)$, $F_6(f.)$, $F_3(q.a.)$, $F_4(d.a.)$, $F_7(d.a.)$, $F_8(q.a.)$. In the last range of $H=(27-60)\ \mathrm{T}$ the third ordering of the exciton levels does exist: $F_5(q.a.)$, $F_6(f.)$, $F_1(d.a.)$, $F_2(f.)$, $F_3(q.a.)$, $F_4(d.a.)$, $F_7(d.a.)$, $F_8(q.a.)$. The scheme of exciton energy levels at a greater values $C=5.65$ represented in Fig. 4b in the range of $(7-24)\ \mathrm{T}$ is the same as in Fig. 4a in the range of $(7-13)\ \mathrm{T}$. In the range of $(24-46)\ \mathrm{T}$, the two lowest exciton levels remain the same $F_1(d.a.)$ and $F_2(f.)$ being succeeded by four nearly degenerate levels $F_3(q.a.)$, $F_4(d.a.)$, $F_5(q.a.)$ and $F_6(f.)$. The remained exciton levels $F_7(d.a.)$ and $F_8(q.a.)$ are well separated from the previous ones.

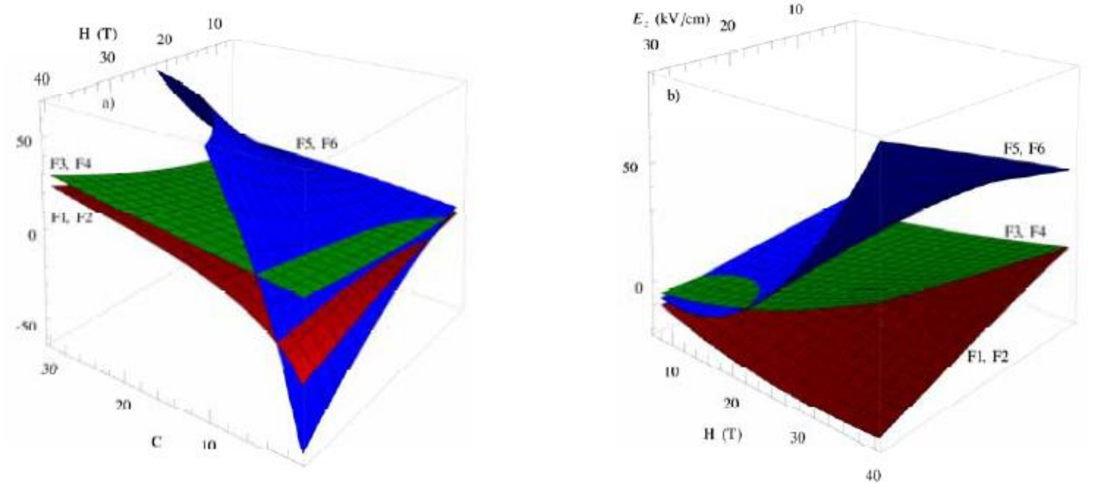

Fig. 5. Energy spectrum of the lower exciton energy levels with wave vector $k=0$ at a given parameter $E_z = 10\ \mathrm{kV/cm}$ and different values of coefficient C and magnetic field strength H (a) as well as at a given coefficient C and different values of parameters E_z and H (b).

Figures 4 and 5 show that the changes of the parameters E_z and C, as well as of the magnetic field strength H, can essentially change the arrangements of the exciton energy levels on the energy scale as well as the intensities of the optical quantum transitions from the ground state of the crystal to the magnetoexciton states.

Conclusions

The strong degeneracy of the heavy hole LLLs is possible due to the influence of the nonparabolic dispersion law, to the spin-orbit coupling, and chirality terms in some regions of the magnetic field strength. This degeneracy can influence the disposition on the energy scale of the energy levels of the 2D magnetoexcitons and the corresponding quantum transitions from the ground state of the crystal.

Acknowledgements

IVP gratefully acknowledges the Foundation for Young Scientists of the Academy of Sciences of Moldova for the financial support (11.819.05.13F).

References

[1] L.D. Landau, Zs. Phys. 64, 629, (1930); L.D. Landau, Collection of papers [in Russian], Nauka, Moscow, p. 47, vol. 1, 1969.

[2] E.I. Rashba, Sov. Phys. Fiz. Tverd. Tela (Leningrad), 2, 1224, (1960).

[3] T. Hakioğlu, M.A. Liberman, S.A. Moskalenko, and I.V. Podlesny, J. Phys.: Cond. Matt., 23, 345405, (2011).

[4] S.A. Moskalenko, I.V. Podlesny, P.I. Khadzhi, B.V. Novikov, and A.A. Kiselyov, Solid State Comm., 151, 1690, (2011).

[5] K.S. Novoselov, E. McCann, S.V. Morozov, V.I. Fal’ko, M.I. Katsnelson, U. Zeitler, D. Jiang, F. Schedin, and A.K. Geim, Nature Physics, 2, 177, (2006).

[6] A.H. Castro Neto, F. Guinea, N.M.R. Peres, K.S. Novoselov, and A.K. Geim, Rev. Mod. Phys., 81, 109, (2009).

[7] S.A. Moskalenko, M.A. Liberman, P.I. Khadzhi, E.V. Dumanov, Ig.V. Podlesny, and V.V. Boţan, Physica E, 39, 137, (2007).

BOSE-EINSTEIM CONDENSATION OF TWO-DIMENSIONAL MAGNETOREXCITONS INTERACTING WITH PLASMONS UNDER THE INFLUENCE OF EXCITED LANDAU LEVELS: COLLECTIVE ELEMENTARY EXCITATIONS

S. A. Moskalenko[1], M. A. Liberman[2,3], D. W. Snoke[4], E. V. Dumanov[1], S. S. Rusu[1], and F. Cerbu[1]

[1] Institute of Applied Physics of the Academy of Sciences of Moldova, Academiei str. 5, Chisinau, MD2028 Republic of Moldova
[2] Department of Physics, Uppsala University, Box 530, Uppsala, SE-751 21Sweden
[3] Moscow Institute of Physics and Technology, Inststitutskii per. 9, Dolgoprudnyi, Moskovsk. obl., 141700, Russia
[4]Department of Physics and Astronomy, University of Pittsburgh, 3941 O'Hara Street, Pittsburgh, Pennsylvania 15260, USA
E-mail: dum@phys.asm.md

(Received 12 June 2012)

Abstract

The collective elementary excitations of two-dimensional magnetoexcitons in a Bose-Einstein condensate (BEC) with wave vector $\vec{k} = 0$ were investigated in the framework of the Bogoliubov theory of quasiaverages. The Hamiltonian of the electrons and holes lying in the lowest Landau levels (LLLs) contains supplementary interactions due to virtual quantum transitions of the particles to the excited Landau levels (ELLs) and back. As a result, the interaction between the magnetoexcitons with $\vec{k} = 0$ does not vanish and their BEC becomes stable. The equations of motion for the exciton operators $d(P)$ and $d^{\dagger}(P)$ are interconnected with equations of motion for the density operators $\rho(P)$ and $D(P)$. Instead of a set of two equations of motion, as in the case of usual Bose gas, corresponding to normal and abnormal Green's functions, we have a set of four equations of motion. Changing the center-of-mass wave vector of a magnetoexciton from 0 to $\vec{P}$, for example, implies changing its internal structure, because the internal distance between the Landau orbits of the quantized electron and hole becomes equal to $\left|\vec{P}\right| l^2$, where l is the magnetic length. The separated electrons and holes remaining in their Landau orbits can take part in the formation of magnetoexcitons as well as in the formation of collective plasma oscillations. These possibilities were not included in previous descriptions of the theory of structureless bosons or in the theory of Wannier-Mott excitons with a rigid relative electron-hole motion structure without the possibility of the intra-series excitations. The internal structure of magnetoexcitons is much less rigid than that of Wannier-Mott excitons, and the possibilities for electrons and holes to take part simultaneously in many processes are much more diverse. This means that we have to deal simultaneously with four branches of the energy spectrum, the two supplementary branches being the optical plasmon branch represented by the operator $\rho(P)$ and the acoustical plasmon branch represented by the operator $D(P)$. The energy spectrum of the collective elementary excitations consists of two exciton-type branches (energy and quasienergy branches), each of them with an energy gap and a

roton-type region, from the gapless optical plasmon branch and from the acoustical plasmon branch, which reveals an absolute instability in the range of small and intermediary wave vectors.

1. Introduction

A two-dimensional electron system in a strong perpendicular magnetic field reveals fascinating phenomena, such as the integer and fractional quantum Hall effects [1-5]. The discovery of the fractional quantum Hall effect (FQHE) fundamentally changed the established concepts about charged single-particle elementary excitations in solids [6-8]. Gauge transformations from the wave functions and creation operators of simple particles to other wave functions and creation operators describe composite particles (CPs) [9, 10] made from previous particles and quantum vortices created under the influence of the magnetic flux quanta [11-19]. Due to the contribution of many outstanding investigations [1-26] as well as many efforts to explain and represent the underlying processes in a clearer way [4, 27, 28], it is possible to make a short summary as follows. One can begin with the concept of composite particles proposed by Wilczek [9] in the form of particles with magnetic flux tubes attached. A posteriori, the flux tubes could be substituted by more concrete formations as point quantum vortices, as was argued by Read [11-14] in a series of papers. In many explanations proposed by Enger [4], it was underlined that in 3D space the particles may obey only Fermi and Bose statistics, whereas in 2D space fractional statistics are also possible, when under the interchanging of two particles, the wave function obtains the phase factor $e^{i\pi\alpha}$ with any fractional values of α. These particles were named “anyons” [9]. The gauge transformations [27] of the wave functions and of the creation and annihilation operators of the initial particles and the corresponding Hamiltonians was a powerful instrument revealing the fundamental physical processes hidden at the first sight in the quantum states of the system. For example, Halperin, Lee, and Read [15] investigated the FQHE for spinless electrons in a half-filled lowest Landau level (LLL) using a gauge transformation from the initial electron creation operator $\psi_e^\dagger(r)$ to another creation operator $\psi^\dagger(r)$ describing a more complicated object comprised of an electron and two vortices:

$$\psi^\dagger(r)=\psi_e^\dagger(r)\exp\left[-i\,\mathrm{m}\int d^2\vec r'\theta(\vec r-\vec r')\hat\rho(\vec r')\right]; \qquad \theta(\vec r-\vec r')=\arctan\frac{y-y'}{x-x'} \tag{1}$$

when the integer number *m* is even and equals 2. Here $\hat\rho(\vec r')=\psi_e^\dagger(r')\psi_e(r')=\psi^\dagger(r')\psi(r')$ and $\theta(\vec r-\vec r')$ is the angle between the vector $\vec r-\vec r'$ and the axis x. It has a singular expression.

The transformation of type (1) must be accompanied by the transformation of the electromagnetic field $\vec A$, adding to it a gauge vector potential $\vec a$ with the components

$$\begin{gathered} a_i=-\frac{\hbar cm}{q}\partial_i\arctan\frac{y}{x}=\frac{\hbar cm}{q}\in^{ij}\partial_j\ln r \\ \vec a=\frac{\hbar cm}{q}\frac{\left(\vec i y-\vec j x\right)}{r^2}=\frac{\hbar cm}{qr}\vec e_\theta;\quad \vec e_\theta=\left(\vec i Sin\theta-\vec j Cos\theta\right) \end{gathered} \tag{2}$$

Here q is the electric charge of the starting particles and $\in^{ij}$ is an antisymmetric tensor. Vector $\vec a$ coincides exactly with the velocity of a vortex with the strength κ

$$\vec{\mathrm{v}}(r)=\frac{\kappa\vec e_\theta}{2\pi r}. \tag{3}$$

This means that the gauge transformation revealed the existence of the vortices in the system created by the magnetic flux quanta. Vortex (2) has a potential flow almost everywhere excluding the point $\vec{r} = 0$. The “magnetic” field strength $b(\vec{r})$ created by the gauge Chern-Simons potential $a(\vec{r})$ equals [4, 24, 27]

$$\begin{gathered} b(r) = Curl\vec{a}(r) = \in^{ij} \partial_i a_j = -\frac{\hbar c m}{q} \Delta \ln r = -\phi_0 m \delta^{(2)}(\vec{r}) Sgn(q) \\ \phi_0 = \frac{2\pi\hbar c}{|q|}; \quad \frac{\Delta \ln r}{2\pi} = \delta^{(2)}(\vec{r}); \quad q = |q| Sgn(q); \quad \int b(r) d^2\vec{r} = \oint \vec{a} d\vec{l} = -m\phi_0 Sgn(q) \end{gathered} \tag{4}$$

The “magnetic” field strength has also a singularity, being different from zero only at the point $\vec{r} = 0$. But the “magnetic” field flux is different from zero despite the fact that the vortex area is zero. These singular vortices are called point vortices.

Girvin, MacDonald and Platzman [19] elaborated the theory of the collective elementary excitation spectrum in the case of the FQHE, closely analogous to Feynman's theory of superfluid helium. The predicted spectrum has a gap at $\vec{k} = 0$ and a deep magneto-roton minimum at finite wavevector, which is a precursor to the gap collapse associated with Wigner crystal instability.

In this paper, we study a coplanar electron-hole (e-h) system with electrons in a conduction band and holes in a valence band, both of which have Landau levels in a strong perpendicular magnetic field. Earlier, this system has been studied in a series of papers [29-37] mostly dedicated to the theory of 2D magnetoexcitons. This system bears some resemblance to the case of a bilayer electron system with only conduction band occupied, in which the Landau level in each of two adjacent 2D layers is half occupied, adding free charge in a thin metallic layer grown nearly but separated from the bilayer. The system may be described as a having Landau levels half occupied by holes in one layer and half occupied by electrons in another layer. The ground state of this system may be viewed as a Bose-Einstein condensation, or more properly a BCS state, of electron-hole pairs, i.e., excitons at high density [38-43]. The system we are interested in has only one layer, with electrons in conduction band and holes in the valence band of the same layer created by optical excitation or by p-n doping injection (both of these methods can be called "pumping"). In this case, there is an intrinsic metastability, since electrons in the conduction band can drop down into the valence band and recombine with holes there. However, we assume that the recombination rate of the electrons with holes has such a slow rate that the number of electrons and holes is nearly conserved. Unlike the case of the bilayer electron system with a half-filled lowest Landau level, in the case of a single excited layer which we consider, the density of excitons can be quite low, so that the electron Landau level and the separate hole Landau level are each only slightly occupied, and Pauli exclusion and phase space filling do not come in to play.

We are interested in the distribution of the flux quanta in the case of an electron-hole system with equal average numbers of electrons and holes $\bar{N}_e = \bar{N}_h$ with filling factor $\nu = \bar{N}_e / N$, where N is the total number of flux quanta. In the case of fractional integer filling factor, there are an integer number of flux quanta per each e-h pair. The creation of the vortices in this case is not studied at the present time.

Another related system is the case of a pumped bilayer system [44-54], such as coupled semiconductor quantum wells (CQWs). While the geometry of this system with two adjacent layers is similar to the bilayer electron system discussed above, it is actually more similar in its main properties to the pumped single-layer electron-hole system which is the topic of this paper. In this system, the main effect of the bilayer structure is to put a tunneling barrier between the electrons which are in one layer and the holes which are in the other layer. This makes it possible to experimentally realize the condition given above of negligible electron-hole recombination; experimentally, exciton lifetimes of up to 40 ms have been observed [52, 54], and the long lifetimes allow diffusion of the excitons over macroscopic distances [44] and equilibration to the lattice temperature in a harmonic potential [45]. Like the pumped single-layer system discussed here, the electrons in the conduction band and the holes in the valence band can each be at very low density. One drawback of this system is that it causes the interactions of the excitons to be enhanced, due to their alignment in the direction perpendicular to the layers, giving a strong dipole-dipole interaction [46]. For a comparison of the half-filled bilayer system and the pumped bilayer system, see [54].

In this bilayer system with nearly negligible recombination, a magnetic field can be applied in the direction perpendicular to the layers to create magnetoexcitons of the type considered here. So far, there has been no evidence of Bose-Einstein condensation in this system. The magnetoexciton regime can be reached, however, as shown in Fig. 1. At high magnetic field, the exciton energy shifts up to higher energy following the Landau level energy, as expected. The fast shift to lower energy seen at low magnetic field has been explained as due to the effect of the disorder on the tunneling current in the samples [47].

Recently, another group has used magnetic field to study the Mott transition from insulating exciton gas to conducting plasma [48]. They were able to show that the magnetic response of the system changed sharply when the system had undergone a Mott transition. The Mott transition of exciton gas to plasma is in general still a quite difficult problem receiving much study [49, 50].

One reason why BEC has not been observed clearly in either the simple pumped bilayer system or the pumped magnetoexciton bilayer system may be that the condensate occurs in a "dark" state which does not emit light. It has been proposed [55-57] that condensation of excitons will always occur in a dark state if one exists; some evidence of BEC of dark excitons has been reported in [52]. The existence of two types of excitons—dark and bright excitons—is related to their spin structure. In GaAs, the lowest exciton state splits into a J=2 doublet which does not emit light, by symmetry, and a J=1 doublet which emits light. In the present paper, we do not take into account the spin structure of the excitons.

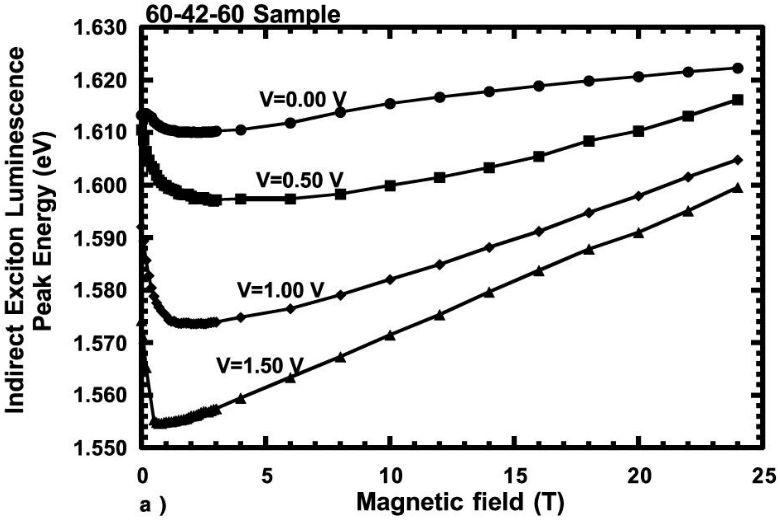

Fig. 1. Energy of the indirect exciton photon emission as a function of magnetic field, for several values of the electric field (from [45]).

Our paper is organized as follows. In Section 2, we deduce the Hamiltonian of the supplementary interactions between electrons and holes lying in the lowest Landau levels (LLLs) due to their virtual quantum transition from the LLLs to excited Landau levels (ELLs) in the processes of Coulomb scattering. It is interesting that this interaction due to the influence of the ELLs is possible to express in terms of two-particle operators in the form of density fluctuation operators. In Section 3, the full Hamiltonian containing the basic Coulomb interaction as well as the supplementary interaction is taken through the operation of gauge symmetry breaking so as to study the Bose-Einstein condensation (BEC) of magnetoexcitons. The traditional way is to follow the Keldysh–Kozlov–Kopaev [58] method describing the BEC of excitons in the electron-hole representation, which leads to the subsequent Bogoliubov u-v transformation of the creation and annihilation operators of the initial and final Fermi-type quasiparticles. In the present paper, we have chosen another variant proposed by Bogoliubov in his theory of quasiaverages [59]. Both methods are equivalent, but the second variant is preferable for our purposes, because we will operate with the integral two-particle operators rather than with single-particle Fermi-type operators. In Section 4, we deduce the equations of motion for the integral two-particle operators and for the corresponding Green's functions. The truncation of the equations of motion permit us to obtain a Dyson equation in a 4×4 matrix form and to determine the self-energy parts $\Sigma_{i,j}$ with $i,j=1,2,3,4$. Section 5 is devoted to the analytical and numerical calculations of the energy spectrum in different approximations. The conclusions are presented in Section 6.

2. Hamiltonian of the supplementary interaction

The Hamiltonian of the Coulomb interaction of the electrons and holes lying on their LLLs has the form

$$H_c=\frac{1}{2}\sum_{\vec{Q}} W_{\vec{Q}}\left[\rho(\vec{Q})\rho(-\vec{Q})-N_e-N_h\right]-\mu_e N_e-\mu_h N_h \tag{5}$$

Here $\rho(\vec{Q})$ are the density fluctuation operators expressed through the electron $\rho_e(\vec{Q})$ and hole $\rho_h(\vec{Q})$ density operators as follows

$$\begin{gathered}\rho_e(\vec{Q})=\sum_t e^{iQ_y t l^2} a^{\dagger}_{t-\frac{Q_x}{2}} a_{t+\frac{Q_x}{2}};\ \ \rho_h(\vec{Q})=\sum_t e^{iQ_y t l^2} b^{\dagger}_{t+\frac{Q_x}{2}} b_{t-\frac{Q_x}{2}}\\ \rho(\vec{Q})=\rho_e(\vec{Q})-\rho_h(-\vec{Q});\ \ D(\vec{Q})=\rho_e(\vec{Q})+\rho_h(-\vec{Q});\\ N_e=\rho_e(0);\ \ N_h=\rho_h(0);\ \ N=N_e+N_h;\ \ W_{\vec{Q}}=\frac{2\pi e^2}{\varepsilon_0 S\left|\vec{Q}\right|}e^{-Q^2 l^2/2}\end{gathered} \tag{6}$$

The density operators are integral two-particle operators. They are expressed through the single-particle creation and annihilation operators $a^{\dagger}_p, a_p$ for electrons and $b^{\dagger}_p, b_p$ for holes. ε_0 is the dielectric constant of the background; μ_e and μ_h are chemical potentials for electrons and holes.

The supplementary indirect interactions between electrons and holes appear due to the simultaneous virtual quantum transitions of two particles from the LLLs to excited Landau levels (ELLs) and their return back during the Coulomb scattering processes. This interaction was deduced in [37]. It has a general attractive character and has the form

$$\begin{gathered}H_{\mathrm{suppl}}=-\frac{1}{2}\sum_{p,q,s}\phi_{e-e}(p,q;s)a_p^{\dagger}a_q^{\dagger}a_{q+s}a_{p-s}-\\-\frac{1}{2}\sum_{p,q,s}\phi_{h-h}(p,q;s)b_p^{\dagger}b_q^{\dagger}b_{q+s}b_{p-s}-\sum_{p,q,s}\phi_{e-h}(p,q;s)a_p^{\dagger}b_q^{\dagger}b_{q+s}a_{p-s}\end{gathered}\tag{7}$$

An important property of this quartic form constructed from single-particle operators is the possibility to transcribe it through the integral two-particle operators $\hat{\rho}(\vec{Q})$ and $\hat{D}(\vec{Q})$ as follows [60]:

$$H_{\mathrm{suppl}}=\frac{1}{2}B_{i-i}N-\frac{1}{4N}\sum_{Q}V(Q)\rho(\vec{Q})\rho(-\vec{Q})-\frac{1}{4N}\sum_{Q}U(Q)D(\vec{Q})D(-\vec{Q})\tag{8}$$

Paper [60] contains a detailed derivation of the Dyson equation, but the approach of solution is completely different.

The estimates give the values [37, 60]

$$\begin{gathered}U(\vec{Q})\cong U(0)e^{-Q^2l^2/2};\;\; U(0)=2A_{i-i};\;\; \frac{1}{N}\sum_{\vec{Q}}U(\vec{Q})=B_{i-i}+\Delta(0);\\ V(\vec{Q})\approx V(0)=0;\;\; A_{i-i}=0.481\frac{I_l^2}{\pi\hbar\omega_c};\;\; B_{i-i}=0.432\frac{I_l^2}{\pi\hbar\omega_c};\;\; \Delta(0)=0.688\frac{I_l^2}{\pi\hbar\omega_c}\end{gathered}\tag{9}$$

Here I_l is the ionization potential of magnetoexcitons and $\hbar\omega_c$ is the cyclotron frequency at $m_e=m_h$. The full Hamiltonian describing the interaction of electrons and holes lying on the LLLs is

$$H=H_{Coul}+H_{\mathrm{suppl}}\tag{10}$$

3. Breaking of the gauge symmetry. Bose-Einstein condensation of magnetoexcitons with k=0

In [30-36], Bose-Einstein condensation (BEC) of magnetoexcitons with wave vector $\vec{k}$ different from zero was considered without taking into account the influence of the excited Landau levels (ELLs). However, the case of BEC with $\vec{k}=0$ was impossible to incorporate in the previous description because these magnetoexcitons form an ideal Bose gas: in that model, the interaction between two magnetoexcitons with electrons and holes lying on the LLLs and with $\vec{k}=0$ equals exactly zero. This prediction of ideal behavior is an artifact of the assumptions of the theory and made approximations, however. To consider BEC of magnetoexcitons with $\vec{k}=0$, it is necessary to take into account the influence of the ELLs, represented by Hamiltonian (8).

As discussed in previous papers [31-37, 61], the breaking of the gauge symmetry of Hamiltonian (10) can be achieved using the Keldysh–Kozlov–Kopaev [58] method using the unitary transformation

$$D(\sqrt{N_{ex}})=\exp[\sqrt{N_{ex}}(d^{\dagger}(\vec{k})-d(\vec{k}))]\tag{11}$$

where $d^{\dagger}(k)$ and $d(k)$ are the creation and annihilation operators of the magnetoexcitons. In the electron-hole representation they are [31-37]:

$$d^{\dagger}(\vec{P}) = \frac{1}{\sqrt{N}}\sum_{t} e^{-iP_y t l^2} a^{\dagger}_{t+\frac{P_x}{2}} b^{\dagger}_{-t+\frac{P_x}{2}};$$
$$d(\vec{P}) = \frac{1}{\sqrt{N}}\sum_{t} e^{iP_y t l^2} b_{-t+\frac{P_x}{2}} a_{t+\frac{P_x}{2}}; \tag{12}$$

BEC of magnetoexcitons leads to the formation of a coherent macroscopic state as a ground state of the system with wave function

$$\left|\psi_g(\vec{k})\right\rangle = \hat{D}(\sqrt{N_{ex}})\left|0\right\rangle; \quad a_p\left|0\right\rangle = b_p\left|0\right\rangle = 0 \tag{13}$$

Here $\left|0\right\rangle$ is the vacuum state for electrons and holes. In spite of the fact that we have kept an arbitrary value of $\vec{k}$, nevertheless our main goal is the BEC with $\vec{k} = 0$. The transformed Hamiltonian (10) looks like

$$\mathcal{H} = D\left(\sqrt{N_{ex}}\right) H D^{\dagger}\left(\sqrt{N_{ex}}\right) \tag{14}$$

and is succeeded, as usual, by the Bogoliubov *u-v* transformations of the single-particle Fermi operators

$$\alpha_p = D\left(\sqrt{N_{ex}}\right) a_p D^{\dagger}\left(\sqrt{N_{ex}}\right) = u a_p - \mathrm{v}\left(p - \frac{k_x}{2}\right) b^{\dagger}_{k_x - p}; \quad \alpha_p\left|\psi_g(\vec{k})\right\rangle = 0$$
$$\beta_p = D\left(\sqrt{N_{ex}}\right) b_p D^{\dagger}\left(\sqrt{N_{ex}}\right) = u b_p + \mathrm{v}\left(\frac{k_x}{2} - p\right) a^{\dagger}_{k_x - p}; \quad \beta_p\left|\psi_g(\vec{k})\right\rangle = 0 \tag{15}$$

Instead of this traditional way of transforming the expressions of the starting Hamiltonian (10) and of the integral two-particle operators (6) and (12), we will use the method proposed by Bogoliubov in his theory of quasiaverages [59], remaining in the framework of the original operators. The new variant is completely equivalent to the previous one, and both of them can be used in different stages of the calculations. For example, the average values can be calculated using wave function (13) and *u-v* transformations (15), whereas the equations of motion for the integral two-particle operators can be simply written in the starting representation.

Hamiltonian (10) with the broken gauge symmetry in the lowest approximation has the form

$$\begin{aligned}\mathcal{H} = {} & \frac{1}{2}\sum_{\vec{Q}} W_{\vec{Q}}\left[\rho(\vec{Q})\rho(-\vec{Q}) - N_e - N_h\right] - \mu_e N_e - \mu_h N_h + \\ & + \frac{1}{2}B_{i-i}N - \frac{1}{4N}\sum_{Q} V(Q)\rho(\vec{Q})\rho(-\vec{Q}) - \frac{1}{4N}\sum_{Q} U(Q)D(\vec{Q})D(-\vec{Q}) - \\ & - \tilde{\eta}\sqrt{N}\left(d^{\dagger}(k) + d(k)\right)\end{aligned} \tag{16}$$

Another smaller term, proportional to $\tilde{\eta}$, has been dropped for simplicity. Here the parameter $\tilde{\eta}$, which determines the breaking of the gauge symmetry, depends, as in the case of weakly non-ideal Bose-gas considered by Bogoliubov [59], on the chemical potential μ and on the square root of the density. In our case, the density is proportional to the filling factor $\nu = \mathrm{v}^2$. We have

$$\mu = \mu_e + \mu_h; \quad \bar{\mu} = \mu + I_l; \quad N_{ex} = \mathrm{v}^2 N; \quad \tilde{E}_{ex}(k) = -I_l - \Delta(k) + E(k);$$
$$\tilde{\eta} = (\tilde{E}_{ex}(k) - \mu)\mathrm{v} = (E(k) - \Delta(k) - \bar{\mu})\mathrm{v}; \qquad E(k) = 2\sum_{Q} W_Q Sin^2\left(\frac{[K\times Q]_z l^2}{2}\right); \tag{17}$$

In the special case of $\vec{k}=0$ we obtain

$$\tilde{\eta}=-(\bar{\mu}+\Delta(0))\mathrm{v} \tag{18}$$

4. Equations of motion for the integral two-particle operators. Green's functions, Dyson equation and self-energy parts

The equations of motion for the integral two-particle operators with wave vectors $\vec{P}\neq 0$ in the special case of BEC of magnetoexcitons with $\vec{k}=0$ are

$$\begin{aligned}
& i\hbar\frac{d}{dt}d(\vec{P})=[d(\vec{P}),\hat{\mathcal{H}}]=(-\bar{\mu}+E(\vec{P})-\Delta(\vec{P}))d(\vec{P})-2i\sum_{\vec{Q}}\tilde{W}(\vec{Q})Sin\left(\frac{[\vec{P}\times\vec{Q}]_z l^2}{2}\right)\rho(\vec{Q})d(\vec{P}-\vec{Q})-\\
& -\frac{1}{N}\sum_{\vec{Q}}U(\vec{Q})Cos\left(\frac{[\vec{P}\times\vec{Q}]_z l^2}{2}\right)D(\vec{Q})d(\vec{P}-\vec{Q})+\tilde{\eta}\frac{D(\vec{P})}{\sqrt{N}};\\
& i\hbar\frac{d}{dt}d^{\dagger}(-\vec{P})=[d^{\dagger}(-\vec{P}),\hat{\mathcal{H}}]=(\bar{\mu}-E(-\vec{P})+\Delta(-\vec{P}))d^{\dagger}(-\vec{P})+\\
& +2i\sum_{\vec{Q}}\tilde{W}(\vec{Q})Sin\left(\frac{[\vec{P}\times\vec{Q}]_z l^2}{2}\right)d^{\dagger}(-\vec{P}-\vec{Q})\hat{\rho}(-\vec{Q})+\\
& +\frac{1}{N}\sum_{\vec{Q}}U(\vec{Q})Cos\left(\frac{[\vec{P}\times\vec{Q}]_z l^2}{2}\right)d^{\dagger}(-\vec{P}-\vec{Q})D(-\vec{Q})-\tilde{\eta}\frac{D(\vec{P})}{\sqrt{N}};\\
& \quad i\hbar\frac{d}{dt}\rho(\vec{P})=[\rho(\vec{P}),\hat{\mathcal{H}}]=\\
& \quad =-i\sum_{\vec{Q}}\tilde{W}(\vec{Q})Sin\left(\frac{[\vec{P}\times\vec{Q}]_z l^2}{2}\right)[\rho(\vec{P}-\vec{Q})\rho(\vec{Q})+\rho(\vec{Q})\rho(\vec{P}-\vec{Q})]+\\
& \quad +\frac{i}{2N}\sum_{\vec{Q}}U(\vec{Q})Sin\left(\frac{[\vec{P}\times\vec{Q}]_z l^2}{2}\right)\left[D(\vec{P}-\vec{Q})D(\vec{Q})+D(\vec{Q})D(\vec{P}-\vec{Q})\right];\\
& \quad i\hbar\frac{d}{dt}\hat{D}(\vec{P})=[\hat{D}(\vec{P}),\hat{\mathcal{H}}]=\\
& \quad -i\sum_{\vec{Q}}\tilde{W}(\vec{Q})Sin\left(\frac{[\vec{P}\times\vec{Q}]_z l^2}{2}\right)[\rho(\vec{Q})D(\vec{P}-\vec{Q})+D(\vec{P}-\vec{Q})\rho(\vec{Q})]+\\
& \quad +\frac{i}{2N}\sum_{\vec{Q}}U(\vec{Q})Sin\left(\frac{[\vec{P}\times\vec{Q}]_z l^2}{2}\right)[D(\vec{Q})\rho(\vec{P}-\vec{Q})+\rho(\vec{P}-\vec{Q})D(\vec{Q})]+2\tilde{\eta}\sqrt{N}\left[d(\vec{P})-d^{\dagger}(-\vec{P})\right];
\end{aligned} \tag{19}$$

Following equations of motion (19), we introduce four interconnected retarded Green's functions at $T=0$ [62, 63]:

$$\begin{aligned}
& G_{11}(\vec{P},t)=\left\langle\left\langle d(\vec{P},t);X^{\dagger}(\vec{P},0)\right\rangle\right\rangle; \quad G_{12}(\vec{P},t)=\left\langle\left\langle d^{\dagger}(-\vec{P},t);X^{\dagger}(\vec{P},0)\right\rangle\right\rangle;\\
& G_{13}(\vec{P},t)=\left\langle\left\langle \frac{\rho(\vec{P},t)}{\sqrt{N}};X^{\dagger}(\vec{P},0)\right\rangle\right\rangle; \quad G_{14}(\vec{P},t)=\left\langle\left\langle \frac{D(\vec{P},t)}{\sqrt{N}};X^{\dagger}(\vec{P},0)\right\rangle\right\rangle;
\end{aligned} \tag{20}$$

as well as their Fourier transforms $G_{ij}(\vec{P},\omega)$, for which the equations of motion of the same type as the equations of motion (19) were obtained. These Green's functions can be called one-operator Green's functions, because they contain only one two-particle operator of the type $d^{\dagger}$, d, ρ, D. However, on the right side of the corresponding equations of motion, there is a second generation of two-operator Green's functions containing the different products of the two-particle operators mentioned above. For them, the second generation of the equations of motion was deduced, containing in their right sides the Green's function of the third generation. They are three-operator Green's functions for which it is necessary to deduce the third generation of equations of motion. But we have stopped here the evolution of the infinite chains of equations of motion for multi-operators Green's function following the procedure proposed by Zubarev [63]. The truncation of the chains of the equations of motion and the decoupling of the one-operator Green's functions from the multi-operator Green's functions was achieved by substituting the three-operator Green's functions by one-operator Green's functions multiplied by the average value of the remaining two operators. The average values were calculated using the ground state wave function (13) and the *u*-*v* transformations (15). The Zubarev procedure is equivalent to a perturbation theory with a small parameter of the type $\mathrm{v}^2(1-\mathrm{v}^2)$, which represents the product of a filling factor $\nu=\mathrm{v}^2$ and the phase-space filling factor $(1-\mathrm{v}^2)$ reflecting the Pauli exclusion principle.

The closed system of Dyson equations has the form

$$\sum_{j=1}^{4} G_{1j}(\vec{P},\omega)\Sigma_{jk}(\vec{P},\omega)=C_{1k}; \qquad k=1,2,3,4 \tag{21}$$

There are 16 different components of the self-energy parts $\Sigma_{jk}(\vec{P},\omega)$ forming a 4×4 matrix. They are

$$\Sigma_{11}(\vec{P},\omega)=\hbar\omega+i\delta+\bar{\mu}-E(\vec{P})+\Delta(\vec{P})-\frac{\left\langle D(A)D(-A)\right\rangle}{N^2}\sum_{\vec{Q}\neq\vec{P}}\frac{U^2(\vec{Q})Cos^2\left(\frac{[\vec{P}\times\vec{Q}]l^2}{2}\right)}{\hbar\omega+i\delta+\bar{\mu}-E(\vec{P}-\vec{Q})+\Delta(\vec{P}-\vec{Q})};$$

$$\Sigma_{21}(\vec{P},\omega)=0;$$

$$\Sigma_{31}(\vec{P},\omega)=i\frac{\left\langle D(A)d(-A)\sqrt{N}\right\rangle}{N^2}\sum_{\vec{Q}\neq\vec{P}}\frac{U(\vec{Q})U(\vec{Q}-\vec{P})Cos\left(\frac{[\vec{P}\times\vec{Q}]l^2}{2}\right)Sin\left(\frac{[\vec{P}\times\vec{Q}]l^2}{2}\right)}{\hbar\omega+i\delta+\bar{\mu}-E(\vec{P}-\vec{Q})+\Delta(\vec{P}-\vec{Q})};$$

$$\Sigma_{41}(\vec{P},\omega)=-\tilde{\eta}+U(\vec{P})\frac{\left\langle d(0)\right\rangle}{\sqrt{N}}+2\frac{\left\langle D(A)d(-A)\sqrt{N}\right\rangle}{N}\sum_{\vec{Q}\neq\vec{P}}\frac{\tilde{W}(\vec{Q})(U(\vec{P})-U(\vec{Q}-\vec{P}))Sin^2\left(\frac{[\vec{P}\times\vec{Q}]l^2}{2}\right)}{\hbar\omega+i\delta+\bar{\mu}-E(\vec{P}-\vec{Q})+\Delta(\vec{P}-\vec{Q})}-$$

$$-\frac{\left\langle D(A)d(-A)\sqrt{N}\right\rangle}{N^2}\sum_{\vec{Q}\neq\vec{P}}\frac{U(\vec{Q})U(\vec{P})Cos^2\left(\frac{[\vec{P}\times\vec{Q}]l^2}{2}\right)}{\hbar\omega+i\delta+\bar{\mu}-E(\vec{P}-\vec{Q})+\Delta(\vec{P}-\vec{Q})};$$

$$\Sigma_{12}(\vec{P},\omega)=0;$$

$$\Sigma_{22}(\vec{P},\omega)=\hbar\omega+i\delta-\bar{\mu}+E(\vec{P})-\Delta(-\vec{P})-\frac{\langle D(A)D(-A)\rangle}{N^2}\sum_{\vec{Q}\neq-\vec{P}}\frac{U(\vec{Q})U(-\vec{Q})Cos^2\left(\frac{[\vec{P}\times\vec{Q}]l^2}{2}\right)}{\hbar\omega+i\delta-\bar{\mu}+E(-\vec{P}-\vec{Q})-\Delta(-\vec{P}-\vec{Q})};$$

$$\Sigma_{32}(\vec{P},\omega)=i\frac{\langle d^{\dagger}(A)D(-A)\sqrt{N}\rangle}{N^2}\sum_{\vec{Q}\neq-\vec{P}}\frac{U(\vec{Q})U(-\vec{Q}-\vec{P})Cos\left(\frac{[\vec{P}\times\vec{Q}]l^2}{2}\right)Sin\left(\frac{[\vec{P}\times\vec{Q}]l^2}{2}\right)}{\hbar\omega+i\delta-\bar{\mu}+E(-\vec{P}-\vec{Q})-\Delta(-\vec{P}-\vec{Q})};$$

$$\Sigma_{42}(\vec{P},\omega)=\tilde{\eta}-U(-\vec{P})\frac{\langle d^{\dagger}(0)\rangle}{\sqrt{N}}-2\frac{\langle d^{\dagger}(A)D(-A)\sqrt{N}\rangle}{N}\sum_{\vec{Q}\neq-\vec{P}}\frac{\tilde{W}(\vec{Q})(U(-\vec{Q}-\vec{P})-U(\vec{P}))Sin^2\left(\frac{[\vec{P}\times\vec{Q}]l^2}{2}\right)}{\hbar\omega+i\delta-\bar{\mu}+E(-\vec{P}-\vec{Q})-\Delta(-\vec{P}-\vec{Q})}-$$

$$-\frac{\langle d^{\dagger}(A)D(-A)\sqrt{N}\rangle}{N^2}\sum_{\vec{Q}\neq-\vec{P}}\frac{U(\vec{Q})U(-\vec{P})Cos^2\left(\frac{[\vec{P}\times\vec{Q}]l^2}{2}\right)}{\hbar\omega+i\delta-\bar{\mu}+E(-\vec{P}-\vec{Q})-\Delta(-\vec{P}-\vec{Q})};\qquad(22)$$

$$\Sigma_{13}(\vec{P},\omega)=0;$$

$$\Sigma_{23}(\vec{P},\omega)=0;$$

$$\Sigma_{33}(\vec{P},\omega)=\hbar\omega+i\delta-\frac{\langle D(A)D(-A)\rangle}{N^2(\hbar\omega+i\delta)}\sum_{\vec{Q}\neq\vec{P}}U(\vec{Q})(U(-\vec{Q})-U(\vec{Q}-\vec{P}))Sin^2\left(\frac{[\vec{P}\times\vec{Q}]l^2}{2}\right);$$

$$\Sigma_{43}(\vec{P},\omega)=0;$$

$$\Sigma_{14}(\vec{P},\omega)=-2\tilde{\eta};$$

$$\Sigma_{24}(\vec{P},\omega)=2\tilde{\eta};$$

$$\Sigma_{34}(\vec{P},\omega)=0;$$

$$\Sigma_{44}(\vec{P},\omega)=\hbar\omega+i\delta-\frac{2\langle D(A)D(-A)\rangle}{N(\hbar\omega+i\delta)}\sum_{\vec{Q}\neq-\vec{P}}\tilde{W}(\vec{Q})(U(\vec{Q}-\vec{P})-U(\vec{P}))Sin^2\left(\frac{[\vec{P}\times\vec{Q}]l^2}{2}\right)+$$

$$+\frac{\langle D(A)D(-A)\rangle}{N^2(\hbar\omega+i\delta)}\sum_{\vec{Q}\neq\vec{P}}U(\vec{Q})(U(\vec{P})-U(-\vec{Q}))Sin^2\left(\frac{[\vec{P}\times\vec{Q}]l^2}{2}\right);$$

5. Energy spectrum of the collective elementary excitations

The self-energy parts (22) contain the average values of two-operator products, which appeared after the decoupling of the three-operator Green's functions by expressing them through one-operator Green's functions. The average values were calculated using the ground state wave function (13) and the coefficients of the u-v transformation (15). For operators $\hat{D}(\vec{Q})$, $\hat{\rho}(\vec{Q})$, $d(\vec{Q})$ and $d^{\dagger}(\vec{Q})$ with $\vec{Q}\neq 0$ we have

$$\begin{aligned}
&\left\langle D(\vec{Q})D(-\vec{Q})\right\rangle = 4u^2\mathrm{v}^2 N;\\
&\left\langle \rho(\vec{Q})\rho(-\vec{Q})\right\rangle = 0;\\
&\left\langle D(\vec{Q})d(-\vec{Q})\right\rangle = \left\langle d^\dagger(\vec{Q})D(-\vec{Q})\right\rangle = -2u\mathrm{v}\sqrt{N};\\
&\left\langle \rho(\vec{Q})d(-\vec{Q})\right\rangle = \left\langle d^\dagger(\vec{Q})\rho(-\vec{Q})\right\rangle = 0\\
&\left\langle d(0)\right\rangle = \left\langle d^\dagger(0)\right\rangle = u\mathrm{v}\sqrt{N};\\
&u^2+\mathrm{v}^2=1; \quad N=\frac{S}{2\pi l^2}
\end{aligned} \tag{23}$$

Averages (23) have extensive values depending on N. For the condensate with $\vec{k}=0$, they do not depend on the wave vector $\vec{Q}$. At the point $\vec{Q}=0$ their values do not coincide with (15), changing by a jump. Expressions (23) have a small parameter of the perturbation theory in the forms $u^2\mathrm{v}^2=\mathrm{v}^2(1-\mathrm{v}^2)$, $u\mathrm{v}^3$ and $u\mathrm{v}$. The chemical potential $\bar{\mu}$ and the parameter $\tilde{\eta}$ of the quasiaverage theory are

$$\begin{aligned}
&\bar{\mu}+\Delta(0)=2\mathrm{v}^2(B_{i-i}-2A_{i-i}+\Delta(0))=0.1rI_l\mathrm{v}^2\\
&\tilde{\eta}=-0.1rI_l\mathrm{v}^3;\\
&0<r=\frac{I_l}{\hbar\omega_c}\le 1;\ \ I_l=\frac{e^2}{\varepsilon_0 l}\sqrt{\frac{\pi}{2}}
\end{aligned} \tag{24}$$

Here l is the magnetic length, ε_0 is the dielectric constant of the background and I_l is the ionization potential of the magnetoexciton. The chemical potential $\bar{\mu}$ has an increasing dependence on the concentration of electrons n_e or of magnetoexcitons n_{ex}, which are proportional to the filling factor $\nu=\mathrm{v}^2$ as follows

$$n_e=n_{ex}=\frac{\mathrm{v}^2}{2\pi l^2} \tag{25}$$

This means that the system of Bose-Einstein condensed magnetoexcitons with wave vector $\vec{k}=0$ is stable against collapse. Its stability is completely due to the influence of the ELLs. In spite of the fact that the supplementary interaction has an overall attractive character and its average values in the Hartree approximation remain attractive; nevertheless, the exchange-type Fock terms as well as other terms arising due to the Bogoliubov *u-v* transformation give rise to a repulsive interaction in the system, which is necessary to stabilize the BEC of magnetoexcitons with $\vec{k}=0$. The role of the exchange Fock terms supplying a repulsion in conditions of overall attraction is similar to the case of the electron plasma, when the exchange Fock terms supply an effective attraction and lowering of the energy per particle in the condition of an overall Coulomb repulsion between the electrons [64]. The influence of the exchange Fock terms is the same in the case of electron-hole liquid (EHL) [65]. Another system with mixed interactions, the Wannier-Mott excitons with different spin projections, was investigated in [66]. It was shown that the coherent pairing of excitons leads to Bose-Einstein condensation of biexcitons. There the excitons with opposite spin projections and attractive interaction formed the biexcitons, whereas other excitons with parallel spin projections and repulsive interactions stabilized the Bose-Einstein condensate of biexcitons. The situation with magnetoexcitons also does not coincide exactly with the Bogoliubov model of a weakly non-ideal Bose gas with pure repulsive interaction, because the presence of the attractive Hartree terms mentioned above.

This difference will be reflected in the structure of the energy spectrum of the collective elementary excitations. The collective elementary excitation spectrum obtained by Bogoliubov [59] is gapless. It has a linear dependence on the wave vector in the range of long wavelengths and a quadratic dependence in another range of spectrum. Similar results were obtained by Beliaev [67] as well as by Keldysh and Kozlov [58], who first proposed the theory of the BEC of Wannier-Mott excitons in the electrons-hole description.

The influence of the attractive Hartree terms will generate the gap in the energy spectrum of the exciton branches of the collective elementary excitations, which will be studied below. The influence of the ELLs and their stabilizing role in the theory of the BEC of magnetoexcitons with nonzero wave vector $\vec{k}$ quickly decreases with increasing kl. In the range of $kl \geq 0.5$, the Bose–Einstein condensate becomes unstable in the Hartree–Fock–Bogoliubov approximation [37]. Only in the range of $kl \sim 3-4$ does the ability to stabilize the condensate appear, taking into account the Anderson-type coherent excited states and the correlation energy calculated on this base. Under these conditions, a metastable dielectric liquid phase (MDLP) formed by Bose-Einstein condensed magnetoexcitons with kl ≈ 3-4 was found [35]. The collective elementary excitations under these conditions were investigated in [61].

In the case of $k=0$, the self-energy parts (22) contain only the coefficients linear in $U(P)$, or quadratic dependences of the types $U(Q)U(-Q)$ and $\tilde{W}(Q)U(-Q-P)$ which reflect the influence of the ELLs. The equations of motion for the exciton operators $d(P)$ and $d^{\dagger}(-P)$ are interconnected with equations of motion for the density operators $\rho(P)$ and $D(P)$. Instead of a set of two equations of motion, as in the case of the usual Bose gas corresponding to normal and abnormal Green's functions, we have a set of four equations of motion. Changing the center-of-mass wave vector of the magnetoexciton, for example, from 0 to $\vec{P}$, means changing its internal structure, because the internal distance between the Landau orbits of the quantized electron and hole becomes equal to $\left|\vec{P}\right| l^2$. The separated electrons and holes remaining in their Landau orbits can take part in the formation of magnetoexcitons as well as in collective plasma oscillations. These possibilities were not considered in the theory of structureless bosons or in the case of Wannier-Mott excitons with a rigid relative electron-hole motion structure without the possibility of the intra-series excitations. In the case of magnetoxcitons, their internal structure is much less rigid than in the case of Wannier-Mott excitons and the possibilities for electrons and holes to take part simultaneously in many processes are much more diverse. Instead of the branches of the energy spectrum corresponding to normal and abnormal Green's functions we have dealt simultaneously with four branches of the energy spectrum, the two supplementary branches being the optical plasmon branch represented by the operator $\rho(P)$ and the acoustical plasmon branch represented by the operator $D(P)$. One can see that the equations of motion for the operators $d(P)$ and $d^{\dagger}(-P)$ reflect the interaction of excitons with optical and acoustical plasmons but do not contain the direct interaction between themselves. The interaction with acoustical plasmons also takes place through the quasiaverage constant $\tilde{\eta}$.

The equation of motion for the acoustical plasmon operator $D(P)$ contains the interaction with optical plasmons and the direct interaction with the magnetoexcitons. The optical plasmon motion is more separated from the equations of motion of other partners. It does not contain the direct interconnection with exciton branches, and the dispersion equation for the optical plasmon will be separated from the dispersion equation of the other three partners. In spite of this, optical plasmon branches are also influenced by the ground state of the system formed by the Bose-Einstein condensed magnetoexcitons with $k=0$, because the self-energy part $\Sigma_{33}(\vec{P},\omega)$ also depends on averages (23). On the contrary, the equation of motion of the acoustical plasmon operator is closely interconnected with the equation of motion of the both exciton operators and its energy spectrum cannot be found out separately. Unlike the usual theory of a Bose gas, the interaction between the magnetoexciton branches is not direct, but indirect, being mediated by the direct interaction with the plasmons. These peculiarities make our case different from those considered earlier in [58, 59, 67].

The cumbersome dispersion equation is expressed in general form by the determinant equation

$$\det\left|\Sigma_{ij}(\vec{P},\omega)\right|=0 \tag{26}$$

Due to the structure of the self-energy parts (22) it separates into two independent equations. One of them concerns only the optical plasmon branch and has a simple form

$$\Sigma_{33}(\vec{P},\omega)=0 \tag{27}$$

It does not include at all the chemical potential $\bar{\mu}$ and the quasiaverage constant $\tilde{\eta}$. The second equation contains the self-energy parts Σ_{11}, Σ_{22}, Σ_{44}, Σ_{14}, Σ_{41}, Σ_{24}, and Σ_{42}, which include the both parameters $\bar{\mu}$ and $\tilde{\eta}$. The second equation has the form

$$\Sigma_{11}(\vec{P};\omega)\Sigma_{22}(\vec{P};\omega)\Sigma_{44}(\vec{P};\omega)-\Sigma_{41}(\vec{P};\omega)\Sigma_{22}(\vec{P};\omega)\Sigma_{14}(\vec{P};\omega)-\Sigma_{42}(\vec{P};\omega)\Sigma_{11}(\vec{P};\omega)\Sigma_{24}(\vec{P};\omega)=0 \tag{28}$$

The solution of the equation (27) is

$$\left(\hbar\omega(P)\right)^2=\frac{\langle D(P)D(-P)\rangle}{N^2}\sum_Q U(Q)\left(U(-Q)-U(Q-P)\right)Sin^2\left(\frac{[P\times Q]_z l^2}{2}\right) \tag{29}$$

The right hand side of this expression at small values of P has a dependence $\left|P\right|^4$ and tends to saturate at large values of P. The optical plasmon branch $\hbar\omega_{OP}(P)$ has a quadratic dispersion law in the long wavelength limit and saturation dependence in the range of short wavelengths. Its concentration dependence is of the type $\sqrt{\mathrm{v}^2(1-\mathrm{v}^2)}$ what coincides with the concentration dependences for 3D plasma $\omega_p^2=\frac{4\pi e^2 n_e}{\varepsilon_0 m}$ [64] and for 2D plasma $\omega_p^2(q)=\frac{2\pi e^2 n_s q}{\varepsilon_0 m}$ [68], where n_e and n_s are the corresponding electron densities. The supplementary factor $(1-\mathrm{v}^2)$ in our case reflects the Pauli exclusion principle and the vanishing of the plasma oscillations at $\nu=\mathrm{v}^2=1$. The obtained dispersion law is represented in Fig. 2. A similar dispersion law was obtained in the case of 2D electron-hole liquid (EHL) in a strong perpendicular magnetic field [69], when the influence of the quantum vortices created by electron and hole subsystems is compensated exactly. But the saturation dependences in these two cases are completely different. In the case of Bose-Einstein condensed magnetoexcitons, it is determined by the ELLs, whereas in the case of EHL [69] it is determined by the Coulomb interaction in the context of the LLLs.

The solutions of the dispersion equation (28) describe the exciton energy branch, the exciton quasienergy branch and the acoustical plasmon branch. The ideal magnetoexciton gas can exist only in the case $\mathrm{v}^2=0$, with an infinitesimal number of excitons, but without plasma. The real parts $\sigma_{ij}(\vec{P},\omega)$ of the self-energy parts $\Sigma_{ij}(\vec{P},\omega)$ are

$$\begin{aligned}
&\sigma_{11}(\vec{P},\omega)=\hbar\omega+\bar{\mu}-E(P)+\Delta(P); && \bar{\mu}+\Delta(0)=0;\\
&\sigma_{22}(\vec{P},\omega)=\hbar\omega-\bar{\mu}+E(P)-\Delta(-P); && \tilde{\eta}=0;\\
&\sigma_{33}(\vec{P},\omega)=\sigma_{44}(\vec{P},\omega)=\hbar\omega; && \Delta(P)\approx\Delta(0);
\end{aligned}\tag{30}$$

The excitation of magnetoexcitons means to transfer one of them from the ground state with energy $-I_l$ to the excited state $-I_l+E(P)$. For this reason the magnetoexciton excitation spectrum equals $\hbar\omega_{ex}(P)=\pm E(P)$, whereas the plasma oscillation frequency vanishes $\hbar\omega=0$. This ideal variant is represented in Fig. 3. In the case of a non-ideal Bose-gas with $\nu\neq 0$, the self-energy parts contain terms linear in $U(P)$ and a term quadratic in the interaction constant with unknown frequency in the denominators under the summation symbols. These terms increase the number of the solutions, but can also be taken into account by an iteration method. In this case, one can obtain corrections to the earlier solutions.

The first step in this procedure gives the real parts of the self-energy parts

$$\begin{aligned}
&\sigma_{11}(\vec{P},\omega)=\hbar\omega+\bar{\mu}-E(P)+\Delta(P);\\
&\sigma_{22}(\vec{P},\omega)=\hbar\omega-\bar{\mu}+E(-P)-\Delta(-P);\\
&\sigma_{41}(\vec{P},\omega)=-\tilde{\eta}+U(P)\frac{\langle d(0)\rangle}{\sqrt{N}};\\
&\sigma_{42}(\vec{P},\omega)=\tilde{\eta}-U(-P)\frac{\langle d(0)\rangle}{\sqrt{N}};\\
&\sigma_{14}(\vec{P},\omega)=-2\tilde{\eta};\quad \sigma_{24}(\vec{P},\omega)=2\tilde{\eta};\\
&\sigma_{44}(\vec{P},\omega)=\hbar\omega;
\end{aligned}\tag{31}$$

The dispersion laws for two exciton branches and the acoustical plasmon branch are

$$\begin{aligned}
&\hbar\omega=\pm\sqrt{\left(\bar{\mu}-E(\vec{P})+\Delta(0)\right)^2+4\tilde{\eta}\left(\tilde{\eta}-\frac{U(\vec{P})\langle d(0)\rangle}{\sqrt{N}}\right)}\\
&\hbar\omega_{AP}(P)=0
\end{aligned}\tag{32}$$

In [37] the coefficient $(B_{i-i}-2A_{i-i}+\Delta(0))/I_l$ was determined to be $0.05r$. The rate r is $r=I_l/\hbar\omega$. The main parameters $(\bar{\mu}+\Delta(0))$, $\tilde{\eta}$ and $\frac{U(0)\langle d(0)\rangle}{\sqrt{N}I_l}=2\frac{A_{i-i}u\mathrm{v}}{I_l}$ are

$$(\bar{\mu}+\Delta(0))=0.1r\mathrm{v}^2I_l;\ \tilde{\eta}=-0.1r\mathrm{v}^3I_l;\qquad \frac{U(0)\langle d(0)\rangle}{\sqrt{N}}=0.3ru\mathrm{v}I_l;\qquad u^2+\mathrm{v}^2=1 \tag{33}$$

Expression (32) was found as follows:

$$\frac{\hbar\omega}{I_l}=\pm\sqrt{\left(0.1r\mathrm{v}^2-\frac{E(P)}{I_l}\right)^2+0.4r\mathrm{v}^3\left(0.1r\mathrm{v}^3+0.3ru\mathrm{v}e^{-\frac{P^2l^2}{2}}\right)} \tag{34}$$

In the limit $P\to 0$ there is a gap in the energy spectrum

$$\hbar\omega_{ex}(0)=2\sqrt{|\tilde{\eta}|U(0)\frac{\langle d(0)\rangle}{\sqrt{N}}}=0.346r\mathrm{v}^2\sqrt{u}I_l \tag{35}$$

It depends on the Hartree term of the overall attractive interaction in the system proportional to $-U(P)$, with $U(P) > 0$, as well as on the quasiaverage theory parameter $\tilde{\eta}$ and on the amplitude of the condensate $\langle d(0) \rangle / \sqrt{N}$.

Unlike the case of a simple Bose gas with repulsive interactions, the collective excitations of the magnetoexcitons in a BEC with $k = 0$ need a finite amount of energy. The magnetoexciton subsystem is incompressible when only the excitons themselves are taken into account and compressible when the optical plasmon branch is excited. In this approximation, the acoustical plasmon branch vanishes.

The energy spectrum described by expressions (32) and (34) begins with a gap in the limit $P \to 0$ and has a roton-type behavior with a minimum in the point P_l, determined by the equality $E(P_1) = 0.1 r \mathrm{v}^2 I_l$ and the minimal value $\hbar\omega_{ex}(P_1) = I_l \sqrt{0.12 r^2 u \mathrm{v}^4 e^{-P_1 l^2/2}}$. After the minimum the dispersion law transforms gradually in the energy spectrum of a free magnetoexciton. It is represented in Fig. 4 for a specific value of the rate $r = 1/2$. This energy spectrum can be compared with another spectrum obtained by Girvin, MacDonald and Platzman [19] in the case of a two-dimensional one-component plasma (2DOCP) under the conditions of the FQHE. Both of them have the gaps, roton-type minima and saturation-type dependences at $P \to \infty$. We believe that the gaps are connected with the existence of the attractions in the systems.

In the case of the FQHE, the electrons have an attractive interaction with their correlation quasiholes formed by the many-fold vortices attached to each electron. As was mentioned by Lee and Zhang [25], if this interaction was neglected the energy spectrum could be gapless with quadratic dispersion law in the region $P \to 0$.

In the case of a coplanar 2D e-h system under the conditions of magnetoexciton formation, the attraction is created by the influence of the ELLs. The magnetoexcitons are embedded in the attractive bath with activation energy $U(0) = 2A_{i-i}$. The exchange Fock terms and partially the Bogoliubov *u-v* transformation terms give rise to a repulsive interaction. Taking into account the quadratic terms of the self-energy parts (22) proportional to the constants $U(Q)U(P-Q)$, $U(Q)\tilde{W}(P-Q)$ and containing the unknown value $\hbar\omega$ in the denominators increases the number of solutions, which in our case is doubled. Two branches of the exciton-type collective elementary excitations are drawn in Fig. 5 by solid lines. Here the dotted line shows also the main exciton-type energy branch. The lower dispersion curve in Fig. 5 coincides in fact with the main exciton branch designed in Fig. 4. The second branch in Fig. 5 is practically parallel to the lower energy branch, being shifted on the energy scale by the value $U(0)$. We believe that this branch describes the more complicated process in which the previous excitation with wave vector P is accompanied by the excitation of the a second magnetoexciton with $k = 0$ from the condensate in the bath, adding to it an activation energy $U(0)$ and transforming it into a free magnetoexciton with the same wave vector $k = 0$, but outside of the attractive bath. As a result of this double excitation, two magnetoexcitons from the condensate with $k = 0$ embedded in the attractive bath are transformed into an elementary excitation with wave vector $P \neq 0$ and another magnetoexciton with $k = 0$ but outside the bath. The supplementary energy needed for this is the activation energy $U(0) = 0.306 r I_l$.

The acoustical plasmon branch has a dispersion law completely different from the optical plasmon oscillations. It has an absolute instability beginning with small values of wave vector going on up to the considerable value $pl \approx 2$. In this range of wave vectors, the optical plasmons have energies which do not exceed the activation energy $U(0)$. It means that the optical plasmons containing the opposite-phase oscillations of the electron and hole subsystems without displacement as a whole of their center of mass are allowed in the context of the attractive bath. On the other hand, the in-phase oscillations of the electron and hole subsystems in the composition of the acoustical plasmons are related to the displacements of their center of mass. Such displacements can take place only if their energy exceeds the activation energy $U(P)$. As a result, the acoustical plasmon branch has an imaginary part represented by the dashed line and is completely unstable in the region of wave vectors $pl \leq 2$. At greater values $pl > 2$ the energy spectrum is real and nonzero, approaching to the energy spectrum of the optical plasmons. The influence of the attractive bath $U(P)$ is represented by the dotted line. It vanishes in the limit $p \to \infty$. These properties of the acoustical plasmon branch are reflected in Fig. 6.

The starting Hamiltonian (10) has two continuous symmetries. One is the gauge global symmetry U(1) and another one is the rotational symmetry SO(2). The resultant symmetry is U(1)×SO(2). The gauge symmetry is generated by the operator N of the full particle number, when it commutes with the Hamiltonian. It means that the Hamiltonian is invariant under the unitary transformation $U(\varphi)$ as follows

$$U(\varphi)HU^{-1}(\varphi) = H; \quad U(\varphi) = e^{iN\varphi}; \quad \left[H, N\right] = 0 \tag{36}$$

The operator $\hat{N}$ is named as symmetry generator. The rotational symmetry SO(2) is generated by the rotation operator $\hat{C}_z(\varphi)$ which rotates the in-plane wave vectors $\vec{Q}$ on the arbitrary angle φ around z axis, which is perpendicular to the layer plane and is parallel to the external magnetic field. Coefficients $W_{\vec{Q}}$, $U(\vec{Q})$, $V(\vec{Q})$ in formulas (6) and (9) depend on the square wave vector $\vec{Q}$ which is invariant under the rotations $\hat{C}_z(\varphi)$. This fact determines the symmetry SO(2) of the Hamiltonian (10). The gauge symmetry of Hamiltonian (10) after the phase transition to the Bose-Einstein condensation (BEC) state is broken as it follows from expression (16). In the frame of the Bogoliubov theory of quasiaverages it contains a supplementary term proportional to η. The gauge symmetry is broken because this term does not commute with the operator N. More so, this term is not invariant under the rotations $C_z(\varphi)$, because the in-plane wave vector $\vec{k}$ of the BEC is transformed into another wave vector rotated by the angle φ in comparison with the initial position. The second continuous symmetry is also broken. In such a way the installation of the Bose-Einstein condensation state with arbitrary in-plane wave vector $\vec{k}$ leads to the spontaneous breaking of the both continuous symmetries. We will discuss the more general case of $\vec{k} \neq 0$ considering the case of $\vec{k} = 0$ as a limit $\vec{k} \to 0$ of the cases with small values $\vec{kl}$<<1. One can remember that the supplementary terms in Hamiltonian (10) describing the influence of the ELLs are actual in the range of small values $\vec{kl}$ <0.5. Above, we established that the number of the broken generators (BGs) denoted as N_{BG} equals to two ($N_{BG} = 2$).

The Goldstone theorem [70] states that the breaking of the continuous symmetry of the system leads to the appearance in the energy spectrum of the collective elementary excitations of the gapless branch equivalent to the massless particle in the relativistic physics. It occurs because the system with continuous symmetry has initially a set of the degenerate minimal values of the potential energy leading to a set of degenerate vacuum states. For example, the dependence of the potential energy on the order parameter may be Mexican hat like. The selection of one single vacuum state among the manifold of vacua and the fixing of the order parameter phase takes place due to quantum fluctuations and breaks spontaneously the continuous symmetry. The excitations over the selected vacuum transferring the system to the adjacent vacua and changing only the phase of the order parameter without change of its absolute value does not need any energy in the long wavelengths limit. Just these circumstances lead to the appearance of the gapless dispersion laws. These branches of the collective elementary excitations are named as the Nambu-Goldstone (NG) modes [70, 71]. They are of two types. One of them, of the first-type has a linear (or odd) dispersion law in the range of the small wave vectors, whereas the second-type has a quadratic (or even) dependence on the wave vector in the same region. The number of the NG modes in the system with many broken continuous symmetries was determined by the Nielsen and Chadha [72] theorem. It states that the number of the first-type NG modes N_I being accounted once and the number of the second type NG modes N_{II} being accounted twice equals or prevails the number of broken generators N_{BG}. It looks as follows $N_I + 2N_{II} \geq N_{BG}$. In our case the optical plasmon branch has the properties of the second-type NG modes. We have $N_I = 0$; $N_{II} = 1$ and $N_{BG} = 2$. It leads to the equality $2N_{II} = N_{BG}$. The Goldstone theorem guarantees that the NG modes do not acquire mass at any order of quantum corrections. Nevertheless, sometimes soft modes appear, which are massless in the zeroth order, but become massive due to quantum corrections. They were introduced by Weinberg [73], who has shown that these modes emerge if the symmetry of an effective potential of zeroth order is higher than that of the gauge symmetry. Following [74], these modes are currently named as the quasi-Nambu-Goldstone modes, in spite of the fact that their initial name proposed by Weinberg was pseudo-NG modes. Georgi and Pais [75] demonstrated that the quasi-NG modes also occur in the cases in which the symmetry of the ground state is higher than that of the Hamiltonian.

The authors of [74] underlined that the spinor BEC are ideal systems to study the physics of the quasi-Nambu-Goldstone(NG) modes, because these systems have a great experimental manipulability and well established microscopic Hamiltonian. In [74], it was shown that the quasi-NG modes appear in a spin-2 nematic phase. The ground state symmetry of the nematic phase at zeroth order approximation is broken by quantum corrections, thereby making the quasi-NG modes massive. The number n of the quasi-NG modes was determined by Georgi and Pais [75] in the form of a theorem. It was explaned and represented in [74] as follows:

$$n = \dim(\tilde{M}) - \dim(M) \tag{37}$$

where $\tilde{M}$ is the surface on which the effective potential assumes its minimal values to the zeroth order and $\dim(\tilde{M})$ is the dimension of this surface. The dimension $\dim(M)$ determines the number of the NG modes. This implies that M is a submanifold of $\tilde{M}$ and n is the dimension of the complementary space of M inside $\tilde{M}$ [74]. Returning to the case of 2D magnetoexcitons in the BEC state with wave vector $\vec{k}$ different from zero described by Hamiltonian (16), one can remember that both continuous symmetries existing in the initial form (10) are lost. It occurs because of the presence of the term $\tilde{\eta}(d^{\dagger}_{\vec{k}} + d_{\vec{k}})$ in the frame of the Bogoliubov theory of quasiaverages. Nevertheless, the energy of the ground state, as well as the self-energy parts $\Sigma_{ij}(P,\omega)$, which determine the energy spectrum of the collective elementary excitations, depends only on the modulus of the wave vector k and does not depend at all on its direction. All these expressions have a rotational symmetry SO(2), in spite of the fact that

Hamiltonian (16) has lost it. On our mind we have the condition described by Georgi and Pais [75] favoring the emergence of the quasi-NG modes. We are explaining the existence of the gapped, massive exciton-type branches of the collective elementary excitations obtained in our calculations just by these considerations.

We now discuss the damping rates of the obtained solutions and other possibilities related with the existence of the quantum vortices as a result of possible quantum fluctuations.

The damping rates of the obtained energy branches are determined by the imaginary parts of the self-energy parts

$$\Sigma_{ij}(\vec{P},\omega)=\sigma_{ij}(\vec{P},\omega)+i\Gamma_{ij}(\vec{P},\omega) \tag{38}$$

In the case of diagonal self-energy parts they are

$$\begin{aligned}&\Gamma_{11}(\vec{P},\omega)=\Gamma_{22}(-\vec{P},-\omega)=\\&=\frac{\langle D(P)D(-P)\rangle}{N^2}\pi\sum_Q U^2(Q)Cos^2\left(\frac{[P\times Q]_z l^2}{2}\right)\delta\left(\hbar\omega+\bar{\mu}-E(P-Q)+\Delta(P-Q)\right); \quad (39)\\&\Gamma_{33}(\vec{P},\omega)=\Gamma_{44}(\vec{P},\omega)=0\end{aligned}$$

The damping rates $\Gamma_{11}(\vec{P},\omega)$ and $\Gamma_{22}(\vec{P},\omega)$ are nonzero in complementary regions of the frequencies and wave vectors and can be calculated using the zero order dependences $\omega_{ex}(P)$ represented in Fig. 3 without taking into account the fine details revealed in Fig. 4.

The absolute values of the damping rates are drown in Fig. 7. They are smaller than the corresponding real parts represented in Fig. 4, which means that the obtained results have a physical sense. The damping rate of the optical plasmon branch in our description equals zero.

But there are also other possibilities in addition to equations of motion (22). They are related with the noncommutativity of the density operators $\rho(P)$ and $\rho(Q)$. This is given by

$$\rho(\vec{P}-\vec{Q})\rho(\vec{Q})=\rho(\vec{Q})\rho(\vec{P}-\vec{Q})+2iSin\left(\frac{[\vec{P}\times\vec{Q}]_z l^2}{2}\right)\rho(\vec{P}) \tag{40}$$

and permits us to rewrite the nonlinear term into another form selecting a linear term as follows:

$$\begin{aligned}&-i\sum_Q W(Q)Sin\left(\frac{[P\times Q]_z l^2}{2}\right)\left[\rho(P-Q)\rho(Q)+\rho(Q)\rho(P-Q)\right]=\\&=\frac{1}{m}E(P)\rho(P)-i\sum_Q W(Q)Sin\left(\frac{[P\times Q]_z l^2}{2}\right)\times\\&\times\left[\left(1-\frac{1}{m}\right)\rho(P-Q)\rho(Q)+\left(1+\frac{1}{m}\right)\rho(Q)\rho(P-Q)\right]; \quad (41)\\&E(P)=2\sum_Q W(Q)Sin^2\left(\frac{[P\times Q]_z l^2}{2}\right);\\&m=\pm1;\pm2;\pm3... \quad 0<|\nu|=\frac{1}{|m|}\le 1\end{aligned}$$

Variant (22) corresponds to $m\to\infty$ and $\nu<1$. Adopting variant (41) we could use the zero-order Green's function with proper energy $E(p)/m$. We believe that this value is of the same type as the interaction energy of one electron with one vortex from the composition of the m-fold vortex attached to the electron. Although the influence of the vortices created by electrons and holes is compensated in the mean-field approximation, they can appear in the form of quantum fluctuations. Instead of the plasmon-type spectrum with the square frequency proportional to the electron-hole concentration we will obtain another type dependence reflecting the existence of vortices in the form of quantum fluctuations. The energy spectrum and the damping rates would be different from our results discussed above, but can be obtained exactly in the same way. Similar possibilities appear for the exciton-type operators. The assembly of new composite states arises.

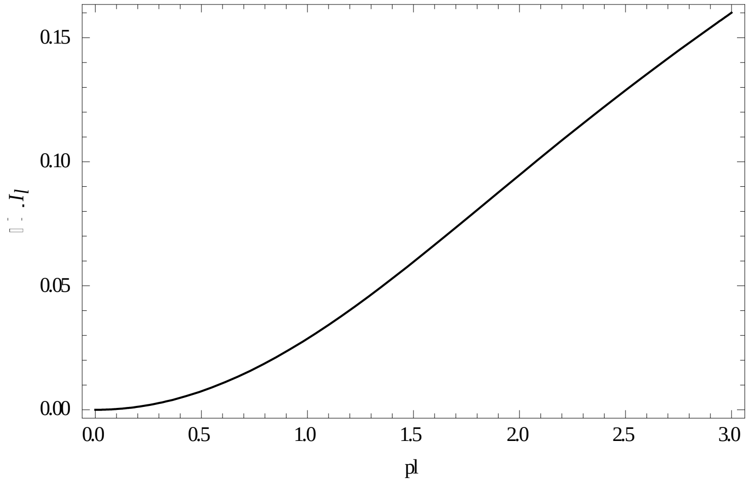

Fig. 2. The energy spectrum of the optical plasmon branch in the system of Bose-Einstein condensed magnetoexcitons with wave vector $\vec{k} = 0$, filling factor $\nu = \mathrm{v}^2 = 0.1$, under the influence of excited Landau levels with parameter $r = 1/2$.

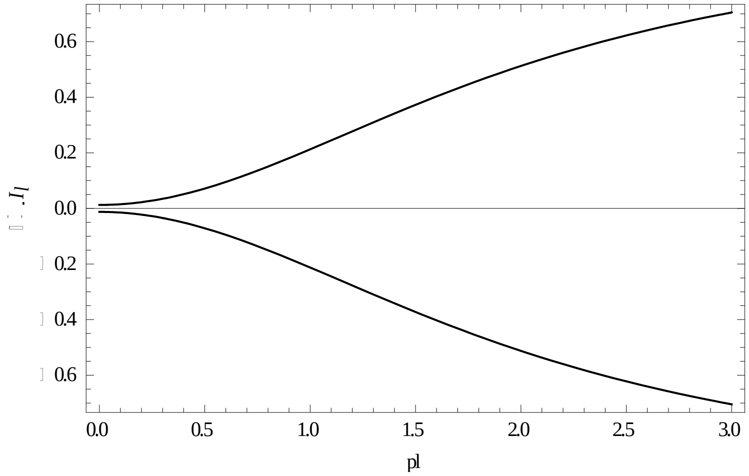

Fig. 3. The energy spectrum of the exciton branches in the case of an ideal BEC of magnetoexcitons with $\vec{k} = 0$ and filling factor equal to zero.

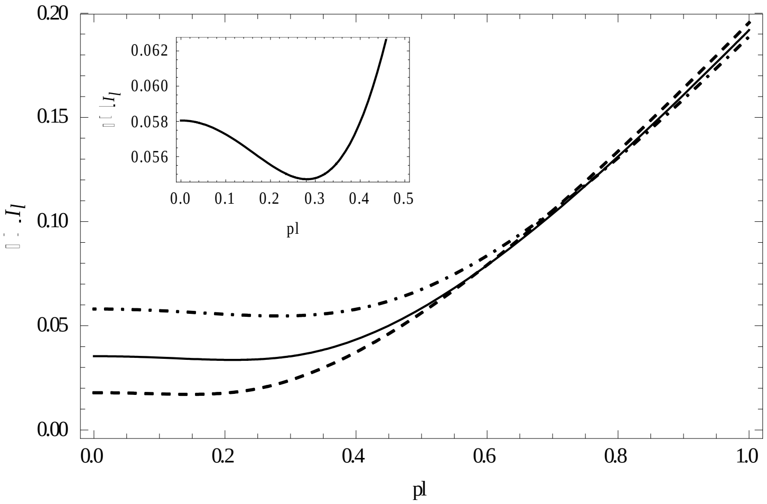

Fig. 4. The energy spectrum of the exciton branches in the case of a BEC of magnetoexcitons with $\vec{k}=0$ under influence of ELLs with parameter $r=1/2$, without activation processes. The solid line corresponds to the energy spectrum with filling factor $\nu = \mathrm{v}^2 = 1/5$, the dashed line corresponds to the filling factor $\nu = \mathrm{v}^2 = 1/10$, and the dot-dashed line to $\nu = \mathrm{v}^2 = 1/3$.

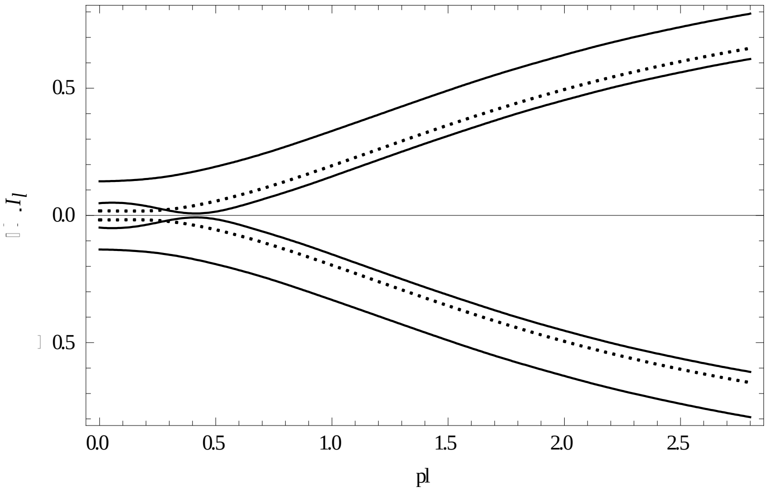

Fig. 5. The energy spectrum of the exciton branches in the case of a BEC of magnetoexcitons with $\vec{k}=0$ and filling factor $\nu = \mathrm{v}^2 = 0.1$ under the influence of ELLs with parameter $r=1/2$, taking into account the supplementary activation of the condensed magnetoexcitons and the formation of the second exciton branch. The dotted line represents the solution of Fig. 3.

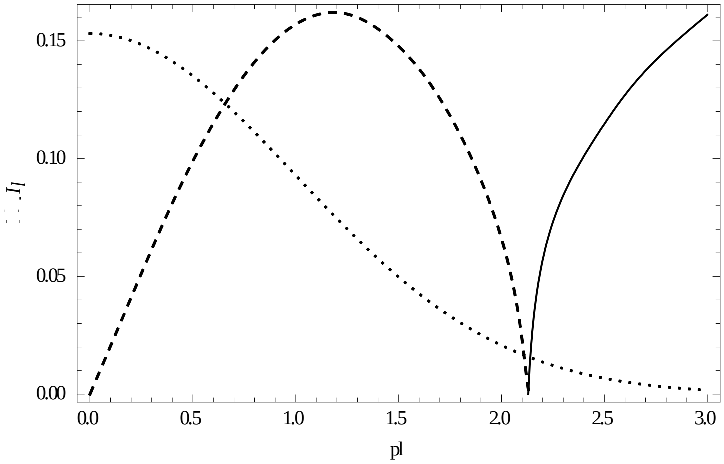

Fig. 6. The dispersion law of the acoustical plasmon branch. The solid line represents the real part, and the dashed line corresponds to the imaginary part. The dotted line gives the value $U(P)$.

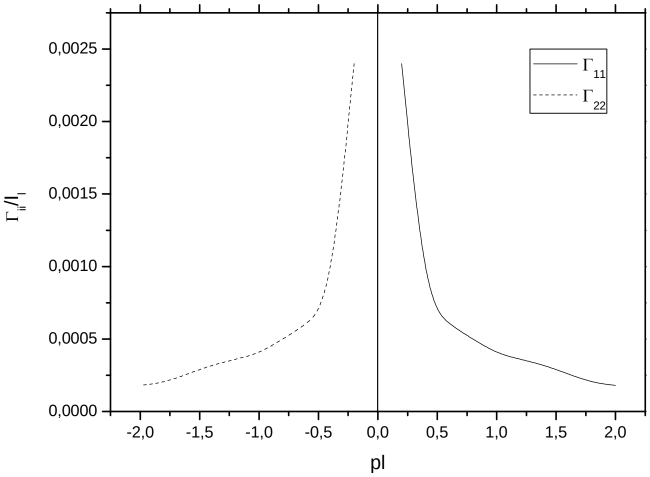

Fig. 7. The damping rates $\Gamma_{11}(\vec{P},\omega)$ and $\Gamma_{22}(\vec{P},\omega)$ of the diagonal self-energy parts.

6. Conclusions

The energy spectrum of the collective elementary excitations of a 2D electron-hole (e-h) system in a strong perpendicular magnetic field in a state of Bose-Einstein condensation (BEC) with wave vector $\vec{k}=0$ has been investigated in the framework of Bogoliubov theory of quasiaverages. The starting Hamiltonian describing the e-h system contains not only the Coulomb interaction between the particles lying on the lowest Landau levels, but also a supplementary interaction due to their virtual quantum transitions from the LLLs to the excited Landau levels and back. This supplementary interaction generates, after the averaging on the ground state BCS-type wave function, direct Hartree-type terms with an attractive character, exchange Fock-type terms giving rise to repulsion, and similar terms arising after the Bogoliubov u-v transformation. The interplay of these three parameters gives rise to the resulting nonzero interaction between the magnetoexcitons with wave vector $\vec{k} = 0$ and to stability of their BEC.

The equations of motion for the exciton operators $d(P)$ and $d^{\dagger}(P)$ are interconnected with equations of motion for the density operators $\rho(P)$ and $D(P)$. Instead of a set of two equations of motion as in the case of usual Bose gas, corresponding to normal and abnormal Green's functions, we have a set of four equations of motion. The change of the center-of-mass wave vector of the magnetoexciton, for example from 0 to $\vec{P}$, means the change of its internal structure because the internal distance between the Landau orbits of the quantized electron and hole becomes equal to $\left|\vec{P}\right| l^2$.

The separated electrons and holes remaining on their Landau orbits can take part in the formation of magnetoexcitons as well as in collective plasma oscillations. These possibilities were not taken into consideration in the theory of structureless bosons or in the case of Wannier-Mott excitons with a rigid relative electron-hole motion structure without the possibility of the intra-series excitations. Magnetoexcitons have an internal structure that is much less rigid than standard Wannier-Mott excitons and the possibilities for electrons and holes to take part simultaneously in many processes are much more diverse. Instead of the branches of the energy spectrum corresponding to normal and abnormal Green's functions, we have to deal simultaneously with four branches of the energy spectrum, the two supplementary branches being the optical plasmon branch represented by the operator $\rho(P)$ and the acoustical plasmon branch represented by the operator $D(P)$.

The energy spectrum of the collective elementary excitations consists of four branches. Two of them are excitonic-type branches, one of them being the usual energy branch whereas the second one is the quasienergy branch representing the mirror reflection of the energy branch. The other two branches are the optical and acoustical plasmon branches. The exciton energy branch has an energy gap due to the attractive interaction terms, which needs to be overcome for excitation, as well as a roton-type region in the range of intermediary values of the wave vectors. At higher values of wave vector, its dispersion law tends to saturation. The optical plasmon dispersion law is gapless with quadratic dependence in the range of small wave vectors and with saturation-type dependence in the remaining part of the spectrum. The acoustical plasmon branch reveals an absolute instability of the spectrum in the range of small and intermediary values of the wave vectors. In the remaining range of the wave vectors, the acoustical plasmon branch has a real value of the energy spectrum approaching the energy spectrum of the optical plasmon branch in the limiting case of great wave vectors.

Acknowledgments

This work was supported in part by the Department of Energy under Grant DE-FG02-99ER45780. S.A.M. thanks V.A.Moskalenko and I.V.Podlesny for useful discussions. E.V.D. thanks the Foundation for Young Scientists of the Academy of Sciences of Moldova for financial support (11.819.05.13F).

References

[1] The Quantum Hall Effect, Edited by E.Prange and S.M.Girvin, Springer-Verlag, New York, pp. 419, (1986)

[2] S. Das Sarma, and A. Pinczuk, Perspectives in Quantum Hall Effects, John Wiley & Sons, Inc., New York, 430 p., (1997)

[3] H.L.Stormer, Rev. Mod. Phys. 71, 875-889 (1999)

[4] H.Enger "Vortices in Chern-Simons-Ginzburg-Landau Theory and the fractional quantum Hall effect", Thesis submitted to the degree of Candidatus Scientiarum Department of Physics, University of Oslo, September 1998

[5] E.I.Rashba, Pure Appl. Chem. 67, 409, (1995).

[6] D.C.Tsui, H.L.Stormer, and A.C.Gossard, Phys. Rev. Lett. 48, 1559, (1982).

[7] R.B.Laughlin, Phys. Rev. Lett. 50, 1395, (1983).

[8] A.H.MacDonald, E.H.Rezayi, and D.Keller, Phys. Rev. Lett. 68, 1939, (1992)

[9] F.Wilczek, Phys. Rev. Lett., 48, 1144, (1982); 49, 957, (1982)

[10] J.K.Jain, Composite Fermions, Cambridge University Press, Cambridge, (2007)

[11] N.Read, Phys. Rev. Lett., 62, 86, (1989)

[12] N.Read, Semicond. Sci. Techn., 9, 1859, (1994)

[13] N.Read, arxiv. Cond-mat (9501090V), 19 Jan., (1995)

[14] N.Read, Phys. Rev. B, 58, 16262, (1998)

[15] B.L.Halperin, P.A.Lee, and N.Read, Phys. Rev. B, 47, 7312, (1993)

[16] S.M.Girvin, The Quantum Hall Effect: Novel Excitations and Broken-Symmetries. Indiana University, USA, Chapters 9 and 10 in Ref 1, (1998)

[17] S.M.Girvin and A.H.MacDonald, Phys. Rev. Lett., 58, 1252, (1987)

[18] S.C.Zhang, T.H.Hanson, and S.Kivelson, Phys. Rev. Lett., 62, 82, (1989)

[19] S.M.Girvin, A.H.MacDonald, and P.M.Platzman, Phys. Rev. Lett., 54, 581, (1985); Phys. Rev. B, 33, 2481, (1986)

[20] R.B.Laughlin, Rev. Mod. Phys., 71, 863, (1999)

[21] S.Kivelson, C.Kallin, D.P.Arovas, and J.Schrieffer, Phys. Rev. Lett., 56, 873, (1986)

[22] D.H.Lee, G. Baskaran, and S.Kivelson, Phys. Rev. Lett., 59, 2467, (1987)

[23] R.B.Laughlin, Phys. Rev. Lett., 60, 2677, (1988)

[24] S.S.Chern and J.Simons, Pro. Nat. Acad. Sci., 68, 791, (1971)

[25] D.H.Lee and S.C.Zhang, Phys. Rev. Lett., 66, 1220, (1991)

[26] C.Kallin and B.I.Halperin, Phys. Rev. B, 30, 5655, (1984)

[27] R.Jackiw and So Young Pi, Phys. Rev. D, 42, 3500, (1990)

[28] L.K.Myklebust, Quantized vortices, cand. Scient. Thesis, University of Oslo, (1996)

[29] I.V.Lerner and Yu.E.Lozovik, Zh. Eksp. Teor. Fiz. 78, 1167, (1980)

[30] I.V.Lerner and Yn.E.Lozovik, J. Low Temper. Phys. 38, 333, (1980)

[31] I.V.Lerner and Yn.E.Lozovik, Zh. Eksp. Teor. Fiz. 80, 1488, (1981) [Sov.Phys.-JETP 53, 763, (1981)].

[32] A.B.Dzyubenko and Yn.E.Lozovik, Fiz. Tverd. Tela (Leningrad) 25, 1519, (1983); 26, 1540, (1984) [Sov. Phys. Solid State 25, 874, (1983); 26, 938, (1984)]; J. Phys. A, 24, 415, (1991)

[33] D.Paquet, T.M.Rice, and K.Ueda, Phys. Rev. B, 32, 5208, (1985);

[34] T.M.Rice, D.Paquet and K.Ueda, Helv. Phys. Acta, 58, 410, (1985).

[35] S.A.Moskalenko, M.A.Liberman, D.W.Snoke, and V. Botan, Phys. Rev. B, 66, 245316, (2002)

[36] S.A.Moskalenko, M.A.Liberman, D.W.Snoke, V.Botan, and B. Johansson, Physica E, 19, 278, (2003); V.Botan, M.A.Liberman, S.A.Moskalenko, D.W.Snoke, and B.Johansson, Physica B, 346-347 **C**, 460, (2004)

[37] S.A.Moskalenko, M.A.Liberman, P.I.Khadzhi, E.V.Dumanov, Ig.V.Podlesny, and V.Botan, Sol. State Comm., 140/5, 236, (2006); S.A.Moskalenko, M.A.Liberman, P.I.Khadzhi, E.V.Dumanov, Ig.V.Podlesny, and V.Botan, Physica E, 39/1, 137-149, (2007)

[38] I.B.Spielman, J.P.Eisenstein, L.N.Pfeiffer, and K.W.West, PRL, 84, 5808, (2000)

[39] Min Hongki, Ra.Bistritzer, Su Jung-Jung, and A.H.MacDonald, PRB, 78, 121401(R), (2008)

[40] A.D.K.Finck, J.P.Eisenstein, L.N.Pfeiffer, and K.W.West, PRL, 104, 016801, (2010)

[41] Ya.S.Barlas, R.Cote, J.Lambert, and A.H.MacDonald, PRL, 104, 096802, (2010)

[42] P.Giudici, K.Muraki, N.Kumada, and T.Fujisawa, PRL, 104, 056802, (2010)

[43] D.Basu, L.F.Register, A.H.MacDonald, and S.K.Banerjee, PRB, 84, 035449, (2011)

[44] Z.Vörös, R.Balili, D.W.Snoke, L.Pfeiffer, and K.West, Phys. Rev. Lett. 94, 226401 (2005)

[45] Z.Vörös, D.W.Snoke, L.Pfeiffer, and K.West, Phys. Rev. Lett. 97, 016803 (2006)

[46] Z.Vörös and D.W.Snoke, Phys. Rev. Lett. 103, 016403 (2009)

[47] S.Denev, V.Negoita, an`d D.W.Snoke, B.Laikhtman, K.Eberl, and L.Pfeiffer, Phys. Rev. B 66, 205304 (2002)

[48] M.Stern, V.Garmider, V.Umansky, and I.Bar-Joseph, Phys. Rev. Lett. 100**,** 256402 (2008)

[49] D.Semkat, F.Richter, D.Kremp, G.Manzke, W.-D.Kraeft, and K.Henneberger, Phys. Rev. B 80, 155201 (2009).

[50] D.W.Snoke, Solid State Com. 146, 73, (2008).

[51] V.Negoita, D.W.Snoke, and K.Eberl, Solid State Com. 113, 437 (2000).

[52] N.W.Sinclair, J.K.Wuenschell, Z.Vörös, B.Nelsen, D.W.Snoke, M.H.Szymanska, A.Chin, J.Keeling, L.N.Pfeiffer, and K.W.West, Phys. Rev. B 83, 245304 (2011)

[53] V.Negoita, D.W.Snoke, and K.Eberl, Appl. Phys. Lett. 75, 2059 (1999)

[54] D.W. Snoke, The book chapter ”*Dipole excitons in coupled quantum wells*” (in progress)

[55] M.Combescot, O.Betbeder-Matibet, and R.Combescot, Phys. Rev. Lett. 99, 176403, (2007); M.Combescot and M.N.Leuenberger, Solid State Com. 149, 13, (2009)

[56] T.Hakioglu and M.Sahin, Phys.Rev.Lett. 98, 166405, (2007)

[57] M.A.Can and T.Hakioglu, Phys.Rev.Lett. 103, 086404, (2009)

[58] L.V.Keldysh, and A.N.Kozlov, Zh. Eksp. Teor. Fiz. 54, 978 (1968) [Sov.Phys. JETP 27, 52 (1968)].

[59] N.N. Bogoliubov, Selected works, vol 1, 2 (New-York: Gordon and Breach Sci. Publ., 1990)

[60] S.A.Moskalenko, M.A.Liberman, E.V.Dumanov, S.S.Rusu, and I. Sanduleac, Mold. J. Phys. Sci. 9, 16, (2010)

[61] S.A.Moskalenko, M.A.Liberman, E.V.Dumanov, J. Nanoelectron. Optoelectron. 4, 52 (2009)

[62] A.A.Abrikosov, L.P.Gor’kov, and I.E.Dzyaloshinskii, Methods of quantum field theory in statistical physics (Dover, New York, 1975) 444 p.

[63] D.N.Zubarev, Sov. Phys. Uspekhi Fiz. Nauk 71, 71 (1960)

[64] D.Pines, Elementary excitations in solids (Benjamin, New York, 1963)

[65] T.M.Rice, Solid State Physics (H.Ehrenreich, F.Seitz, D.Turnbull, eds., Academic, New York, 1977) p.32

[66] S.A.Moskalenko and D.W.Snoke, Bose-Einstein condensation of excitons and biexcitons and coherent nonlinear optics with excitons (Cambridge University Press, Cambridge UK, New York USA, 2000) 415 p.

[67] S.T.Beliaev, Zh.Eksp.Teor.Fiz. 34, 417, 433 (1958) [Sov. Phys. JETP **7**, 299 (1958)]

[68] S.Das Sarma and A.Madhukar, Phys. Rev. B 23, 805 (1981)

[69] S.A.Moskalenko, M.A.Liberman, E.V.Dumanov, A.G.Stefan, and M.I. Shmiglyuk, J.Phys.: Condens. Matter 21, 235801 (2009)

[70] J.Goldstone, Nuovo Cimento 19**,** 154 (1961)
[71] Y.Nambu, Phys.Rev. 117**,** 648 (1960); Phys. Rev. Lett. 4**,** 380 (1960)
[72] H.B.Nielsen and Chadha, Nucl.Phys. B 105**,** 445 (1976)
[73] S.Weinberg, Phys. Rev. Lett. 29**,** 1698 (1972)
[74] S.Uchino, M. Kobayashi, N. Nitta, and M. Ueda, Phys. Rev. Lett. 105**,** 230406 (2010)
[75] H.Georgi and A. Pais, Phys. Rev. D 12**,** 508 (1975)

EFFECTS OF COMPLEXING AGENTS ON CHEMICALLY DEPOSITED $Mg_{1-X}N_XS$ THIN FILMS

I. E. Ottih[1] and A. J. Ekpunobi[2]

[1]*Department of Industrial Physics, Anambra State University, Uli, Nigeria*
[2]*Department of physics and Industrial physics, Nnamdi Azikiwe University Awka, Nigeria*
E-mail: Ifyottih@yahoo.com

(Received 5 June 2012)

Abstract

Thin films of magnesium nickel sulphide (MgNiS) were grown on glass substrates using the chemical bath deposition (CBD) technique at room temperature. Effects of volumes of the complexing agent on the optical properties of the films were studied by depositing MgNiS thin films under different volumes of ammonia. The optical properties of the deposited films were investigated by measuring the optical absorbance of the films and the normal incident of light in a range of 200–1000 nm using a Janway 6405 UV–VIS spectrophotometer. Other properties, such as transmittance, reflectance, and energy gap, were calculated from the absorbance values. The low reflectance and large band gap make the films good materials for anti reflection coatings and absorber layers of solar cells, respectively.

1. Introduction

The energy needs of most countries have been met by non-renewable energy resources, such as petroleum. Recently, the cost of these non-renewable energy resources has increased. As a result, emphasis is shifted to renewable energy. The major problem with renewable energy is that the conversion efficiency has been so low. Scientists grow thin films to find which of them can help to increase this conversion efficiency.

An MgNiS thin film is one of the ternary chalcogenide films. These films have been investigated for specific applications in super ionic conducting materials [1, 2]. Ternary alloy compounds are increasingly being studied for efficient solar energy conversion through photoelectrochemical solar cell [3], and have become potential candidates for these applications [4]. A number of thin film deposition techniques of advanced technologies have been employed in the preparation of ternary thin films. However, a low-cost and less sophisticated chemical bath deposition (CBD) technique seems to be much better [5]. The CBD technique produces good quality film [6, 7]. This method has been applied in producing the emerging materials for solar cells, protective coatings, and solar thermal control in buildings and is being adopted by some industries [8, 9]. The CBD technique is convenient for producing large area devices, and there is possibility to control film thickness by adjusting the growth parameter [10, 11]. Polycrystalline grown MgNiS thin films are semiconducting materials with direct band gap transition. This research reports the effects of varied volumes of the complexing agent on the optical properties of the grown films. The possible applications of the films were discovered from their properties. The studied optical properties include the absorbance (A), transmittance (T) reflectance (R), thickness (T), and band gap energy of the films. These properties were determined from the equations found in the literature [12].

2. Materials and method

The preparation of MgNiS thin films on glass slides were carried out using the CBD technique. The glass slides were previously degreased in hydrochloric acid for 24 h, washed with a detergent, rinsed in distilled water, and dried in air. The acid treatment caused the oxidation of halide ions in glass slides used as a substrate thereby introducing functional groups called nucleation and epitaxial centers on which the thin films were grafted. The degreased cleaned surfaces have the advantage of providing nucleation centers for film growth and hence yield highly adhesive and uniformly deposited films.

The reaction bath for the deposition of MgNiS contained 10 ml of 1.0M of $MgCl_2$, 10 ml of 1.0M of $SC(NH_2)_2$, 10 ml of 1.0 M of $NiCl_2$, and 10 ml of 14.0 M of ammonia. Fifty milliliters of distilled water was added to make up 90 ml in a 100-ml beaker. The ammonia solution was used for dual purposes: as a complexing agent and as an alkaline medium for the growth. The function of the complexing agent is to slow down the reaction in order to eliminate spontaneous precipitation. The equations for the reaction and deposition of MgNiS are as follows:

$$MgCl_2 + 3NH_4 \leftrightarrow [Mg\,(NH_3)_4]^{2+} + 2Cl^-$$

$$[Mg\,(NH_3)_4]^{2+} \leftrightarrow Mg^{2+} + 3NH_4$$

$$NiCl_2 + 3NH_4 \leftrightarrow [Ni\,(NH_3)_4]^{2+} + 2Cl^-$$

$$[Ni\,(NH_3)_4]^{2+} \leftrightarrow Ni^{2+} + 3NH_4$$

$$SC(NH_2)_2 + OH^- \leftrightarrow CH_2N_2 + H_2O + HS$$

$$HS^- + OH^- \leftrightarrow H_2O + S^{2-}$$

$$Mg^{2+} + Ni^{2+} + S^{2-} \leftrightarrow MgNiS\downarrow$$

The sulphide ions are released by the hydrolysis of thiourea, but Mg^{2+} and Ni^{2+} ions are from complexes which the solution of $MgCl_2$ and $NiCl_2$ forms with NH_3. Mg^{2+}, Ni^{2+}, and S^{2-} that are present in the solution combine to form MgNiS molecules, which are adsorbed on the glass rod. The heterogeneous nucleation and growth take place by ionic exchange of reactive S^{2-} ions. This process is referred to as ion by ion process; in this way, MgNiS films were deposited on glass slides as uniform and adherent thin films. Five depositions were made with five different values of varied volumes of the complexing agent shown in Table 1 below and labeled as $E_6 - E_{10}$. For each deposition, the glass slide, which was mounted on the beaker with the synthetic material, was taken out of the beaker, rinsed with distilled water, and allowed to dry in air. The grown films were characterized for optical absorbance using a Janway 6405 UV–VIS spectrophotometer. Other properties, such as film transmittance, reflectance, thickness, and band gap energy were determined from the obtained absorbance values. The compositions of the films were studied through an energy dispersive X-ray fluoresce [EDXF] technique.

Table 1. Preparation of MgNiS thin films with varied volumes of ammonia

Slide no.	Vol. of $MgCl_2$ (ml)	Conc. $MgCl_2$ (M)	Vol. $NiCl_2$ (ml)	Conc. $NiCl_2$ (M)	Vol. of NH_3 Solution (ml)	Vol. of $SC(NH_2)_2$ (ml)	Conc. $SC(NH_2)_2$ (M)	Vol. of Distilled H_2O (ml)	Dip. Time (h)
E_6	10.0	1.0	10.0	1.0	5.00	10.0	1.0	50.0	12.0
E_7	10.0	1.0	10.0	1.0	7.50	10.0	1.0	50.0	12.0
E_8	10.0	1.0	10.0	1.0	10.00	10.0	1.0	50.0	12.0
E_9	10.0	1.0	10.0	1.0	12.50	10.0	1.0	50.0	12.0
E_{10}	10.0	1.0	10.0	1.0	15.00	10.0	1.0	50.0	12.0

3. Results and discussion

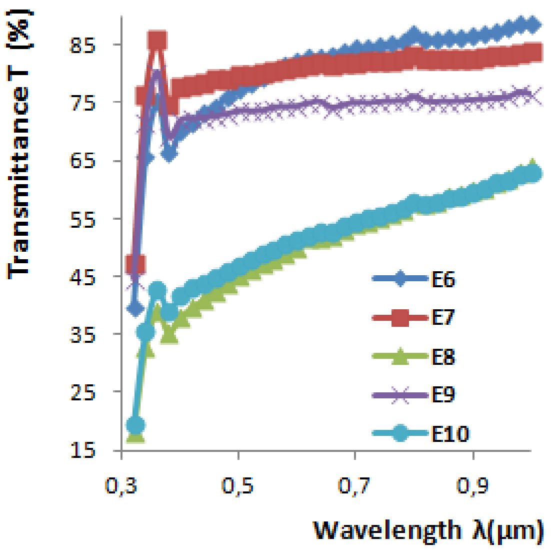

Fig. 1. Spectral transmittance of MgNiS thin films (Slide E_6-E_{10})

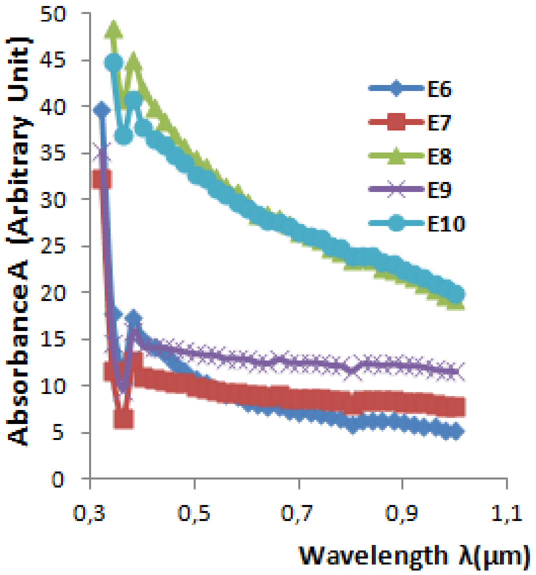

Fig. 2. Spectral absorbance of MgNiS thin films (Slide E_6-E_{10})

Figure 1 shows that MgNiS thin films with high transmittance values of (75-85%) in the UV, visible, and near infrared regions of electromagnetic spectrum are obtained when small volumes of ammonia were used during deposition. This is shown by the films on slides E_6 and E_7. This implies that the lesser the used ammonia volume, the higher the transmittance. Thin films of high transmittance, such as that on slides E_6 and E_7, can be used for photosynthetic coatings. This is possible because they are likely to exhibit selective transmittance of photosynthetic radiation. This radiation aids in the process of photosynthesis for green plants.

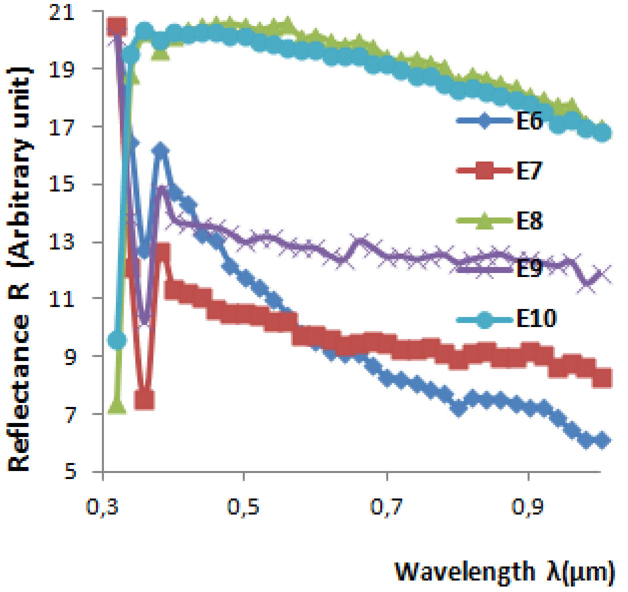

Fig. 3. Spectral reflectance of MgNiS thin films (Slide E_6-E_{10})

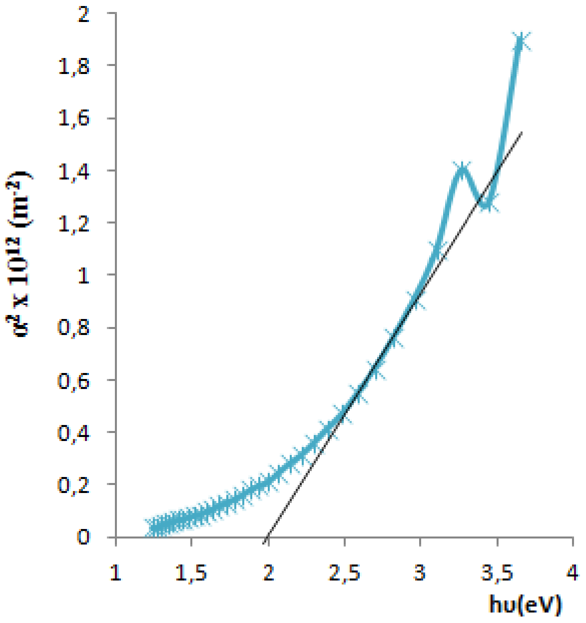

Fig. 4. A plot of absorption coefficient squared versus photon energy of MgNiS for E_6 - E_{10}

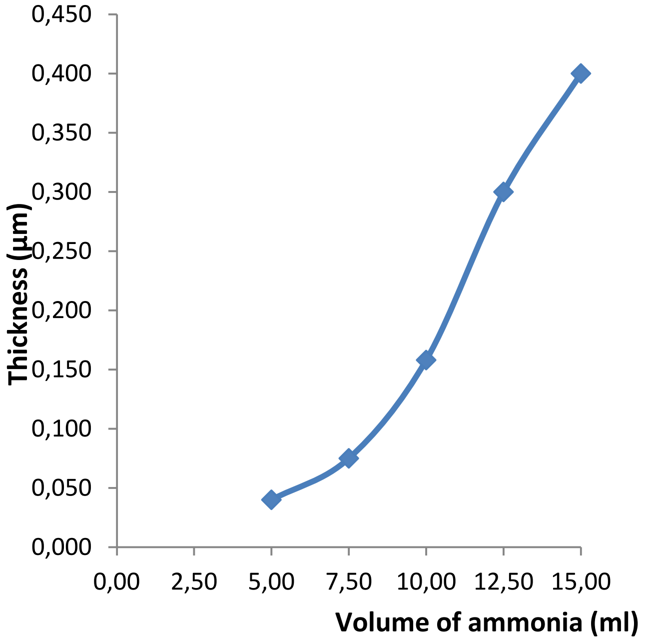

Fig. 5. Variationof thicness with volume of ammonia for MgNiS thin films (slide E_6-E_{10})

Figure 2 shows that the absorbance of the MgNiS thin film grown with the smallest volume of ammonia (5 ml) has the lowest value of absorbance closely followed by the film with next in volume ammonia solution. This is illustrated by films on slides E_6 and E_7 which have 5-15% absorbance in the UV, visible, and near infra red regions of electromagnetic spectrum. The implication of this is that the smaller the used ammonia volume, the smaller the absorbance value. Thin films of MgNiS of low absorbance are used to coat windows for people living in the cold parts of the world. This is because their transmittance is always high. More so, they can be used to make materials used in making poultry houses.

Figures 3 shows the reflectance spectra of MgNiS thin film grown in this work. A close observation of the plot reveals that the reflectance value of MgNiS thin film is low. Films of low reflectance are very useful in the solar energy production. This is comparable with the results obtained when CdS, which is a II–VI semiconductor, was doped with transition metal Ni [13–15]. They are used as antireflection thin films which are coated at the flat plate solar collector. With this thin film, the loss of incident solar radiation on the solar collector plates due to reflection is drastically reduced.

The plot of value of absorption coefficient squared versus photon energy for the MgNiS thin film is shown in Fig. 4. The band gap energy was determined from the graph. This is done by extrapolating the straight portion of the graph to a point where α^2 is equal to zero; the value of photon energy at this point is equal to the band gap energy of the MgNiS thin film. On a close look at the graph, it is observed that the band gap energy for the film is about 2.0 eV [16, 17]; the band gap was 3.6 and 3.9 eV, respectively, for MgS, but with the doping with transition metal Ni, a reduced band gap value of 2.0 eV was obtained. This is in agreement with the results of [18, 19] reported about the effect of a transition metal on the band gap of semiconductor thin films. This implies that MgNiS thin films are of high band gap energy and can be used in the absorber layer of a solar cell. This is because absorption of photon energy occurs only when the band of the absorber layer is higher than the energy of the photon.

Figure 5 indicates the relationship of thickness with the used ammonia solution volume. The plot reveals that the thickness increases as the used ammonia solution volume increases. It also indicates that a nanofilm of 0.05 μm was produced with 5 ml of ammonia (complexing agent). As more and more ammonia solution was added, the thickness continued to increase. The maximum thickness of 0.40 μm was obtained when 15 ml of ammonia was used. This also implies that the molecular flux to the surface of the substrate is directly proportional to the used ammonia volume.

4. Compositional Characterization

The compositional analysis was dome by the EDXRF technique. This was done for a period of 3000 s after which the spectrum was saved for quantitative analysis. In this work, samples E_6, E_8, and E_{10} were selected for this analysis. Cd^{109} source was used to analyze the quantity of Mg, while ^{55}Fe was used for the determination of the quantity of sulphide. The amounts of Mg^{2+}, Ni^{2+}, and S^{2-} for various films are shown in Table 2 below.

Table 2. Compositional analysis of $Mg_{1-x}Ni_xS$ thin films

Slide no.	Composition (x)	Mg content wt %	Ni content wt %	S content wt %	Impurity Cl_2 wt %
E_6	0.100	52.17	1.81	45.00	1.00
E_8	0.150	51.19	3.98	44.83	-
E_{10}	0.300	50.77	4.14	44.09	1.00

From the composition studies, the grown films are slightly rich in Mg^{2+}, whereas S^{2-} is almost constant. The above table shows that the content of Mg^{2+} decreases with increasing nickel content.

5. Conclusions

MgNiS thin films have been successfully deposited on glass slides using chemical bath deposition techniques. The optical studies showed that the films have low reflectance values in the UV, VIS – NIR regions. This makes the film suitable for coating in solar collector plates as anti reflection films. With these thin films,the loss of incident radiation due to reflection on the solar collector plates is reduced. Also, MgNiS films were found to have high absorbance in the UV region. This property makes the film a good material for solar control coatings. The thickness of the film was found to be of the range 0.05μm – 8.50μm. The film band gap energy was determined to be 2.0eV. From this large band gap value, the film is therefore used in the absorber layer of solar cell.

References

[1] D.N. Okoli, A.J. Ekpunobi, , and C.E. Okeke, Pac. J. Sci. Technol., 7, 59, (2006).

[2] I. Ecketora, Physics of Thin Films, 2nd edn., Plenum Press, New York, 3451–3459, 1982.

[3] F.C. Eze and C.E. Okeke, Int. J. Chin. Soc. For Mater. Sci. 47, 31 (2003).

[4] G.K. Padam and S.U. Rao, Solar Energy Mater., 13, 297 (1986).

[5] C. Wang, W.X. Zhang, X.M. Zhang, and Y. Xie, Mater. Res. Bull., 30, 1609 (1986).

[6] B. Subramanian, J. Mahalongun, C. Sanjeeviraja, M. Jayachandran, and M. Chockalingam, Thin Solid Films, 357, 119 (1999).

[7] K.L. Chopra and Malhotra, Thin Film Technology and Applications, Tata McGraw Hill, New Delhi, 237-249, 1985.

[8] B.R. Sankapal, R.S. Mane, and C.D. Lokhande, Building Materials from Fluorogypsum, 10th Annual General Meeting of the Mater. Res. Soc. of India, Bhapal, 201–212, 1999.

[9] M.N. Nnabuchi, Pac. J. Sci. and Technol. 6, 105 (2005).

[10] S.C.Ezugwu, F.I.Ezema, and R.U.Osuji, Opt. Adv. Mater. Rap. Comm., 3, 141 (2009).

[11] J.J.Pankove, Optical process in semiconductor, Prentice Hall, New York. 475–480, 1971.

[12] F.I. Ezema and R.U. Osuji, J. Sol. Ener. 14**,** 90 (2003).

[13] R.B. Kale, S.D. Sarlole, and C.D. Lokhande, Appl. Surf. Sci., 25, 820 (2006).

[14] I.E. Ottih, A..J. Ekpunobi and P. Ekwo, J. African Phys. Rev. Phys., 6, 1 (2011).

[15] R.B. Srinivasa and R.T. Suba, Chalc. Lett. 8, 39 (2010).

[16] J. Gutowski, P. Michler, H. Ruckmann, H. Brunig, M. Rowe, K. Sebald, and T. Voss, Phys. Stat. Sol. B23, 70 (2000).

[17] M.N. Nnabuchi, Pac. J. Sci. Technol. 6, 105 (2005).

[18] I.E. Ottih and A.J. Ekpunobi, J. Basic Phys. Res., 1, 17 (2010).

[19] I.E. Ottih and A.J.Ekpunobi, Pac. J. Sci. Technol., 12, 351 (2011).

EFFECTIVE TEMPERATURE OF QUASI-TWO-DIMENSIONAL ELECTRONS IN A STRONG ELECTRIC FIELD

M. M. Babayev

Institute of Physics, National Academy of Sciences of Azerbaijan, Baku, Azerbaijan
E-mail: mirbababababayev@yahoo.com

(Received 11 September 2012)

Abstract

The heating of electrons by a strong electric field directed along the plane of the free movement of electrons inside a quantum well with parabolic potential of confinement has been investigated. The case of strong degeneracy of the electron gas and the absence of phonon heating has been considered. It has been shown that the dependence of the electron temperature on the electric field is close to a quadratic dependence.

1. Introduction

Since recently, a great deal of attention has been given to the study of the thermoelectric and thermomagnetic effects in low-dimensional systems [1-8].

The heating of electrons in a strong electric field leads to a substantial change in the values of thermoelectric and thermomagnetic effects, as well as their dependence on material parameters (electron density and temperature). In addition, it leads to a dependence of the above-mentioned effects on the applied electric field, which makes it possible to control the magnitude of effects by means of an electric field. In theoretical calculations of thermoelectric and thermomagnetic effects in a strong electric field, the first step is to calculate the average electron energy (the effective electron temperature). In this work, we have calculated the effective electron temperature of strongly degenerate electron gas in a quantum well with a parabolic confining potential. To calculate the electric current along the plane of the free movement of the electrons, the Boltzmann equation method was used. We took into account the mechanisms of electron scattering by impurity ions, both deformation and piezoelectric potentials of acoustic phonons. Since scattering by optical phonons is inefficient at low temperatures, we did not consider this mechanism. In calculating the relaxation times of electrons, we also took into account the screening of scattering potentials.

2. Basic equations of the problem

We consider a simple model for the quantum well, in which a two-dimensional electron gas is confined in the x-direction and the temperature gradient is parallel to the *y*-axis. The parabolic confining potential can be written as $U_x = m\omega_0^2 x^2/2$, where m is the effective mass of a conduction electron, and ω_0 is the parameter of the parabolic potential. In this model, the electron dispersion law in the absence of a magnetic field has the form

$$\varepsilon = \left(\frac{1}{2} + N\right)\hbar\omega_0 + \frac{\hbar^2 k^2}{2m}, \tag{1}$$

where N is the oscillation quantum number, $\vec{k}\left(k_y, k_z\right)$ is the wave vector of electrons.

The dielectric function of a two-dimensional electron gas depends only on $\vec{q}_2\left(q_y, q_z\right)$ components of the wave vector of phonons $\vec{q}\left(q_x, q_y, q_z\right)$:

$$\varepsilon\left(q_2\right) = 1 + \frac{2me^2 e^{\frac{1}{2}R^2 q_2^2} erfc\left(\frac{Rq_2}{\sqrt{2}}\right)}{\sqrt{\pi}\hbar^2 \chi\, q_2}, \tag{2}$$

where χ is the static dielectric constant and $R = \left(\hbar / m\omega_0\right)^{1/2}$ is the "oscillator length."

If the interelectron collision rate (ν_{ee}) is much higher than that of electron-lattice energy scattering (ν_{ep}), the isotropic part of the electron distribution function $f\left(\vec{p}, \vec{r}\right)$ can be described as the Fermi-Dirac distribution with an effective temperature T_e:

$$f_0\left(p, \vec{r}\right) = \frac{1}{\exp\left(\frac{\varepsilon - \zeta\left(T_e\right)}{k_0 T_e}\right) + 1}. \tag{3}$$

Here $\vec{p}$, $\vec{r}$, ε and $\zeta\left(T_e\right)$ are the momentum, coordinates, energy, and chemical potential of electron, respectively.

In most experimental studies [1-2] the average energy of electrons satisfies the condition $\bar{\varepsilon} < \hbar\omega_0$, i.e. the electrons are mostly at the zeroth oscillator level ($N = 0$) and the density of states of the 2D electron gas becomes a constant: $g\left(\varepsilon\right) = \frac{m}{\pi\hbar^2}$. In this case, the expression for the chemical potential is as follows:

$$\zeta\left(T_e\right) = k_0 T_e \ln\left[\exp\left(\frac{\pi\hbar^2 n}{mk_0 T_e}\right) - 1\right] + \frac{\hbar\omega_0}{2}, \tag{4}$$

where n is the areal density of electrons.

In view of the quasi-elasticity of electron scattering by acoustic phonons, the distribution function of electrons in strong electric fields (as in weak fields) can be written as

$$f\left(\vec{p}, \vec{r}\right) = f_0\left(\varepsilon, \vec{r}\right) + \vec{f}_1\left(\varepsilon, \vec{r}\right)\frac{\vec{p}}{p}, \quad \left|\vec{f}_1\right| << f_0. \tag{5}$$

The effective electron temperature can be found from the balance equation: in the steady state, the energy gained by an electron system from the electric field $\sigma_2\left(\vartheta\right)E^2$ equals the energy transferred to the phonon system [9]:

$$\sigma_2\left(\vartheta\right)E^2 = W_{ep}\left(\vartheta\right). \tag{6}$$

Here $\vartheta = T_e/T$ is the dimensionless electron temperature, $\sigma_2(\vartheta)$ is the conductivity of two-dimensional electron gas in a strong electric field.

In weak electric fields (in the absence of electron heating), the conductivity of the electron gas in a quantum well studied in [10]. In the same way, we can calculate the conductivity of the quantum well in strong electric fields. For the conductivity of a quantum well with the spectrum of (1), we obtain

$$\sigma_2(\vartheta) = \frac{e^2 k_0 T \vartheta}{\pi \hbar^2} \int_0^\infty \left(-\frac{\partial f_0}{\partial y} \right) \frac{y}{\nu_e(y)} dy, \quad y = \frac{\varepsilon - \frac{\hbar\omega_0}{2}}{k_0 T \vartheta} = \frac{\hbar^2 k^2}{2 m k_0 T \vartheta}, \quad \vartheta = \frac{T_e}{T}. \qquad (7)$$

Here $\nu_e(x)$ is the total electron momentum scattering rate due to scattering centres. We have taken into account the mechanisms of electron scattering by impurity ions (i), both deformation (da) and piezoelectric (pa) potentials of acoustic phonons:

$$\nu_e(y) = \nu_{da}(y) + \nu_{pa}(y) + \nu_i(y). \qquad (8)$$

The scattering rate accociated with da scattering is

$$\nu_{da}(y) = \frac{2\sqrt{2} m k_0 T E_1^2}{\pi\sqrt{\pi}\,\hbar^3 \rho s^2 R} \int_0^1 \frac{x^2}{\varepsilon^2(x)\sqrt{1-x^2}} dx. \qquad (9)$$

Here E_1 is the parameter of the deformation potential [11], ρ is the density of the material, s is the sound velocity in the crystal, and

$$\varepsilon(x) = 1 + \frac{m e^2 R e^{2y^2x^2} erfc\left(\sqrt{2} y x\right)}{\sqrt{\pi}\hbar^2 \chi y x}, \quad x = \frac{q_2}{2k}, \quad y = Rk. \qquad (10)$$

The scattering rate accociated with pa scattering is

$$\nu_{pa}(y) = \frac{m k_0 T e^2 \beta^2 R}{\pi \hbar^3 \chi^2 \rho s^2 y} \int_0^1 e^{2y^2x^2}\, erfc\left(\sqrt{2} y x\right) \frac{x}{\varepsilon^2(x)\sqrt{1-x^2}} dx. \qquad (11)$$

Here $\beta = \sqrt{0.8} e_{14}/\chi$, e_{14} is the parameter of the piezo-electric potential [11]. The scattering rate accociated with impurity scattering is

$$\nu_i = \frac{4\pi m n_i Z^2 e^4 R^2}{\hbar^3 \chi^2 y^2} \int_0^1 e^{2y^2x^2} erfc(yx)^2 \frac{1}{\varepsilon^2(x)\sqrt{1-x^2}} dx, \qquad (12)$$

where Ze and n_i are the charge and areal density of impurity ions, respectively.

For a highly degenerate electron gas ($e^{\eta_0} >> 1$) from Eq. (7) we obtain

$$\sigma_2(\vartheta_e) = \frac{e^2 n}{m \nu_e(\eta_0)}, \quad \eta_0 = \frac{\zeta(T_e)}{k_0 T_e} - \frac{\hbar\omega_0}{2 k_0 T_e} \approx \frac{\pi\hbar^2 n}{m k_0 T_e}. \qquad (13)$$

3. Scattering of the electron energy

The rate of energy loss of the electron system by acoustic phonons is

$$W_{ep} = \sum_{\vec{q}} \hbar\omega_q \left(\frac{\partial N_q}{\partial t} \right)_{ep} . \tag{14}$$

Here $\left(\frac{\partial N_q}{\partial t} \right)_{ep}$ is the rate of change in the number of phonons with wave vector $\vec{q}$ due to the emission and absorption of phonons by all the electrons [9]:

$$\left(\frac{\partial N_q}{\partial t} \right)_{ep} = \frac{4\pi}{\hbar} \sum_{k_y, k_z} \left\{ \begin{array}{l} \left| \left\langle \vec{k}, N_q + 1 \left| V(\vec{r}) \right| \vec{k} + \vec{q}_2, N_q \right\rangle \right|^2 \delta\left(\varepsilon_{\vec{k}, N_q + 1} - \varepsilon_{\vec{k} + \vec{q}_2, N_q} \right) f\left(\vec{k} + \vec{q}_2 \right) \left[1 - f\left(\vec{k} \right) \right] - \\ - \left| \left\langle \vec{k} + \vec{q}_2, N_q - 1 \left| V(\vec{r}) \right| \vec{k}, N_q \right\rangle \right|^2 \delta\left(\varepsilon_{\vec{k} + \vec{q}_2, N_q - 1} - \varepsilon_{\vec{k}, N_q} \right) f\left(\vec{k} \right) \left[1 - f\left(\vec{k} + \vec{q}_2 \right) \right] \end{array} \right\} . \tag{15}$$

The interaction energy of the electron with the lattice $V(\vec{r})$ in the case of scattering by the deformation potential has the form [12]

$$V(\vec{r}) = \frac{iE_1}{\sqrt{NM}} \sum_{\vec{q}} \frac{q}{\varepsilon(q_2)} \left[b(\vec{q}) e^{i\vec{q}\vec{r}} + b^*(\vec{q}) e^{-i\vec{q}\vec{r}} \right], \tag{16}$$

and in the case of scattering by a piezoacoustic potential

$$V(\vec{r}) = -\frac{e\beta}{\sqrt{NM}} \sum_{\vec{q}} \frac{q}{\varepsilon(q_2)} \left[b(\vec{q}) e^{i\vec{q}\vec{r}} + b^*(\vec{q}) e^{-i\vec{q}\vec{r}} \right]. \tag{17}$$

Substituting Eqs. (16) and (17) in Eq. (15), we obtain

$$\left(\frac{\partial N_q}{\partial t} \right)_{ep} = \frac{m\sqrt{2mk_0T_e}\,E_1^2}{4\pi^2\hbar^3 Rs_0\rho x\varepsilon^2(x)} \int_0^\infty dz \frac{e^{z-\eta_0+\delta x^2}}{\sqrt{z}\left(e^{z-\eta_0+\delta x^2} + 1 \right)^2} F(x) . \tag{18}$$

Here

$$F(x) = \int_{-\infty}^{+\infty} dt\varphi(t) e^{-\frac{t^2}{2}} \left[t^2 + x^2 + \left(\frac{e\beta R}{E_1} \right)^2 \right], \quad \varphi(t) = \frac{e^{\gamma\sqrt{t^2+x^2}} - e^{\gamma_e\sqrt{t^2+x^2}}}{\sqrt{t^2+x^2}\left(e^{\gamma\sqrt{t^2+x^2}} - 1 \right)}, \tag{19}$$

$$t = Rq_x, x = Rq_{||}, \ \delta = \frac{\hbar^2}{8mR^2 k_0 T_e}, \ \gamma = \frac{\hbar s_0}{k_0 TR}, \ \gamma_e = \frac{\hbar s_0}{k_0 T_e R}. \tag{20}$$

For a highly degenerate electron gas ($e^{\eta_0} >> 1$) Eq. (18) has the form

$$\left(\frac{\partial N_q}{\partial t} \right)_{ep} = \frac{m\sqrt{mk_0T_e}\,E_1^2}{\sqrt{2}\pi\hbar^3 Rs_0\rho x\varepsilon^2(x)\sqrt{\eta_0 - \delta x^2}} \int_0^\infty dt\varphi(t) e^{-\frac{t^2}{2}} \left[t^2 + x^2 + \left(\frac{eE_{pz}R}{\chi E_1} \right)^2 \right]. \tag{21}$$

Substituting Eq. (18) into Eq. (14), for the rate of energy loss of the electronic system we obtain

$$W_{ep} = \frac{Vm\sqrt{2mk_0T_e}E_1^2}{4\pi^4\hbar^2\rho R^5}\int_0^{t_\mathrm{m}} dt \int_0^{x_\mathrm{m}} dx \frac{\left(t^2+x^2\right)^{1/2}}{\varepsilon^2(x)} F(x) \int_0^\infty dz \frac{e^{z-\eta_0+\delta x^2}}{\sqrt{z}\left(e^{z-\eta_0+\delta x^2}+1\right)^2}. \tag{22}$$

Here $t_\mathrm{m} = x_\mathrm{m} = 2kR = \frac{2R}{\hbar}\sqrt{2m\left(\bar{\varepsilon}-\frac{\hbar\omega_0}{2}\right)}$, $\bar{\varepsilon}$ is the average energy of electrons, and V is the volume of the crystal. For a highly degenerate electron gas Eq. (22) has the form

$$W_{ep} = \frac{Vm^2k_0T_eE_1^2}{2\pi^4\hbar^3\sqrt{2\pi n}\rho R^5}\int_0^{2R\sqrt{2\pi n}} dt \int_o^{2R\sqrt{2\pi n}} dx \frac{\left(t^2+x^2\right)^{1/2}}{\varepsilon^2(x)\sqrt{1-\frac{x^2}{8\pi nR^2}}} F(x). \tag{23}$$

4. Effective temperature of a highly degenerate electron gas

Using Eqs.(13) and (23) into Eq. (6), for the electron temperature we obtain the following expression:

$$\vartheta \cdot I(\vartheta) = \left(\frac{E}{E_{ch}}\right)^2, \quad E_{ch}^2 = \frac{m^3k_0TL_xE_1^2\nu_e(\eta_0)}{(2\pi n)^{3/2}\pi^3\hbar^3e^2R^5\rho}, \tag{24}$$

where

$$I(\vartheta) = \int_0^{x_m} dx \frac{1}{2\varepsilon^2(x)\sqrt{\left(1-\left(x/x_\mathrm{m}\right)^2\right)}}\left(y_m\sqrt{x^2+y_m^2}+x^2\ln\left(\frac{y_m+\sqrt{x^2+y_m^2}}{x}\right)\right)\times$$

$$\times\int_0^\infty dt \frac{\varphi(t)}{\sqrt{t^2+x^2}} e^{-\frac{t^2}{2}}\left[t^2+x^2+\left(\frac{e\beta R}{E_1}\right)^2\right], \; x_\mathrm{m} = y_\mathrm{m} = 2R\sqrt{2\pi n}. \tag{25}$$

Since $I(\vartheta)$ depends on the electron temperature through $\varphi(t)$, in the general case, from (24) it is impossible to obtain an analytical form of the dependence of the electron temperature on the electric field. Consider the limit cases. In the case of weak heating of the electron gas ($\vartheta - 1 << 1$), the expansion of $\varphi(t)$ in powers of ($\vartheta - 1$) gives

$$\vartheta = 1 + \left(\frac{E}{E_{ch0}}\right)^2, \quad E_{ch0}^2 = \frac{m^3k_0TL_xE_1^2\nu_e(\eta_0)I_0\gamma}{(2\pi n)^{3/2}\pi^3\hbar^3e^2R^5\rho}. \tag{26}$$

Here I_0 is independent of the electron temperature and is calculated by Eq. (25), substituting

$$\varphi(t) = \frac{e^{\gamma\sqrt{t^2+x^2}}}{\left(e^{\gamma\sqrt{t^2+x^2}}-1\right)}.$$

In the case of strong heating ($\theta >> 1$) from Eq. (24) we obtain

$$\vartheta = \left(\frac{E}{E_{ch1}} \right)^2 , \quad E_{ch1}^2 = \frac{m^3 k_0 T L_x E_1^2 \nu_e \left(\eta_0\right) I_1}{(2\pi n)^{3/2} \pi^3 \hbar^3 e^2 R^5 \rho} , \qquad (27)$$

Here I_1 is independent of the electron temperature and is calculated by Eq. (25) substituting $\varphi(t) = \frac{1}{\sqrt{t^2 + x^2}}$. As seen from (30) at $\theta >> 1$, the dependence of the electron temperature on the electric field is a quadratic dependence.

5. Numeral Results and Discussion

In the general case, the dependence of the electron temperature on the electric field can be computed from Eq. (24) by numerical calculation. We apply our theoretical results to the 2D degenerate electron gas in $GaAs/Al_xGa_{1-x}As$ quantum wells, with the areal electron density $n = 1,78 \cdot 10^{11} cm^{-2}$, the mobility $22.7\, m^2/Vs$, the width of the quantum well $L_x = 10^{-8} m$ [1], the mass density $\rho = 5.3 \times 10^3\ kq/m^3$, the longitudinal sound velocity $s = 5 \cdot 10^5\ m/s$, the effective mass of electrons $m = 0.067 m_0$ (m_0 is the free electron mass), the static dielectric constant $\chi = 12.9$, the acoustic deformation potential $E_1 = 7,4 eV$, and the piezoelectric constant $e_{14} = 0.16\, C/m^2$ [11]. To estimate the value of the parabolic potential parameter, we use the condition of $R \approx L_x/2$, then we get $\omega_0 = 7 \cdot 10^{13} s^{-1}$. At these values of the parameters, the conditions of quantum limit ($N = 0$) and the strong degeneracy of electron gas ($\hbar\omega_0 / 2 \le \zeta < 3\hbar\omega_0 / 2$) are satisfied. Estimation shows that the dominant mechanizm of scattering of the electron momentum is the scattering by ionized impurities. For the value of the electron mobility $22.7\, m^2/Vs$, we obtain for the ion density: $n_i = 3 \cdot 10^9 cm^{-2}$.

Numerical results for the dependence of dimensionless electron temperature ϑ on the electric field E, at the lattice temperature $T = 3K$, are shown in Fig. 1. As shown in Fig. 1, the dependence of ϑ on E (curve *1*) is close to a quadratic dependence. For comparison, Fig. 1 shows also the results of calculations of $\vartheta(E)$ by Eq. (26), which refers to the case of weak heating (curve *2*) and by Eq. (27), which refers to the case of strong heating (curve *3*). As seen in Fig. 1, Eq. (27) satisfactorily describes the degree of electron heating at $\vartheta \ge 3$.

Numerical results for the dependence of electron temperature T_e on the electric field E, at the different lattice temperature are shown in Fig. 2. For a given value of the electric field, with increasing lattice temperature T, the electron temperature T_e increases, but the degree of heating $\vartheta = T_e/T$ decreases.

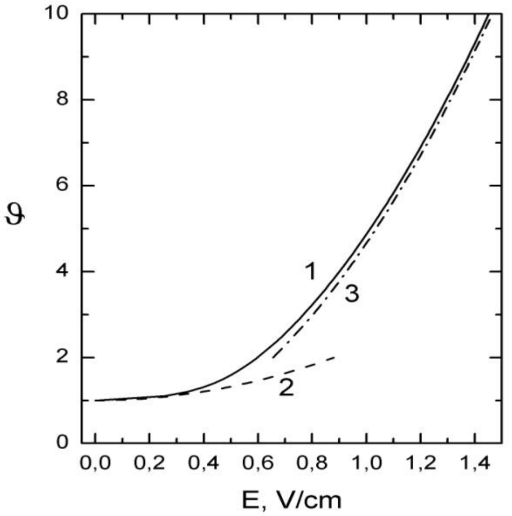

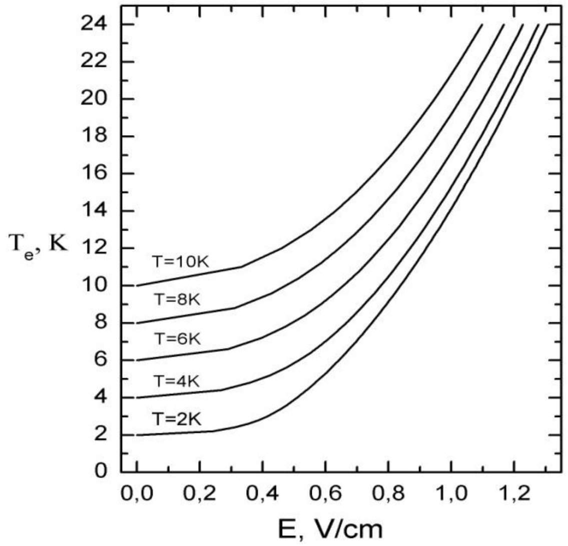

Fig. 1. Dependence of dimensionless electron temperature ϑ on electric field at $T = 3K$ (curve *1*). Curves *2* and *3* are the results of calculations in the cases $\vartheta - 1 << 1$ and $\vartheta >> 1$, respectively.

Fig. 2. Dependences of effective electron temperature T_e on electric field at different temperatures of the crystal.

References

[1] R.Fletcher, J.C.Maan, and G.Weimann, Phys.Rev.B, 32, 8477 (1985).

[2] R.Fletcher, J.J.Harris, C.T.Foxon, M.Tsaousidou, and P.N.Butcher, Phys.Rev.B, 50, 14991 (1994).

[3] S.K.Lyo, Phys.Rev.B, 38, 6345 (1988).

[4] S.S.Kubakaddi, B.G.Mulimani, V.M.Jali, Phys.Stat.Sol.(b),137, 683 (1986).

[5] S.S. Kubakaddi and P.N.Butcher, J. Phys.: Condens. Matter, 1, 3939 (1989).

[6] M.W.Wu, N.J.M.Horing, and H.L.Cui, Phys.Rev.B, 54, 5438 (1996).

[7] F.M.Hashimzade, M.M.Babayev, and Kh.A.Hasanov, Japan. J. Appl. Phys., 47, 8200 (2008).

[8] F.M.Hashimzade, M.M.Babayev, B.H.Mehdiyev, and Kh.A.Hasanov, J. Phys.: Conference Series, 245, 012015 (2010).

[9] Ester M. Conwell, High field transport in semiconductors, , New York, London: Academic Press, 338, 1967.

[10] F. M. Hashimzade, Kh. A. Hasanov, and M. M. Babayev, Phys.Rev. B, 73, 235349(1-8), (2006).

[11] V.F. Gantmacher, I.B. Levinson, Carrier Scattering in Metals and Semiconductors, Amsterdam, New-York: Elsevier, 352, 1987.

[12] B. M. Askerov, Electron Transport Phenomena in Semiconductors, Singapore: World Scientific, 318, 1994.

EFFECT OF THE SCREENING ON THE POLARON MASS IN A SEMICONDUCTOR HOLLOW NANOCYLINDER

S. M. Seyid-Rzayeva

Institute of Physics, National Academy of Sciences of Azerbaijan,
Javida str. 33, Baku, AZ-1143 Azerbaijan
E-mail: s-nisa@rambler.ru

(Received 11 September 2012)

Abstract

The effect of the screening effect of the electron–phonon interaction on a weakly coupling Frohlich polaron mass has been investigated in a semiconductor hollow nanocylinder (HNC). General analytical expressions for the polaron mass have been obtained in arbitrary values of nanocylinder radius r_0, taking into account screening as well as considering transitions between the subbands of dimensional quantization. The dependence of the polaron mass for the ground and excited states on nanocylinder radius has been represented on the basis of our numerical calculations. According to research carried out, it has been established that the screening contribution to polaron mass taking into account the virtual transitions from the ground state to subbands n = ±1, ±2, ±3, as well as the transitions from the polaron excited state with n = 1 to subbands n = −1, ±2,±3, is significant for $a = r_0/r_p < 1$ values, where r_p is the polaron radius. For values of the parameter a > 1 the screening contribution to polaron mass decreases with increasing r_0, but the decrease of the polaron correction to the mass due to screening is still more than 30 %.

1. Introduction

One of the main characteristic parameters of the polaron is its effective mass, which can be determined from the experiments on the cyclotron and magneto-phonon resonance. In [1], the valence intraband transitions in p-doped InAs quantum dots (QDs) were studied by means of far-infrared resonance (FIR) magneto-optical technique. It was shown that a model taking into account the hole-LO phonon coupling is able to predict the experimental results. The experiments demonstrate the fact that the intraband magneto-optical transitions occur between hole polaron states.

A number of theoretical and experimental works concern the problem of the effect of the screening of electron-phonon interaction on the magnitude of the polaron cyclotron- resonance (CR) mass. Klimin and Devreese have theoretically investigated cyclotron-resonance spectra for a polaron gas in a GaAs/AlAs quantum well taking into account the screening of the electron-phonon coupling [2]. In [3] it was shown that, including the screening, the polaron cyclotron-resonance mass correction is reduced as compared to a calculation without taking into account the effect of screening. It was concluded that the static screening approach gives good results for the polaron cyclotron-resonance mass renormalization in the relevant magnetic field region. CR data of the 3D bulk system n-GaAs and of the 2D electron system of AlGaAs-GaAs heterojunction were presented in [4]. Polaron effects are found to be significant in both system; however, the polaron effect is found to be weaker in the 2D electron gas of an AlGaAs-GaAs heterojunction than in 3D bulk n-GaAs crystal.

In recent years the rapid development of nanotechnology has made it possible to design a low-dimensional system of complex geometric shapes in the form of rings, spirals, tubes, etc. [5, 6]. This situation has aroused interest in new theoretical and experimental studies of low-dimensional systems. Among them, the nanotubes (NT) present the great interest.

Our recent paper [7] was devoted to the effect of screening of the electron-phonon interaction with weak coupling on the polaron binding energy in a semiconductor NT. To solve this problem, we used the results of computation of the electron dielectric permeability for an infinitely long semiconductor NT given in [8]. Here we use the same technique to calculate the polaron correction to the mass in NT, which is essentially a hollow nanocylinder (HNC).

Thus, the aim of the present study is to theoretically investigate the effect of the screening of the electron-phonon interaction on the Fröhlich polaron mass in a semiconductor HNC, taking into account transitions between the subbands of dimensional quantization just as is done in calculating the binding energy of the polaron.

2. Energy states, electron wave functions and the matrix element of the electron-phonon coupling

We consider an HNC with radius r_0 on the surface of which there is a 2D gas of mobile electrons. According to the results of [9], the quantized energy spectrum and normalized wave function in a one-particle approximation are given as follows:

$$\varepsilon_{nk} = \frac{\hbar^2 k^2}{2m} + \frac{\hbar^2 n^2}{2m r_0^2}, \tag{1}$$

$$\psi_{nk}(Z,\varphi) = \frac{1}{\sqrt{2\pi L}} e^{i(kZ+n\varphi)}. \tag{2}$$

Here m is the effective mass of an electron, φ and Z are the cylindrical co-ordinates, L is the length of the cylinder along NC-axis in the Z-direction, and $n = 0, \pm 1, \pm 2, ...$ are the number of subband of dimensional quantization. Quasi-momentum $\hbar\vec{k}$ corresponds to the motion of electrons on a cylinder surface along the Z-axis.

Taking into account the expression for Fourier component of scalar potential $\Phi_{\vec{q}}$ [9]

$$\Phi_{q_\perp q_Z} = i\sqrt{\frac{2\pi\hbar\omega_L}{\in^* V}} \frac{1}{\sqrt{q_\perp^2 + q_z^2}} e^{-i\left(q_\perp r_0 \cos\varphi + q_z z\right)}$$

the matrix element $M_{n-n', q_\perp q_Z}$ for the energy $(-e\sum_{\vec{q}} \Phi_{\vec{q}})$ of the electron-phonon coupling is calculated with wave function (2) for any n, n'

$$M_{n-n', q_\perp q_Z} = -\hbar\omega_L \sqrt{\frac{4\pi\alpha\, r_p}{V}} \frac{i^{(n-n'+1)}}{\sqrt{q_\perp^2 + q_Z^2}} J_{|n-n'|}(q_\perp r_0). \tag{3}$$

Here $q_{\perp}, q_Z$ are the transverse and longitudinal phonon wave vector of $\vec{q}\,, \omega_L$ is the limiting LO phonon frequency, $\alpha = \sqrt{\frac{m}{2\hbar\omega_L}} \frac{e^2}{\hbar}\left(\frac{1}{\varepsilon_\infty} - \frac{1}{\varepsilon_0}\right)$ is the electron-phonon coupling parameter, $r_p = \sqrt{\hbar/2m\omega_L}$ is the polaron radius; $\varepsilon_0, \varepsilon_\infty$ is the static and high-frequency dielectric permeability, respectively, and $J_{|n-n'|}(q_{\perp} r_0)$ is the Bessel function of the index $\Delta n = n - n'$. In deriving (3) it was taken into account that the phonon-electron interaction at low temperatures leads to virtual electron transitions with the emission of one LO-phonon.

3. Polaron mass

Using the perturbation theory, a task with regard to a weak coupling Fröhlich polaron has been solved in the quasi-two-dimensional systems [10]. In this paper, an analytical expression for the polaron correction to the effective electron mass is calculated taking into account the intersubband transitions.This analytical expression for the polaron contribution to the mass gives the well-known value $\Delta m/m\alpha = \pi/8$ in the limit of a two-dimensional case. Here $\Delta m = m_p - m$, m and m_p are the electron and polaron effective masses.

In this study, we will investigate the effect of screening on the Fröhlich polaron mass at low temperatures on the semiconductor HNC surface. To obtain an analytical expression for the polaron effective mass, it is necessary to calculate the correction to the electron energy $\Delta E_{n,\vec{k}}$ due to its interaction with the LO-phonons. The calculation is carried out within the framework of the standard perturbation theory.

Taking into account the screening effect, the expression for the polaron correction to the energy $\Delta E_{n,\vec{k}}$ in the second-order perturbation theory, is defined as follows [7]:

$$\Delta E_{n,\vec{k}} = \sum_{n',\vec{q}} \frac{\left|M_{n-n',q}\right|^2}{(\varepsilon_{n\vec{k}} - \varepsilon_{n'\vec{k}-\vec{q}} - \hbar\omega_L) \in^2_{|n-n'|}(q)}\,. \tag{4}$$

Here $\in_{|n-n'|}(q)$ is determined by the expression [7]

$$\in_{|n-n'|}(q) = 1 - \frac{2\,m\,e^2}{\pi\,\hbar^2 \in_0 q} I_{|n-n'|}(qr_0) K_{|n-n'|}(qr_0) \sum_{n=-n_F}^{n_F} \ln\left[\frac{(n+n')(n-n') - q\,(q-2\,k_F)\,r_0^2}{(n+n')(n-n') - q\,(q+2\,k_F)\,r_0^2}\right]. \tag{5}$$

Here $I_{|n-n'|}(qr_0)$, $K_{|n-n'|}(qr_0)$ are the modified Bessel functions of the first and second kind, respectively.

After integration over the polar angle φ in (4), we obtain the following expression for the correction to the polaron energy in the new dimensionless variables $x = r_p q_{\perp}$, $z = r_p q$, $\kappa = r_p k$, $a = r_0/r_p$:

$$\Delta E_{n,\kappa} = -\frac{\alpha\hbar\omega_L}{\pi} \sum_{n'} \int_0^\infty \int_{-\infty}^\infty \frac{\left|J_{n-n'}(ax)\right|^2}{(x^2+z^2)\left(z^2 + 2\kappa z + a^{-2}(n'^2 - n^2) + 1\right)} \frac{1}{\in^2_{|n-n'|}(z)} x\,dx\,dz\,. \tag{6}$$

Limiting ourselves to second-order terms we expand the integrand of (6) in powers of κ:

$$\Delta E_{n,\kappa} = \Delta E_{n,0} + A_n \kappa^2 \tag{7}$$

The integration over x in (11) leads to the following results:

$$\Delta E_{n,0} = -\frac{2\alpha}{\pi}\hbar\omega_L \sum_{n'}\int_0^\infty \frac{I_{|n-n'|}(az)K_{|n-n'|}(az)}{\left(z^2+a^{-2}(n'^2-n^2)+1\right)\in^2_{|n-n'|}(z)}\,dz\,, \tag{8}$$

$$A_n = -\frac{8\alpha}{\pi}\hbar\omega_L \sum_{n'}\int_0^\infty \frac{z^2\, I_{|n-n'|}(az)K_{|n-n'|}(az)}{\left(z^2+a^{-2}\left(n'^2-n^2\right)+1\right)^3\in^2_{|n-n'|}(z)}\,dz, \tag{9}$$

Where: $I_{|n-n'|}(az)$ и $K_{|n-n'|}(az)$ are the modified Bessel functions of the first and second kind, respectively.

Let us write the expression for the polaron mass taking into account the second term in the (7), which transform as follows:

$$A_n\kappa^2 = \frac{A_n}{\hbar\omega_L}\frac{\hbar^2k^2}{2m}\,, \quad \frac{1}{m_p} = \frac{1}{m}\left(1+\frac{A_n}{\hbar\omega_L}\right), \quad m_p = m(1-A_n/\hbar\omega_L)\ . \tag{10}$$

Polaron mass calculations were performed by means of equations (5), (9), and (10) for GaAs with the following values of the parameters:

$r_p = 4nm$; $e = 1.6\times10^{-19}C$; $m = 0.067\,m_0$,
$m_0 = 9.1\times10^{-31}kg$, $\in_0 = 12.8$, $\hbar = 6.6\times10^{-34}Js$, $\kappa_F = 0.1a^{-1}$.

The results of numerical calculations for dependences ($\Delta m/m\alpha$) on the ratio $a = r_0/r_p$ are presented in Fig. 1 for the band state with $n = 0$. Here it is assumed that the Fermi level is located in the zero band.

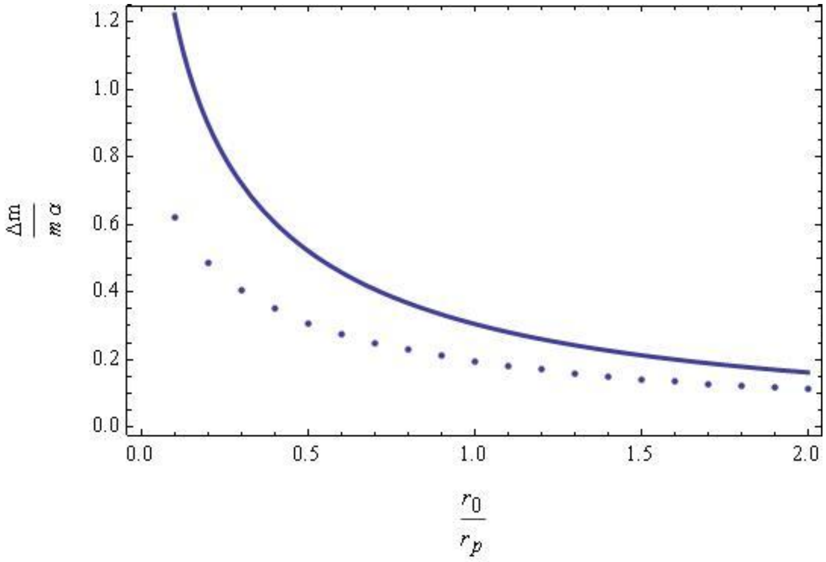

Fig. 1. Dependence of $\Delta m/m\alpha$ on the r_0/r_p ratio for the ground band state with $n = 0$: (a) solid curve is obtained without screening and (b) dotted curve is obtained taking into account screening. Here the Fermi level is located in the zero band.

The solid curve in Fig. 1 corresponds to the case without screening, but the dotted curve is obtained taking into account the screening effect. In both cases, transitions between subbands of dimensional quantization are not considered.

Using equations (9) and (10), polaron correction to the mass for the band state with $n = 0$

was calculated taking into account transitions to the subbands $n = \pm 1, \pm 2, \pm 3$.

In this case, the Fermi level is also placed in the zero band. The calculation results for the dependences $\Delta m / m\alpha$ on the parameter r_0/r_p are presented in Fig. 2. This figure shows the nonmonotonic dependence on the polaron radius. A slight minimum of the curve corresponds approximately to a value of $r_p = 2r_0$.

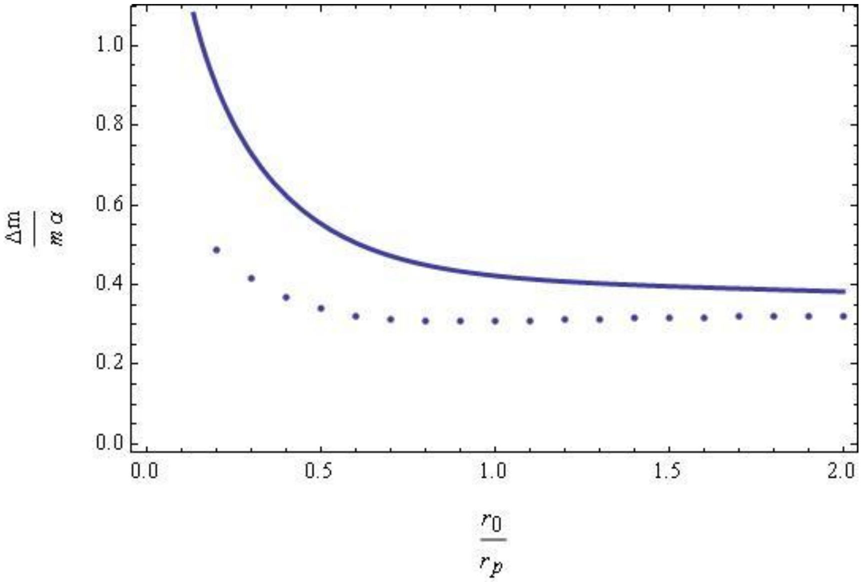

Fig. 2. Dependence of $\Delta m / m\alpha$ on the r_0/r_p ratio taking into account the transitions from the ground band state with $n = 0$ to subbands $n = \pm 1, \pm 2, \pm 3$: (a) the solid curve is obtained without taking into account screening and (b) the dotted curve is derived taking into account screening. The Fermi level is placed in the zero band.

It is evident from the dotted curve in Fig. 2 that the value of $\Delta m / m\alpha$ approached its well-known value of $\pi/8$ with increasing value of the NC radius r_0/r_p [10]. As distinct from the solid curve in Fig. 1, the value of $\Delta m / m\alpha$ in this figure does not approach the value $\pi/8$ with increasing NC radius. According to these results, we conclude that, for deriving correct expressions for the polaron effective mass for any given values of r_0/r_p in 2D systems, it is necessary to take into account the intersubband transitions.

A comparison of the dotted curves of Figs. 1 and 2 suggests that the observed the slight minimum in the dotted curve of Fig. 2 is due to the intersubband transitions. By means of equations (9) and (10), similar calculations were for the excited polaron in the subband with $n = 1$. The results of these numerical calculations for the dependences $\Delta m / m\alpha$ on the r_0/r_p ratio are given below in Fig. 3. In this case, for the polaron being in $n = 1$ state, the intersubband transitions to the states with n = -1,±2, ±3 are taken into account. The Fermi level is placed in the zero band.

By means of equations (9) and (10), similar calculations were performed for the case of location of the Fermi level in the subband with $n = 1$. Fermi wave numbers κ_{F0} *and* κ_{F1} corresponding to the states $n = 0$ and $n = 1$ are related through the ratio

$$\kappa_{F0}^2 = \kappa_{F1}^2 + a^{-2} \qquad (11)$$

The results of numerical calculations for the dependences $\Delta m / m\alpha$ on the r_0/r_p ratio are given in Fig. 4 for the polaron in the state $n = 1$ taking into account the intersubband transitions to the states with $n = -1, \pm 2, \pm 3$.

A comparison of the results presented by the dotted curves in Figs. 3 and 4 suggests that the screening effect on the polaron correction to the mass increases with increasing Fermi level.

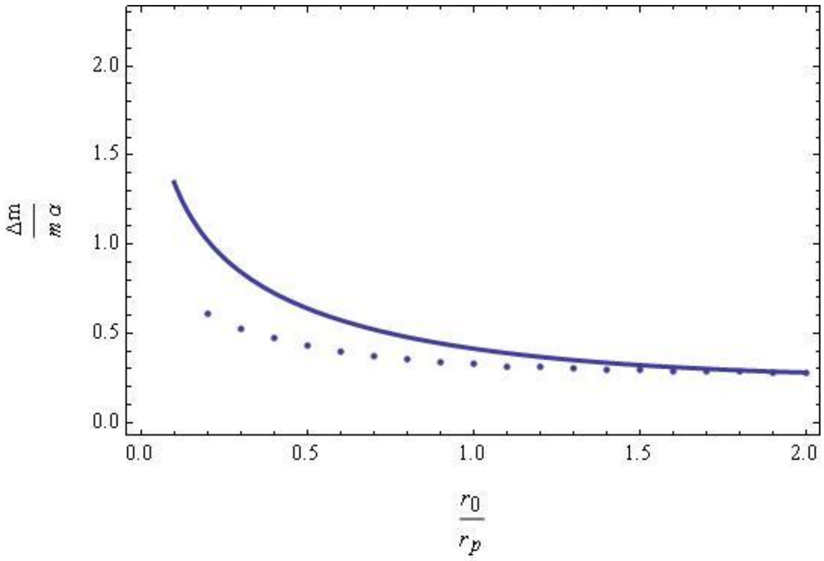

Fig. 3. Dependence of $\Delta m / m\alpha$ on the r_0 / r_p ratio taking into account transitions from excited state with $n = 1$ to subbands n = -1, ±2, ±3: (a) the solid curve is obtained without taking into account screening and (b) the dotted curve is derived taking into account screening. The Fermi level is placed in the zero band.

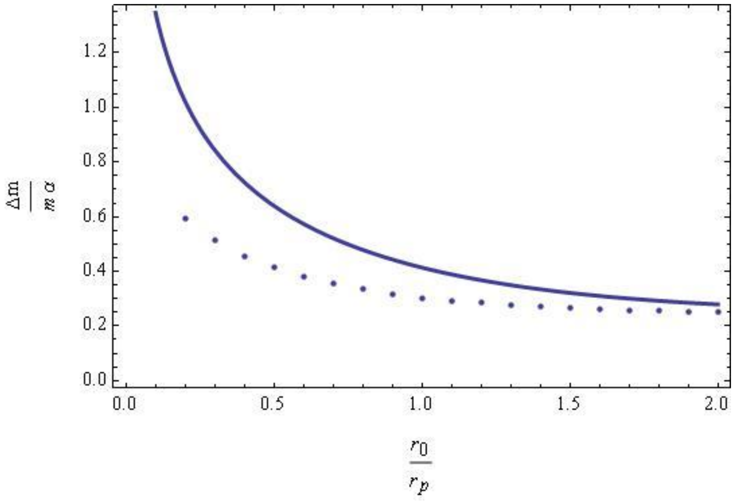

Fig. 4. Dependence of $\Delta m / m\alpha$ on the r_0 / r_p ratio taking into account transitions from the excited state of the polaron with $n = 1$ to subbands n =-1, ±2, ±3: (a) the solid curve is obtained without taking into account screening and (b) the dotted curve is derived taking into account screening. In this case, the Fermi level is placed in subband with $n = 1$.

4. Conclusions

From the dependence of the polaron correction to the mass on the radius of HNC for the ground and excited states presented in Figs. 1-4, it follows that screening contribution to the polaron mass is significant for the values a < 1. For the specified value a = 0.5 in Fig. 2 the polaron correction to the mass decreases approximately by 35% in comparison with the case without screening. For the values of the parameter a > 1 the screening contribution to polaron mass decreases with increasing HNC-radius, but the decrease in the polaron correction to the mass due to screening is still more than 30%.

Thus, the obtained numerical calculation results confirmed the significance of the screening contribution to the polaron mass.

Acknowledgments

I thank Prof. F. M. Hashimzade for valuable suggestions and useful discussions while this study was carried out.

References

[1]] V. Preisler, R. Ferreira , S. Hameau, L.A. de Vaulchier, and Y. Guldner, Phys. Rev. B 72, 115309 (2005).

[2] S.N. Klimin, J.T. Devreese, Phys. Rev. B 68, 245303 (2003).

[3] Wu. Xiaoguang, F.M. Peeters, J.T. Devreese, Phys. Rev B 36, 9760 (1987).

[4] H. Sigg, P.Wyder, J.A.Perenbom, Phys. Rev B 31, 5253 (1985).

[5] V.Ya. Prinz, V A . Seleznev, A K. Gutakovsky, A V. Chehovskiy, V V. Preobrazhenskii, M.A. Putyato, and T. A. Gavrilova, Phys.E, 6, 828 (2000).

[6] V Ya. Prinz, A.V. Chehovskiy, V V. Preobrazhenskii, B.R. Semyagin, and A.K. Gutakovsky, Nanotecnology, 13, 231 (2002).

[7] S.M. Seyid-Rzayeva, Physica Scripta 85, 035707 (2012).

[8] R.Z.Vitlina, L.I. Magarill, and A.V. Chaplik, JETP Lett. 86, 132 (2007).

[9] N.M. Guseynov, O.Z. Alekperov, S.S. Guseynova, Modern Phys. Lett. B 20, 1771 (2006).

[10] N.M.Guseinov, K.A.Rustamov, and S.M. Seyid-Rzayeva, Modern Phys. Lett.B 5, 139 (1991).

Al-DOPING EFFECTS ON THE STRUCTURAL AND OPTICAL PROPERTIES OF ZnO: Al THIN FILMS PREPARED BY THE SOL-GEL METHOD

D. Djouadi, A. Aksas, and A. Chelouche

Laboratoire de Génie de l'Environnement (LGE), Université de Béjaia , Algérie
E-mail: djameldjouadi@yahoo.fr

(Received 5 June 2012)

Abstract

Aluminum-doped zinc oxide thin films were deposited on glass substrates by the sol-gel technique. The effect of the Al concentration in the starting solution on the structural and optical properties of ZnO : Al thin films were studied. The molar ratio of the dopant (aluminum nitrate) in the solution [Al/Zn] was varied between 1% and 3%.The deposition of the layers was realized performed at room temperature by the dip-coating technique. The obtained films were inserted to a furnace and annealed at 500°C for 60 min. The X-ray diffraction (XRD), Fourier transform infrared spectroscopy (FT-IR), and optical transmittance were used to characterize the elaborated samples. XRD results show that the films have hexagonal structure and grow preferentially along the crystallographic direction (002). The average crystallite size estimated by the Scherrer formula is about 5 nm. FT-IR spectrometry showed all types of molecular vibrations in the films and confirmed the formation of a ZnO semiconductor in the samples. The refractive index and thickness of layers were determined from the optical transmittance spectra. We observed that an increase in the Al content in the solution leads to an increase in the films thickness and a decrease in their refractive index.

1. Introduction

ZnO thin films have gained considerable importance in various fields of research in recent decades because of many potential applications. It is both a semiconductor and a dielectric photoconductor and can be used as an optical waveguide. ZnO is nontoxic and has some special unique optical and electronic properties. The room temperature excitonic energy and bandgap of the ZnO semiconductor are 3.37 eV and 60 meV, respectively. It is also characterized by a high transmission coefficient which exceeds 90% in the visible. Since ZnO has a wide bandgap, it can be doped to improve its physical properties. ZnO based films are being actively studied because of their applications in solar cells [1], gas sensors [2], piezoelectric transducers [3], ultrasonic oscillators [4], and optoelectronic applications [5]. The deposition techniques of thin films are many and varied. They include the laser ablation [6], magnetron sputtering [7], the chemical vapor deposition [8], spray pyrolysis [9], and sol-gel process [10-12].

In this work, ZnO and ZnO : Al thin films were prepared by the sol-gel procedure and deposited on glass substrates by the dip-coating technique. The results of structural and optical characterizations of the synthesized films are reported and discussed.

2. Experimental

The precursor solution was prepared by the sol-gel method by mixing dihydrate zinc acetate, ethanol, diethanolamine (DEA), and aluminum nitrates for doping in adequate proportions of mass and volume. The solution concentration was 0.6 M. Ethanol and DEA were used as a solvent and catalyst, respectively. The prepared pure and Al doped ZnO solutions were kept under continuous magnetic stirring at 40°C for 1 h. The glasses used as substrates were first washed with a liquid detergent, rinsed with distilled water, and then immersed in 4 M nitric acid for 24 h. Then they were rinsed under ultrasound with ethanol and distilled water during 15 min at T= 60°C. Finally, after rinsing with bi-distilled water, slides were dried at T = 200°C for 24 h in the ambient air. The deposition was carried out using a KSV dip-coater using a dip-draw speed of 20 mm/min. The number of deposited layers on the slides was 3. The annealing of the resulting thin films was conducted in the ambient air in a muffle furnace at 500°C. Amorphous zinc oxide was transformed into pure and Al-doped ZnO after the thermal treatment. The as-prepared thin films were characterized by X-ray diffraction (XRD) at grazing incidence. The XRD measurements were performed with a PanAlytical diffractometer operating at 40 kV and 30 mA using Cu-$K\alpha$ radiation (λ = 1.54 Å). FTIR spectra were recorded with a Shimadzu Iraffinity-1 spectrometer. The optical transmittance spectra were obtained using a Jobin-Yvon HR460 UV-visible single beam spectrophotometer.

3. Results and discussion

Figure 1 show the XRD spectra registered under grazing incidence for the pure and Al-doped ZnO thin films prepared by the sol-gel method associated with the dip-coating technique deposition. All samples were annealed at 500°C for one hour. It is found that the films grow in a preferred crystallographic orientation along a c-axis perpendicular to the substrate surface. All spectra exhibit a dominant (002) peak located near 2θ=34.5°. The peak positions indicate that ZnO crystallites have a hexagonal structure. The low intensity of these peaks is due to the very small thickness (<100 nm) of the films and their enlargement is due to the nanometric size of ZnO crystallites (<10 nm) [13].

The peak intensity decreases with increasing Al content due to the crystalline quality degradation. With increasing Al content, the (002) peak slightly narrows. This shows that the crystallite size increases with increasing impurity concentration. With an increase in the Al concentration, the (002) peak shifts to smaller diffraction angles (2θ = 34.82° (pure ZnO), 34.78° (ZnO : Al 1%), 34.56° (ZnO : Al 2%), and 34.34° (ZnO : Al 3%)). Many authors attribute this shift to the substitution of zinc atoms with those of aluminum in the hexagonal structures [6]. The crystallite size calculated from the Scherrer's formula for the (002) peak varies between 2.34 and 2.62 nm. The found lattice parameters are constant and show that the impurities do not affect the ZnO crystalline lattice.

To confirm the formation of ZnO and ZnO : Al semiconductors, the resulting samples were characterized by Fourier transform infrared spectroscopy (FT-IR). The obtained IR spectra are shown in Fig. 2. The absorption bands located at 1024 cm^{-1} and 540 cm^{-1} are due to the bending vibration of Si-O bond of the substrate (glass) and to the bending vibration of the Al-O bond, respectively. The two bands centered around 460 and 420 cm^{-1} are due to ZnO [14]. We can note that the band attributed to ZnO is remarkable because it is representative of good crystallization of the layers and increases in absorbance with increasing aluminum content.

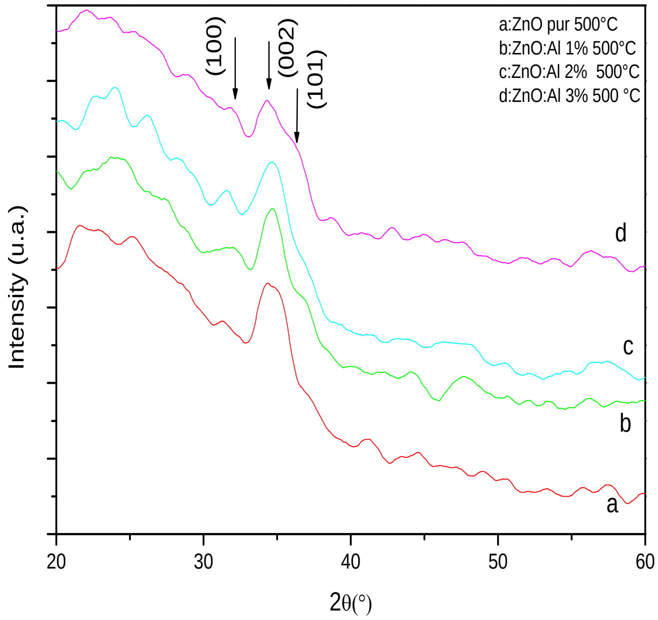

Fig. 1. XRD spectra of the prepared thin films.

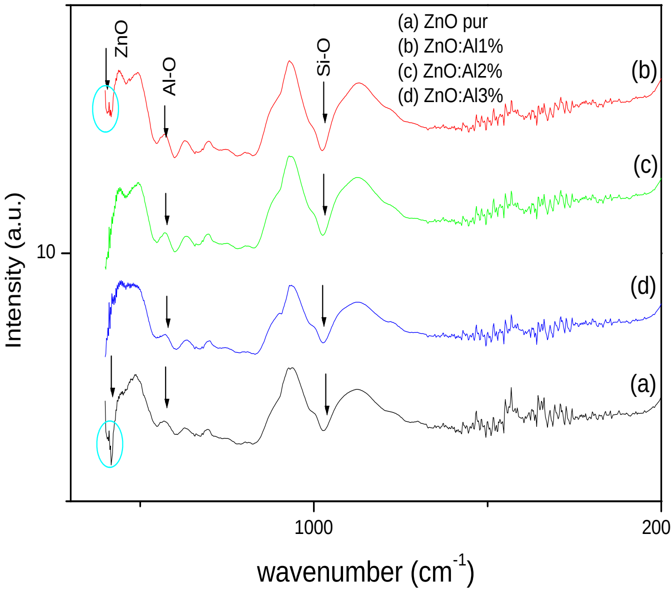

Fig. 2. FTIR spectra of the prepared ZnO and ZnO : Al films.

To study the effect of the degree of doping on the optical transmittance of the thin films, we show in fig. 3 the optical transmittance spectra for the resulting samples. It is found that the curve slopes and the transmittance increase with increasing aluminum concentration in the films. The doped films become more transparent. The increase in transmittance in the visible with increasing Al content is due to increasing of the band gap. This increase can be explained by the Burstein-Moss effect: the charge carriers introduced by aluminum atoms in the layers satisfy the energy bands located above the conduction band thus causing a widening of the optical gap.

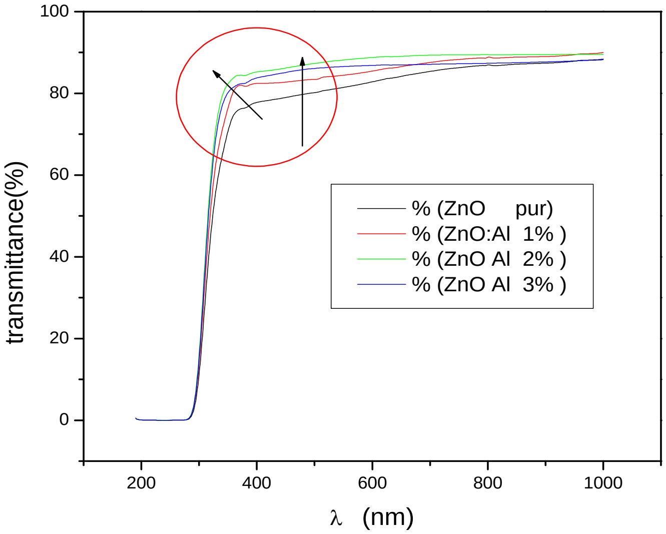

Fig. 3. Transmittance spectra of the prepared ZnO and ZnO : Al films.

The refractive index and thicknesses of the films were determined from optical transmittance versus wavelength spectra [15]. The evolution of these parameters with degree of doping is shown in Fig. 4.

With increasing Al content in the samples, the refractive index decreases and the films thickness increases. This is can be explained by the fact that the introduction of Al atoms into ZnO increases the charge carrier concentration in the ZnO : Al films as was confirmed by electrical resistivity measurements carried out by Xue et al. [16]. The authors of this work showed that the resistivity decreases with increasing aluminum content, which increases the charge carrier concentration in the films. On the other hand, Kim et al. [6] reported that the refractive index decreases when the charge carrier concentration increases. Also, doping effect increases the optical gap which is directly related to the material refractive index.

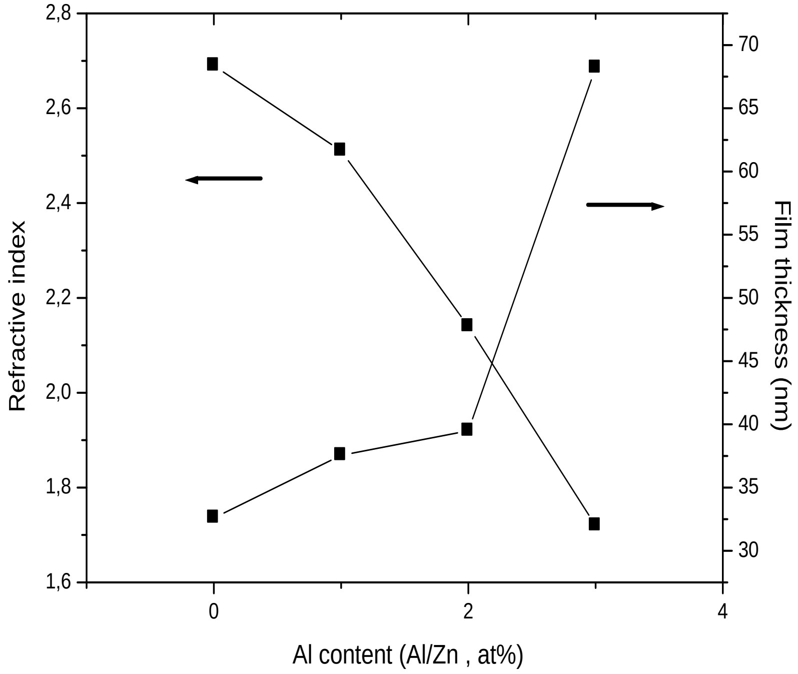

Fig. 4. Variation of refractive index and films thickness with degree of doping with Al.

4. Conclusions

ZnO and ZnO: Al thin films were prepared by the sol-gel and deposited by dip-coating technique on glass substrates. The effects of aluminum content on the structural and optical properties of the films were observed. The pure and Al doped ZnO deposited films showed a preferred orientation along the axis perpendicular to the c-surface of the substrate. The ZnO: Al nanocrystallites have a hexagonal wurtzite structure. The obtained XRD spectra revealed that the introduced aluminum atoms do not affect the ZnO crystalline structure. The prepared samples exhibited a high UV-visible transmission (80%). An amplification of the ZnO absorption band with Al content was observed in the FTIR spectra. An increase in the Al concentration in the samples decreases the refractive index and increases the film thickness.

References

[1] M. Krunks, A. Katerski, T. Dedova, I. Oja Acik, and A. Mere, Solar Energy Mater. Solar Cells 92, 9, 1016 (2008).

[2] S.C. Ko, Y.C. Kim, S.S. Lee, S.H. Choi, and S.R. Kim, Sensors Actuators A 103, 130 (2003).

[3] S.H. Lee, S.S. Lee, J.J. Choi, J.U. Jeon, and K. Ro, Microsyst. Technol. 11, 416 (2005).

[4]. D.L. Devoe, Sensors Actuators A 88, 263 (2001).

[5] U. Ozgur, Y.I. Alivov, C. Liu, A. Teke, M.A. Reshchikov, S.Dog¢an, V. Avrutin, S.-J. Cho, and H. Morkoc, J. Appl. Phys. 98, 041301 (2005).

[6] H. Kim, A. Piqué, J. S. Horwitz, H. Murata, Z. H. Kafafi, C. M. Gilmore, and D. B. Chrisey, Thin Solid Films 377-378, 798 (2000).

[7] P.M. Ratheesh Kumar, C. Sudha Kartha, K.P. Vijayakumar, T. Abe, Y. Kashiwaba, F. Singh, and D.K. Avasthi, Semicond. Sci. Tech. 20, 120 (2005).

[8] T. M. Barnes, K.Olson, and C.A. Woldena, Appl. Phys. Lett. 86, 11, 112112 (2005).

[9] V. Musat , B. Teixeira, E. Fortunato, R.C.C. Monteiro, and P. Vilarinho , Surf. Coat. Technol. 180–181, 659 (2004).

[10] Z.Q. Xu , H. Deng, J. Xie, Y. Li, and X.T. Zu, Appl. Surf. Sci. 253, 476 (2006).

[11] R.E. Marotti, C.D. Bojorge, E. Broitman, H.R. Cánepa, J.A. Badán E.A. Dalchiele, and A.J. Gellman, Thin Solid Films 517, 1077 (2008).

[12] M. Igalson and C. Platzer-Bjorkman, Solar Energy Mater. Sol. Cells 84, 93 (2004).

[13] C. D. Bojorge ,H. R. Canepa , U. E. Gilabert,D. Silva , E. A. Dalchiele, and R. E. Marotti, J. Mater. Sci.: Mater. Electron. 18, 1119 (2007).

[14] K.P. Bhuvana, J. Elanchezhiyan, N. Gopalaktishnan, and T. Balasubramanian, Appl. Surf. Sci. 255, 2026 (2008).

[15] M. Caglar, Y. Caglar, and S. Ilican, J. Optoel. Adv. Mater. 8, 4, 1410 (2006).

[16] S.W. Xue, X.T. Zu, W.G. Zheng, H.X. Deng, and X. Xiang, Physica B 381, 209 (2006).

INTERBAND ABSORPTION OF LIGHT IN BISMUTH NANOSTRUCTURES

N. B. Mustafayev[1,2]

[1]*Institute of Physics, Azerbaijan National Academy of Sciences, Baku, Azerbaijan*
[2]*Physics Department, Azerbaijan National Academy of Aviation, Baku, Azerbaijan*
e-mail: nadirmustafayev@gmail.com

(Received 11 September 2012)

Abstract

Interband absorption of light in bismuth nanostructures has been studied in the framework of a complex model for electron spectrum of Bi, such as the Cohen model, the Abrikosov-Falkovsky model, and the McClure model. The obtained results differ qualitatively from those obtained in the framework of simple band models, such as the parabolic band model and the Lax two-band model. It is shown that both the interband transition with quantum number conservation and the interband transition without quantum number conservation are allowed in the framework of complex models for electron energy spectrum of Bi. Due to the interband transitions without quantum number conservation (these transitions are forbidden in simple band models), the peak of optical absorption in measured spectra can occur at lower photon energies than in the spectra simulated in the framework of simple band models. A similar difference between the peaks was observed by Black et al. in Bi nanowires. The interband transitions without quantum number conservation substantially complicate the oscillation pattern and the identification of absorption peaks. The frequency dependence of the coefficient of interband absorption calculated in the framework of the McClure model has pronounced peaks, whereas in the simple band models this dependence has a step-like pattern. It is concluded that the McClure model enables the oscillation behavior of interband absorption in bismuth nanostructures to be properly described.

1. Introduction

Bismuth is a semimetal with a small band overlap and a very anisotropic electron effective mass tensor. For a bismuth structure of small enough thickness for significant quantum confinement to occur, the structure undergoes a transition from a semimetal with a small band overlap to a semiconductor with a small direct band gap. This transition, as well as other quantum effects, occurs in bismuth structures at relatively large thicknesses because of the small effective mass and small band overlap of bulk bismuth.

Bismuth nanostructures are promising for optical applications because of their unusual properties. For example, quantum wells, quantum dots, and quantum wires usually have to be doped in order to populate the lowest subband and to allow for optical excitation of the electrons to higher subbands. In bismuth nanostructures, the lower subbands are partially filled with electrons, and intersubband transitions can be observed even in undoped samples.

It should be noted that many commonly used approximations are not valid for bismuth. For example, a simple parabolic band model is not applicable for the description of electron energy spectrum at the *L*-point of the Brillouin zone, since the *L*-point electronic bands are extremely anisotropic and have strong nonparabolic effects. Several models were proposed to describe the energy spectrum of Bi [1]: the Lax model (this model is also called the ellipsoidal nonparabolic model), the Cohen model (or the nonellipsoidal nonparabolic model), the Abrikosov-Falkovsky model, the McClure model, and the McClure-Choi model.

The Lax model is a comparatively simple two-band model. This model is often used for studying quantum size effects in Bi films [2] and wires [3-5]. The Lax model makes it possible to obtain qualitative but not quantitative agreement with experimental results. For example, the local minimum in the transmission, which corresponds to a peak in the optical absorption, occurs at higher photon energies in the calculated spectra compared to the experimentally measured spectra [5]. A possible explanation for the discrepancy is that the Lax two-band model is unable to take into account the far-band contributions.

The aim of the present paper is to study optical absorption in bismuth nanostructures in the framework of complex models taking into account the far-band contributions. It follows from calculations that the results obtained in the framework of the complex models (such as the Cohen model, the Abrikosov-Falkovsky model, and the McClure model) differ qualitatively from the results obtained in the framework of the simple models (such as the parabolic model and the Lax model).

For example, in the framework of simple models, the threshold of interband absorption is defined as $\hbar\omega_0 = E_g + 2E_F$, where E_g is an energy gap at the L-point of the Brillouin zone, and E_F is the Fermi energy. This is because only interband transitions with the selection rule $N_v = N_c$ (where N_v is an initial state in the valence band, and N_c is a final state in the conduction band) are allowed in the simple models. In the framework of the complex models, interband transitions with both the selection rule $N_v = N_c$ and the selection rule $N_v + N_c = 2l + 1$ (where l is an integer) are allowed; therefore, the interband absorption at frequencies less than ω_0 becomes possible.

The frequency dependence of the coefficient of interband absorption $\alpha(\omega)$ in Bi quantum wells calculated in the framework of complex models has pronounced peaks, whereas the dependence $\alpha(\omega)$ calculated in the framework of simple models does not have these peaks. In simple models, as it is known, this dependence has a step-like pattern [6].

2. Energy spectrum

The Fermi surface of electrons in Bi consists of three valleys tilted at a small angle with respect to the basal plane. The valleys transfer into each other under a rotation of $\pm 120^\circ$ around the trigonal z axis. If the quantization axis is parallel to z, the wave function for electrons can be tried in the form of a one-column matrix with elements $C_j U_j f_j(z) \exp(ik \cdot \rho)$, where $k = (k_x, k_y, 0)$ and $\rho = (x, y, 0)$, the x axis is parallel to the binary axis, the y axis is parallel to the bisectrix axis (the small tilt angle may be neglected), U_j are the Bloch functions, C_j are unknown coefficients and $f_j(z)$ are unknown functions which can be derived from a solution of the differential equation system obtained using an effective Hamiltonian of the energy spectrum model. If the Bloch functions have the same value at both boundaries of quantum-well structure, the condition of size quantization takes the quasi-classical form. In this case, the conduction and valence bands are described by wave functions of the form

$$\psi_{\mathbf{k},N}^{j} = \exp(ik \cdot \rho)\left(A_{\mathbf{k},N}^{j} \sin\frac{\pi Nz}{d} + B_{\mathbf{k},N}^{j} \cos\frac{\pi Nz}{d}\right). \tag{1}$$

Here N is a quantum number, d is the thickness of quantum-well structure. The explicit forms of $A_{\mathbf{k},N}^{j}$ and $B_{\mathbf{k},N}^{j}$ are determined by the model parameters and the Bloch functions. The cumbersome expressions for $A_{\mathbf{k},N}^{j}$ and $B_{\mathbf{k},N}^{j}$ are not given here.

It should be noted that, for the complex models of energy spectrum, it is necessary to impose a zero boundary condition for the total wave function rather than for the envelopes. In the case of simple models, the zero boundary condition for envelopes $f_j(0) = f_j(d) = 0$ coincide with the zero boundary condition for the total wave function $\psi(\rho,0) = \psi(\rho,d) = 0$. However, in the case of complex models, these conditions do not coincide with each other. It is impossible to construct all $f_j(z)$ simultaneously in the form of partial solutions. The functions $f_j(z)$ are related to each other via the initial set of equations. It may be shown that the zero boundary condition for the total wave function leads to the following boundary condition for the envelopes:

$$\{1 + R_j(z_0)\nabla_z\} f_j(z_0) = 0. \tag{2}$$

Here z_0 has two values: $z_0 = 0$ and $z_0 = d$. There is a relation between $R_j(z_0)$ and the values of the Bloch functions fixed at the boundaries of quantum-well structure. Condition (2) coincides formally with those obtained in [7]. In [7], the quantity R is a real constant (with the dimension of length) which yields information about surface properties of crystals.

One can derive the electron spectrum in quantum-well structure from solution of the Schrödinger equation using the effective Hamiltonian of the energy spectrum model. From calculations made, for example, using the effective Hamiltonian of the McClure model [8], it follows that the electron energy spectrum is of the form

$$\left(E - \frac{\alpha_c}{2}k_y^2\right)\left(E + E_g + \frac{\alpha_v}{2}k_y^2\right) = Q_{11}^2 k_x^2 + Q_{22}^2 k_y^2 + Q_{33}^2\left(\frac{\pi N}{d}\right)^2. \tag{3}$$

Here Q_{ii} are matrix elements of the velocity operator which characterize the $\kappa \cdot p$ interaction between the valence and conduction bands in the three principle directions, α_c and α_v are the free electron and far-band contributions to the inverse band-edge effective mass of the conduction and valence bands, respectively, in the direction of the isoenergetic surface elongation. The parameters of the McClure model were determined in [9].

3. Optical absorption

The coefficient of interband absorption calculated in the framework of complex models is of the form $\alpha = \alpha_1 + \alpha_2$, where α_1 corresponds to transitions with the selection rule $N_v = N_c$, and α_2 corresponds to the transitions with the selection rule $N_v + N_c = 2l + 1$ (Fig. 1b). This occurs because, for direct interband transitions, the dipole matrix elements calculated using (1) are of the form

$$\langle \sigma_c N_c | p_i | \sigma_v N_v \rangle = M_{1,i}\delta_{N_c N_v} + M_{2,i}\kappa_{N_c N_v}. \tag{4}$$

Here σ_v and N_v are the spin and quantum numbers of the initial state in valence band, σ_c and

N_c are the spin and quantum numbers of the final state in conduction band, $M_{1,i}$ and $M_{2,i}$ are cumbersome expressions,

$$\delta_{N_c N_v} = \begin{cases} 0; & N_c \neq N_v \\ 1; & N_c = N_v \end{cases}$$

$$\kappa_{N_c N_v} = \begin{cases} 0; & N_c - N_v = 2l \\ \dfrac{2d}{\pi} \dfrac{N_c N_v}{(N_c + N_v)(N_c - N_v)}; & N_c - N_v = 2l + 1 \end{cases}$$

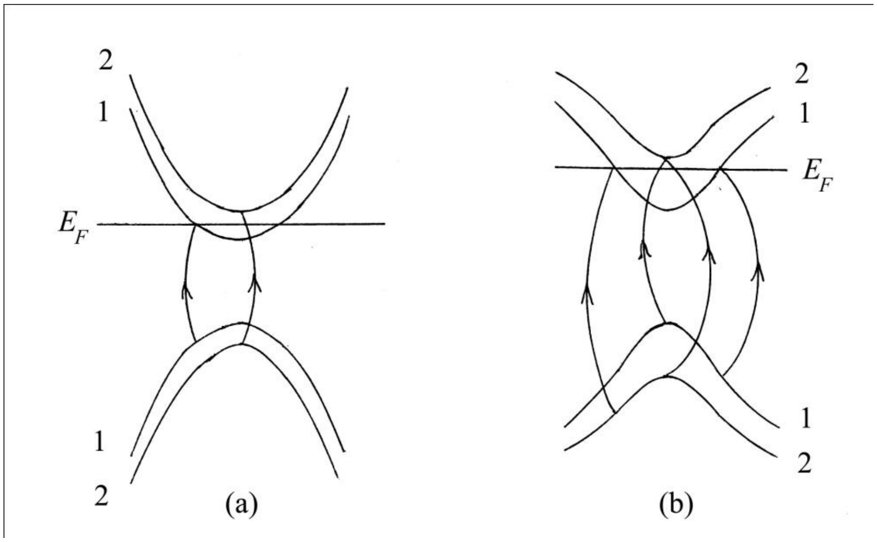

Fig. 1. Interband transitions in (a) simple and (b) complex models for the energy spectrum of Bi quantum-well structures.

If the polarization vector is parallel to the binary axis ($i = x$), the expression for α_1 is of the relatively simple form

$$\alpha_1 = \alpha_0 \sum_N \sqrt{1 - 2m}\, K(m) H(\chi). \tag{5}$$

Here

$$\alpha_0 = \frac{3}{2} \left(\frac{4e^2}{nc\hbar d} \right) \frac{Q_{11}}{\sqrt{E_g (\alpha_c + \alpha_v) + 4Q_{22}^2}},$$

n is the index of refraction, c is the velocity of light, $K(m)$ is the first complete elliptic integral, $H(\chi)$ is the Heaviside function,

$$m = \frac{b^2}{a^2 + b^2},$$

$$a^2 = b^2 + \frac{2}{\mu + 1} + \frac{4\lambda}{(\mu + 1)^2},$$

$$\mu = \frac{\alpha_v}{\alpha_c},$$

$$\lambda = \frac{2Q_{22}^2}{E_g \alpha_c},$$

$$\eta = \frac{\hbar\omega}{E_g},$$

$$\varepsilon_0 = \frac{\pi Q_{33}}{E_g d},$$

$$b^2 = \frac{1}{\mu+1}\left(-\frac{\mu+1+2\lambda}{\mu+1} + \sqrt{\left(\frac{\mu+1+2\lambda}{\mu+1}\right)^2 + \eta^2 - 1 - 4\varepsilon_0^2 N^2}\right),$$

$$\varepsilon_F = \frac{E_F}{E_g},$$

$$\varepsilon_N = \frac{1}{2}\left(-1+\sqrt{1+4\varepsilon_0^2 N^2}\right),$$

$$\chi = \begin{cases} \eta - 1 - 2\varepsilon_N\ ; & \varepsilon_F < \varepsilon_1 \\ \eta - 1 - 2\varepsilon_F\ ; & \varepsilon_F > \varepsilon_1 \end{cases}$$

The expression for α_2 is of rather cumbersome form, so it is not given here. Though $\alpha_2 < \alpha_1$, the interband transitions without quantum number conservation substantially complicate the oscillation pattern and the identification of absorption peaks.

To simplify the problem, consider here only the case where $\varepsilon_F < \varepsilon_1$. From the solution of the electroneutrality equation at helium temperature, it follows that the Fermi level is located below the bottom of the first subband if $d = 30\,\text{nm}$, where the overlap between the L and T bands disappears and the Bi quantum-well structure undergoes a semimetal-semiconductor transition. The frequency dependence of the coefficient of interband absorption calculated in the framework of the McClure model for a 30-nm-thick quantum-well structure at helium temperature is plotted in Fig. 2 It is evident from this figure that the frequency dependence has pronounced peaks.

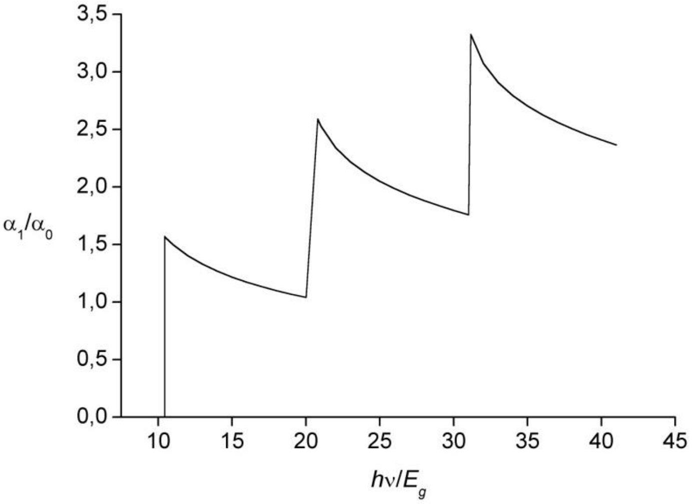

Fig. 2. Frequency dependence of the coefficient of interband absorption calculated in the framework of the McClure model for a 30-nm-thick Bi quantum-well structure at helium temperature.

4. Discussion

Optical absorption in thin Bi films under the conditions of a quantum size effect was first observed in [10]. In [10], the spectral dependence of transmission of the Bi films evaporated on a KBr substrate was measured at room temperature. The following results were obtained: a shift of the red edge of the optical absorption upon the variation in film thickness d, a semimetal-semiconductor transition at $d = 30\,\text{nm}$, a nonmonotonic spectral dependence of the optical transmission, and a shift of the absorption maximum near the absorption edge with changing film thickness. The results were qualitatively explained in the framework of the parabolic band model.

A further research of the optical absorption in Bi films was made in [11, 12]. In [11], a blueshift of the IR absorption measured on Bi films epitaxially grown on BaF_2 substrates was observed. From far-infrared reflectivity, the plasma frequencies ω_p of films as a function of film thickness d were determined. With decreasing film thickness, ω_p initially increased and then abruptly decreased near $d = 10\,\text{nm}$. This was considered as a sign of a semimetal-semiconductor transition caused by the quantum size effect.

In [12], the reflectivity and transmittivity of thin monocrystalline bismuth films on barium fluoride were measured in a spectral range of 80 to $4000\,\text{cm}^{-1}$. The measurements were performed at room temperature and at 5 K. At 5 K, thickness-dependent absorption maxima occurred at the film thickness less than 50 nm. These maxima were interpreted as transitions between subbands of the valence and conduction bands at the *L*-points of the Brillouin zone. The spectral position of the maxima was explained assuming an elevated gap energy due to the lattice mismatch between the films and the substrates.

Optical absorption in Bi nanowires prepared inside the pores of anodic alumina was studied in [3-5]. In [3, 4], the contributions to the optical absorption from both intersubband and direct interband transitions were modeled, and the results were compared to the measured absorption spectra. The theory for the absorption resulting from a direct interband transition did not show agreement with the experimentally measured data. The smaller intensity absorption peaks were thus attributed to optical absorption resulting from intersubband transitions, but the intersubband theory did not explain the large peak near $\sim 1000\,\text{cm}^{-1}$. The magnitude of the energy shift of this peak with a change in wire diameter, as well as the overall shape of the absorption spectra near this absorption peak, was not explained.

In [5], the optical absorption resulting from indirect transitions was studied in order to explain the observed spectra. Although the spectra simulated and measured in [5] are similar, the local minimum in the transmission, which corresponds to a peak in the optical absorption, occurs at a higher photon energy in the simulated spectra than in the experimentally measured spectra. For example, in 45-nm-diameter wires at room temperature, the wave numbers of the simulated and measured absorption peaks differ by $\sim 400\,\text{cm}^{-1}$. This difference can result from approximations used in [5]. For example, the approximation of the *L*-point bands by the Lax two-band model makes it impossible to take into account the contributions from bands outside of the two-band model.

Infrared transmission spectroscopy measurements on single bismuth nanowires of various diameters *d* were presented in [13]. The strong absorption signal was attributed to interband transitions. The blueshift was assigned to quantum size effects leading to the *d*-dependent splitting of the energy bands and to a respective shift of energy gaps.

In [3-5] and [10-13], the experimental results were analyzed in the framework of simple models (the parabolic band model and the Lax two-band model). The complex models (such as the Cohen model, the Abrikosov-Falkovsky model, and the McClure model) were not used. In [14-16], we used the Cohen model and the Abrikosov-Falkovsky model to study optical absorption and electronic Raman scattering in thin Bi films. In the present paper, the McClure model is used. It follows from calculations that the results obtained in the framework of the complex models qualitatively differ from the results obtained in the framework of the simple models.

For example, only interband transitions with quantum number conservation are allowed in simple models (Fig. 1a); therefore, the threshold of interband absorption is defined as $\hbar\omega_0 = E_g + 2E_F$. In the framework of complex models, both the interband transition with quantum number conservation and the interband transition without quantum number conservation are allowed; so, the interband absorption at frequencies less than ω_0 is possible.

As an illustration, consider the simple situation (Fig. 1b) where only the first subband is filled. The energy for electron transition from the state $N_v = 1$ to the state $N_c = 2$ ($\hbar\omega = E_g + E_{c,2}$) is less than the energy for electron transition from the state $N_v = 1$ to the state $N_c = 1$ ($\hbar\omega_0 = E_g + 2E_F$). If E_F is near the bottom of the second subband, the difference in energy $\hbar(\omega_0 - \omega) \approx E_F$.

According to [4], in 41.5-nm-diameter wires at room temperature, the Fermi energy E_F lies 48 meV above the lowest L-point conduction band minimum. Therefore, the difference in energy between the interband transition with quantum number conservation and the interband transition without quantum number conservation is $\hbar(\omega_0 - \omega) = 387\ \text{cm}^{-1}$. This value is in close agreement with the difference ($\sim 400\ \text{cm}^{-1}$) in wave numbers of the simulated and measured absorption peaks in 45-nm-diameter wires [5]. Thus, due to the interband transitions without quantum number conservation, the peak of optical absorption in measured spectra can occur at lower photon energies than in the spectra simulated in the framework of the Lax model. These transitions are forbidden in the Lax model, but they are allowed in the framework of complex models.

The frequency dependence of the coefficient of interband absorption calculated in the framework of the complex models has pronounced peaks (Fig. 2). The dependence $\alpha(\omega)$ calculated in the framework of simple models does not have these peaks. In simple models, as it is known, this dependence has a step-like pattern [6]. Thus, complex models of electron spectrum describe the oscillation behavior of interband absorption in low-dimensional Bi structures better than the parabolic band model and the Lax two-band model.

5. Conclusions

In the framework of complex models for electron energy spectrum of Bi, such as the Cohen model, the Abrikosov-Falkovsky model, and the McClure model, both the interband transition with quantum number conservation and the interband transition without quantum number conservation are allowed. Due to the interband transitions without quantum number conservation (these transitions are forbidden in simple band models), the peak of optical absorption in measured spectra can occur at lower photon energies than in the spectra simulated in the framework of simple band models. The interband transitions without quantum number conservation substantially complicate the oscillation pattern and the identification of absorption peaks. The frequency dependence of the coefficient of interband absorption calculated in the framework of the complex models has pronounced peaks, whereas in simple band models this dependence has a step-like pattern. The use of the McClure model makes it possible to properly describe the oscillation behavior of interband absorption in low-dimensional Bi structures.

References

[1] Edel'man V.S., Sov. Phys. Usp. 20, 819 (1977).
[2] Zaluzny M. and Lukasik A., Phys. Status Solidi B 137, 607 (1986).
[3] Black M.R., Padi M., Cronin S.B., Lin Y.-M., Rabin O., McClure T., Dresselhaus G., Hagelstein P.L., and Dresselhaus M.S., Appl. Phys. Lett. 77, 4142 (2000).
[4] Black M.R., Lin Y.-M., Cronin S.B., Rabin O., and Dresselhaus M.S., Phys. Rev. B 65, 195417 (2002).
[5] Black M.R., Hagelstein P.L., Cronin S.B., Lin Y.-M., and Dresselhaus M.S., Phys. Rev. B 68, 235417 (2003)
[6] Davies J.H., The Physics of Low-Dimensional Semiconductors: An Introduction, Cambridge, University Press, Cambridge, 1998.
[7] Volkov V.A. and Pinsker T.N., Sov. Phys. JETP 43, 1183 (1976).
[8] McClure J.W., J. Low Temp. Phys. 25, 527 (1976).
[9] Akhmedov S.Sh., Herrmann R., Kashirin K.N., Krapf A., Kraak V., Ponomarev Ya.G., and Subakova M.V., Sov. Phys. JETP 70, 370 (1990).
[10] Lutskii V.N. and Kulik L.A., JETP Lett. 8, 80 (1968)
[11] Takaoka S. and Murase K., J. Phys. Soc. Japan 54, 2250 (1985).
[12] Peschke Ch., Phys. Status Solidi B 191, 325 (1995).
[13] Cornelius T.W., Toimil-Molares M.E., Neumann R., Fahsold G., Lovrincic R., Pucci A., and Karim S., Appl. Phys. Lett. 88, 103114 (2006).
[14] Mustafaev N.B. and Shakhtakhtinskii M.G., Phys. Status Solidi B 124, K151 (1984).
[15] Gadzhiev A.T., Gashimzade F.M., and Mustafaev N.B., Solid State Phys. 30, 3146 (1988).
[16] Gadzhiev A.T., Gashimzade F.M., and Mustafaev N.B., J. Phys.: Condens. Matter 3, 4677 (1991).

SOME PROPERTIES OF Bi_2Te_3 AND PbTe CRYSTALS AND CONVERTERS ON THEIR BASIS

D. F. Meglei

Institute of Electronic Engineering and Nanotechnology „D.Ghitsu”,
Academy of Sciences of Moldova, Academiei str. 3/3, Chisinau, MD 2028, Republic of Moldova
E-mail: meglei@iieti.asm.md

(Received 10 May 2012)

Abstract

Owning to the miniaturization of solid state electronic devices, the problem of studying the physical and physicochemical processes in low-dimensional condensed systems, in addition to scientific interest, is of particular practical significance. In theoretical terms, this is due to the fact that a one-dimensional model has simpler solutions; in the experimental aspect, this is the possibility to obtain highly perfect single crystals, the size effects in which are more severe than, for example, in thin layers, because of two-dimensional limitations. In practical terms, these systems can be used in all modern fields of solid state electronics, because these materials make it possible to solve some problems in instrument engineering related to miniaturization, improving the accuracy and stability, and expanding the range of allowed climatic and mechanical effects. A small diameter of a microwire (MW) ($1 \cdot 10^{-6}$ m) provides a significant reduction in the weight and dimensions of elements made of MWs and decreases their mechanical, thermal, and electrical inertia. A solid insulation protects the core material from the interaction with the environment, which contributes to an increase in the stability, strength, and other parameters of sensors prepared on their basis. Narrow-gap semiconductors, such as lead telluride (PbTe) and bismuth telluride (Bi_2Te_3), are promising materials for thermoelectrics, optoelectronics, and laser technology. Therefore, systems of complex components based on them, in particular, thin films and MWs, have been intensively studied in recent years [1-5], the more so as the problem of production of converters on their basis cannot be considered solved at the moment.

1. Technique for the Preparation of Glass-Insulated MWs

For the first time, thin metal wires in glass insulation were obtained in 1924 using a conventional gas heater [6]. However, this method was not used widely because of the low production efficiency.

Cylindrical single-crystal wire crystals (WCs) of bismuth in glass insulation were prepared by liquid phase casting by the Ulitovsky method [7, 8]. Using this technique, Bi WCs with the diameters of the core and glass insulation ranging from a few tens of fractions to a few tens and hundredths of microns were prepared.

The casting of Bi MWs has several features:

(1) The melting point of Bi is much lower than the softening temperature of glass used for the casting of MWs; therefore, it is necessary to overheat the material to obtain a capillary.

(2) In the experiments, various types of glass (Nonex glass, Pyrex, C37-2, molybdenum glass, etc.) were tested.

(3) The choice of the glass–material pair for the formation of MWs plays an important role for

the successful casting of MWs. The adhesion between the material and the glass is very important, because the melt is drawn by a moving capillary only in the interaction between the material and the glass. Good adhesion of Bi and glass is provided by the presence of a thin oxide film on the surface of molten Bi.

(4) Experiments and calculations show that the mass of Bi after melting is suspended only due to the ponderomotive forces of the electromagnetic field of the inductor (the critical mass is 0.4-0.8 g). This is explained by the low capillary constant and high electrical resistance of bismuth. Despite this, owning to the existence of relatively viscous glass insulation, it is possible to draw a microwire from a droplet whose mass is much higher than critical. The shape of a Bi droplet differs from conventional; it has a shape of a bulb with the top directed downward to the capillary.

(5) A sharp temperature decrease along the height of the droplet is observed at 300-400°C; as a result, its upper part is located in a less intense electromagnetic field. In connection with this circumstance, the melt in the upper part of the droplet is additionally suspended due to the interaction with the glass insulation, which is more viscous. This explains the above methods [7] for high-speed drawing of masses higher than the critical one.

The totality of the above factors makes it possible to prepare bismuth MWs that are more uniform along the axis than metal ones.

By controlling the temperature of the droplet, the capillary drawing rate, and the ampoule lowering rate, it is possible to obtain fairly long WCs with different diameters.

Later on, the technique for preparing glass-insulated MWs from various semiconductor materials with necessary physical parameters, such as bismuth telluride (Bi_2Te_3), lead telluride (PbTe), Bi doped with different impurities, was optimized.

The crystallization of MWs occurs due to supercooling at the solid-melt interface (the cooling rate is about 10^5-10^6 deg/s). The value of supercooling is characterized by the expression

$$\theta_{min} = (\lambda \kappa)^{-1} (\varepsilon/\kappa)^{\varepsilon/2g} \left[(2 \lambda g \theta_{nn} - \gamma v g) / (\gamma v g)^{\varepsilon/\kappa} \right]^{\kappa/2g},$$

where $\varepsilon = v^2 / 2a - [(v^2 / 4a^2 + 2 \alpha / \lambda R)]^{½}$;

$$\kappa = v / 2a + [(v^2 / 4a^2 + 2 \alpha / \lambda R)]^{½};$$

$$g = [v^2 / 4 a^2 + 2 \alpha / \lambda R]^{1/2} .$$

Here λ is the thermal conductivity, *a* is the temperature conductivity, α is the heat transfer coefficient, θ_{nn} is the melting temperature, γ is the density, R is the core radius, and *v* is the rate of casting.

Supercooling and high rates of crystallization lead to the growth of a single-crystal core of MWs.

The results of studies of the resulting MWs showed that, along the length of MWs prepared from different materials, there are many breaks, which do not depend on the type of the used glass. The main causes of their occurrence are the high rate of their crystallization and the different temperature coefficient of linear expansion of the material and the glass. The high rate of crystallization contributes to the supercooling in the melt, which results in the formation of spontaneous crystallization centers, which contribute to the appearance of new centers of crystallization. The melt in a glass capillary is located between two crystallization centers, which are attracted to each other during crystallization, which leads to the formation of microcracks in

MWs.

In addition, during the formation of MWs, due to the evaporation of the molten material, the vacuum pressure over it decreases, which also leads to the formation of microcracks. Therefore, to prepare MWs of PbTe (Fig. 2), we used the method of filling glass capillaries under an inert gas pressure; for Bi_2Te_3, we used an evacuated and hermetically sealed tube. In the latter case, we adapted the setup for casting by the Ulitovsky method; that is, we replaced the inductor by a resistance furnace with a stabilized temperature [4, 9].

The quality of the resulting MWs was estimated visually using a NEOPHOT-30 microscope and studying the microstructure of longitudinal sections. The analysis revealed a number cracks along the length of the MWs, which are caused by the high rate of crystallization and the different coefficient of thermal expansion of the material and the glass. These microcracks are removed by zone recrystallization.

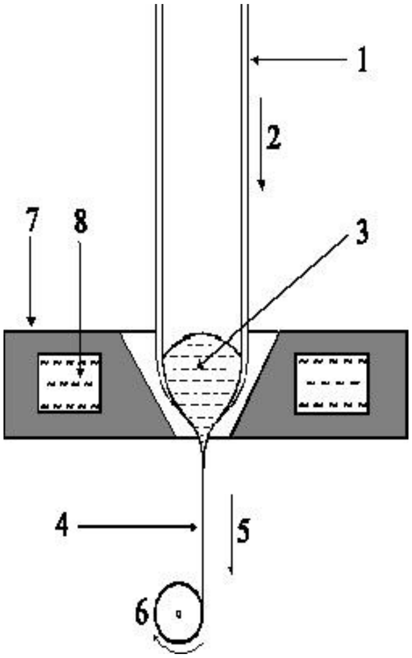

Fig. 1. Schematic representation of the setup for drawing MWs by the Ulitovsky method: (1) glass tube, (2) direction of movement of the tube, (3) liquid material, (4) MW in glass insulation, (5) direction of MW, (6) MW receiving unit, (7) high-frequency inductor, and (8) water for cooling the inductor.

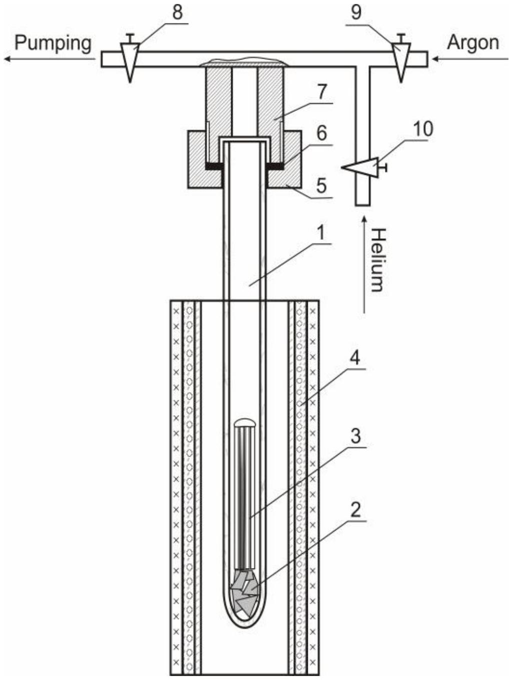

Fig. 2. Diagram of a setup for the preparation of MWs under an inert gas pressure: (1) quartz tube, (2) PbTe material, (3) quartz capillary, (4) electric furnace, (5) screw, (6) gasket, (7) bushing, (8, 9, 10) vacuum valves.

The highest quality PbTe MWs are obtained by filling quartz glass capillaries with the material under an inert gas pressure; the method is as follows: evacuated quartz tube *1* (Fig. 2) with weighted material *2* and dead-end quartz capillaries fixed above it are loaded into high-temperature furnace *4* in such a way that the capillaries and the material are in the working zone of the furnace (at a temperature above the temperature of the liquid material). After melting of the material and immersion of the capillaries into the molten material, an excess pressure of

$P = (2\text{-}12) \cdot 10^2$ Torr is formed in the tube due to an inert gas; as a result, the capillaries are filled with the melt. Subsequently, the directional crystallization of the melt occurs inside the capillaries.

The disadvantage of this method is that the WC length is on the order of 3–5 cm.

2. Preparation of a Bifilar MW

The preparation of a bifilar MW is similar to that of an MW with a single core and a coaxial MW. To obtain a bifilar MW, we use two glass tubes with a diameter of 5-6 mm sealed on one side; a few grams of a metal, semimetal, or semiconductor material in the form of small granules are placed into the tubes. After evacuation to a pressure of 10^{-5} Torr, they are soldered to one another as shown in Fig. 3.

Here, tube *1* is filled with granular material *2*; another tube *3* is filled with another granular material *4*. The resulting double tube is placed into a heated resistive furnace, in which the materials in the two tubes melt, and the tube glass softens. Next, using a glass rod, we come in contact with the lower end of the softened tubes; a part of glass is drawn into two capillaries, which are bifilar soldered and filled with different materials, and is wound, using a special receiver, in the form of a single bifilar MW in glass insulation with two electrical conductors insulated from one another.

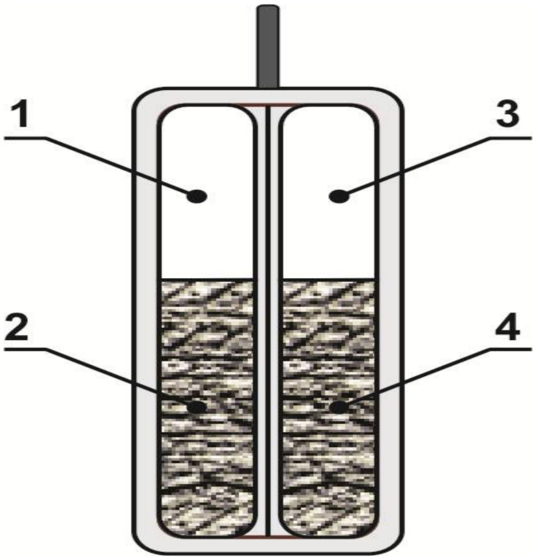

Fig. 3. Tubes for the preparation of a bifilar MW.

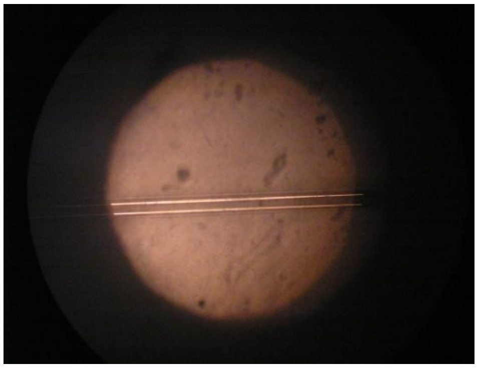

Fig. 4. Segment of a bifilar MW.

Depending on the temperature of the furnace, the rate of lowering the tube in the furnace, and the drawing rate of the MW, we can prepare MWs with various diameters.

Figure 4 shows, as an illustration, a segment of a bifilar MW of semiconductor thermoelectric materials. Here (Fig. 3) *1* and *3* are glass insulation; *2* and *4* are conductive electrodes of a thermoelectric material of *n*- and *p*-type conduction.

We shall describe the example of the preparation of a bifilar MW from bismuth telluride thermoelectric material with *n*- and *p*-type conduction.

In tube *1* (Fig. 3) with an outer diameter of 4-5 mm, we load 4-5 g of bismuth telluride of the *n*-type conduction; in tube *3* with the same diameter, we place the bismuth telluride material of the *p*-type conduction with the same weight. After evacuation of the double tube, using our facility, we obtain a bifilar MW (Fig. 4) an outer diameter of 20-60 μm and a diameter of conducting electrodes of 10-30 μm depending on the process. Depending on the amount of material, the MW length can vary from 10 m to 100-200 m [11].

3. Thermoelectric Properties of PbTe MWs

Crystal MWs of PbTe of the *n*-type conduction were prepared using original materials in the form of a chemical compound with excess lead with respect to the stoichiometric composition, and with excess tellurium for the *p*-type [12].

Studies of the temperature dependence of the electric conductivity of the MWs based on PbTe of *n*- and *p*-type conduction (Figs. 5 and 6, respectively) in a temperature range of 80-350 K showed the following:

- The electric conductivity σ is metallic; it decreases with increasing temperature; in addition, the intrinsic conductivity is not observed in the temperature range under study.

- The electric conductivity σ depends on the diameter of the MW and increases with decreasing diameter.

The increase in σ with decreasing diameter can be explained as follows. For charge carriers of *n*- or *p*-type, the relation between σ, carrier concentration, and mobility μ can be expressed as

$$\sigma_{p,n} = e\, p(n)\, \mu_{p,n} .$$

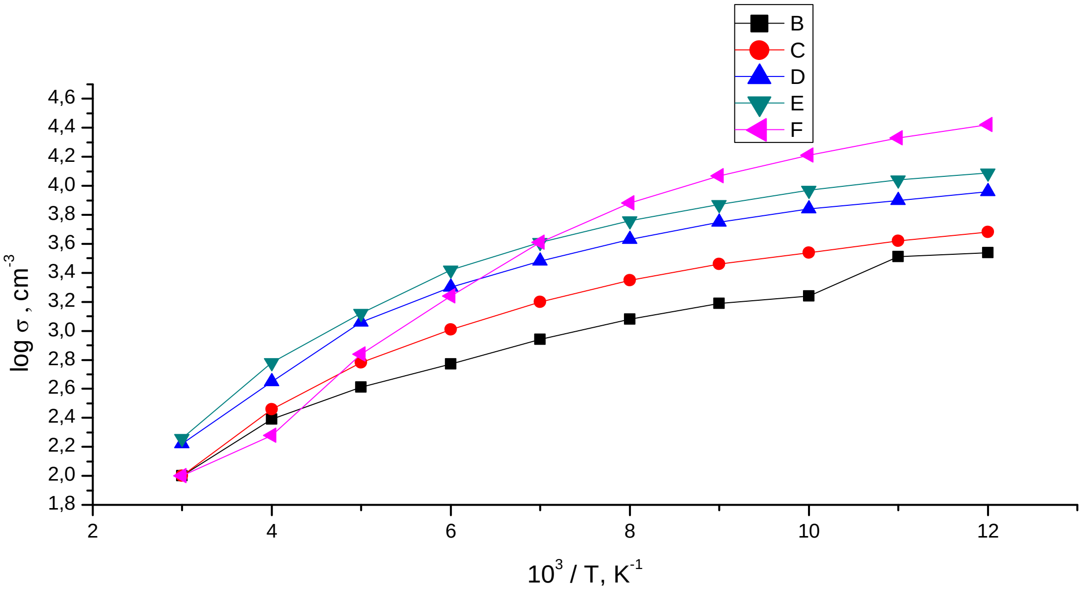

Fig. 5. Temperature dependence of MWs of *n*-type conduction: (B) d = 125.0 μm; (C) d = 92.0 μm; (D) d = 51.0 μm; (E) d = 33.0 μm; (G) d = 15.0 μm; (F) n = 1.2 · 10^{18} cm^{-3} at T = 77 K.

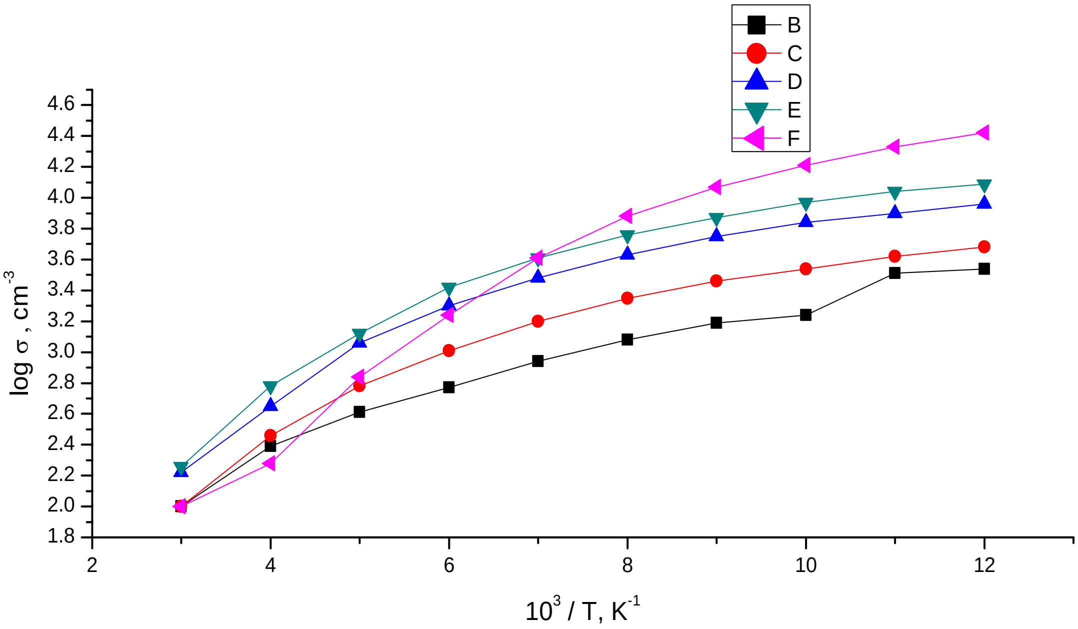

Fig. 6. Temperature dependence of MWs of *p*-type conduction: (B) d = 103.0 μm; (C) d = 45.0 μm; (D) d = 29.3 μm; (E) d = 17.8 μm; (F) p = 1.47 · 10^{18} cm^{-3} at T = 77 K.

It follows from the expression for $\sigma_{p,n}$ that its increase can be caused by an increase in the concentration of p (n) or mobility $\mu_{p,n}$. Studies of the temperature dependence of the thermopower of MWs of various diameters showed (Figs. 7 and 8, respectively) that the thermoelectric coefficient $\alpha_{p,n}$ remains almost unchanged with decreasing diameter of MW.

The expression for coefficient α

$$\alpha_{p(n)} = \pm k/e\ [\ A + \ln (2(2\pi m_{p(n)}kT)^{3/2} / p\ (n)\ h^3\ )\ ]$$

suggests that the charge carrier concentration p (n) in the studied samples does not depend on the diameter of the MW; hence, the increase in the conductivity σ depends on the increase in the charge carrier mobility. Therefore, the increase in the mobility with decreasing diameter is indicative of an improvement of the structure and homogeneity of MWs with decreasing diameter.

If we compare the results of measurements of σ and α of MWs and bulk crystals, we can conclude that the values of σ and α of the MWs range within the values of the physical parameters of bulk crystals grown by the Bridgman method. This means that the resulting MWs exhibit the same properties as bulk crystals.

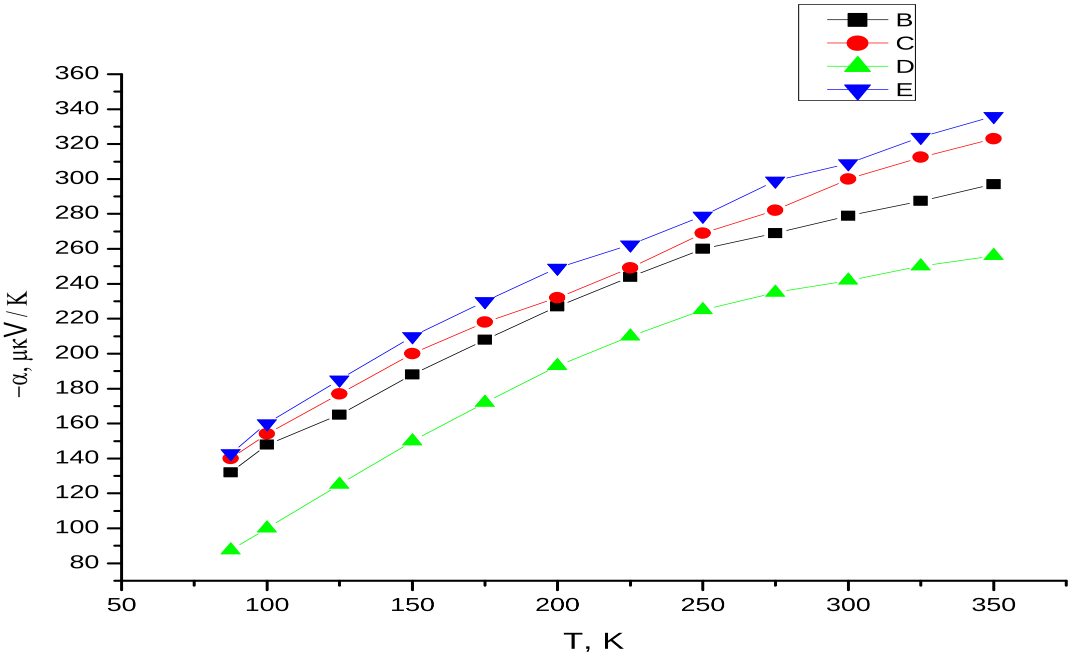

Fig. 7. Temperature dependence of the thermopower of MWs of *n*-type conduction: (B) d = 125.0 μm; (C) d = 51.0 μm; (E) d = 15.0 μm; (D) n = 1.2 · 10^{18} cm^{-3} at T = 77 K.

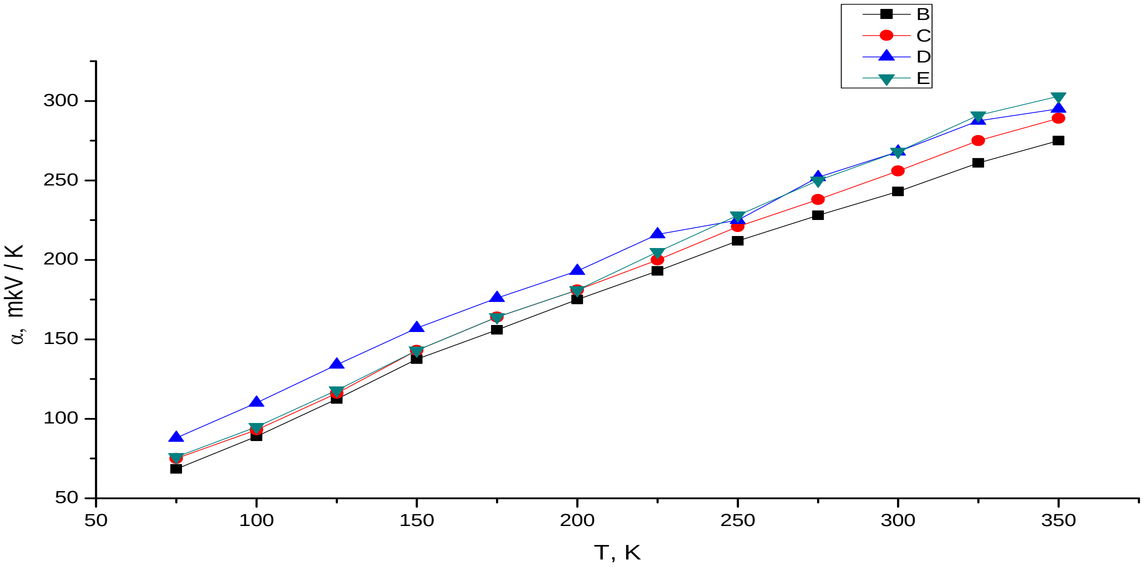

Fig. 8. Temperature dependence of the thermopower of MWs of *n*-type conduction: (B) d = 103.0 μm; (C) d = 45.0 μm; (D) d = 17.8 μm; (E) p = 1.47 · 10^{18} cm^{-3} at T = 77 K.

4. Thermoelectric Properties of MWs Based on Bismuth Telluride

The electric and thermoelectric properties were measured using a conventional technique for samples with a length of 5-7 mm cut from different parts of the MW.

The study of the dependence of physical parameters on the process conditions for MWs showed that the thermoelectric coefficient α for the samples of the hole *p*- or electron *n*-conduction at 300 K are in the range, respectively:

$\alpha_p = +(150 \div 300)$ μV/K; $\alpha_n = -(100 \div 140)$ μV/K; $\rho_p = (1 \div 7) \bullet 10^{-3}$ Ω•cm; $\rho_n = (1 \div 3) \bullet 10^{-3}$ Ω•cm [13].

To improve the MW parameters, we performed enormous work on their annealing at different temperatures and duration. The results of the treated samples are shown in Figs. 9-12.

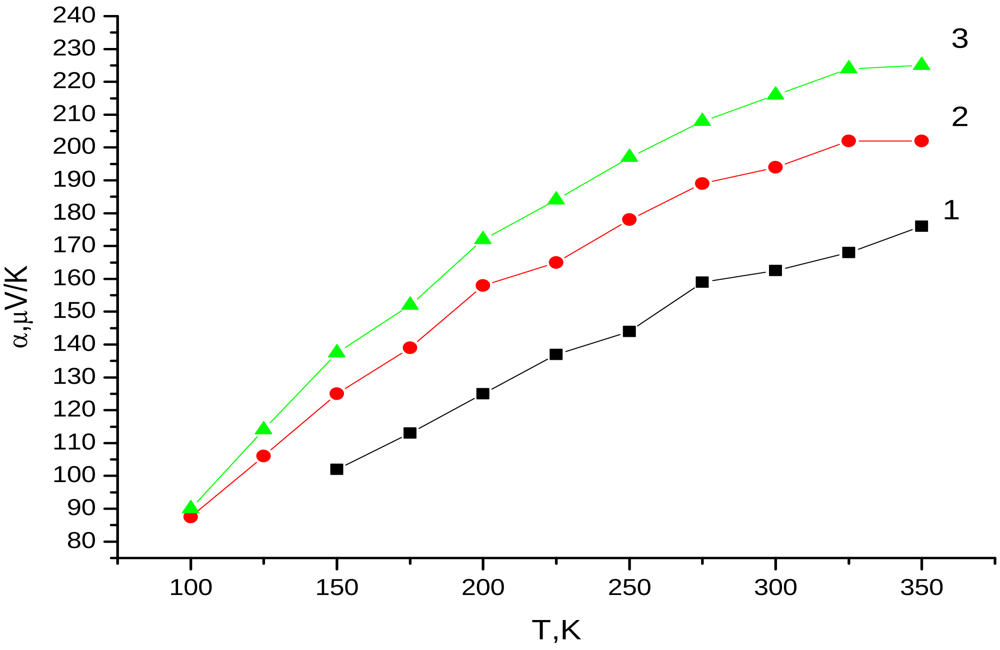

Fig. 9. Temperature dependence of the thermoelectric coefficient of the *p*-type samples: (1) before treatment, (2) after treatment, (3) samples treated at 473 K. The annealing time is 24 h.

These figures show that the isothermal annealing increases both thermopower and resistivity in the samples of the hole conduction; the higher the temperature and annealing time, the higher their parameters.

The results for samples of *n*-type are shown in Figs. 12 and 13. It is evident from the figures that, unlike *p*-type, the resistivity decreases after annealing.

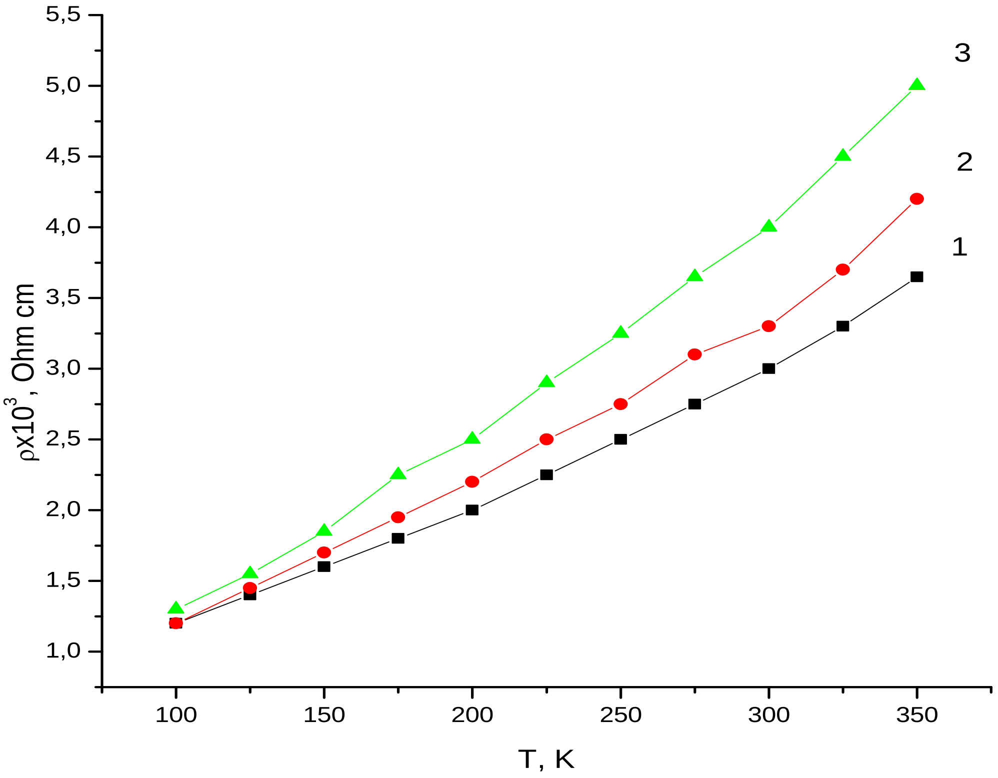

Fig. 10. Temperature dependence of the resistivity of the *p*-type samples: the notation is the same as in Fig. 9.

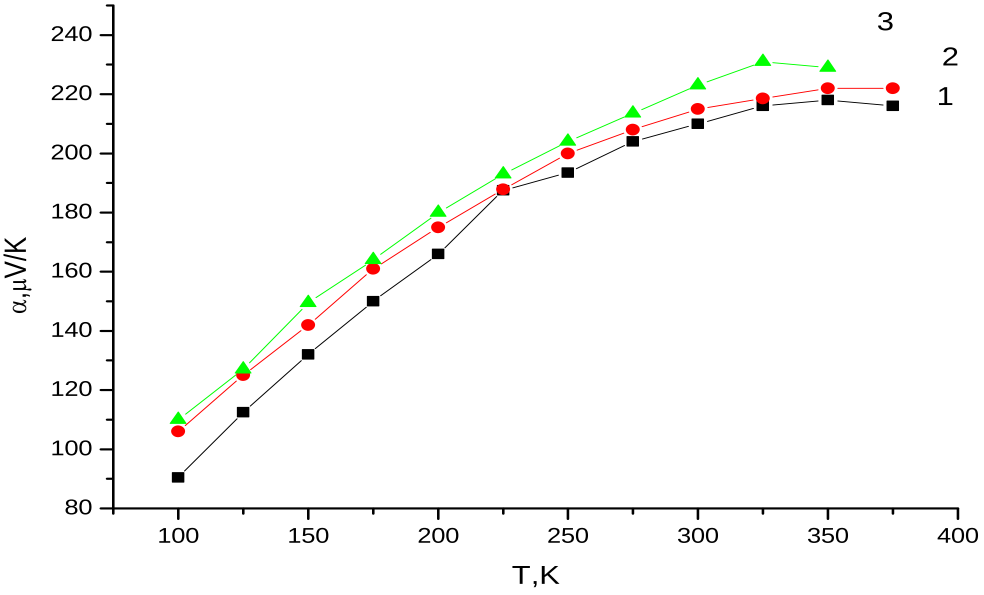

Fig. 11. Temperature dependence of the thermoelectric power of *n*-type samples treated at 450 K in the time interval of (1) 48 h, (2) 96 h, and (3) 73 h.

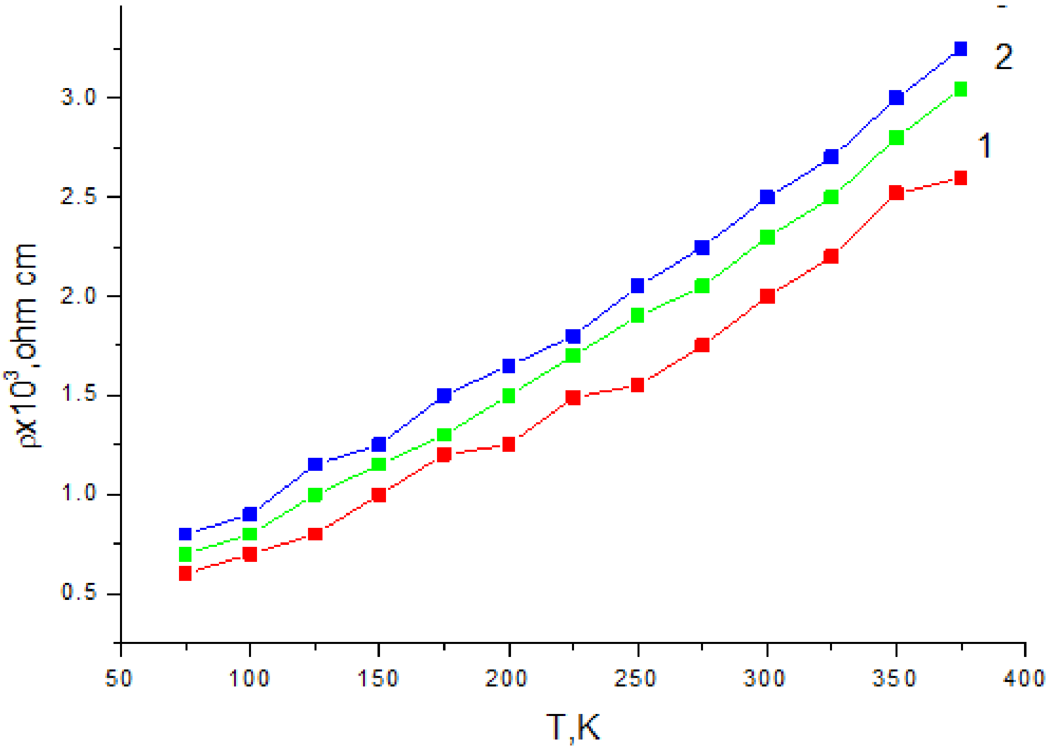

Fig. 12. Temperature dependence of the resistivity of *n*-type samples treated at 450 K in the time interval of (1) 1 h, (2) 72 h, and (3) 96 h.

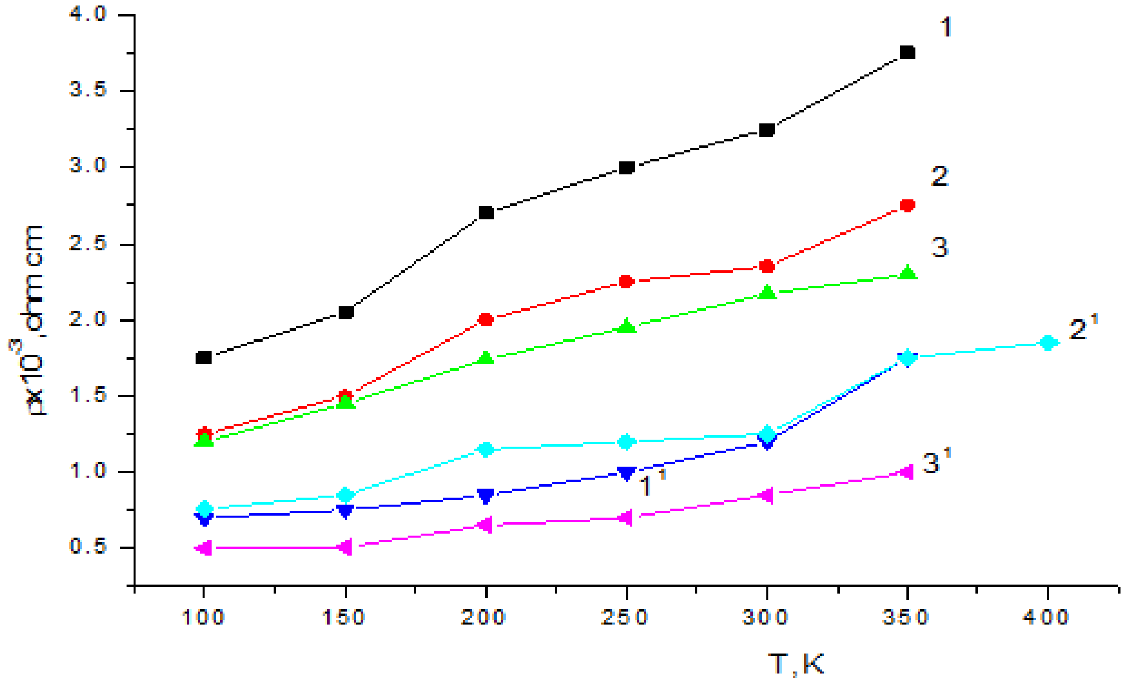

Fig. 13. Temperature dependence of the resistivity of *n*-type samples: (1, 2, 3) untreated and (1', 2', 3') treated.

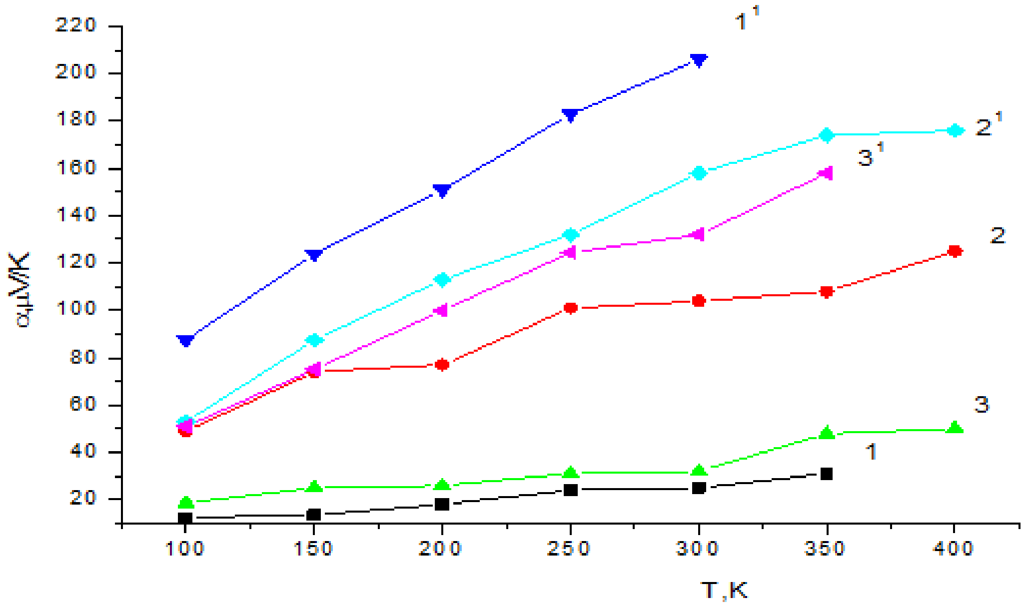

Fig. 14. Temperature dependence of the thermoelectric coefficient of *n*-type samples: (1, 2, 3) untreated and (1', 2', 3') treated.

The change in the annealing temperature of MWs leads to a shift of the maxima in the temperature dependence of thermopower to the range of lower temperatures, which is attributed to the occurrence of intrinsic conductivity at lower temperatures.

To perform aging tests, we used MWs of the two types of conduction before and after annealing for different temperatures and time of annealing. Prior to treatment, we measured resistivity and thermopower. The samples were tested at a temperature of 70°C for 60 h; after that, the samples were stored at room temperature for a month. After the measurement of parameters, the samples were subjected to repeated thermal annealing at 100°C for 40 h; after that, they were stored at room temperature for two months. The results of measurements showed an increase in the parameters after the aging test for untreated MWs and an insignificant change in the treated samples. Therefore, we recommend treating MWs at required temperatures before using in converters.

5. Thermal Efficiency of MWs

According to the theory of thermoelectricity, the efficiency of material of the thermoelectric branches is determined by the quantity

$$Z = \alpha^2\sigma/\kappa,$$

where Z is the thermal efficiency, α is the thermopower, σ is the electric conductivity, and κ is the heat conductivity of the material. The formula shows that it is proportional to $\alpha^2\sigma$ and inversely proportional to κ. Based on this, we shall further discuss in more detail the behavior of the parameter $\alpha^2\sigma$, i.e., the so-called thermoelectric power. Figures 15 and 16 show the temperature dependence of thermoelectric power for the MW of the *n*-type (Fig. 15) and *p*-type (Fig. 16). The calculation showed that, if we assume that the heat conductivity of the MW is equal to that of bulk crystals, then, at 300 K, the thermal efficiency of the PbTe material is $Z = 0.7 \cdot 10^{-3}$ K^{-1}.

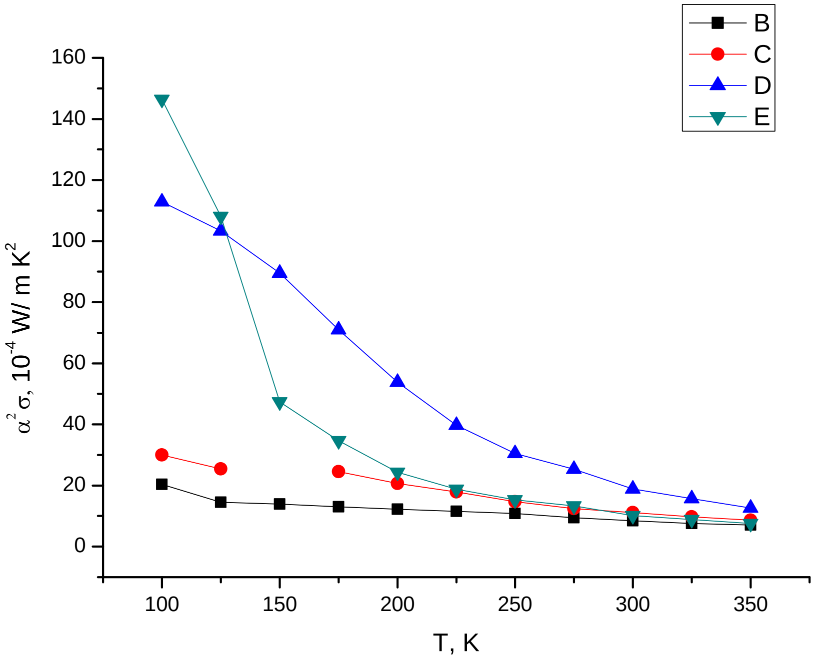

Fig.15. Temperature dependence of the thermoelectric power of *n*-type PbTe MWs: (B) d = 125.0 µm; (C) d = 51.0 µm; (D) n = 1.2 · 10^{18} cm^{-3} at 77 K; (@E) d = 15.0 µm.

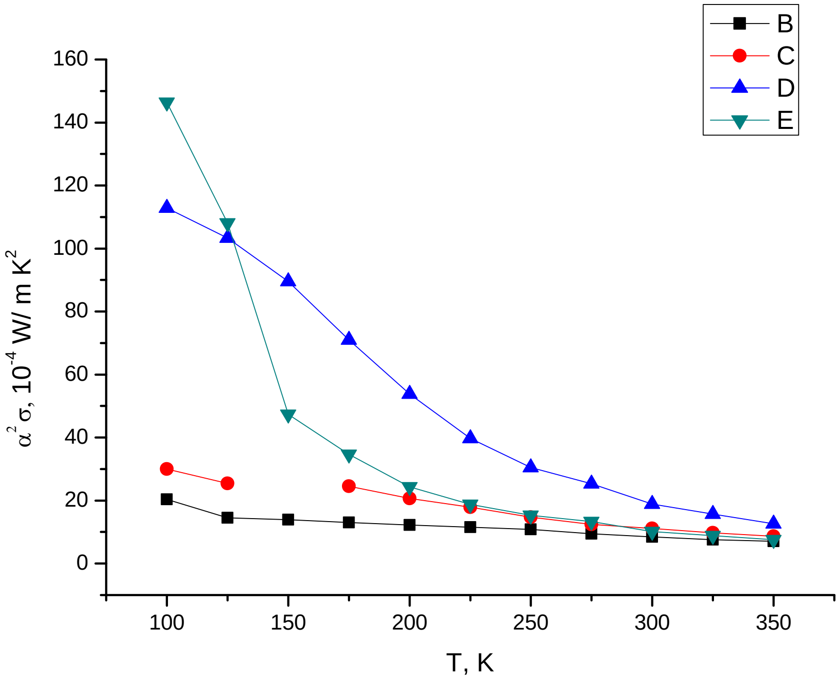

Fig. 16. Temperature dependence of the thermoelectric power of *p*-type PbTe MWs: (B) d = 103.0 µm; (C) d = 45.0 µm; (E) p = 1.47 · 10^{18} cm^{-3} at 77 K; (D) d = 17.8 µm

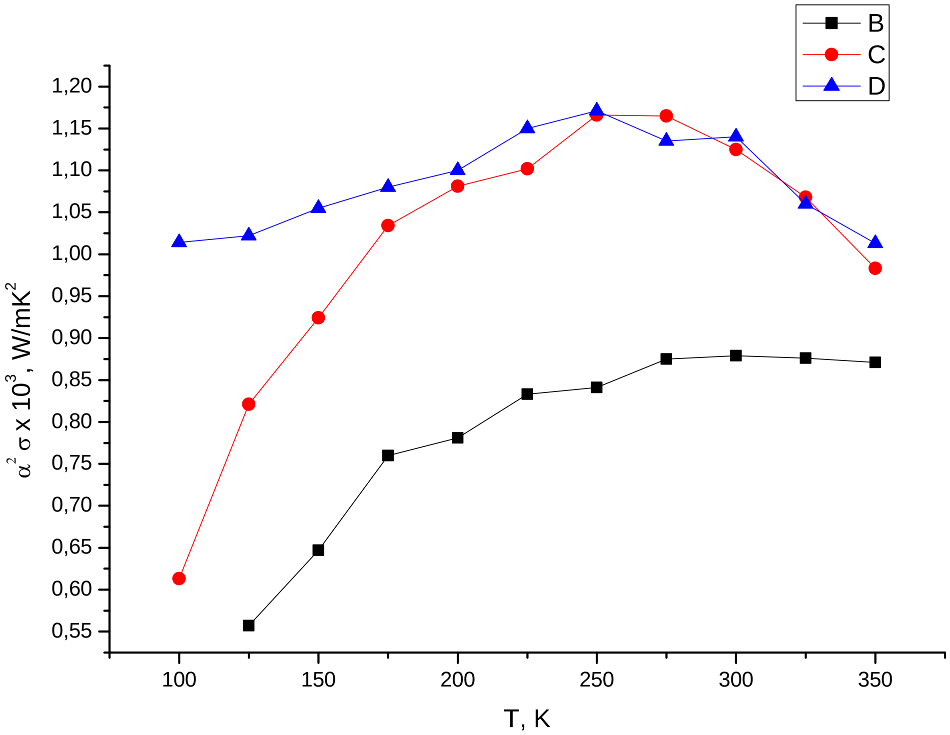

Fig. 17. Temperature dependence of the thermoelectric power of *p*-type Bi_2Te_3 MWs: (B) before treatment; (C) treated at 473 K; (D) treated at 520 K for 24 h.

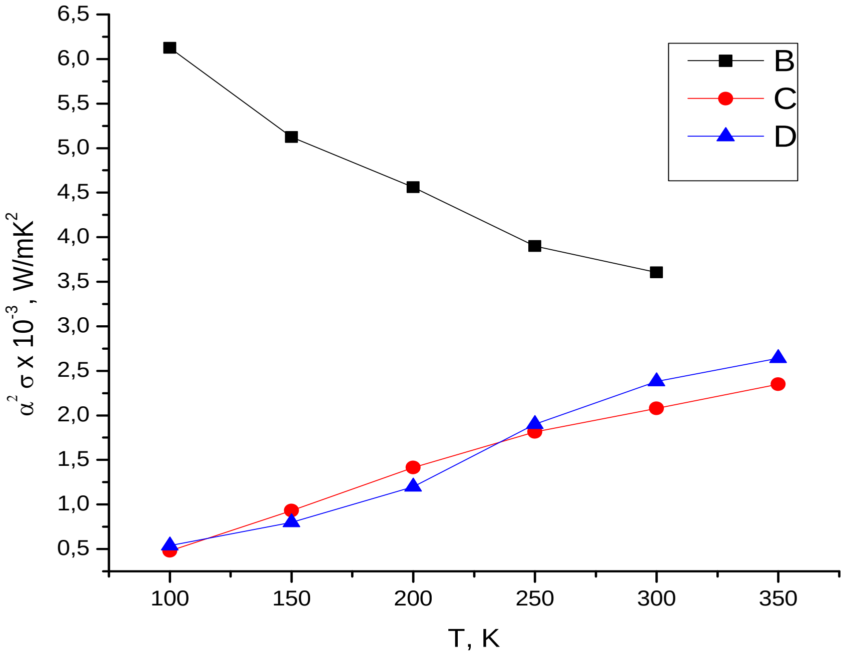

Fig. 18. Temperature dependence of the thermoelectric power *p*-type Bi_2Te_3 MWs: the notation is the same as in Fig. 17.

The thermal efficiency of the Bi_2Te_3 samples of *p*-type conduction at 300 K is *ZT* = 0.24; for *n*-type samples *ZT* = 0.51.

6. Converters Based on Glass-Insulated MWs

Infrared (IR) Detectors Based on PbTe Wires

Owing to the diffusion of lead, *p*-n junctions were formed on the resulting *p*-type PbTe WCs. The current-voltage characteristics (CVCs) of the *p*-n junctions were measured for the samples placed in evacuated glass Dewar vessels and cooled by liquid nitrogen to a temperature of 80 K.

Figure 19 shows the CVCs of *p*-n junctions for different wire diameters. It is evident that the reverse branches are characterized by low values of saturation current, which begins to rise at biases greater than 1.5 V. The shape of the forward branches of CVCs heavily depends on wire diameters, a decrease in which leads to an increase in series resistance and to a deviation of the CVC from an ideal dependence. The forward CVC branch in a voltage range of 0.02-0.076 V exhibits a region of an exponential change in current with voltage, which is characteristic of the recombination nature of current. The dynamic resistance at zero bias is in a range of $(1.5–5) \cdot 10^5\ \Omega$.

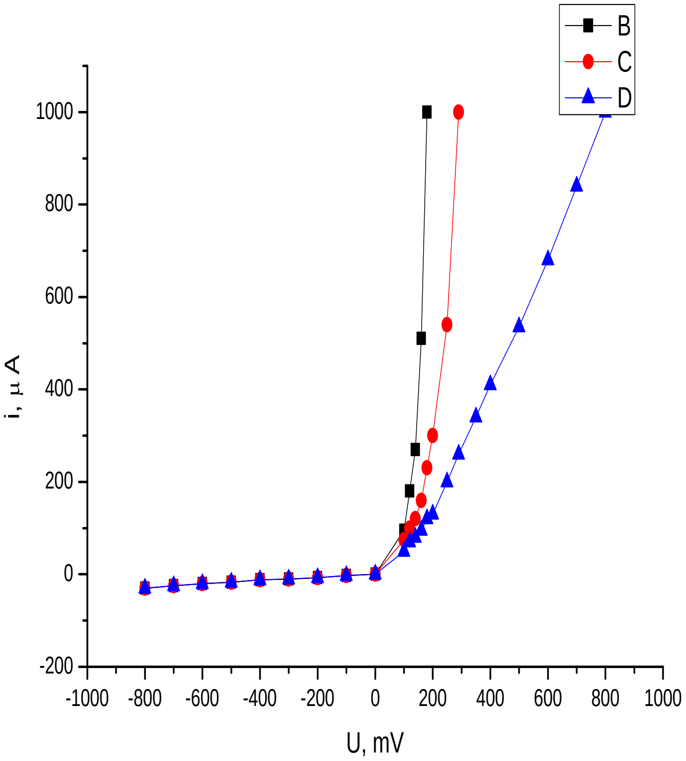

Fig. 19. Current-voltage characteristics of *p*-n junctions: (B) d = 73.3 μm; (C) d = 41.0 μm; (D) d = 33.0 μm.

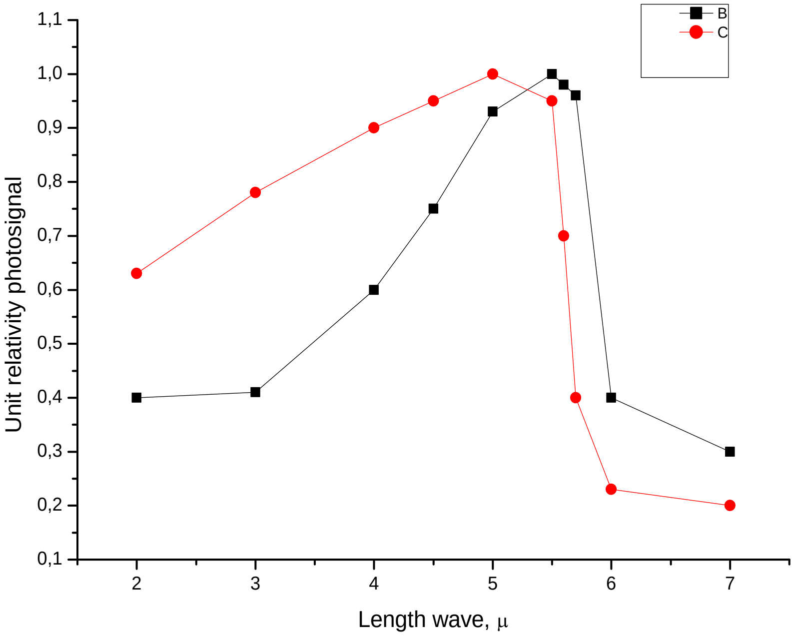

Fig.20. The spectral characteristics of IR detectors.

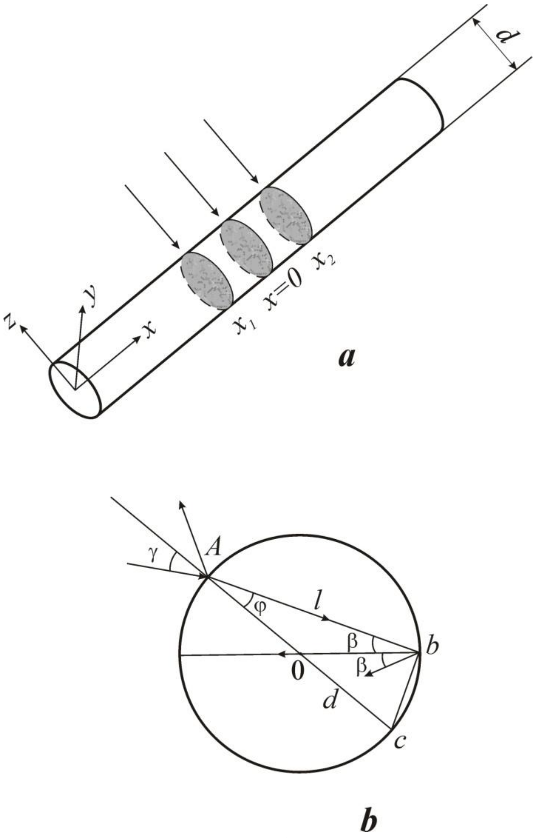

Fig. 21. (a) Geometry of the *p*-n junction and (b) incident radiation propagation paths in it.

The measurement of the CVCs of *p*-n junctions made it possible to estimate the charge carrier concentration in *p*- and *n*-regions of the sample. It was found that, for a sample with a thickness of 40 μm, the electron concentration in the *n*-type region is $N_d = 7.4 \cdot 10^{23}$ cm^{-3}, while for the *p*-type region $N_p = 3 \cdot 10^{24}$ cm^{-3}.

The spectral characteristics of IR detectors are depicted in Fig. 20, which shows that the sensitivity of the detectors has a peak before the long-wavelength limit, which is determined by the band gap. The maximum sensitivity of the measured diodes was about 10^5 V/W at 80 K.

Figure 21 shows the geometry of the *p-n* junction and the travel paths of the incident radiation in a sample with a circular cross section. For this geometry of the propagation of incident radiation, in the calculation of absorption, we must take into account multiple reflections of the beam from the back wall of the sample and the effect of the cylindrical lens of the radiation detector.

This analysis for PbTe is fairly simple, because the refractive index of these single crystals is high ($n = 5.64$) [14]. It is readily seen from the Fig. 21b that the chord length l along which the beam propagates is almost equal to the diameter of the sample. In fact, the ABC triangle show that $\sin \varphi = (1/n) \sin \gamma$. Since the angle γ can take values of 0 to 90°, the maximum difference of l from d is ~1.7% ($l = d \cos\varphi$). Thus, accurate to 2%, $l = d$ for any incidence in the range $0 \leq \gamma \leq 900$ and all subsequent multiple internal reflections occur along the chord $l = d$; the generation of charge carriers in the cylindrical sample is similar to samples with a square section whose width and thickness are equal to l. Thereupon, according to [15], the rate of carrier generation

$$g = [\ \eta\alpha I(1-R_s)/h\nu\ ]\ (\ 1-e^{-\alpha d}\ )/\ (\ 1-R_s\, e^{-\alpha d}\ ).$$

The short-circuit photocurrent for the case of the absence of surface generation is as follows:

$$i_\phi = (e^2\mu_n N_d \tau_e S/\varepsilon\varepsilon_0) \int_0^{x1}[\ g(x)\, dx + e^2\ \mu_p N_p \tau_p S/\varepsilon\varepsilon_0\ (\ \int_0^{x2} g(x)\ d(x)\ ].$$

Here μ_n and μ_p are the mobilities of electrons and holes, N_d and N_p are the carrier concentrations, τ_e and τ_p are carrier lifetimes, $\varepsilon = 400$ is the dielectric constant, and S is the area of the p-n junction. Since the absorption coefficient α is a function of electric field E and photon energy $h\nu$, the integration of the last expression is rather complicated. According to the Poisson equation [15]

$$E = -\ e\ N_d\ (\ x - x_1\ )\ /\ \varepsilon\varepsilon_0 \quad \text{at } x_1 \leq x \leq 0 \quad \text{and}$$
$$E = \ \ e\ N_p\ (\ x - x_2\ )/\ \varepsilon\varepsilon_0 \quad \text{at } 0 \leq x \leq x_2,$$

the problem is significantly simplified.

If the photon energy is higher than the band gap E_g, for direct allowed transitions, α takes the form [16]

$$\alpha\ = A\ (h\gamma-E_g)^{1/2}[\ 1- G(h\gamma,E)],\ \text{where } A = \pi c^2\ (2m_r)^{3/2}\ E_g/\ (3m_n n\varepsilon_0 c h^3\gamma),$$

according to [17],

$$G(h\gamma,E) = -E_0^{3/2} \cos\ [4(h\gamma-E_g)^{3/2}/(3E_0^{3/2})]/\ 4(h\gamma-E_g)^{3/2}.$$

According to [20], for the saturation current i_s, we have

$$i_s = e n_i^2 S/\tau^{1/2} \cdot\{\ D_n^{1/2}\ \mathrm{cth}[l/(D_n\tau)^{1/2}]/\ (N_a- N_d) + D_p^{1/2}\ \mathrm{cth}\ [l\ /\ (D_p\tau)^{1/2}\ ]\ /\ N_d\}.$$

Here n_i is the intrinsic concentration of charge carriers, D_n and D_p are the diffusion coefficients of electrons and holes, and l is the half-width of the p-n junction. Knowing the photocurrent and the saturation current, we can determine the photo-emf of the p-n junction:

$$V = kT/e \cdot \ln(\ i_\phi\ /\ i_s + 1\ ).$$

The calculated value of photo-emf V = 456 mV is in good agreement with experimental data (200-500 mV).

The calculated detectability, which is limited by thermal noise, is

$$D^* = 1/c\, I \cdot (kT/4R_tS_1) \cdot \ln(i_ф/i_s + 1) = 5.6 \cdot 10^{11}\ \text{cm Hz}^{1/2}/\text{W}.$$

If we neglect the dependence of α on electric field, the value of photocurrent decreases almost two fold.

Thus, our data show the following. The used geometry of propagation of the incident radiation at the *p*-*n* junction is more appropriate for the design of IR detectors. In the calculation of their parameters, it is necessary to take into account the Franz-Keldysh effect. The cylindrical form of the *p*-*n* junction plays the role of concentration of incident beams.

7. Injection Lasers Based on PbTe WCs

Interest in injection lasers in WCs is caused the possibility to prepare an optron pair, i.e., a source and a detector of radiation, in a spectral range of 3-5 μm in one and the same fiber. To prepare the lasers, we used $Pb_{1-x}Gd_xTe$ (x = 0.0005) WCs of *p*-type conduction with resistivity $\rho \approx (3\text{-}6) \times 10^{-4}\ \Omega$ cm at 77 K. We studied the junctions whose plane is parallel to the cylindrical surface of the WC (coaxial). The region of *n*-type conduction was subjected to diffusion annealing at 973 K in an atmosphere of $Pb_{0.51}Te_{0.49}$ for 90 s; the *n*-layer had a thickness of 20 μm and a length of 0.2-0.5 mm. The configuration of the cylindrical diodes and their location on a copper crystal holder are shown in Fig. 22.

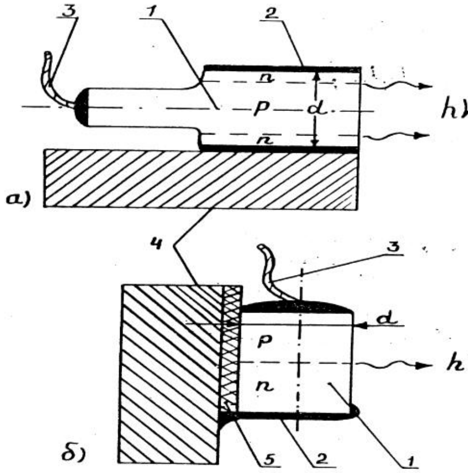

Fig. 22. Configuration of (a) coaxial and (b) transverse laser diodes.

The resistance of the diodes at liquid nitrogen temperature was about 1 Ω. The stimulated emission was measured in a pulse mode at *T* = 4.2 K. The current pulse duration was 1 μs; the pulse repetition frequency was 170 Hz. The emission spectra were recorded using an IKS-31 monochromator, a detector based on Ge:Au, and a V9-5 stroboscopic converter B9-5.
The threshold current density was 0.1-0.5 kA/cm^2 for the coaxial lasers.

Figure 23 shows the emission spectra of laser diodes with the mode structure in the spectra, which is indicative of lasing.

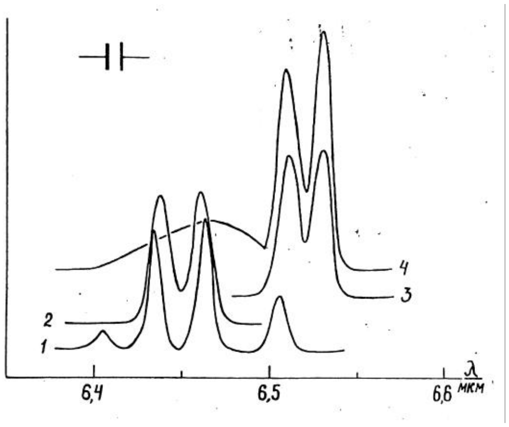

Fig. 23. Emission spectra of (1, 2) transverse and (3, 4) coaxial diodes with different resonator length *l*: $d_1 = 120.0$ μm, $d_2 = 70.0$ μm; $l_{3,4} = 110.0$ μm, $d_3 = 56.0$ μm, and $d_4 = 21.0$ μm.

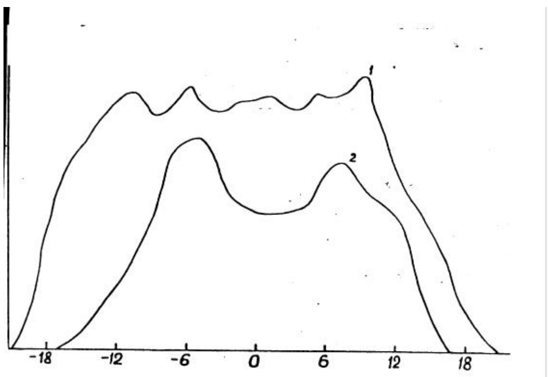

Fig. 24. Directional radiation pattern in the *p*-n junction plane: (1) transverse and (2) coaxial.

The generation of a coaxial diode was observed at a wavelength corresponding to the band gap of PbTe at 4.2 K (Fig. 23, curve *3*). As the length of its resonator *l* decreased, the emission intensity increased, and a wing of spontaneous emission appeared on the short-wave side (Fig. 23, curve *4*). In this case, the mode spacing ($\Delta\lambda \approx 200 - 250$ Å) did not change; that is, it did not depend on the resonator length. The threshold current density slightly increased with decreasing resonator length. These facts indicate that the distribution of current along the wires is inhomogeneous, the mode structure is formed at lengths of the ring *p*-n junction $l \leq 0.2$ mm, and the absorption of radiation (mostly short-wave) occurs on the rest passive part of the crystal.

Figure 24 (curve *2*) shows the directional radiation pattern for a coaxial diode. However, a final conclusion about the spatial distribution of radiation is difficult to make as yet, because the intensity of radiation of the diodes was relatively low. Thus, the results on stimulated emission in the *p*-n junctions in PbTe CWs suggest the possibility of their use as lasers in a wavelength range of 3-6 μm.

8. Microthermocouples

The studied bifilar MW was used as a basis for the preparation of microthermocouples to measure the temperature of various solid, liquid, gaseous, and biological objects by a contact method.

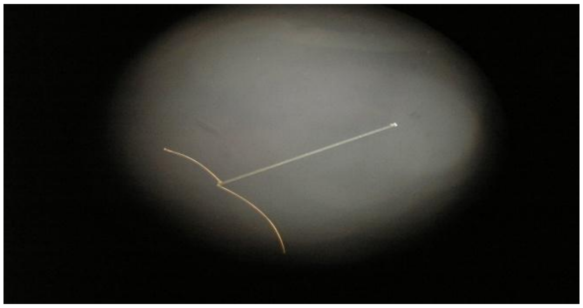

Fig. 25. Microthermocouple based on a bifilar MW.

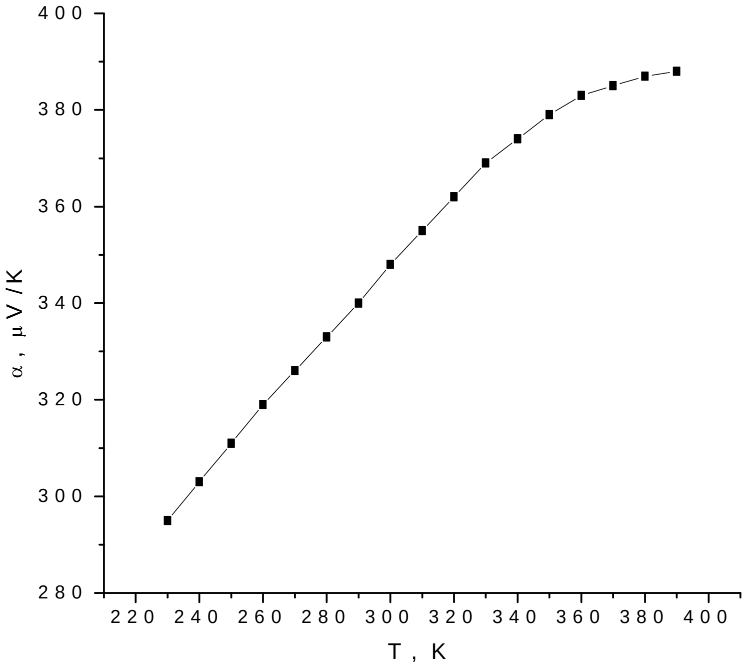

Fig. 26. Temperature dependence of the thermoelectric power of the thermocouple.

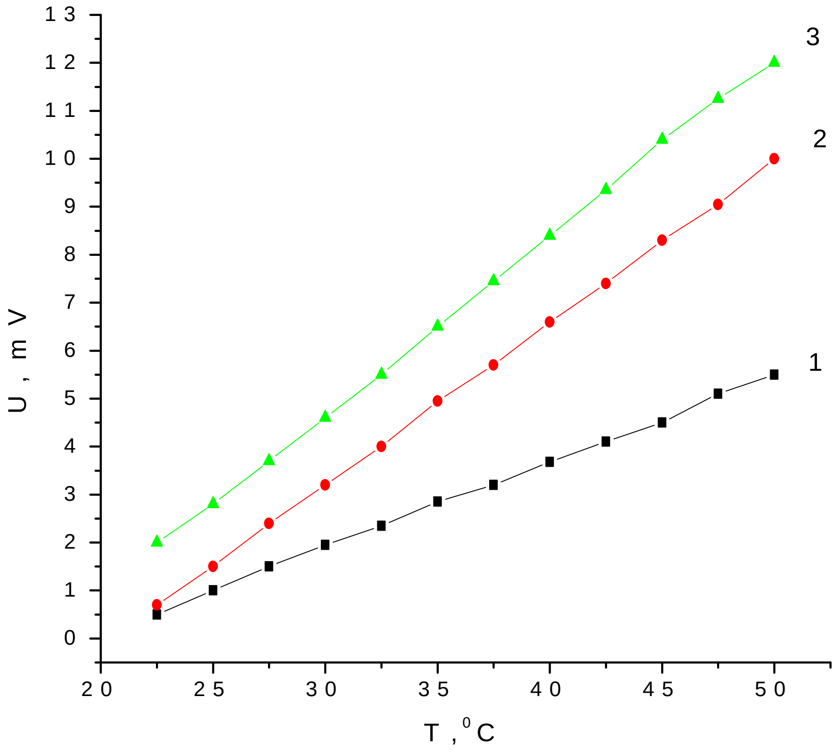

Fig. 27. Temperature dependence of the electric current of the thermocouple.

It is evident that the temperature dependence of signal is linear in a temperature range of 230-270 K. After annealing of the MW, the signal of the microthermocouple is on the order of 2-12 mV in a temperature range of 23-50°C.

9. Microelectrodes

The microelectrode is a glass capillary with a glass-insulated microthermocouple based on Bi_2Te_3 of *n*- and *p*-type conduction placed in it. It serves for removing the biopotentials and measuring the temperature of living organisms and plants. The length of the active part is 5-45 mm; the diameter of the active part is 0.5-1.0 mm, and the area of the contacting region is 50 μm^2.

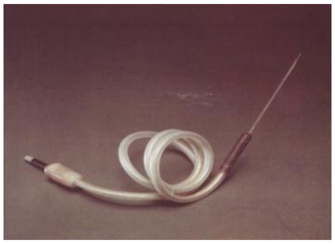

Fig. 28. Microelectrode.

10. Conclusions

- The technique for the preparation of MWs from thermoelectric materials based on PbTe and Bi_2Te_3 by the Ulitovsky method and by the filling of capillaries under an inert gas pressure has been optimized. The highest-quality MWs of lead telluride have been prepared by the second method.
- A technique for the preparation of a bifilar MW based on Bi_2Te_3 using a modified Ulitovsky method has been developed.
- The temperature dependences of the resistivity and thermopower of the MWs in a temperature range of 77-350 K have been measured.
- The thermal efficiency of the MWs has been calculated and compared with the thermal efficiency of bulk samples.
- The PbTe-based MWs were used to prepare IR detectors and injection lasers; the Bi_2Te_3-based MWs were used to prepare a microthermocouple with a high sensitivity and microelectrodes for removing the biopotentials and measuring the local temperature of microorganisms, living organisms, and plants.

References

[1] D.M.Freik, M.A. Galushchak, and L.I. Mezhilovskaya, Fizika i tehnologiya poluprovodnikovyh plenok, L'vov, Vyshcha Shkola, 1988, 152 p.

[2] W. Lu, J. Fang, K.L.Stokes, and J. Lin, J. Am. Chem. Soc., 126, 11798 (2004).

[3] T. Gutsul, A. Nikorich, and A. Todosichuk, Stabilizatsiya oleinovoy kislotoy nanochastits PbTe, poluchennyh metodom HTSPS, 2nd Int. Conf. "Telecommunications, Electronics and Informatics," Proceedins, V.II, Chisinau, 2008, p.279–284.

[4] D.F. Megley, M.P. Dyntu, and S.V. Donu, Osobennosti rosta nitevidnyh kristallov tellurida svintsa olova, International Conference ICT+ „Information and Communication Technologies – 2009”, Proceedins, Chisinau, 2009, p.105–107.

[5] D.F. Meglei, V. Kantser, and M. Dantu, Mold. J. Phys. Sci. 2, 2, 177 (2003).
[6] G.F.Taylor. Phys. Rev. 23, 655 (1924).
[7] E.Ya. Badinter, N.R.Berman, et al., Litoy mikroprovod i ego svoystva, Shtiintsa, Kishinev, 1973, 318 p.
[8] A.V. Ulitovskii and N.M. Averin, USSR Author's Certificate 161325, MKI g 03 C 29/-00, Byull. Izobret., 7, 14 (1964)
[9] D. Meglei, Mold. J. Phys. Sci. 9, 70 (2010).
[10] V. Canter, D. Meglei, and A. Rusu, Precedeu de obţinere a microfiorului coaxial, Brevet de inventie no. 2752 , 2005.04.30. BOPI nr. 4/2005.
[11] D. Meglei, M. Dantu, E. Condrea, and A. Rusu, Procedeu de confectionare a microconductorului bifilar. Brevet de inventie h01b 13/06, h01b 3/08 A 2008 0209, 2009.12.22.
[12] V.F. Banar', F.G. Donika, and A. Shkurpelo, Izv. Akad. Nauk MSSR, ser. Fiz.-Tech. Mat. Nauk 3, 66 (1982).
[13] M.P. Dyntu, V.G. Kantser, D.F. Meglei, Int. Semicond. Conf. 19-th Ed., October 9-12, Sinaia, Romania, 109 (1996).
[14] C.S. Evans and J.S. Secly, J. Phys. Suppl. 29, 11-12, 4 (1968).
[15] R. Smith, Poluprovodniki, Mir, Moscow, 1982, 467 p.
[16] T. Moss, G. Barel, and B. Ellis, Poluprovodnikovaya optoelektronika, Mir, Moscow, 1976, 431 p.
[17] Opticheskie svoystva poluprovodnikov A^3B^5, edited by R. Uillardson and A. Bir, Sov. Radio, Moscow, 1970, 488 p.
[18] A. Ambrozyak, Konstruktsiya i tehnologiya poluprovodnikovyh fotoelektricheskih priborov, Sov. Radio, Moscow, 1970, 392 p.

GAS SENSING CHARACTERIZATION OF TELLURIUM THIN FILMS BY THE KELVIN PROBE TECHNIQUE

D. Tsiulyanu [1,*], S. Marian [2], and O. Mocreac[1]

[1] *Technical University, bd. Dacia 41, Chisinau, MD-2060, Moldova;*
[2] *Daimler AG, D-71059, Sindelfingen, Germany; *E-mail: tsiu@molddata.md*

(Received 11 September 2012)

Abstract

The sensing behavior of tellurium films at room temperature was tested with environmental pollutant gases, such as NO_2, CO, O_3, and water vapor, using the Kelvin probe technique. A significant sensitivity was observed for nitrogen dioxide. The detection range for NO_2 was between 0.5–5.0 ppm in air with controlled humidity. The response and the recovery time are rapid with good reproducibility and high sensibility. The work function measurements showed that chalcogenide semiconductors in question are well-suited materials for the detection of not only small concentrations of NO_2, but also for humidity sensing. The relative humidity of 45% induces the work function change $\Delta\phi$ of approximately 200 mV at room temperature. It is shown that the "strong" chemisorption of nitrogen dioxide results in an increase in both work function change $\Delta\Phi > 0$ and electrical conductivity $\Delta\sigma > 0$ because of the additional charging of the surface and band bending. The effect of water vapor is due to a simple physical adsorption of polar water molecules oriented perpendicular to the surface with a negative pole inward. As a result, the dipole component of the work function increases, i.e., $\Delta\Phi > 0$, but the free lattice holes become more localized at the surface and the conductivity of the p-type chalcogenide layer decreases $\Delta\sigma < 0$.

1. Introduction

In recent years, a considerable attention has been given to the possibility of using chalcogenide glassy semiconductors as the sensitive layer in chemical sensors for the analysis of industrial solutions [1] and pollutant gases [2]. Usually, the changes of the conductivity of these layers as sensitive parameter have been studied. A significant progress in investigating the sensing properties of these materials can be achieved by means of Kelvin probe (KP) measurements. The piezoelectrically driven Kelvin probe is a simple and fast technique to monitor the variation of surface potential during adsorption and desorption of gases from environment [3, 4]. In addition, the work function setup exhibits a good stability, because the sensitive layer is not electrically treated; that is, in contrast to conduction sensors, electromigration, which is a serious limiting factor for conductive thin film sensors, cannot appear. The KP equipment provides the possibility to measure the relative change of work function $\Delta\Phi$ of the chalcogenide layer in the presence of a carrier gas and during the exposure to a gas mixture of interest. The work function measurements by the KP method have been used in the present work for characterization of the interaction between Te based thin films and some harmful gases as well as water vapor at room temperature.

2. Experimental

For the work function measurements, a commercial Kelvin probe (Besocke GmbH, Julich, Germany) was used. It consists of a gold grid reference electrode, oscillating via piezoelectric transducer normally to the sample surface at a frequency of about 170 Hz. By use of this technique, the relative change of work function $\Delta\Phi$ of the chalcogenide film was measured in the presence of the carrier gas (ambient air with different degree of humidification) and during exposure to a vapor with different concentration of pollutants:

$$\Delta\Phi = \Phi_{vapour} - \Phi_{air}, \tag{1}$$

where Φ_{air} and Φ_{vapour} are the work function of sensitive film measured in air and in the presence of vapor of interest, respectively.

The measurement gas composition was controlled by a gas flow system, which controls the humidity, the flow of the carrier gas (dry ambient air, < 1% humidity) and the specific sample gas as load. Sample gases can be introduced into the system using gas sources of known concentration or permeation tubes. All measurement data were recorded with a computer controlled setup.

Tellurium (purity 99.999 %) based thin films were deposited by thermal vacuum evaporation from tantalum boats onto Pyrex glass substrates. The evaporation was performed at the working pressure of $\approx 10^{-4}$ Pa. The growth rate of the films was on the order of 10 nm/s and the area of deposition was around 50 mm^2. The film thickness determined using a MII-4 microinterferometer was about 60 nm. X-ray analyses and scanning electron microscopy (SEM) were used for structural investigations.

3. Results

Figure 1 shows the work function variation ($\Delta\Phi$) exposing a Te polycrystalline thin film at different concentrations of nitrogen dioxide. The measurements were performed at repeated on /off switching of the NO_2 gas mixture. The dotted line gives the switching schedule.

It is seen that in effect of NO_2 vapor the work function of the tellurium film increases, but after switching off the pollutant gas, the $\Delta\Phi$ curves return to their initial position. NO_2 gas concentrations like 1.9 ppm lead to a variation of work function by around 120 mV. The contact potential difference (CPD) measured in the present work vs. a vibrating gold grid reference electrode is

$$\mathrm{CPD} = (\Phi - \Phi_{Au})/e, \tag{2}$$

where Φ is the work function of sample, Φ_{Au} is the work function of gold grid reference electrode, and e is the elemental charge. On the other hand, the work function value in a semiconductor material is the sum of several terms:

$$\Phi = \mu + \phi_0 + \varphi, \tag{3}$$

where μ is a bulk chemical potential, ϕ_0 is the surface dipole potential and φ is the eventual band bending.

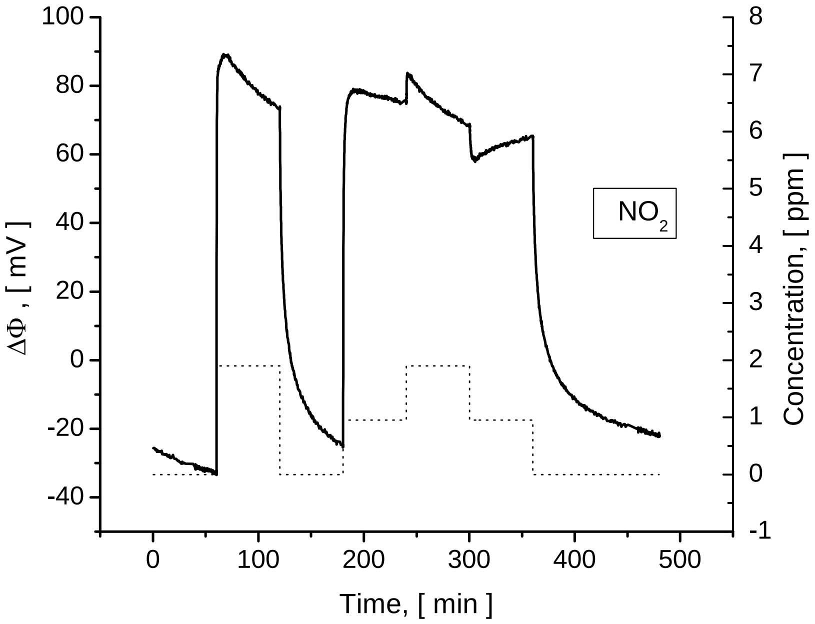

Fig. 1. Work function variation of a tellurium layer exposed to NO_2 according to the profiles shown at the bottom.

Considering the gold as a inert reference material, the work function variation $\Delta\Phi$ due to gas adsorption can be caused by variation of ϕ_0 or /and φ of ChS, which depend on nature and number of adsorbed particles, whiles μ is independent on adsorption, being determined by the nature and state (nature and concentration of impurities, temperature, etc.) of semiconductor; that is,

$$\Delta\Phi = \Delta\phi_0 + \Delta\varphi \qquad (4)$$

Consequently, it is necessary to additionally investigate the presence of either ϕ_0 or /and φ contributions in work function variation caused by gas adsorptions.

In the present work, the influence of nitrogen dioxide, carbon oxide, ozone, and water vapor adsorption on the electrical conduction of thin tellurium films was studied to determine the possible contribution of band bending or of the surface dipole potential in change of $\Delta\Phi$, which cause the CPD variation. Figure 2 shows the current flow though the tellurium film under repeated switching on/off the NO_2 gas mixture at a constant bias voltage. The dotted line gives the switching schedule that is the same as in Fig. 1. It can be observed that the current follows the schedule: increases when the gas is applied and depends on its concentration. Thus, the adsorption of NO_2 results in an increase in both the work function difference ($\Delta\Phi > 0$) and electrical conductivity ($\Delta\sigma > 0$) of the films in question.

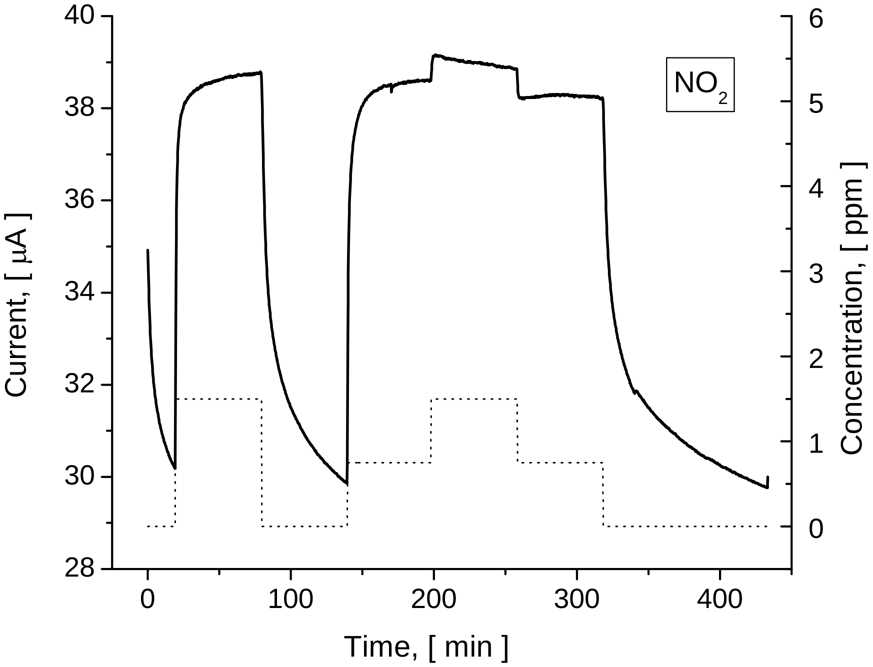

Fig. 2. Current flow though the tellurium film exposed to NO$_2$ at room temperature and a voltage bias of 4 V. The dotted line shows the switching schedule.

As far as the influence of water vapor is concerned, the film's behavior is particular.

Figure 3 shows the temporal evolution of the work function as the surface of a Te layer is exposed to air with different relative humidity. An increase in the relative humidity of the carrier gas (air) leads to a nonmonotonic increase in the work function variation ($\Delta\Phi > 0$). The saturation occurs at an applied relative humidity higher than 45%. The work function change $\Delta\Phi$ is very high with approximately 200 mV. The response and the recovery time (τ_{90}) is only a few minutes. On the other hand, the humidity diminishes the electrical conductivity of the film.

Figure 4 shows the typical response of a tellurium thin film to an impulse of humid (58% RH) air at 23 and 70^{o}C. Dry (1-2% RH) synthetic air was used as reference gas. Switching from dry to wet synthetic air makes the current of the film slightly decrease and achieve a steady state at room temperature in approximately 45 min. The relative resistance of the film increases in this process by ~ 15%.

Thus, the effect of water vapor on electrical conductivity appears to be opposite from that of nitrogen dioxide: the adsorption of water vapor leads also to an increase in the work function change ($\Delta\Phi > 0$) but diminishes the electrical conductivity of the film ($\Delta\sigma < 0$). Note that, as follows from Fig. 4, the humidity response of the sensor heated to 70^{o}C becomes unessential. RH of 58% leads to an increase in relative resistance only by 3–4% at this temperature. This range of $\Delta R / R_0$ variation remained nearly constant during heating to higher temperatures.

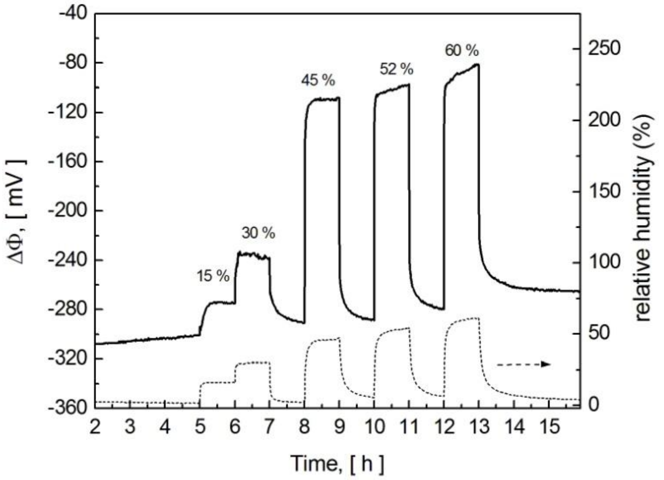

Fig. 3. Response of a Te film towards the humid (15, 30, 45, 52, and 60% RH) air pulse sequence at an operating temperature of 23^0C.

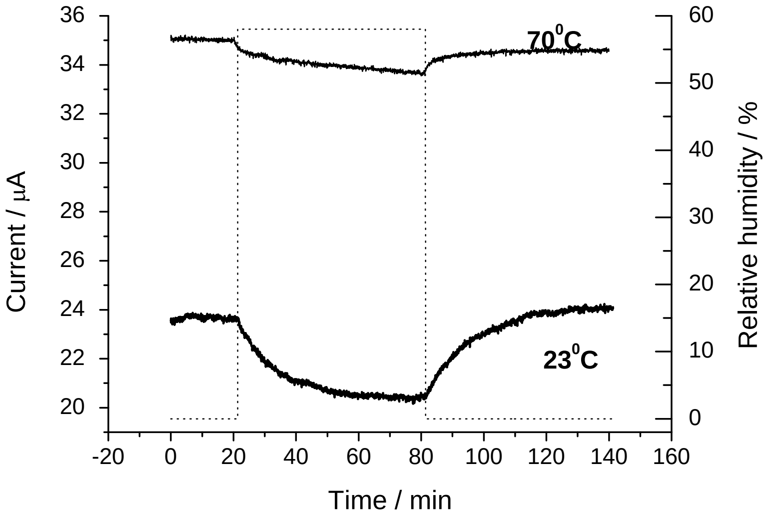

Fig. 4. Response of a tellurium based thin film to an impulse of humid (58 % RH) air at 23 and 70^0C.

4. Discussion

Tellurium and its alloys belong to so-called lone-pair (LP) semiconductor materials [5]. The main feature of lone-pair semiconductors is that the upper part of the valence band is formed from p-state lone-pair electrons. If the network of a LP glassy or crystalline semiconductor contains defects, such as unsaturated chemical bonds (dangling bonds), the interaction between these defects and lone-pair electrons occurs. The dangling bond interacts with neighboring lone-pair, bonding with it by distorting its environment (Fig. 5a). This interaction results in the formation of lattice defects and release of about 10^{13}-10^{15} holes/cm^3, which causes the p-type of conductivity. Since the maximum concentration of dangling bonds takes place namely on the surface, the hole enriched (accumulation) region is formed at the surface; that is, the bands bend up (Fig. 5b). This region includes also the grain boundary.

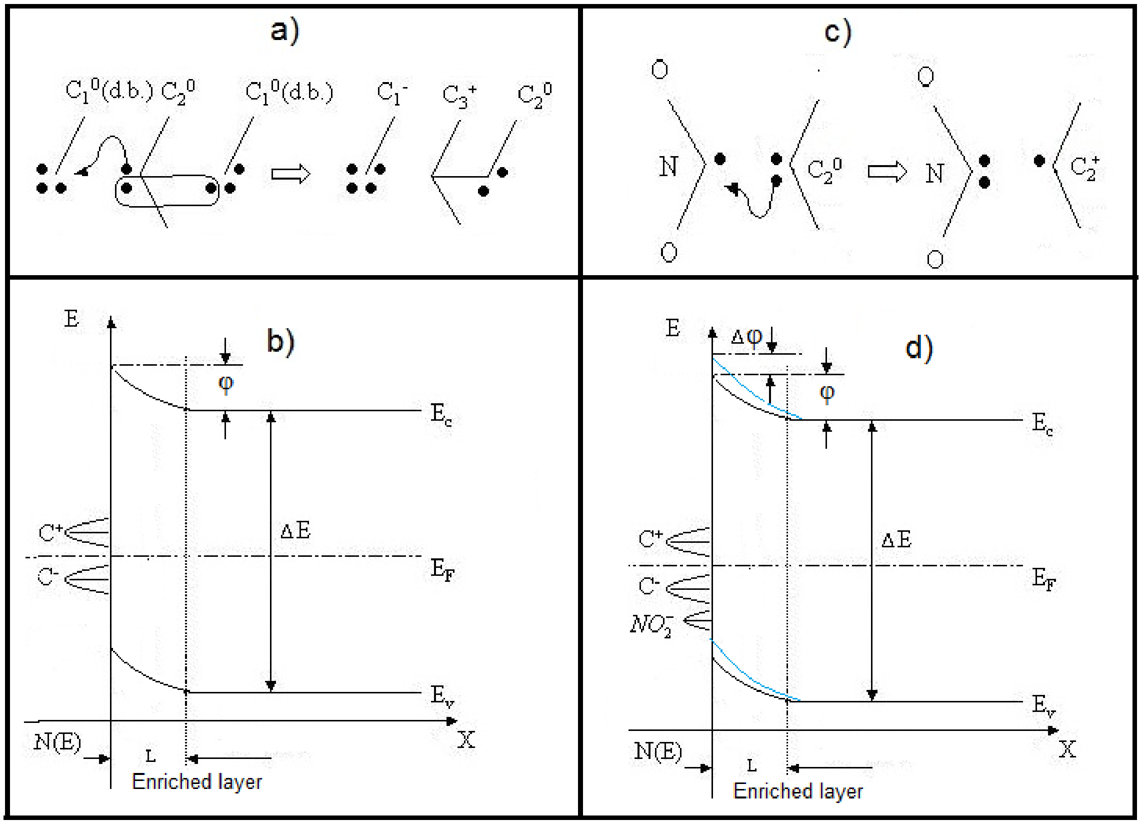

Fig. 5. Model of the dangling bonds - lone pair electrons interactions and the surface state bands at the chalcogenide semiconductor's surface before (a and b) and after (c and d) adsorption of acceptor like (NO_2) gas molecules.

In this respect, the gas sensing is due to variation of hole density or / and their mobility in the accumulation (surface and grain boundary) region in the presence of gaseous media.

When the chalcogenide semiconductor is introduced into a gaseous environment the adsorption of gas molecules occurs, which can produce either donor or acceptor levels. As far as the adsorption of nitrogen dioxide is concerned, its molecule comprises an odd electron [6]; that is, after covalently bonding of nitrogen to oxygen, one of the atoms remains with a single unpaired electron. Being adsorbed on the surface of the Te (grain) surface, the NO_2 molecule acts as a dangling bond (Fig. 5c) which can accept a LP electron to form an electron pair via the reaction:

$$NO_2 + e^- \rightarrow NO_2^- + h \qquad (5)$$

Thus, the capture of a LP electron, i.e., the transition of an electron from the upper part of the valence band to a NO_2 acceptor level, is accompanied by the releasing of an additional hole at the surface. As a result, both the band bending (φ) and electrical conductivity (ϵ) increase (Fig. 5d), which gives rise to an increase in work function ($\Delta\Phi > 0$) and DC current really observed in experiments. It is obvious that chemisorption of others gases implies other surface reactions, which can lead either to an increase or a decrease in the majority carrier density in the grain boundary region and hence to an increase or a decrease in the work function and conductivity of the film. In fact, the response of tellurium based films to ammonia was shown [7] to arise from reduction of tellurium oxide atoms present on the surface and intergrain regions, which also act as acceptors. Note that, in this experiment, the influence of dipole component of the work function, which can arise from the existence of a double electric layer on the surface layer, does not manifest itself evidently. Therefore, the potential drop across such a possible double charged layer is omitted in Fig. 5d.

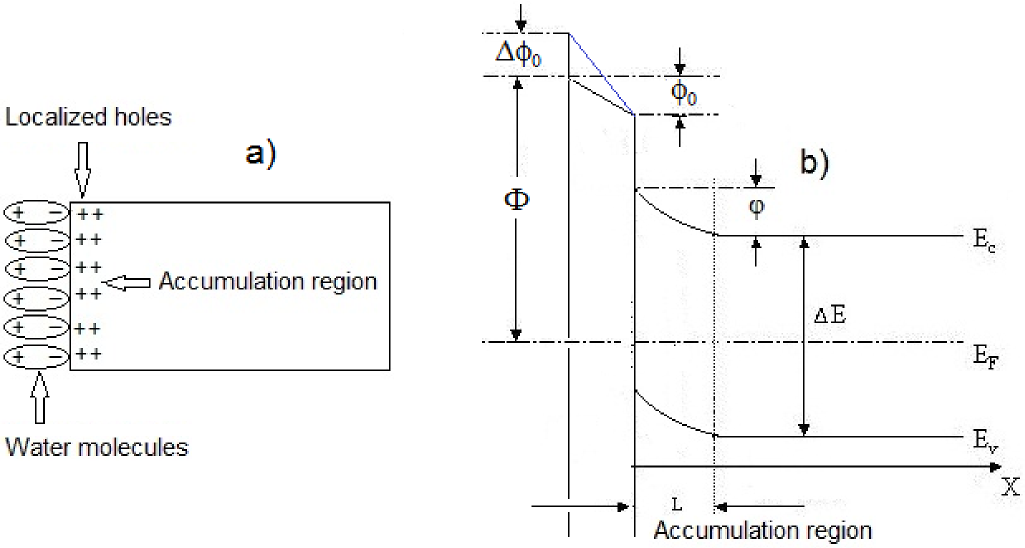

Fig. 6. Formation of an electric double layer by water physisorbtion (a) and its effect on work function of chalcogenide semiconductor (b).

On the other hand, a double electric layer can be easily created and controlled by the adsorption of dipole molecules, such as water one. The water increases the work function change ($\Delta\Phi > 0$) but diminishes the electrical conductivity of the film ($\Delta\sigma < 0$) that could be related to peculiarities of water molecules. It is well known that a water molecule is an unusual molecule. Being threefold coordinated, it exhibits a high ($15\cdot10^{-30} C\cdot m$) dipole moment. As the molecule of H_2O approaches the surface of a positively charged Te film, it rotates and orientates its dipole moment perpendicular to this surface with a negative pole inward. At the same time, the free lattice hole becomes more and more localized at the point of the surface that water molecule approaches, and a very weak bond due to forces of electrostatic polarization is formed. Localization of the same free holes diminishes the electrical conductivity of the film; that is, the opposite of NO_2 response can be observed. Figures 6a and 6b schematically illustrate how a decrease in conductivity and an increase in work function are produced by surface hole localization resulting from the preferential alignment of the water dipoles.

Hence, the effect of water vapor is due to the orientation polarization of H_2O molecules on the surface and the formation of week bonds with an electrostatic origin. Confirmed by experiment, these bonds can be easy removed by heating (Fig. 4), while the effect of water vapor does not disappear completely. This means the orientation polarization of the same physisorbed H_2O molecules is accompanied by their stretching along the dipole, which can result in a "weak" form of chemisorptions. In the "weak" bond, the chemisorbed H_2O molecule forms [8] a valence-saturated and electrically neutral structure, but requires a higher temperature to be removed.

5. Conclusions

- Tellurium thin films can be used in the development of effective work function gas sensitive devices. The sensors can operate at room temperature and show considerably short response times as well as sensitivity in the ppm and sub-ppm concentration range.
- The NO_2 sensing mechanism involves the "strong" chemisorptions, which results in an increase in band bending, work function, and electrical conductivity of the films.
- The effect of water vapor is due to a simple physical adsorption of dipole H_2O molecules accompanied by an increase in potential drop across the electric dipole layer, which results in an increase in work function. Simultaneously, the electrical conductivity of the film decreases due to hole localization resulting from the preferential alignment of the water dipoles with a negative pole inward.

References

[1] Yu.G. Vlasov, Yu.E. Ermolenko, A.V. Legin, and Yu.G. Murzina, J. Anal. Chem. 54, 476, (1999).

[2] S. Marian, K. Potje –Kamloth, D. Tsiulyanu, and H-D. Liess, Thin Solid Films, 359, 108, (2000).

[3] K. Besocke and S. Berger, Rev. Sci. Instrum. 47, 840, (1976).

[4] A.D' Amico, C.D. Natale, R. Paolesse, A. Mantini,C. Goletti, F. Davide, and G. Filosofi, Sens. Actuators, B 70, 254, (2000).

[5] M. Kastner and H. Fritzsche, Phil. Mag. B 37, 199, (1978).

[6] J.Greyson, Carbon, Nitrogen and Sulfur Pollutants and Their Determination in Air and Water, Marcel Dekker Inc., New York. 1990.

[7] S. Sen, K.P. Muthe, N. Joshi, S.C. Gadkari, S.K.Gupta, J. M. Roy, S.K. Deshpande, and J.V. Yakmi, Sens. Actuators, B 98, 154, (2004).

[8] F. Volkenstein , The Electronic Theory of Catalysis on Semiconductors, Pergamon Press, Oxford, 1963.

FORECASTING THE TYPE OF PRECIPITATION FROM CUMULONIMBUS CLOUDS

E. A. Zasavitsky, E. I. Potapov, I. A. Garaba, S. E. Bejenaru, L. I. Korotkova, and V. P. Popova

Institute of Electronic Engineering and Nanotechnologies "D.Ghitu",
Academy of Sciences of Moldova, str. Academiei 3/3, Chisianu, MD 2028 Republic of Moldova
E-mail: efim@nano.asm.md

(Received 1 June 2012)

Abstract

Original techniques for determining the type of precipitation, including the dangerous phenomena on the basis of experimental observations of the cumulonimbus clouds are described. The experimental basis for the developed method was the data of radar observations of the evolution of cumulonimbus clouds over the territory of the Republic of Moldova in 2006–2011 using the ASU-MRL software-hardware radar complex. It is shown that the error of separation of the precipitation type does not exceed 2% of cases and is largely determined by the accuracy of determination of W_{max}.

1. Introduction

Forecasting the type of precipitation from cumulonimbus clouds (*Cb*) with great vertical development is one of the most pressing problems in improving and enhancing the quality of weather forecasts as well as in solving many applied problems which use information about Cb clouds. It is cumulonimbus clouds that are associated with hazard phenomena, such as hailstorms, heavy rainfalls, etc., which often have disastrous effects. The nature shows examples of their negative consequences every year throughout the world, including the Republic of Moldova.

Synoptic forecasting based on weather maps, satellite information, and the thermodynamic state of the atmosphere is generalized probabilistic data on the area of formation of these clouds and their characteristics, without reference to localized areas of the Earth's surface that can be subjected to adverse effects of heavy rainfall or hail from particular *Cb* clouds. In this regard, more detailed information on the distribution of cumulonimbus clouds in space and time is provided by the use of radar aids (weather radars) for researching the radio-echo fields of *Cb* clouds. To date, on the basis of radar and thermodynamic characteristics of clouds, such as radar reflectivity (Z dBZ), maximum reflectivity (Z_{max}), cloud isosurface top temperature with Z = 45 dBZ (Z_{45}), zero degree isotherm height (H_0), and their combinations, some methods (techniques) for forecasting the type of precipitation events have been developed. However, these methods have considerable zones of ambiguity in indicating the precipitation falling on the Earth (22 to 46%) [1–4]; this leads to significant errors in their use in actual practice and to respective consequences.

It is extremely important to improve the methods (techniques) of precipitation type forecasting for the active influences on Cb clouds in implementing the actions (programs) to prevent hail damage, trigger more precipitation, etc. At present, programs of active influence, in varying degrees, are being implemented in many countries, including the Republic of Moldova.

The establishment of a network of "storm warning" of people about hazard weather phenomena on the basis of radar observations of the cloudy atmosphere is currently widespread in many countries.

In all cases, for the implementation of the above actions, forecasting the type of precipitation from high-intensity cumulonimbus clouds is of great importance.

2. Description of the Proposed Model

The proposed method of forecasting the type of precipitation falling on the Earth's surface is based on the modern concepts of the physics of formation and growth of precipitation particles (liquid and ice phases) and conditions of their accumulation and falling out depending on specific thermodynamic and radar characteristics of convective clouds.

The experimental basis for the developed method was the data of radar observations of the evolution of cumulonimbus clouds over the territory of the Republic of Moldova in 2006–2011 using the ASU-MRL software-hardware radar complex in cooperation of the Special Service for Active Influences on Hydrometeorological Processes of the Republic of Moldova and the Institute of Electronic Engineering and Nanotechnology "D.Gitsu," Academy of Sciences.

The study covered 107 days with synoptic and thermodynamic conditions favorable for the development of deep convection clouds; during these days, hailstorms (with varying diameters) and rainfalls (with varying intensity) from Cb clouds were observed. During these days, using the currently available techniques, prognostic stratifications of air temperature and humidity in the troposphere have been plotted and the following parameters have been determined:

- upper convection level (km);
- convection top air temperature (degrees C);
- zero degree isotherm height (km);
- maximum updraft speed, W_{max} (m/s);
- temperature at maximum updraft speed (degrees C);
- altitude of maximum updraft speed (km), etc.

The most important factor that determines the size of hail particles in clouds is updraft speed. To determine it, we use the formula of N. Glushkova, which is widely applied for this purpose [5]:

$$W_{\max} = \sqrt{2\Delta T_{\max} \cdot \eta}\,,\ \ \eta = \frac{T_{h1} - T_{h2}}{T_{h1}} \lg \frac{P_{cond}}{P_m}\,,\ \ \Delta T_m = (T' - T)_{\max} \tag{1}$$

$T_{h1} - P_{cond}$ are the condensation-level temperature and pressure;

T_{h2} and P_m are the temperature and pressure at the upper stratum boundary $(T' - T)_{max}$;

$W = W_{max}$, $(T' - T)_{max}$ is the maximum deviation of the condition curve (T') from the stratification curve(T); it characterizes the instability of the atmosphere.

During the above days, we analyzed 216 convective cells, in which, based on the value of radar parameter Z_{max}, we determined the presence of large precipitation particles in the cloud and recorded the precipitation of hail or rain (ice particles melted in the warm sub cloud layer) on the Earth's surface.

It is found that the separation of the type of precipitation from convective cells of cumulonimbus clouds is most clearly described by the value of dimensionless parameter *K*, which is the ratio between the values of the layer of growth of hail particles in the cloud $\Delta N = N_{45} - H_0$ and the layer of their melting, i.e., the layer below the zero degree isotherm (H_0), as well as by the value of updraft speed in the cloud layer W_{max}. The value of K is calculated through the formula:

$$K = (H_{45} - H_0) / H_0 . \tag{2}$$

The relation of K and W_{max} for various types of precipitation (liquid, ice) is diagrammatically shown in the figure; the table lists the values of these quantities from the curve of their separation.

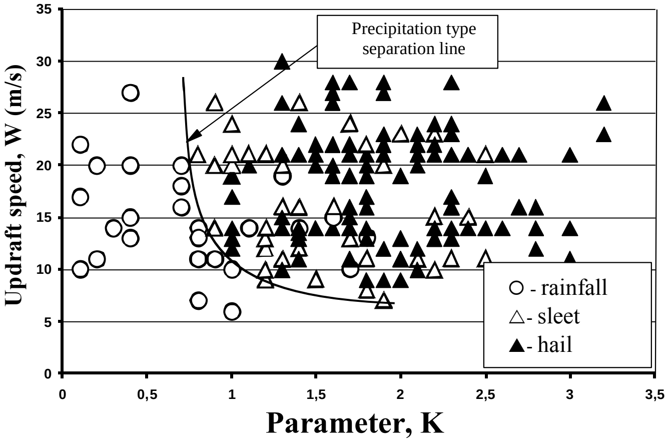

Fig. 1. Type of precipitation from cumulonimbus Cb clouds depending on the values of updraft speed (W_{max}, m/s) and parameter K.

Table 1. Separation of the type of precipitation from cumulonimbus clouds into rain, mixed (rain and solid), and solid precipitation (o—rainfall; Δ—sleet; ▲—hail) according to values of $\mathbf{W_{max}}$ and ***K***

W, m/s	k <1	k =1	k =1.25	k =1.5	k =1.75	k =2.0	k =2.25	k =2.5	k =2.75	k ≥3.0
5 <W<7.5	○	○	○							
7.5 ≤W<10	○	○	○	○/Δ,▲	○/Δ,▲	Δ,▲	Δ,▲			
10 ≤W<12.5	○	○/Δ,▲	○/Δ,▲	○/Δ,▲	○/Δ,▲	Δ,▲	Δ,▲	Δ,▲	▲	▲
12.5 ≤W<15	○	○/Δ,▲	○/Δ,▲	○/Δ,▲	○/Δ,▲	Δ,▲	Δ,▲	Δ,▲	▲	▲
15 ≤W<17.5	○	○/Δ,▲	○/Δ,▲	○/Δ,▲	Δ,▲	Δ,▲	Δ,▲	Δ,▲	▲	▲
17.5 ≤W<20	○	○/Δ,▲	○/Δ,▲	Δ,▲	Δ,▲	Δ,▲	Δ,▲	Δ,▲	▲	▲
20 ≤W<22.5	○	Δ,▲	Δ,▲	Δ,▲	Δ,▲	Δ,▲	Δ,▲	Δ,▲	▲	▲
22.5≤W<25	○	Δ,▲	Δ,▲	Δ,▲	Δ,▲	Δ,▲	Δ,▲	Δ,▲	▲	▲
25≤W<27.5	○/Δ		Δ,▲	Δ,▲	Δ,▲	Δ,▲	Δ,▲	Δ,▲	▲	▲
27.5≤W<30			▲	▲	Δ,▲	Δ,▲	Δ,▲	Δ,▲	▲	▲

The error of separation of the precipitation type does not exceed 2% of cases and is argely determined by the accuracy of forecasting of W_{max}.

To calculate W_{max}, it is necessary to do the following.

1. Based on constant-pressure maps, calculate the prognostic values of temperature (T) and humidity (T_d) at the time of maximum development of convection.
2. On a blank form for an aerological diagram in skew coordinates for the warm period (ADSW), taking into account the obtained values of temperature and humidity, plot a "stratification curve" and a "condition curve" of the atmospheric air. In the absence of advection, it is necessary to use stratification curves (actual) plotted from radiosonde data for 03 h and the ground-level values of T and T_d at the time of maximum heating of the near-ground air.
3. According to the stratification and condition curves on a convective instability (CI-4) aerological diagram, calculate the value of ΔT_m, which is the maximum deviation of the condition curve from the stratification curve, or the degree of contact of the nearest moist adiabatic line and the stratification curve.
4. Based on the stratification and condition curves plotted on a blank form for ADSW, determine the values of other terms appearing in formula (1) and the value of W_{max}.

The zero degree isotherm height (H_0) is also determined according to the stratification curve plotted on a blank form for ADSW.

The maximum level of isosurface with Z = 45 dBZ for each convective cell (its radar image) is determined from a series of vertical cross sections of the cloud that are displayed on a PC monitor after the automatic collection of information on the cloudy atmosphere using an ASU-MRL system.

After substituting the values of N_{45} and H_0 into formula (2), the value of K is calculated.

3. Conclusions

Based on experimental data of radar observations of the evolution of cumulonimbus clouds over the territory of the Republic of Moldova in 2006 ÷ 2011 using the ASU-MRL software-hardware radar complex was developed an original method for determining the type of precipitation, including the dangerous phenomena. In this case error of separation of the precipitation type does not exceed 2% of cases and is largely determined by the accuracy of determination of W_{max}.

References

[1] Yu. A. Dadali Nekotorye zakonomernosti radiolokatsionnykh kharakteristik konvektivnykh oblakov, Trudy Vysokogornogo geofizicheskogo instituta, 1978, issue 47, pp. 53-59.

[2] E.M. Livshits, A.N.Starostin, and V.S.Shvetsov, Metod indikatsii gradovykh oblakov s ispol'zovaniem polozheniya nulevoi izotermy, Trudy Tsentral'noj aerologicheskoi observatorii, 1984, issue 64, pp. 55-61.

[3] M.T.Abshaev, RD 52.37.596-98, Federal'naya sluzhba Rossii po gidrometeorologii i monitoringu okruzhayushchei sredy, Moskow, 1998.

[4] M. Dixon and G. Wiener, J. Atmos. Oceanic Technol., 10, 6, 785 (1993).

[5] N.Sh. Bibilashvili, I.I. Burtsev, and Yu.A. Seregin, Rukovodstvo po organizatsii i provedeniyu protivogradovykh rabot, Leningrad, Gidrometeoizdat, 1981, 168 p.